

Benjamin Balder Grønnberg Andresen

In-process monitoring of layer temperature in fused filament fabrication

Master's thesis in Department of Mechanical and Industrial Engineering

Supervisor: Christer Westum Elverum

Co-supervisor: Martin Steinert

June 2022

Benjamin Balder Grønnberg Andresen

In-process monitoring of layer temperature in fused filament fabrication

Master's thesis in Department of Mechanical and Industrial Engineering

Supervisor: Christer Westum Elverum

Co-supervisor: Martin Steinert

June 2022

Norwegian University of Science and Technology

Faculty of Engineering

Department of Mechanical and Industrial Engineering



Norwegian University of
Science and Technology

Preface

This Master's thesis is written in collaboration with TrollLabs at the Norwegian University of Science and Technology (NTNU). TrollLabs have provided me with the tools and equipment to do my research and has done so in an excellent manner. Giving me unique freedom to use my built-up knowledge to do valuable research in a field that is increasingly growing. This thesis completes my Master's degree at the Department of Mechanical and Industrial Engineering at NTNU in Trondheim, and is worth 30 ECTS credits.

I want to thank everyone at TrollLabs for being patient with my work. The 3D printer that I have used has made a lot of noise, and I am glad to finally turn it off for good. Everyone in the lab has been an absolute joy to work with. Conversations about projects and everyday topics have made this project much more rewarding. Thanks to my co-supervisor, Martin Steinert, for making this project possible and always being there when I needed it. Thanks to Sindre Wold Eikevåg for his engaging ideas, great help, and presence. Finally, I want to thank my supervisor Christer Westum Elverum for excellent guidance, valuable knowledge, and the freedom of independent work.

Last and foremost, I would like to thank my family and friends. The support you have given me through my time at the university is greatly appreciated and will never be forgotten. I will especially thank my sister, Mia. You have always had my back, your support has meant a great deal, and I am eternally grateful.

I am dedicating this thesis to my brother, Einar. Without you, I probably would not have experienced this.

Benjamin Balder Grønneberg Andresen
TrollLabs, NTNU, Trondheim, June 2022

Abstract

Temperature management in Fused Filament Fabrication (FFF) is getting more relevant considering predictable strength in Additive Manufacturing (AM) components. By monitoring layer temperatures in FFF in-process, strength can be determined by comparing layer temperature to strength for a given configuration. Methods to determine layer temperatures in-process is still under development, and non-contact infrared temperature sensors are becoming more applicable. With increasing sensitivity, faster processing times, and more reliable temperature calibrations, non-contact infrared temperature sensors show promising features for layer temperature measurements in FFF. Using a highly accurate non-contact infrared temperature sensor, this project was able to monitor layer temperatures in-process in great detail. Each layer pattern was easily identified, and each movement in the fabrication could be observed. The result was a layer temperature model of the specimen used for the experiments. The potential of full temperature models is introduced, but with an uncertainty of emissivity effect. Through experiments with the non-contact infrared temperature sensor and in-contact thermocouples change in emissivity could be predicted for the material used. This project introduces the use of a precise non-contact infrared temperature sensor for monitoring layer temperatures in-process and the effect of emissivity for dynamic temperatures in FFF.

Sammendrag

Temperaturstyring i Smeltet FilamentStyring (SMS) blir mer relevant for forutsigbar styrke i Additiv Tilvirkete (AT) komponenter. Ved å overvåke lagtemperaturer under prosessen av SMS, kan styrke bestemmes ved å sammenligne lagtemperatur med styrke for en gitt konfigurasjon. Metoder for å bestemme lagtemperaturer i prosessen er fortsatt under utvikling, og berøringsfrie infrarøde temperatursensorer blir mer anvendelige. Med økende følsomhet, raskere behandlingstider og mer pålitelige temperaturkalibreringer, viser berøringsfrie infrarøde temperatursensorer lovende funksjoner for lagtemperaturmålinger i SMS. Ved å bruke en svært nøyaktig berøringsfri infrarød temperatursensor ble dette prosjektet i stand til å overvåke lagtemperaturer i prosessen i detalj. Hvert lagmønster ble lett identifisert, og hver bevegelse i fabrikasjonen kunne observeres. Resultatet ble en lagtemperatur modell av prøven som ble brukt til forsøkene. Potensialet til fulltemperaturmodeller er introdusert, men med en usikkerhet om emissivitetseffekt. Gjennom eksperimenter med den kontaktløse infrarøde temperatursensoren og termoelementer i kontakt med materiale kunne endringer i emissivitet forutses. Dette prosjektet introduserer bruken av en presis berøringsfri infrarød temperatursensor for å overvåke lagtemperaturer i prosessen av SMS og effekten av emissivitet for dynamiske temperaturer i SMS.

Table of Contents

List of Figures	v
List of Tables	vii
List of Abbreviations	viii
1 Introduction	1
1.1 Non-Contact Temperature Monitoring in FFF	1
1.2 Project Goal	1
2 Theory	2
2.1 Infrared Thermometry and Thermal Radiation	2
2.1.1 Emissivity	2
3 Materials and Methods	3
3.1 Materials and Equipment	3
3.1.1 CT-SF22 Infrared Temperature Sensor	3
3.2 Sensor Setup Design	5
3.3 Sensor Setup Calibration	6
3.3.1 Diagonal Aiming	7
3.3.2 Vertical Aiming	10
3.4 Emissivity Tests	12
3.4.1 Observation Angle Test	12
3.4.2 Melt Test	15
3.5 Layer Temperature Measurements	17
3.5.1 In-Process Measurements	19
3.5.2 Specific Measurements	19
4 Results	22
4.1 Emissivity Tests	22
4.1.1 Observation Angle Test	22
4.1.2 Melt Test	24
4.2 Layer Temperature Measurements	26
4.2.1 In-Process Measurements	26
4.2.2 Specific Measurements	29
4.2.3 In-Process Versus Specific Measurements	30

5	Discussion	32
5.1	Method and Results	32
5.1.1	Observation Angle Test	32
5.1.2	Melt test	33
5.1.3	In-process Measurements	34
5.1.4	Specific Measurements	35
5.1.5	In-Process Versus Specific Measurements	36
5.2	Uncertainties	37
5.2.1	Emissivity	37
5.2.2	Geometry	37
5.2.3	Angled Measurements	37
5.2.4	Aiming	37
5.2.5	Noise	37
5.2.6	Vibrations	37
6	Conclusion	38
7	Future Work	39
7.1	Accurate Aiming	39
7.2	Dynamic Emissivity Control	39
7.3	FFF Temperature Modeling	39
7.4	Combining G-code and Temperature Modeling	39
	References	40
	Appendix	43
A	Video presentation	43
B	Data and Calculation	43
C	Mechanical Drawings	73
D	Additional Results	79
E	Python Code	81
F	Engineering Design and Materials, Specialization Project	91

List of Figures

1	Optical chart for the CT-SF22 sensor with the optional lens. D = Distance from the front of the sensor to the object. S = Spot size [1].	4
---	--	---

2	Section of Figure 1. S_1 , S_2 , and D are known values from Figure 1, and d is a measured distance between spot sizes S_1 , S_2	4
3	CAD model of the two designs used as sensor setup.	6
4	Installed sensor setups.	6
5	Calibration setup.	7
6	Adjusting along Y-axis.	7
7	Adjusting along Y-axis.	8
8	Distance between sensor and hotend.	9
9	Measurements used to find the angle of the sensor.	9
10	Example of focal point base length (FPBL) on a flat surface.	10
11	Vertical aiming setup.	11
12	Aiming vertical.	11
13	Representation of equal FPBL and spot size while aiming vertically.	12
14	Angle test jig dimensions, infill pattern, and finished build.	13
15	Thermocouple placement.	13
16	Jig setup in oven.	14
17	Set Angles	15
18	Melt test specimen and setup.	16
19	Measurements done to document the distance between the sensor and test specimen.	17
20	Full melt test setup.	17
21	Full geometry of DogBone structure.	18
22	Obtaining x and y-coordinates for the sensor.	19
23	Obtaining height between sensor and object.	20
24	Red box indicating the lines of code implemented in the G-code. The implemented code ensures the sensor hovers over the appointed object for a given time.	20
25	Cutting procedure of DogBone.	21
26	Full angle test. The green and the blue line indicates the temperature measured by two thermocouples, while the red line indicates the temperatures measured by the infrared temperature sensor.	22
27	Close up of the measurements shown in Figure 26. Displaying each cycle for the designated observation angle of the sensor.	23
28	Internal temperature of the sensor through the Observation Angle Test.	24
29	Displaying all three temperatures with the ramp up of the melt test.	25
30	Displaying all three temperatures with decreasing temperatures of the melt test.	25
31	Melt test after testing. Numbers showing where thermocouples 1 and 2 were placed.	26
32	Readings of a Test Line at the beginning of a print.	26
33	Full In-process measurement of DogBone with printer speed of 30 mm/s.	27

34	Section of the full In-process measurement from Figure 33.	28
35	Section of the section in Figure 34. Displaying temperature readings during a single layer.	29
36	Specific temperature measurement of a Half model printed at 30mm/s.	29
37	Specific temperature measurements versus printer speed of Half and OneFourth model using the CT-SF22 sensor.	30
38	Specific Measurements of Half model versus middle layer temperatures from In-process Measurements.	31
39	Comparison of two different specific measurement methods. Both methods are performed on a OneFourth model.	36
A.1	QR-code to video presentation of how a reversed layer is laid.	43
A.2	QR-code to video presentation of early process of a in-process measurement.	43
D.1	Test line.	79
D.2	OneFourth model specimens.	79
D.3	Half model specimens.	80
D.4	In-process specimens.	81

List of Tables

1	CT-SF22 Specifications	4
2	Fixed settings for test specimen production.	18
3	Printing speeds used and designation for specimens	18

Abbreviations

AM Additive Manufacturing.

CAD Computer Aided Design.

CF Carbon Fiber.

FFF Fused Filament Fabrication.

FPBL Focal Point Base Length.

ISO International Organization for Standardization.

MDF Medium-Density Fibreboard.

ME Material Extrusion.

NTNU Norwegian University of Science and Technology.

PA6 Polyamide 6.

1 Introduction

1.1 Non-Contact Temperature Monitoring in FFF

In the field of Additive Manufacturing (AM), there is an ongoing development from prototyping applications to the manufacturing of actual end-use products [2, 3]. AM offers a lot of advantages over conventional manufacturing in increasing complexity in the parts, Computer Aided Design (CAD) models being directly transferable to the machine via slicing software, and does not require any additional tooling, see Section F. Where conventional manufacturing needs machines, tools, and operators to shape the material into the desired shape, AM is generally performed in a single step [3]. Time is considerably reduced from design to finished product, making it highly compliant for low-volume specialized production. These advantages are attractive for specialized markets such as defense, aerospace, competitive sports, automobile, and medical [4–7].

The field of Fused Filament Fabrication (FFF) is the most common use of AM, since the hardware is accessible both as high-end production equipment and as primary machines for consumer use [2, 8]. Most forms of FFF heat up the plastic filament and build the layers by Material Extrusion (ME) where the molten material is pushed through a nozzle, onto the build plate or past layers. Deposited material should be semi-melted to keep the ideal shape and size [8]. Molecular diffusion in the material during deposition depends on local temperatures and associated times [9]. The residual energy in adjacent regions must be sufficient for good bonding, or distinct boundaries between new and previously deposited material will occur [8]. Process parameters such as tool path, layer thickness, deposition velocity, infill rate, and environment temperature are factors that affect bonding [10, 11]. Although polymer materials mainly have been used for prototypes, mock-ups, and tooling [2], the development of new engineering plastics and fiber-reinforced polymers [12] makes it possible to produce load-bearing end-use products with FFF. Currently, there is a lack of research on the thermal effects on high-performance polymers, as most mechanical properties and manufacturing parameters are tested for commodity polymers that are not suitable for load-bearing applications [9, 13–17]. Continuous mapping of the temperature profiles can provide the necessary information [18] to predict strength through a FFF manufactured components, see Section F. Recordings of temperatures have been obtained by embedding temperature sensors at various locations into middle-planes of printed structures [19] to monitor and map temperatures through components, but with limited local measurements [18]. The non-contact nature of thermography are a promising alternative [18] to embedded temperature sensors. In recent years, infrared imaging techniques have been growing greatly. Improved with increased spatial and temporal resolution of the infrared detectors, faster processing times, higher temperature resolution, and specific image processing. Upgraded sensitivity and more reliable temperature calibrations gives more accurate data than were previously available [20]. However, accurate temperature measurements via infrared thermography is challenging with respect to calibration of emissivity, which is a function of temperature and observation angle [18]. To conclude, additional research on non-contact infrared temperature measurements is requested for the in-process monitoring of layer temperature in FFF.

1.2 Project Goal

As stated, layer temperature monitoring in FFF has great potential. By using a non-contact infrared temperature sensor with an optional lens allowing for precise measurements, this project aims to prove that infrared temperature sensors can monitor and model layer temperatures through FFF in-process. By experimenting with increasing and decreasing temperatures, and changing observation angles, while in-contact thermocouples are measuring the actual temperature, the effect of changing emissivity will be studied. Together, the studies of layer temperature modeling and change in emissivity can prove that non-contact temperature sensors can help determine predictable strength in FFF manufactured components.

2 Theory

2.1 Infrared Thermometry and Thermal Radiation

Infrared sensors can be used contactless, allowing for measurements of inaccessible or moving objects. Infrared thermometers are optoelectronic sensors, they calculate the surface temperature based on infrared radiation emitted from objects [1]. Infrared thermometers essentially consist of four main parts: Lens, spectral filter, detector, and a controller. The lens determines the optical path, which is characterized by the ratio of Distance to Spot size. The spectral filter adjusts the wavelength range, which adjusts the emitted infrared radiation that is transformed into electric signals by the detector and controller [1]. Objects emit a certain amount of infrared radiation depending on their temperature. The intensity of the radiation changes with changing temperatures. Infrared thermometry uses a wave-length range of $1 - 20\mu\text{m}$ for measuring the thermal radiation [1]. Materials have different intensities of the emitted radiation, described by a constant known as the emissivity factor, ϵ (epsilon), further explained in Section 2.1.1. All objects are built of continually vibrating atoms, where higher energy atoms vibrate more frequently. Charged particles, including these atoms, generates electromagnetic waves. Vibration increases with increasing temperatures, and thus the spectral radiant energy [21]. As a result, all objects continually emit radiation at a rate with the wavelength distribution that is determined by the temperature of the object and its spectral emissivity, ϵ . Radiant emission is commonly treated in terms of the concept of a black body. A black body absorbs all radiation and is according to Kirchoff's law, a perfect radiator. "The energy emitted by a blackbody is the maximum theoretically possible for a given temperature." [21].

2.1.1 Emissivity

To evaluate how close a practical blackbody is to an ideal blackbody the concept of emissivity has been introduced. Emissivity is a measure of the deviation of ability to emit thermal radiation between a real surface and a ideal blackbody [22]. Emissivity of a real surface is in principle a function of wavelength, temperature and angle of view [23]. Generally, a wavelength band of $8 - 14\mu\text{m}$ is preferred for high performance imaging due to its higher sensitivity to ambient temperature objects, and better transmission through mist and smoke [21]. Increased observation angles have proven to decrease emissivity according to Sobrino and Cuenca [24]. Theoretically, emissivity values range from 0 to 1, where the value of 1 refers to a blackbody. Physical objects can better be described with a emissivity scale ranging from 0.01 to 0.99 [25]. Highly polished metallic surfaces e.g. aluminum or copper have an emissivity below 0.1, while roughened or oxidized metallic surfaces have values greater than 0.6, depending on amount of oxidation. Most flat-finish paints are around 0.9, non transparent plastics typically 0.95, while water and human skin are about 0.98 [1, 25]. Emissivity is a known factor for most materials, and can be found in various tables. Determination of a unknown emissivity for a material can be done using a thermocouple or a contact sensor, and modify the emissivity factor until the infrared thermometry device is displaying the same value as the thermocouple or the contact sensor [1].

When determining a new emissivity it is important to know about reflected thermal energy. Any thermal energy originating from other objects can reflect off of the target that measured, this concerns especially object with low emissivity, like polished metals [25]. Higher emissivity objects is less influenced by reflected thermal energy, but as emissivity decreases, reflected thermal energy increases. Increased reflected thermal energy effects the measured temperature using radiation thermometry, adjusting the emissivity compensates for the reflection and allows for accurate temperature measurements [26].

3 Materials and Methods

3.1 Materials and Equipment

An overview of central material information, equipment, and software is listed below.

- **Gravograph Laser Ingraver** - A laser cutter from Gravograph was used to manufacture parts for specialized designs.
- **Medium-Density Fibreboard (MDF)** - MDF is used for parts in specialized designs.
- **Modified Creality CR10** - The printer used to produce material samples and components is a modified Creality CR10 [27] with an upgraded hotend, super volcano, bed heater, enclosed heating chamber, and enclosed filament drying chamber. It uses a hardened steel 0.6mm nozzle [27].
- **Polymaker PA6-CF** - The filament used is Polymaker PA6-CF with a diameter of 1.75mm. The nylon filament contains 20% chopped carbon fibers [28]. The filament reels have been stored at room temperature in closed bags with silica bags for six months.
- **SuperSlicer** - The software used to control printer settings and translate models to G-code is SuperSlicer. SuperSlicer is a forked, open access version of PrusaSlicer, allowing more control over settings [29].
- **Fluidd** - Fluidd is a user interface for Klipper, a 3D printer firmware.
- **CT-SF22** - For non-contact temperature measurements, the infrared sensor CT-SF22 from Micro-Epsilon is used.
- **CompactConnect** - Temperature readings from the temperature sensor is processed using the CompactConnect software.
- **ET-959, 2-Channel Thermocouple Thermometer** - Digital thermometer for measuring and monitoring air, surfaces, or liquid temperatures.
- **PK 410 ESAB** - A drying cabinet was used for heated observation angle tests.
- **Single Hot Plate Burner** - A single hot plate burner from Clas Ohlson was used to heat objects. Model no. HP102-T2.
- **GoPro Hero 8** - Recording of experiments is done using a GoPro Hero 8 action camera.
- **Microsoft Excel** - Manually recorded temperature readings are done in Microsoft Excel spreadsheets.
- **NotePad++** - NotePad++ was used to manipulate G-code.
- **JupyterLab** - To process and present data, JupyterLab was used. Writing Python code, data was read, organized, and used to generate figures.

3.1.1 CT-SF22 Infrared Temperature Sensor

The sensor used in this project is a CT-SF22 sensor from Micro-Epsilon. Relevant specifications are given in Table 1. Source: Micro-Epsilon [1].

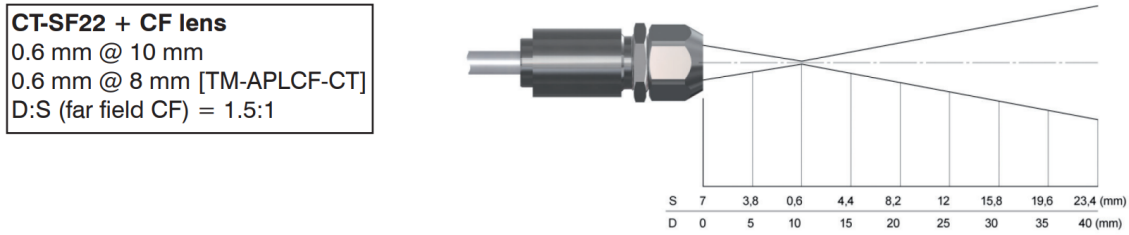


Figure 1: Optical chart for the CT-SF22 sensor with the optional lens. D = Distance from the front of the sensor to the object. S = Spot size [1].

Table 1: CT-SF22 Specifications

CT-SF22	Specifications
Measuring range	$-50 - 975^{\circ}C$
Ambient temperature	$-20 - 180^{\circ}C$
Integrated thermocouple	YES
Spectral response	$8 - 14\mu m$
System accuracy	$\pm 1^{\circ}C$ or $\pm 1\%$
Response time (95 % signal)	150 ms
Emissivity/gain	0.100 ... 1.100 (adjustable via programming keys or software)
Typical applications	Non-metallic surfaces
Weight	40 grams
Interface (optional)	USB, RS232, RS485, CAN, Profibus DP, Ethernet, Modbus RTU, (optional plug-in modules)
Software (optional)	CompactConnect

Measurements of spot size diameter are dependent on the distance between the measuring object and sensor. The optional CF lens allows the measurement of small objects and can be combined with the CT-SF22 model. An optical chart is given in Figure 1. The distance is always measured from the front edge of the sensor. To avoid measuring errors, the object measured should always have at least the same size as the spot size or bigger [1].

Spot sizes in between the distances given in Figure 1 can be calculated using simple trigonometry, see Figure 2.

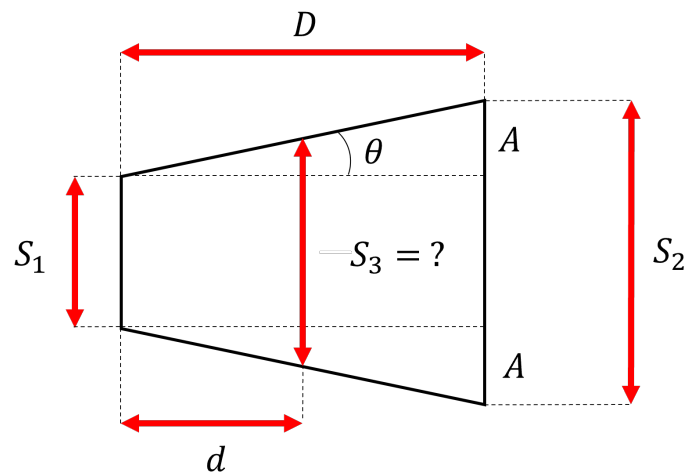


Figure 2: Section of Figure 1. S_1 , S_2 , and D are known values from Figure 1, and d is a measured distance between spot sizes S_1 , S_2 .

Equation 1, 2, and 3 can determine the unknown spot size, S_3 .

$$A = \frac{(S_2 - S_1)}{2} \quad (1)$$

$$\theta = \tan^{-1} \frac{A}{D} \quad (2)$$

$$S_3 = S_1 + 2(\tan \theta * d) \quad (3)$$

3.2 Sensor Setup Design

The sensor was installed before all other experiments to establish its required purpose on the printer. Finding an appropriate setup was essential to see the sensor in its intended environment. By installing the sensor, experiments could be done while printing, but experiments not involving printing could also be performed.

A set of requirements were made for the functionality of the setup. The requirements are listed below;

1. **Adjustable:** The sensor needs to be adjustable to get close to the hotend and aim correctly.
2. **Rigidity:** The setup needs to be rigid to make sure the sensor stays fixed under printing as vibrations occur.
3. **Modular:** The setup needs to be modular to test all sensor angles of interest.
4. **High temperatures:** The setup needs to withstand high ambient temperatures as chamber temperature is set to $70^\circ C$ during experiments. The parts of the setup are close to hotend and super volcano, which holds a temperature of $300^\circ C$ while printing.
5. **Lightweight:** The setup needs to be lightweight not to disrupt the printer's performance.
6. **Non-interference:** The setup cannot interfere with components of the printer or printed parts.

Through CAD, a design with parts made of laser-cut MDF and 3D-printed PA6-CF fulfilled the requirements, see Figure 3. All parts are held together with M5.5 bolts, see Figure 4. Two sensor mounts were designed for aiming. One mount is designed for in-process readings with an angle. The other mount is designed for accuracy to point the infrared temperature sensor 90° down at objects. The sensor mounts are manufactured in PA6-CF because of its melting temperature of $218.5^\circ C$ [28], which means they can withstand the chamber temperature and heat dissipated by the super volcano and hotend. The infill percentage of the mounts is set to 4% to minimize weight. Mechanical drawings of the mounts can be found in Section C. Two existing bolts on the extruder were used as attachment points, making it easy to attach and detach the jig, see Figure 4a. All parts except the sensor mounts and steel bolts are made of laser-cut 6mm MDF, mechanical drawings of the components can be found in Section C.

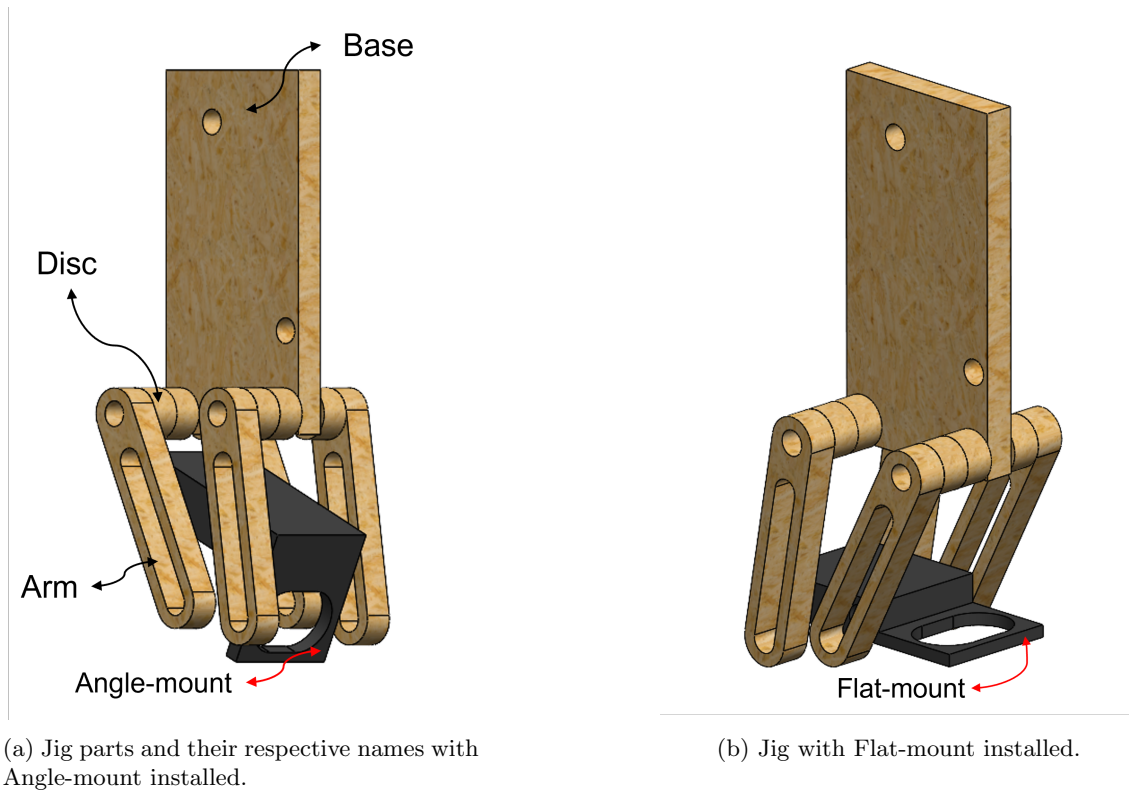


Figure 3: CAD model of the two designs used as sensor setup.

M5.5 bolts were used to lock the sensor positions in place. Note that after a couple of runs in the printing environment, the MDF shrinks due to evaporation moisture, leaving the bolts loose. Re-tightening to bolts is needed to avoid errors. Figure 4 shows the two designs installed with the sensor on the modified Creality CR10.

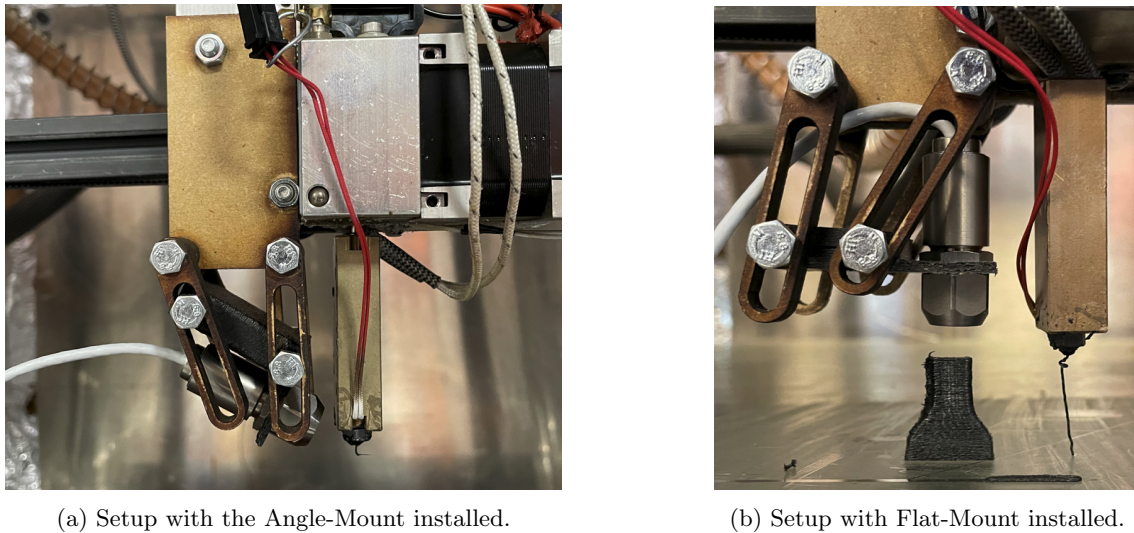


Figure 4: Installed sensor setups.

3.3 Sensor Setup Calibration

Calibration of the sensor setup is essential for proper temperature measurements. The following two sections explain the aiming procedure for the two mounts mentioned.

3.3.1 Diagonal Aiming

Aiming is a matter of precision when operating with the optional lens. As explained in Section 3.1.1 the object measured has to be bigger than the spot size. Having a spot size bigger than the object measured results in errors. Margins of error are small when operating the sensor with the optional lens. Aiming diagonal is meant for in-process measurements, and it is essential to be precise. Aiming was done by turning up the temperature of the hotend to an arbitrary temperature of 60°C so that the sensor could distinguish between surrounding temperatures and hotend temperatures, see Figure 5 for the calibration setup.

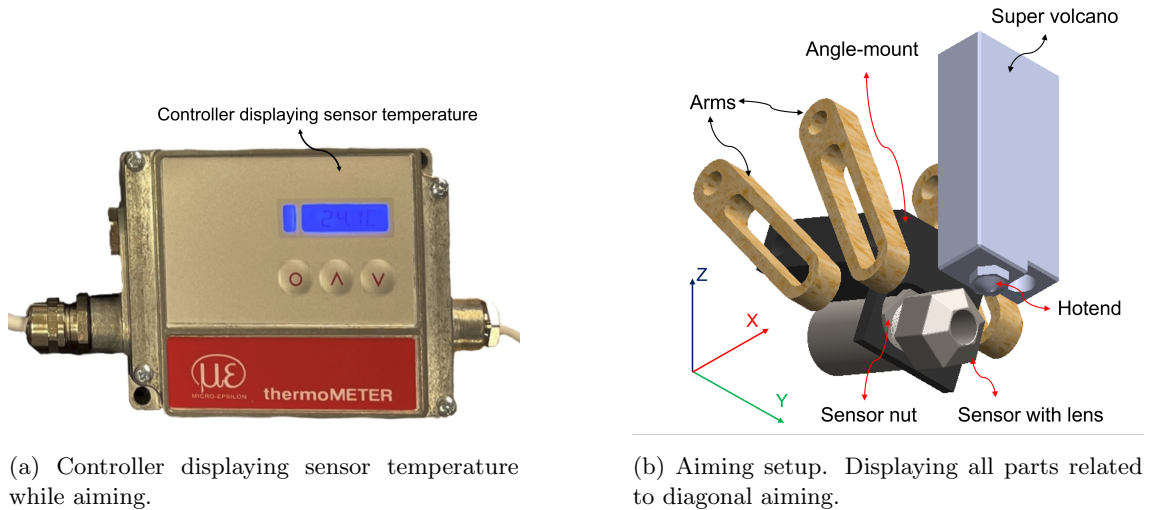


Figure 5: Calibration setup.

Set hotend temperature to 60°C . Manually adjust the sensor along the Y-axis, ensure it hits the lowest point of the hotend by rotating around the Y-axis and monitoring the temperatures on the controller, see Figure 6. The sensor should be lined up with the hotend parallel with the X-axis. The Y-axis is then locked by tightening the sensor nut.

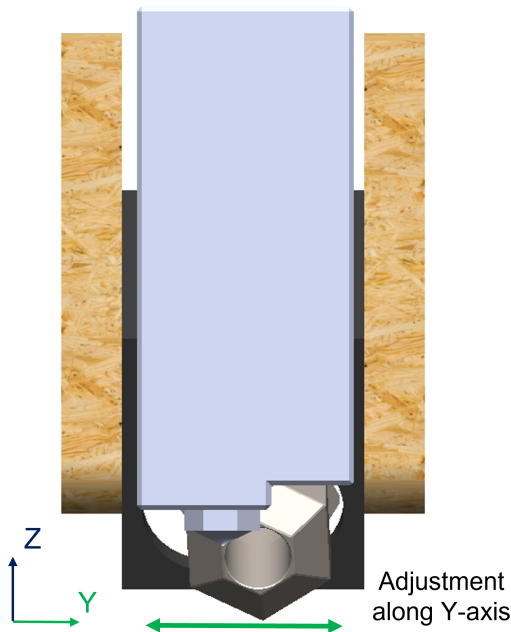


Figure 6: Adjusting along Y-axis.

Further adjustments are made by rotating around the Y-axis, adjusting height along the Z-axis, and distance to hotend along X-axis, see Figure 7. Adjust the length along the X-axis as close as possible to the hotend. Rotate the setup to be higher than the hotend. Measure air temperature, and be attentive when identifying air temperature versus hotend temperature. The point where the controller stops displaying hotend temperatures is the optimum point. Now every axis can be locked by tightening every bolt.

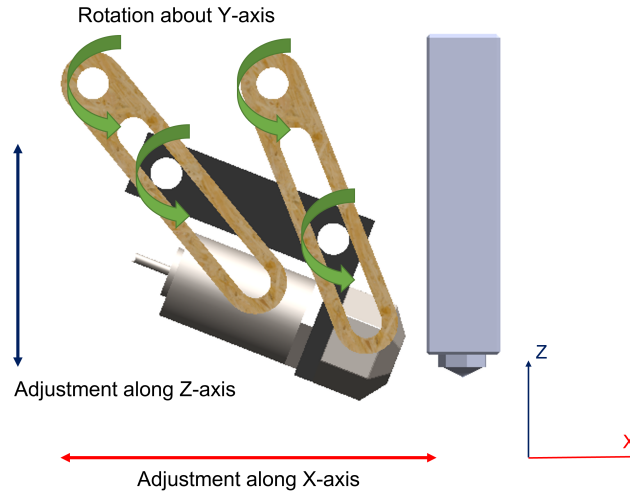


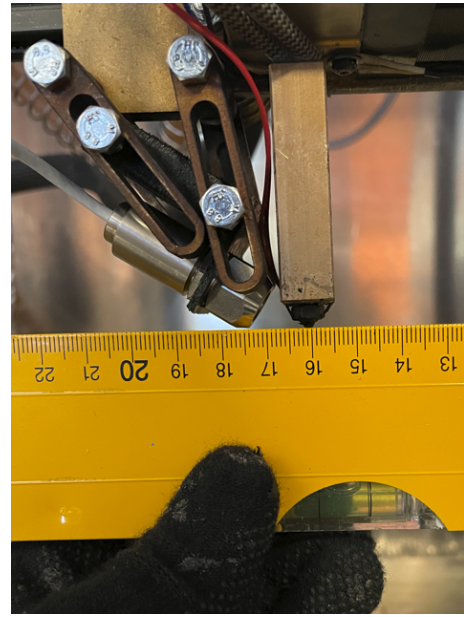
Figure 7: Adjusting along Y-axis.

Hitting this point and then using a cooled-down PA6-CF piece measuring 4 in diameter, close to the hotend, helps confirm that the sensor is aiming at the desired location. The dimensions of the piece of PA6-CF are set based on using a 5mm thick surface for the experiments. Note that, when tightening the bolts, the position of the setup tends to move. Ensure that the correct position is locked by repeatedly using the cooled-down PA6-CF piece and monitoring the controller's temperature, this is crucial to ensure the sensor is measuring on the desired surface.

To get the most accurate measurements and avoid errors, a focal point of 0.6mm is optimum. The sensor needs to have a distance of 10mm from the object measured to have a focal point of 0.6mm, see Figure 1. With the Angle-mount the super volcano interfered with the sensor, limiting the distance from the sensor to the object. The sensor needs to have a certain angle to measure the print's surface, and the sensor body needs to be higher than the hotend not to crash with the print. In Figure 8 distance between the sensor and hotend is measured, and the height of the sensor is assured to be higher than the hotend using a spirit level.



(a) Distance between sensor and hotend.

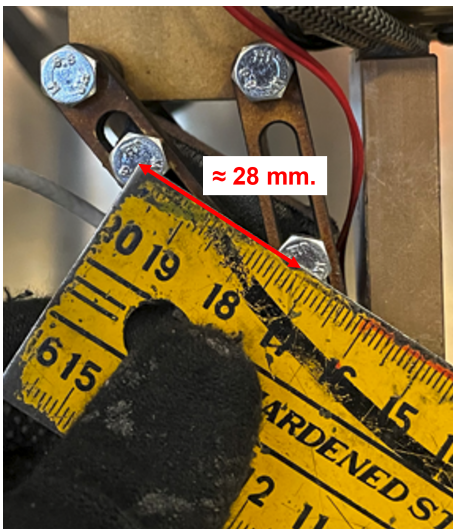


(b) Sensor assured to be higher than the hotend.

Figure 8: Distance between sensor and hotend.

To document the angle of the sensor while mounted, measurements were done to the bolts attaching the mount to the sensor jig, which are always parallel to the sensor. Measuring the distance between the bolts and the horizontal difference, the angle could be approximated using simple trigonometry. From Figure 9, we found that the horizontal distance between the bolts was 24mm, and the diagonal length was 28mm. The angle of the sensor is given by α in Equation 4.

$$\alpha = \cos^{-1} \frac{24}{28} \approx 31^\circ \quad (4)$$



(a) Diagonal distance.



(b) Horizontal distance.

Figure 9: Measurements used to find the angle of the sensor.

Considering Figure 1, measurements with an angle cause the focal point to be stretched at a flat surface, now called Focal Point Base Length (FPBL), see Figure 10.

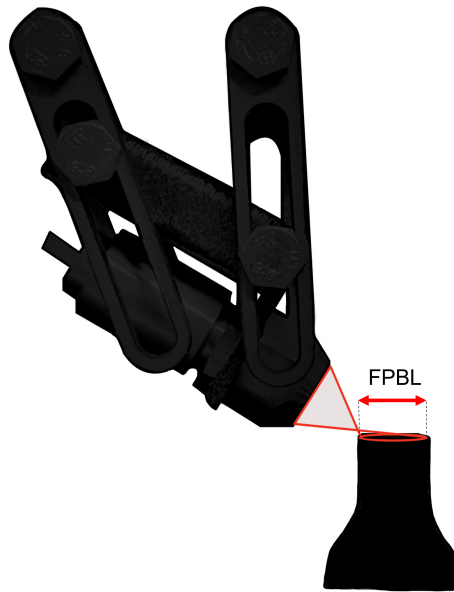


Figure 10: Example of focal point base length (FPBL) on a flat surface.

The focal point initially has a diameter of 2.88mm using the calculation method given in Section 3.1.1 at a distance of 13mm (using the worst-case distance taken from Figure 8a). But gets an FPBL of 11.28mm when the sensor is at an angle of 31° , see Section B for calculations. The FPBL causes room for error and should be further discussed in Section 5.

3.3.2 Vertical Aiming

Vertical aiming is meant for more accurate measurements by getting the desired focal point for the sensor and neglecting the possible heat reflection of the hotend. Vertical aiming uses the flat sensor mount, see Figure 3b, to set the sensor to point vertically down at the printing bed and objects of interest. The vertical aiming can be used for straight line measurements along the X-axis or specific temperature measurements of surfaces by guiding the sensor manually. Navigating the sensor manually involves implementing coordinates into the G-code to hover the sensor above the designated surface.

Manually adjust the sensor along the Y-axis, ensuring it hits the lowest point of the hotend by rotating around the Y-axis and monitoring the temperatures on the controller, see Figure 11 and Figure 5a. The sensor should be pointed and lined up with the hotend, parallel with the X-axis. The Y-axis is then locked by tightening the sensor nut.

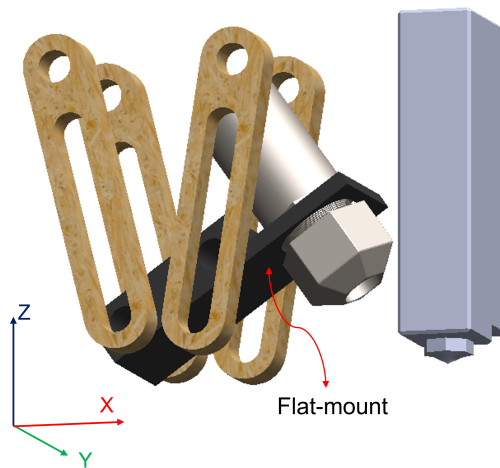


Figure 11: Vertical aiming setup.

After the Y-axis is locked, the sensor can be pointed vertical down parallel with the super volcano, and the bolts can be tightened, see Figure 12.

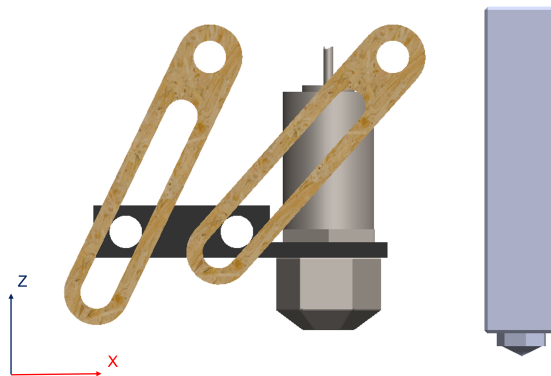


Figure 12: Aiming vertical.

Using vertical aiming, the focal point does not get stretched, as explained in Section 3.3.1. Vertical aiming assures that the FPBL is equal to the spot size and opens for more precise measurements, see Figure 13.



Figure 13: Representation of equal FPBL and spot size while aiming vertically.

3.4 Emissivity Tests

Two emissivity tests were performed to evaluate how the emissivity factor differs for PA6-CF with an increasing observation angle and increasing temperatures. Both tests used two thermocouples to validate the actual temperature of the material, as this is the recommended method to determine the unknown emissivity [1].

3.4.1 Observation Angle Test

As emissivity changes with different observation angles [24], an observation angle test was performed. The test was performed in a temperature-changing environment to observe emissivity changes clearer. A drying cabinet - PK 410 ESAB was used for the heated environment, and a test jig was manufactured in PA6-CF. The jig has implemented angle markers to quickly adjust to four specific angles in-between measurements, see Figure 14a. The distance between the lens and the surface measured is 10mm. The distance between the inner side of the sensor mount and the surface area is 21mm, and the length of the lens is 11mm, see Section C and [1]. Having 10mm between the sensor and the test surface, ensures the smallest focal point, ensuring that the sensor does not measure outside of the appointed test surface.

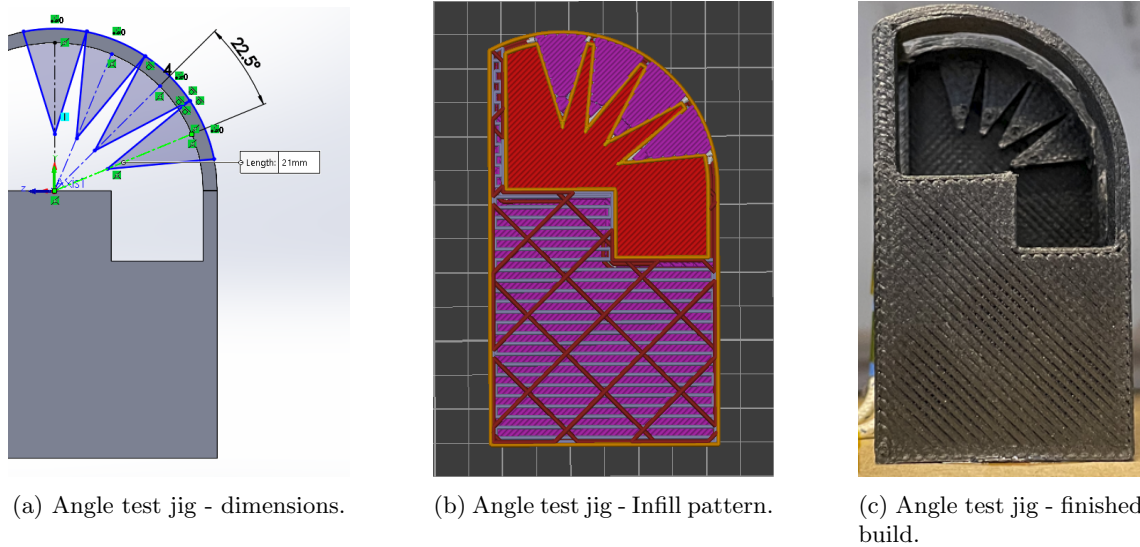


Figure 14: Angle test jig dimensions, infill pattern, and finished build.

The jig is printed with 7.5% infill, see Figure 14b. This low amount of infill makes the surface area 0.32mm thick, so that it heats up effectively. There are other areas in the print that are denser for the thermocouples to measure the temperature of the material rather than the air inside the jig. See Figure 14c for the finished build of the angle test jig.

Two holes were drilled into the jig to fit two thermocouples, see Figure 15a. One thermocouple was placed right underneath where the sensor did its readings, while the other thermocouple was placed in one of the walls on the side of the jig to ensure more contact with the material, see Figure 15b.

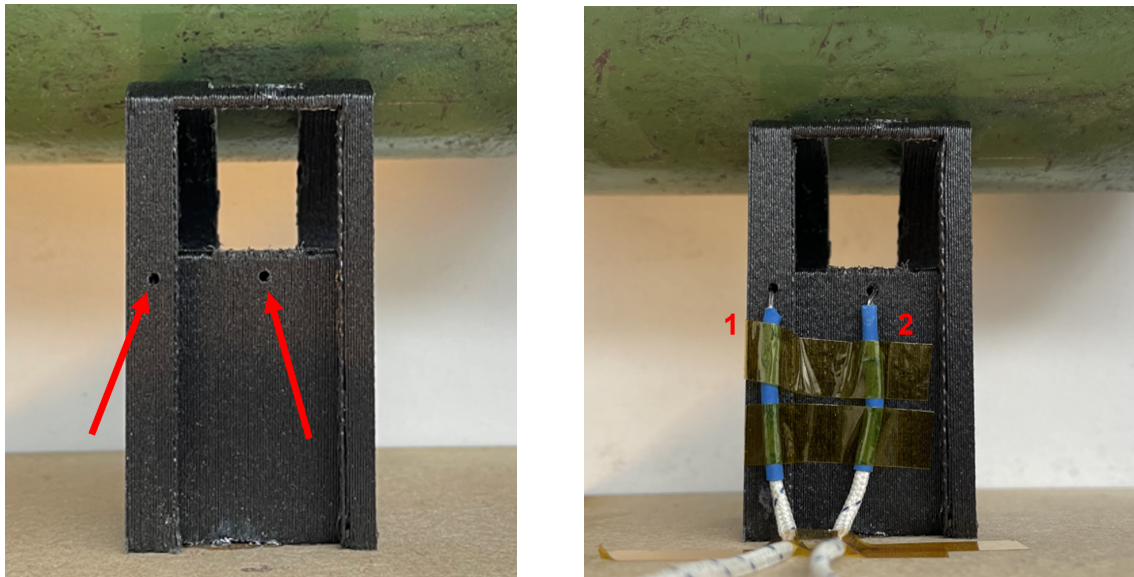


Figure 15: Thermocouple placement.

The jig is glued to an MDF base and placed inside the oven with the sensor and thermocouples. The base is secured with weights on the sides, and all wires run through the venting hole of the

oven, see Figure 16.



Figure 16: Jig setup in oven.

The oven temperature is set to 170°C as the max operating ambient temperature of the sensor is 180°C , see Table 1. The oven used tends to overshoot before stabilizing to the set temperature, setting the operating temperature to 170°C assures the sensor wont get overheated. There is an implemented thermocouple built into the sensor, monitoring the internal temperature of the sensor, see Figure 28 for results.

The sensor is placed at a 0° angle for the first ramp-up to 170°C and left to set to make sure the material heats up to the set temperature before changing the observation angle. Letting the temperature set for each angle is referred to as cycles. Measurements were done between 24 and 32 minutes for each cycle. Adjusting the observation angle for each cycle involves opening the oven and manually adjusting the sensor to the different angles. Four angles were measured in the experiment, angles are shown in Figure 17.

(a) Angle: 0° (b) Angle: 22.5° (c) Angle: 45° (d) Angle: 67.5°

Figure 17: Set Angles

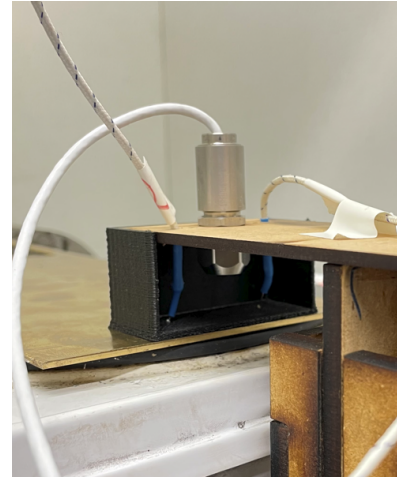
Oven, thermocouple, and sensor temperatures are manually documented for each cycle, see Section B for data. The data is analyzed and documented for further comparisons. Data of the internal temperature is extracted by having CompactConnect running, documenting every reading done by the sensor, Section 4.1.1 for results.

3.4.2 Melt Test

As the emissivity factor changes for increasing temperatures [23], a melt test was performed. The melt test uses two thermocouples to measure the actual temperature of the material as it heats up above melting temperature. As the thermocouples measure the actual temperature, the sensor does readings, and comparisons can be made. A test specimen was designed to block any reflecting heat, and two pits were drilled to fit the thermocouples, see Figure 18a. Mechanical drawings of the melt test specimen can be found in Section C. The test specimen is FFF manufactured in PA6-CF.



(a) Melt test specimen with drilled pits. Numbers showing placement of thermocouples 1 and 2.



(b) Melt test setup. The sensor is mounted in the middle while the two thermocouples are placed approximately 30mm apart.

Figure 18: Melt test specimen and setup.

The thermocouples and sensor are held in place by a contraption that ensures the right height, proper placement for the sensor and thermocouples and leaves electric cords out of harm's way. The thickness of the test specimen and height from the heated surface to the sensor mount is measured to calculate the distance between the sensor and test specimen, see Figure 19. The contraption also ensures that a small amount of pressure is applied from the thermocouples onto the melt test specimen, making sure the thermocouples stay fixed in the pits under the experiment, see Figure 18b. A single burner hot plate was used to heat the test specimen with a piece of thick metal in between. The sensor is connected to a computer running CompactConnect, and an ET-959 high accuracy device measures the temperature of the thermocouples. The emissivity factor is set to $\epsilon = 0.95$ for the first 270 seconds. At this point, the single burner hot plate reaches its highest temperatures. After reaching maximum temperature, the single burner hot plate is turned off. A new emissivity factor is then calculated based on one of the thermocouple temperatures using the integrated emissivity factor calculator in CompactConnect. Which of the two thermocouple temperatures used for the emissivity calculation is based on the temperature closest to the sensor temperature. The whole experiment is documented by recording every reading with a GoPro camera, later analyzing the video and writing the most interesting readings in Microsoft Excel, see Section B for data. The whole setup is displayed in Figure 20, note that the GoPro is not included in the figure.

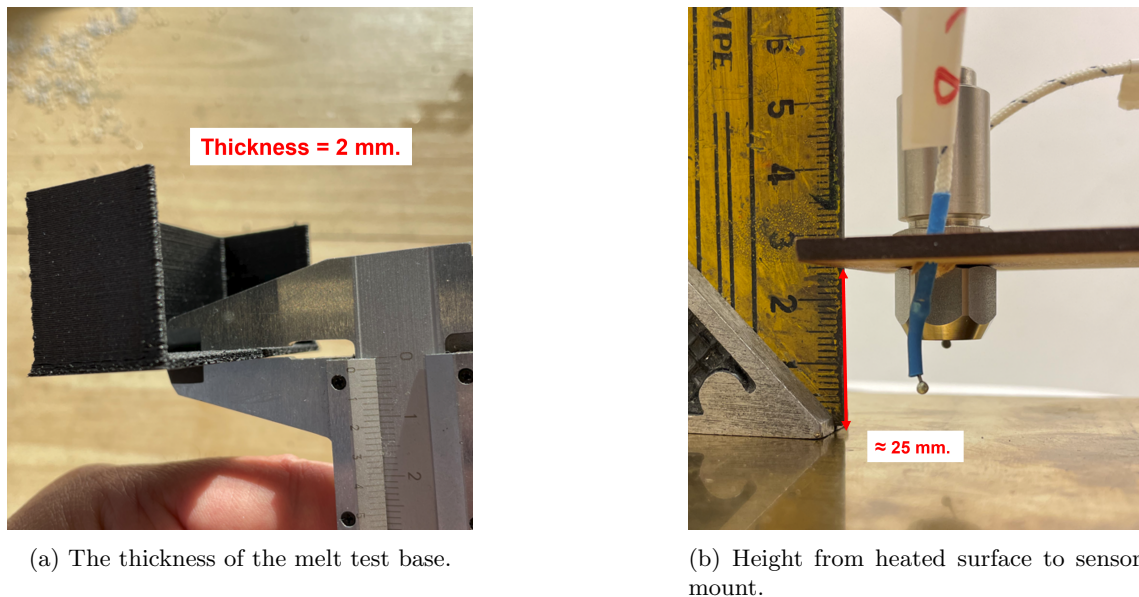


Figure 19: Measurements done to document the distance between the sensor and test specimen.

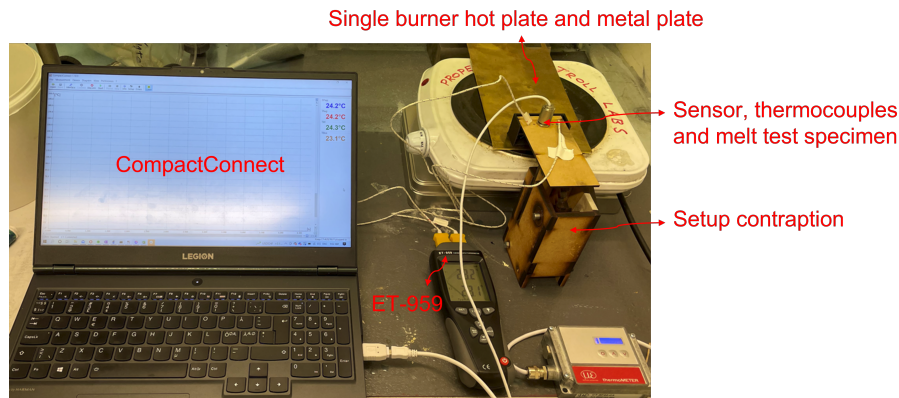


Figure 20: Full melt test setup.

The experiment is executed by starting the readings for the sensor in CompactConnect, turning on the ET-959 device, hitting the record on the GoPro camera, and turning the heat to max on the single burner hot plate. The results can be found in Section 4.1.2.

3.5 Layer Temperature Measurements

This thesis performed two experiments for layer temperature measurements using the CT-SF22 temperature sensor. One experiment entailed measuring diagonally, directly at the printed surface, getting the temperature of the last printed layer as a new layer is printed on top. Measuring diagonally is an in-process temperature measurement. In-process measurements mean having the hotend right by the measured surface. The other experiment was specific measurements of the layer temperature without the hotend present. Specific measurements entail guiding the sensor over the surface of interest, which means there is a delay before the actual reading is done. The experiment was carried out to confirm in-process readings by having a more accurate focal point. There are no obstacles between the sensor and the object with specific measurements, like the super volcano is while measuring diagonally. Also, not having the hotend present can show results of effects of reflection of heat from the hotend if there are any.

All layer temperature measurements with the CT-SF22 sensor were performed on a dogbone structure based on the ISO527 standard, hereby named, *DogBone*. Dimension of the DogBone is given in Figure 21.

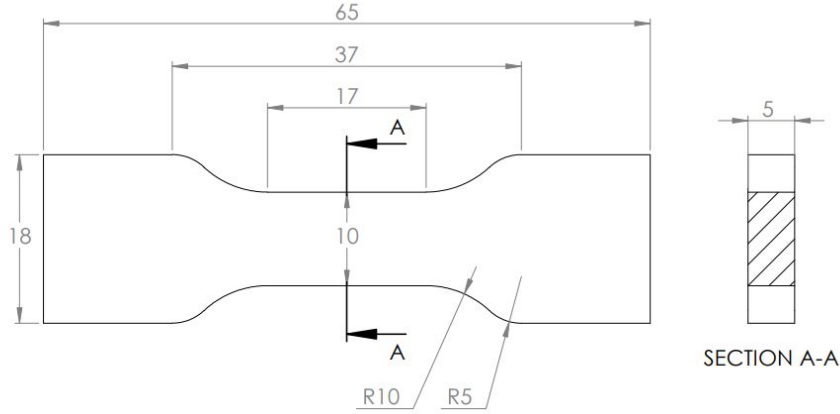


Figure 21: Full geometry of DogBone structure.

The DogBone is printed with fixed settings for consistency, see Table 2.

Table 2: Fixed settings for test specimen production.

Setting	Value
Extruder temperature	300°C
Chamber temperature	70°C
Bed temperature	110°C
Perimeters	1
Layer height	0.32mm
Seam position	Aligned
Infill type	Rectilinear
Infill density	100%
Max acceleration X- and Y- direction	900mm/s ²
Travel speed	180mm/s

Specimens were printed with different speeds to alter the layer temperature, Table 3 gives an overview of the printing speeds used and the designation of the specimens.

Table 3: Printing speeds used and designation for specimens

Printing speed	Specimen designation
4mm/s	v4
5mm/s	v5
6mm/s	v6
7mm/s	v7
8mm/s	v8
9mm/s	v9
10mm/s	v10
11mm/s	v11
12mm/s	v12
14mm/s	v14
16mm/s	v16
18mm/s	v18
20mm/s	v20
25mm/s	v25
30mm/s	v30

3.5.1 In-Process Measurements

In-process measurements aim to capture every layer’s temperature through a geometry. The layer temperature of interest is the previous layer, just as the new layer is printed on top. The procedure to capture the previous layer temperature entailed manipulating the G-code. SuperSlicer sliced the DogBone so that the rectilinear pattern was always laid with the direction the sensor was measuring, measuring the temperature of the newly printed layer instead of the past layer. Reversing the three middle layers should give a clearly visible pattern of the layer temperatures of the previous layer. Reversing the three middle layers can be done using Notepad++. Find the three middle layers in the G-code based on Z-height, and *edit* them in Notepad++ using the commands; *Line Operations* and *Reverse Line Order*. The rectilinear pattern is then printed in the opposite direction of where the sensor is pointing, resulting in measuring the temperature of the last layer printed. The manipulation is done to all specimens listed in Table 3. An analysis of the data is documented and presented using Python in JupyterLab, see Section 4.2.1. Diagonal aiming is required to measure the desired surface, as explained in Section 3.3.1. All in-process measurements used the full geometry of the DogBone (Figure 21) and the settings listed in Table 2 and Table 3. Results can be found in Section 4.2.1.

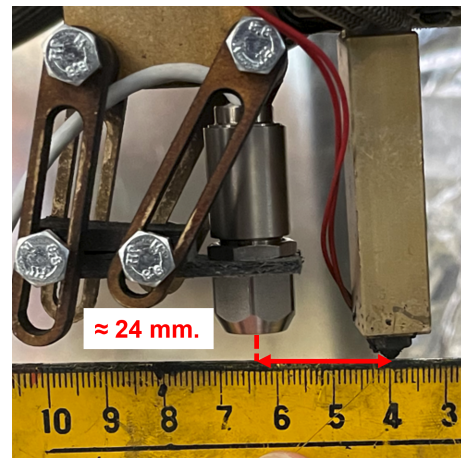
3.5.2 Specific Measurements

Specific measurements of layer temperature were done to assure the precision of the in-process layer measurements. Specific measurements use vertically aiming, as explained in Section 3.3.2. Vertical aiming allows the sensor to get closer to the specimen measured, offering more precision. Vertical aiming assures a more precise focal point, see Figure 13, that obtains precise measurements better. In-process measuring also has the hotend close to the sensor, leaving uncertainties about heat reflection in the readings. Specific measurements have the hotend out of sight from the sensor, neglecting the uncertainty of heat reflection.

Specific measurements entail manipulating the sensor to hover over the object of interest. Use vertical aiming (Section 3.3.2), and measure the distance between the sensor and the hotend, see Figure 22a. Coordinates of the print from SuperSlicer plus the distance between the sensor and hotend give the X-coordinates for the sensor. Using the global Y-coordinates of the object from the slicer gives a precise position on the Y-axis, see Figure 22b.

A distance has to be set between the sensor and the object, this is decided by the Z-height given in the G-code and the fixed height of the sensor. In Figure 23a, an approximate height is 5mm between the sensor and hotend based on the locked position first set. Further, the actual distance is measured using an internal micrometer, see Figure 23b.

To make the sensor hover above the object to document distance and do readings, three lines of code have to be manually implemented into the G-code of the print, see Figure 24. The first line, *M760* opens the valve for the printhead, ensuring no filament is extruded. The second line of code, *G1 X149.89 Y48.43 E0*, is the coordinates that direct the sensor above its appointed object. Lastly, the third line, *G4 P600000* makes the sensor pause over the object, where the time is given in milliseconds, in this case, it is set for 10 minutes for taking measurements between sensor and object. The time set for the tests are 50000ms. The three lines of code are implemented after



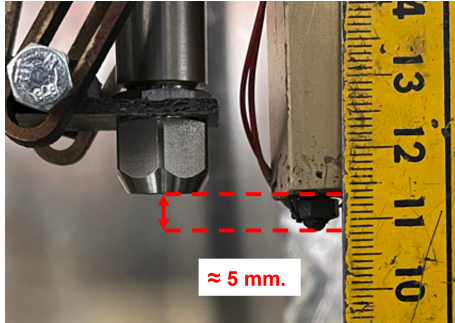
(a) Distance between sensor and hotend.

Object manipulation			
Name:	DogBone_5x10.STL		
World coordinates	X	Y	Z
Position:	125.89	48.43	16.25 mm
Rotate:	0	0	0 °
Scale factors:	100	100	100 %
Size:	18	5	32.5 mm
<input type="checkbox"/> Inches			

(b) Global coordinates of printed specimen obtained from SuperSlicer.

Figure 22: Obtaining x and y-coordinates for the sensor.

the last layer is printed after WIPE_END in the G-code. The procedure is done for each printer speed listed in Table 3.



(a) Approximated height between sensor and hotend.



(b) Measuring the actual height between sensor and object.

Figure 23: Obtaining height between sensor and object.

```
G1 X130.176 Y49.553 E0.06306
G1 X129.247 Y50.482 E0.09910
; INIT stop printing object DogBone_5x10.STL id:0 copy 0
;WIPE_START
G1 F8640;_WIPE
G1 X130.176 Y49.553 E-0.43348
G1 F8640;_WIPE
G1 X130.176 Y48.717 E-0.27585
G1 F8640;_WIPE
G1 X130.169 Y48.723 E-0.00317
;WIPE_END

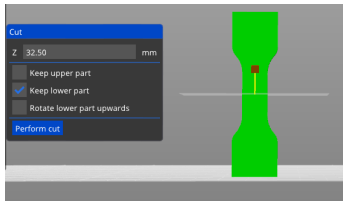
M760
G1 X149.89 Y48.43 E0
G4 P600000

G1 E-0.03750 F3000
G1 Z33.620000 F10800
```

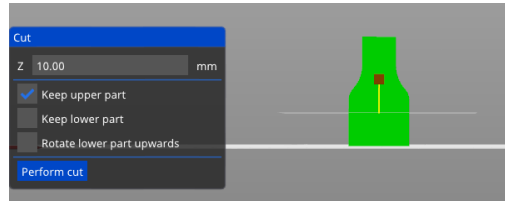
Figure 24: Red box indicating the lines of code implemented in the G-code. The implemented code ensures the sensor hovers over the appointed object for a given time.

All specific measurements used the same coordinates for their experiments. The X and Y-coordinates are given in Figure 24. The distance between the sensor and object was set to 7.5mm. Using Equation 1, 2, and 3 gives a focal point of 2.2mm. A focal point of 2.2mm gives more general measurements of the surface, than a focal point of 0.6mm at a 10mm distance. With these settings, two types of specific measurements were performed.

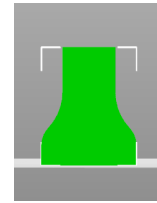
1. **1/2 model:** Involves printing half of the model displayed in Figure 21 and then measuring the temperature of the top layer, essentially measuring the temperature of the mid-layer of the full model. The geometry is referred to as, *Half model*. The cutting procedure is done in SuperSlicer, see Figure 25.
2. **1/4 model:** Involves the same procedure as the first one, only with a smaller model of the original DogBone, see Figure 25c. The model is cut in half, further the bottom 10mm is cut, see Figure 25b. These measurements compare results with former results of layer temperature, done on the same geometry but with a different method. Even though this cut geometry is not exact 1/4 of the DogBone, it is referred to as the *OneFourth model*.



(a) Cutting the DogBone in half.



(b) Cutting the DogBone to *OneFourth*.



(c) One-Fourth model of the original DogBone.

Figure 25: Cutting procedure of DogBone.

Documenting the readings is done with the CompactConnect, using an emissivity factor of $\epsilon = 0.95$. Analyzing the results and getting the global maximum from the readings, further documentation and comparisons can be made. Both experiments use the settings from Table 2 and Table 3. Results can be found in Section 4.2.2

4 Results

This chapter presents the results from emissivity tests, in-process measurements and specific measurements. Results of the in-process measurements, and specific measurements are compared to each other for validation of the in-process measurements. Additional results are given in Section D.

4.1 Emissivity Tests

4.1.1 Observation Angle Test

Figure 26 displays the complete observation angle test with its four cycles. The test was started at 16:30 and ended at 19:16. A ramp-up to 170°C took about 40 minutes, starting to stabilize around 17:10, see Section B for data. The following drops in temperature are due to angle changes, see Figure 27 for more detailed information on each cycle. Between 16:30 and 17:37, the sensor reads a higher temperature than the thermocouples, the time includes cycle 1. During cycle 2, the sensor temperature reading is about the same as the thermocouples. Cycles 3 and 4 show the sensor temperature reading lower than the thermocouples. The plot oscillates for each cycle due to temperature regulations made by the oven. As soon as the oven reaches 170°C , the heat elements turn off. The temperature overshoots reaching a higher temperature than the set temperature. The temperature then decreases before the thermocouple of the oven senses a lower temperature than 170°C . The heat elements then turn back on, and the cycle repeats itself.

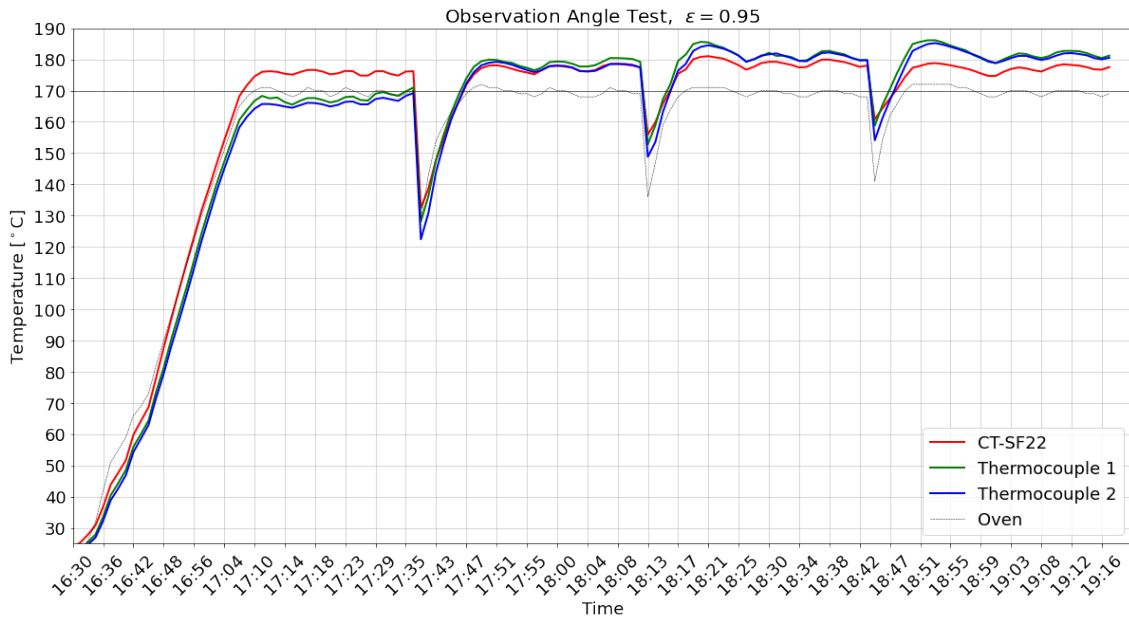


Figure 26: Full angle test. The green and the blue line indicates the temperature measured by two thermocouples, while the red line indicates the temperatures measured by the infrared temperature sensor.

Figure 27 displays each cycle from Figure 26 in more detail. Test time for each cycle is measured from when the oven temperature hits 170°C until a change in angle is made. Cycle 1 had a test time of 27 minutes, cycle 2 a test time of 23 minutes, cycle 3 a test time of 25 minutes, and cycle 4 had a test time of 28 minutes. The following sections explain Figure 27 in more detail:

Cycle 1: Cycle 1 starts at 17:10 and ends at 17:37. Both thermocouples 1 and 2 show lower temperatures than the oven through the cycle. The most significant deviation over the cycle is between the sensor and thermocouple 2 at 17:13, 17:15, 17:16, and 17:18, with a 10.6°C difference. Oven temperature is at the same time 170°C , 168°C , 169°C , and 170°C with the times respectively.

The lowest deviation is between the sensor and thermocouple 1 at 17:37, with a 5.2°C difference. The oven temperature is then 170°C . The thermocouples do not read temperatures of the set temperature before the end of the cycle. The trend of thermocouples 1 and 2 is rising, having temperatures of 168.3°C and 165.7°C , respectively, at the first peak, 17:11. At the end of the cycle, 17:37, thermocouples 1 and 2 have risen to 171°C and 169.2°C , respectively. Sensor temperature stays consistent between 174.8°C and 176.6°C throughout the cycle.

Cycle 2: The second cycle starts at 17:48 and ends at 18:11. The most significant deviation over the cycle is between the sensor and thermocouple 1 at 17:48, with a 2.4°C difference. The oven temperature at the same time is 171°C . The lowest deviation is between the sensor and thermocouple 2 at 17:58, 17:59 and 18:11 with 0°C difference. The oven temperature is then 169°C , 171°C , and 169°C with the times, respectively. All three measured temperatures are above the set oven temperature throughout the cycle, with the sensor reading a maximum of 178.6°C , and thermocouples 1 and 2 reading a maximum of 180.4°C and 179.2°C , respectively. Sensor temperature stays consistent between 175.2°C and 178.6°C through the cycle.

Cycle 3: The third cycle starts at 18:18 and ends at 18:43. The most significant deviation over the cycle is between the sensor and thermocouple 1 at 18:19, with a 4.9°C difference. The oven temperature is at the same time, 171°C . The lowest deviation is between the sensor and thermocouple 2 at 18:43, with 1.7°C difference. The oven temperature is then 168°C . All three temperatures measure above the set temperature, with the sensor reading a maximum of 181°C , and thermocouples 1 and 2 reading a maximum of 185.6°C and 184.5°C , respectively. Sensor temperature stays consistent between 176.7°C and 181°C throughout the cycle.

Cycle 4: The fourth cycle starts at 18:49 and ends at 19:17. The most significant deviation over the cycle are between the sensor and thermocouple 1 at 18:51, with 7.7°C difference. The oven temperature is at the same time, 172°C . The lowest deviation is between the sensor and thermocouple 2 at 19:17, with a 3°C difference. The oven temperature is then 169°C . All three temperatures measure above the set temperature, with the sensor reading a maximum of 178.8°C , and thermocouples 1 and 2 reading a maximum of 186.1°C and 185.2°C , respectively. Sensor temperature stays consistent between 174.4°C and 178.8°C throughout the cycle.

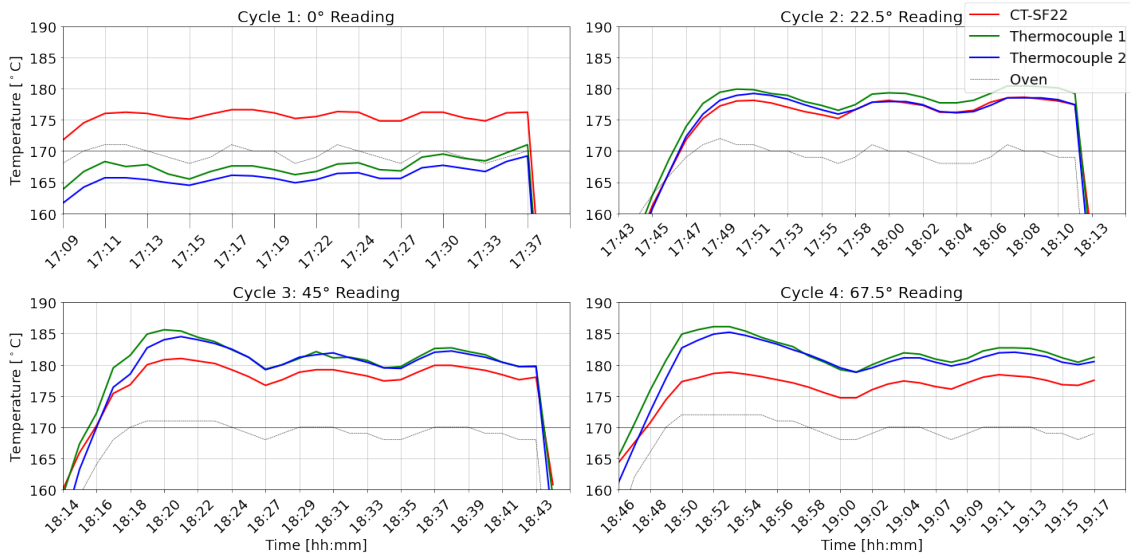


Figure 27: Close up of the measurements shown in Figure 26. Displaying each cycle for the designated observation angle of the sensor.

Figure 28 displays the internal sensor temperature through the entire Observation Angle Test. The plot shows that temperatures never exceed the maximum ambient operating temperature for the sensor, at 180°C .

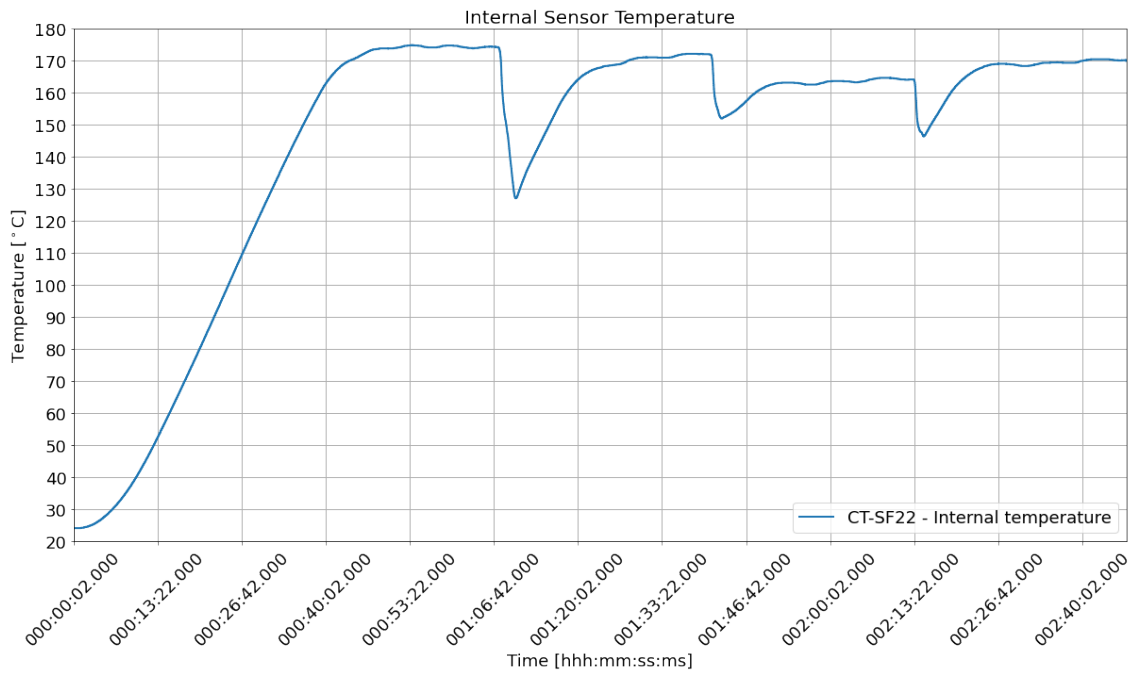


Figure 28: Internal temperature of the sensor through the Observation Angle Test.

4.1.2 Melt Test

Figure 29 show the increasing temperatures of the melt test. The emissivity factor is set to $\epsilon = 0.95$, and data is collected for 270 seconds. Thermocouples 1 and 2 measure about the same temperatures with the same slope for approximately 75 seconds. Between 75 and 150 seconds, thermocouple 2 gets a more gentle slope than thermocouple 1, which continues in a more steady state. After 150 seconds, thermocouple 2 starts to ascend with the same slope as thermocouple 1 again. The sensor measures higher temperatures than both of the thermocouples between 0 and 140 seconds. At 150 seconds, thermocouple 1 starts to measure higher temperatures than the sensor, intersecting at approximately 190°C . Thermocouple 1 continues to read higher temperatures than the sensor through the remaining experiment, ending with a difference of 18.3°C . Thermocouple 2 continues to measure lower temperatures than the two. After about 210 seconds all temperatures show signs of convergence.

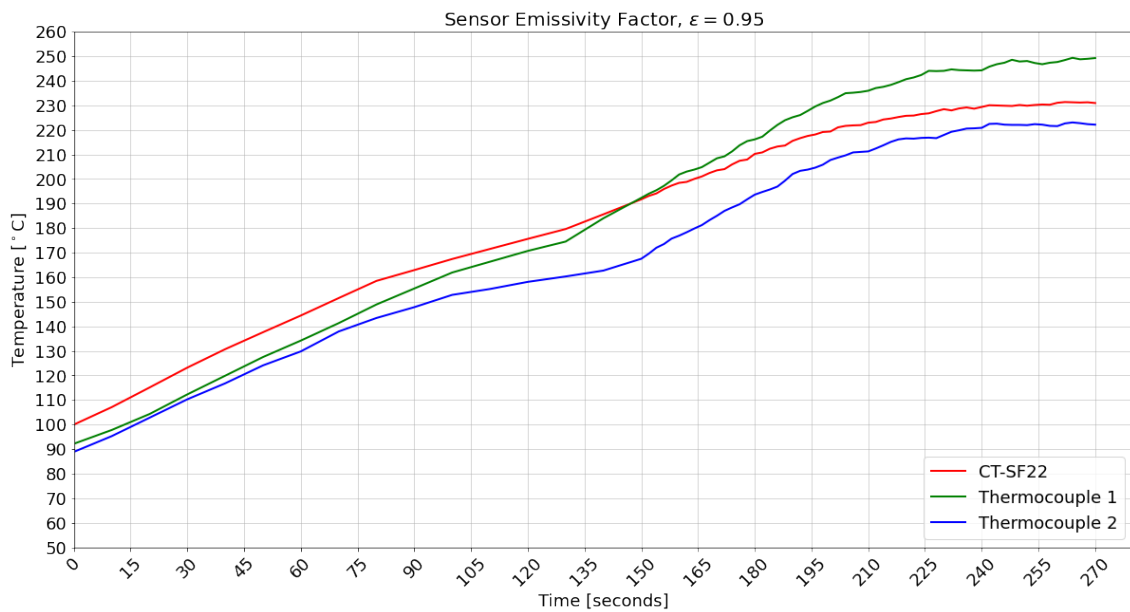


Figure 29: Displaying all three temperatures with the ramp up of the melt test.

Figure 30 displays the decreasing temperature of the melt test. The emissivity factor is set to $\epsilon = 0.857$, and readings are collected for 120 seconds. At this stage, thermocouple 2 has dropped to under 150°C while thermocouple 1 measures close to the sensor temperatures. For the first 84 seconds, thermocouple 1 readings intersects sensor readings seven times. The most significant deviation in the first 84 seconds is thermocouple 1 being 2.4°C higher than the sensor, 2 seconds into the experiment. The last intersection between thermocouple 1 and the sensor is at 84 seconds, with a temperature reading of 193.9°C . After 84 seconds, thermocouple 1 continues to measure lower temperatures than the sensor, the most significant deviation being 3.4°C at 94 seconds. Thermocouple 2 decreases over the entire test period and show signs of oscillation.

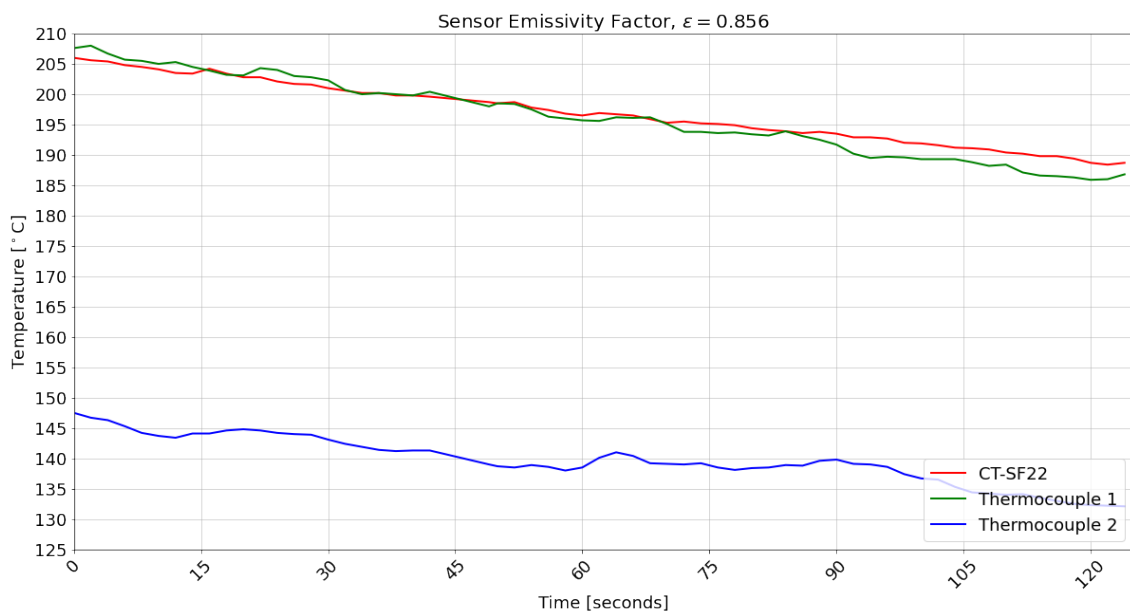


Figure 30: Displaying all three temperatures with decreasing temperatures of the melt test.

Figure 31 show the melt test specimen after testing. The mark to the left shows a bump after thermocouple 1 has been torn out of the melted plastic. The mark on the right shows a sunken

hole, where thermocouple 2 were not needed to be torn out of any melted plastic.

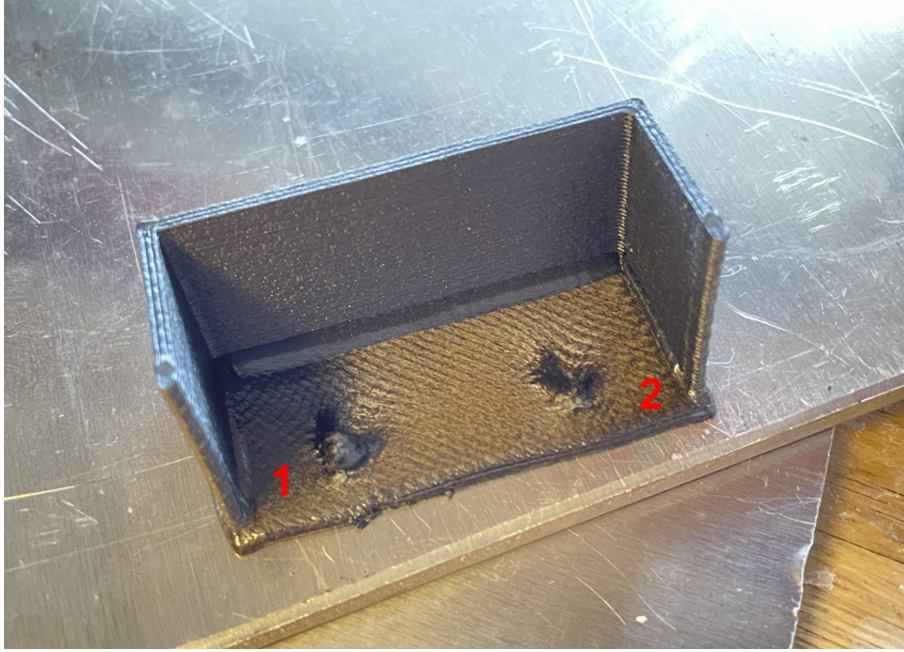


Figure 31: Melt test after testing. Numbers showing where thermocouples 1 and 2 were placed.

4.2 Layer Temperature Measurements

4.2.1 In-Process Measurements

Figure 32 shows the readings of a test line laid before a print. In this case, the test line for *v30* is showcased. It has temperature readings close to 250°C between 3 and 7 seconds. See Figure D.1 for a typical test line.

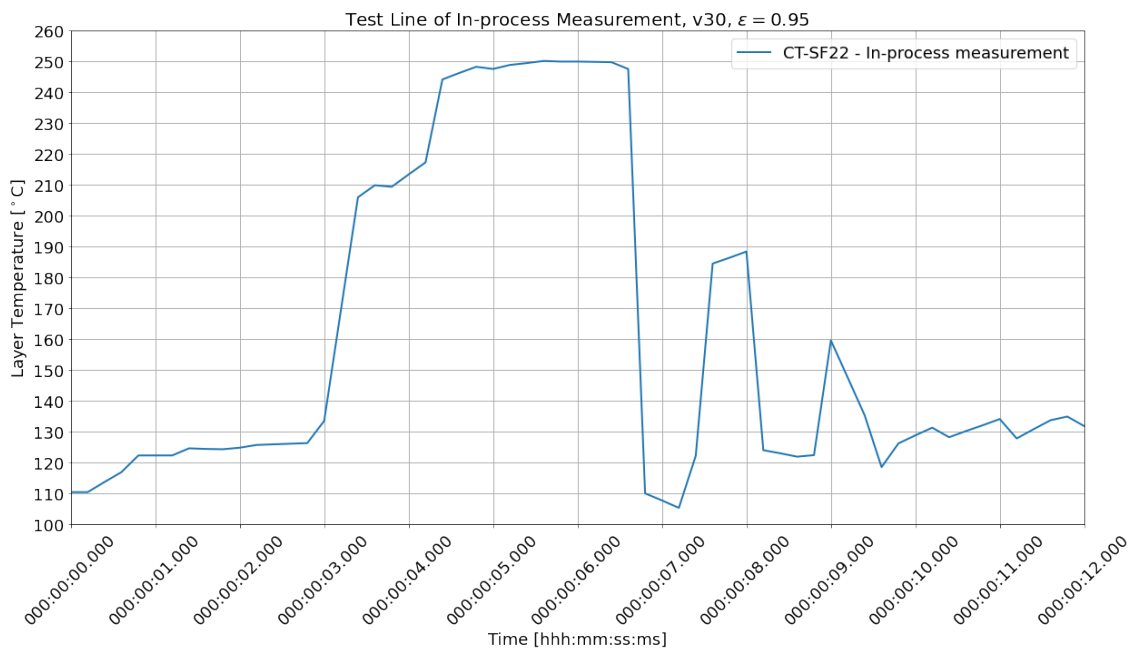


Figure 32: Readings of a Test Line at the beginning of a print.

Figure 33 displays all temperature readings done during a print of a DogBone using the CT-SF22 infrared temperature sensor. The DogBone printed in this case uses a printer speed of 30mm/s. Figure 33 displays a steady increase in temperature up until 1 minute and 22 seconds and further shows consistent temperatures up until 6 minutes and 27 seconds, where the temperatures start to rise, see [30] for detailed data. The increasing temperatures continue for 9 minutes, where it continues to measure the temperature of the approximately 230°C - 235°C maximum for 3 minutes and 6 seconds. At 12 minutes and 6 seconds, the temperature drops before it goes back to continuous measurements of approximate 230°C - 235°C maximum at 12 minutes and 26 seconds. The continuous measurements continue until 16 minutes and 2 seconds, where the temperature decreases steadily until right after 17 minutes and 22 seconds. From 17 minutes and 22 seconds, continuous measurements reach a maximum of 228°C until the end of the print at 24 minutes and 16 seconds.

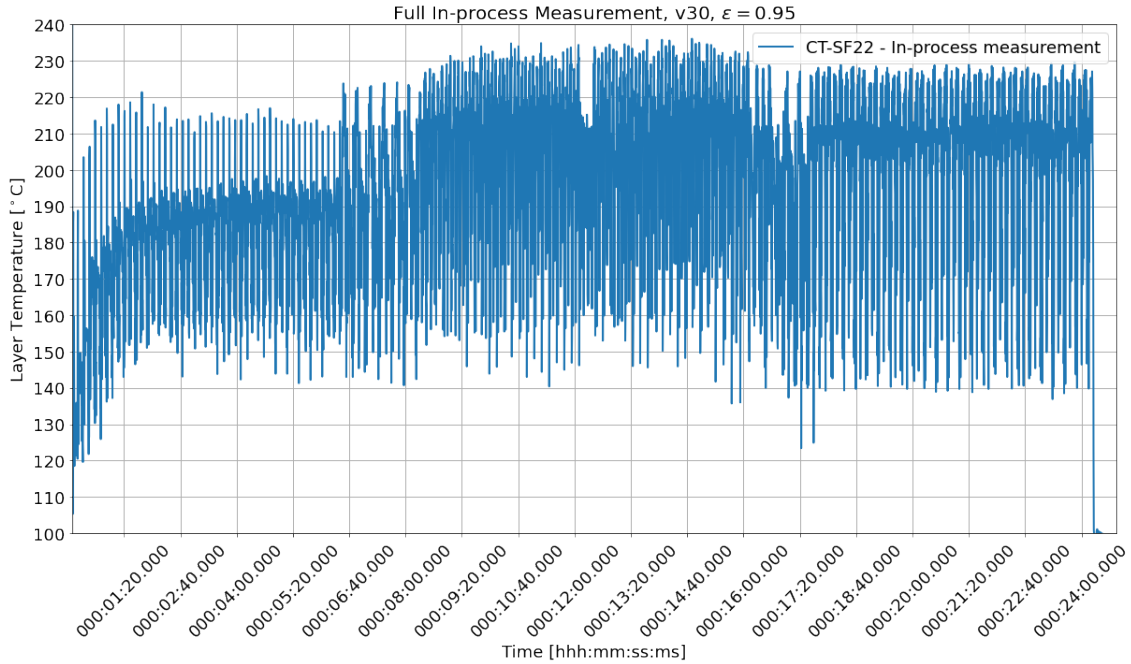


Figure 33: Full In-process measurement of DogBone with printer speed of 30 mm/s.

Figure 34 displays a section of the complete measurement shown in Figure 33. The section considers the three middle layers between 12 minutes and 6 seconds and 12 minutes and 26 seconds. Figure 34 shows the three middle layers having lower temperatures than the layers before 12 minutes and 6 seconds, and after 12 minutes and 26 seconds. Considering only section 1, the local maximums deviates with 15.8°C , considering the maximums within 12 minutes and 6-26 seconds and those outside the mentioned times. With 218.6°C at 12 minutes and 7.6 seconds and 234.4°C at 12 minutes and 5.6 seconds, see [30] for detailed data.

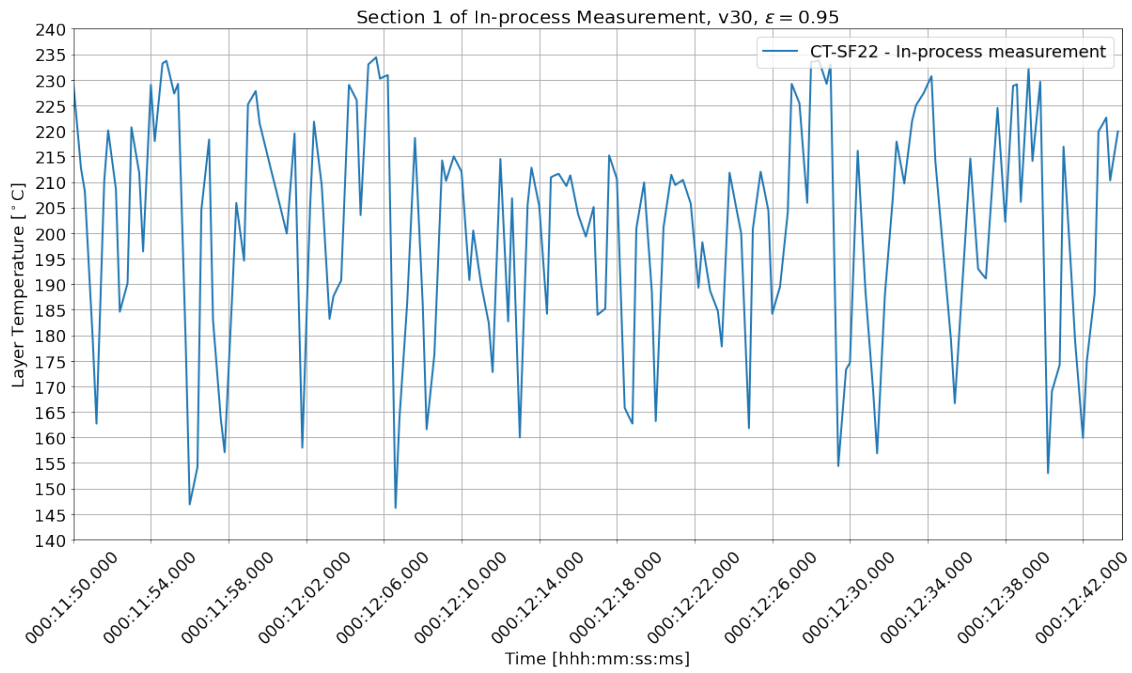


Figure 34: Section of the full In-process measurement from Figure 33.

Figure 35 displays the second layer of the three layers with lower temperatures shown in Figure 34. The pattern consists of three distinct parts:

1. A first peak between 12 minutes and 13.2 seconds, and 12 minutes and 14.4 seconds.
2. A longer peak with decreasing temperatures from 12 minutes and 14.4 seconds until 12 minutes and 16.8 seconds.
3. A last peak between 12 minutes and 16.8 seconds, and 12 minutes and 18.6 seconds.

In the first part, the peak measures 212.8°C at 12 minutes and 13.6 seconds. In the second part, the peak at 12 minutes and 15.6 seconds, the temperature measures 211.3°C . The third peak measures 215.2°C at 12 minutes and 17.8 seconds. Documentation of the **second part and its peak** (211.3°C) is done to further compare layer temperatures of the middle layer of an in-process measurement, see Section B.

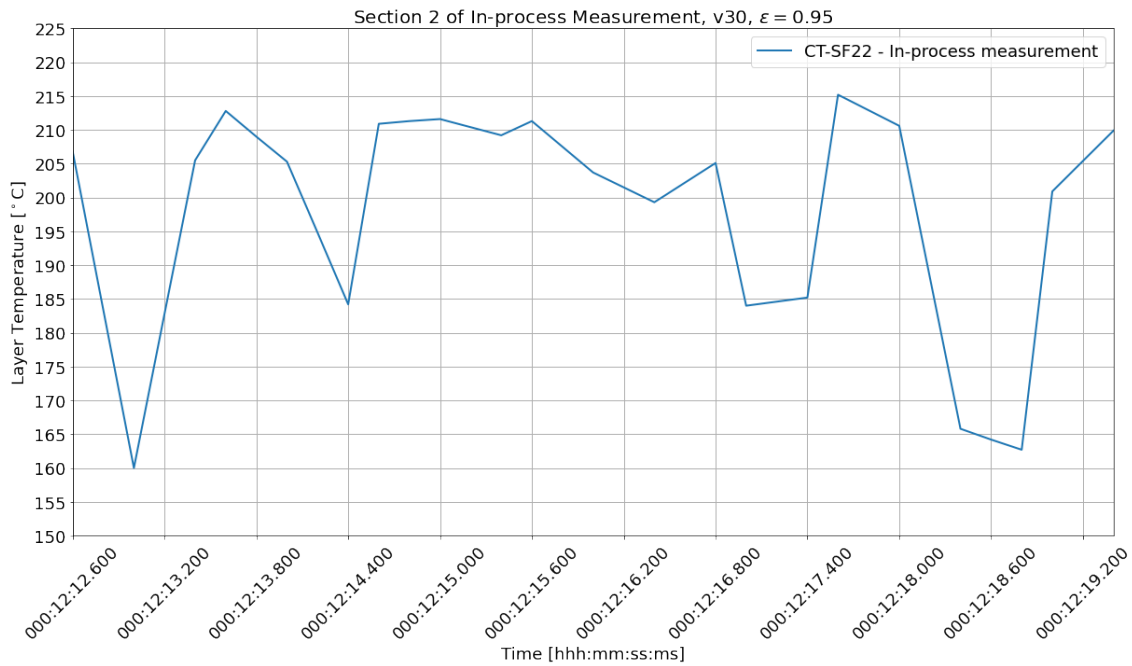


Figure 35: Section of the section in Figure 34. Displaying temperature readings during a single layer.

4.2.2 Specific Measurements

Figure 36 displays a specific reading of a half model printed at 30mm/s. The readings up until 2 minutes and 15.2 seconds are readings of the bed, see [30] for detailed data. At 2 minutes and 15.2 seconds the first reading of the surface temperature is read, the temperature is then 214.4°C . The temperature then rapidly decreases to 153.7°C at 2 minutes and 37.6 seconds. The temperature increases to 154.3°C at 2 minutes and 40.2 seconds before it steadily decreases again. The initial reading of the surface temperature is documented for all printer speeds, see Section B for data.

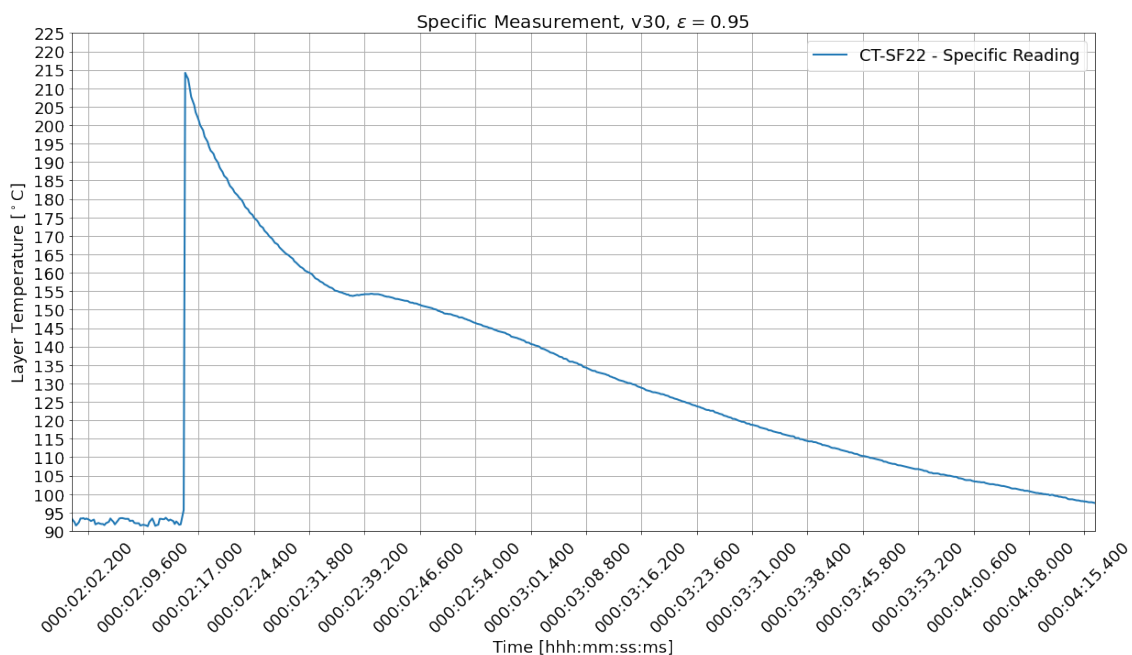


Figure 36: Specific temperature measurement of a Half model printed at 30mm/s.

Figure 37 displays the specific readings are done on the *Half* and *OneFourth* DogBone model. 15 readings are done at speeds between 4 and 30mm/s. The trend is rising for rising printer speeds for both cases. The Half model was reading 160.6°C at the lowest speed of 4mm/s, and the highest reading of 214.2°C at a printer speed of 30mm/s, a difference of 53.6°C . The OneFourth model reading 161.1°C at the lowest speed of 4mm/s, and the highest reading of 211°C at a printer speed of 30mm/s, a difference of 49.9°C . The most significant deviation between the two models is when the printer speed is set to 5mm/s, with a difference of 8.7°C . The lowest deviation between the two models is when the printer speed is set to 20mm s^{-1} , with a difference of 0.3°C . The slope of both models decreases with increasing printer speed. With a difference in temperature of 34.3°C for the half model between printer speeds of 4 and 14mm/s. And a difference of 11.5°C between printer speeds of 20 and 30mm/s.

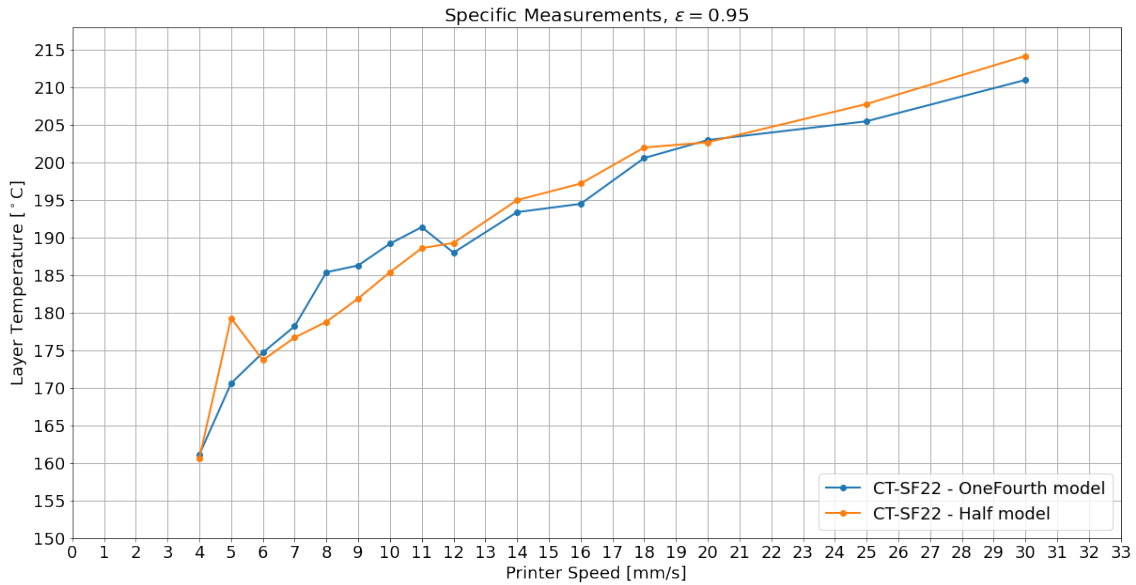


Figure 37: Specific temperature measurements versus printer speed of Half and OneFourth model using the CT-SF22 sensor.

4.2.3 In-Process Versus Specific Measurements

Figure 38 displays all Specific Measurements for the Half model versus all In-process measurements and their middle layer temperatures, see Section B for data. The most significant deviation between specific and in-process measurements is for printer speed 4mm/s, with a deviation of 19.1°C . The lowest deviation are for printer speed, 18mm/s, with a deviation of 0.6°C . The measurements deviate more in certain areas than others. Printing speeds between 4 and 16mm/s have an average deviation of 11.6°C , while printing speeds between 18 and 30mm/s have an average deviation of 2°C .

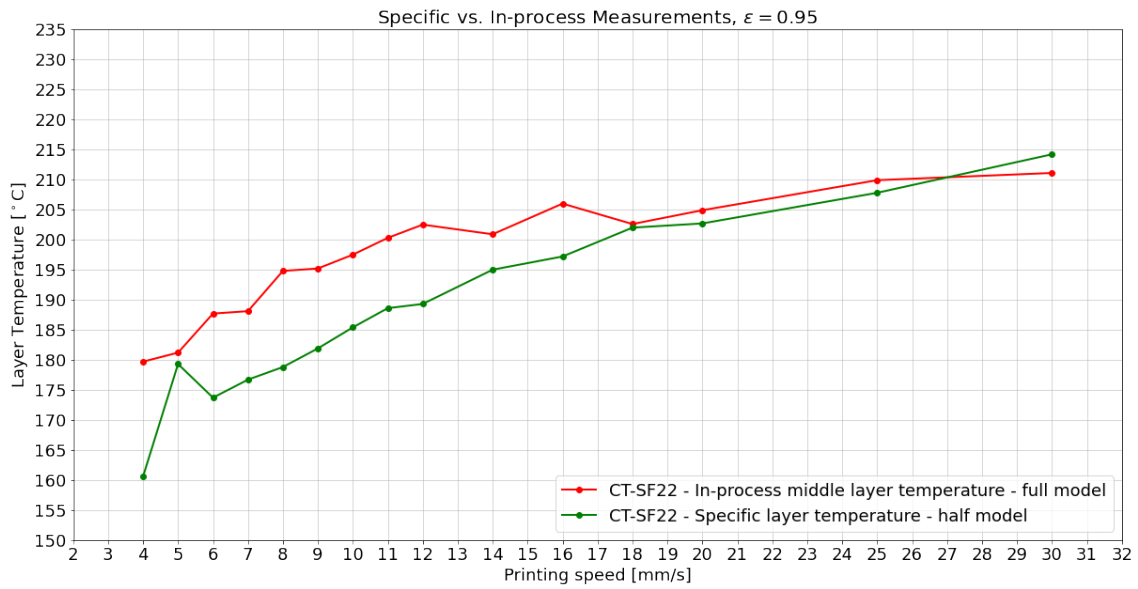


Figure 38: Specific Measurements of Half model versus middle layer temperatures from In-process Measurements.

5 Discussion

5.1 Method and Results

5.1.1 Observation Angle Test

Section 4.1.1 explains the results of the Observation Angle Test. The goal of the test is to find changes in temperature due to changes in the observation angle of the sensor, using two thermocouples that are intended to measure the actual temperature of the material. Thermocouple 1 is placed in the wall section of the test jig, while thermocouple 2 is placed underneath the surface area the sensor is doing its readings, see Figure 15b. Thermocouple 1 is placed in the wall to ensure more contact with the material of the jig, as the infill percentage is higher in the wall section, see Figure 14b. Thermocouple 2 is measuring underneath the surface area of where the sensor is pointing and might not be in contact with the material. The wall section is denser, but there are air holes present, making it more difficult to have proper contact with the material. From Figure 27, cycle 1 shows thermocouple 1 having higher temperatures than thermocouple 2, which is interesting, cause if thermocouple 1 had more contact with the material, it would take a longer time to heat the material rather than the air. It might imply that since there is less air in the wall section than in the area thermocouple 2 is located, it takes a shorter amount of time to heat up the location of thermocouple 1. Even so, if the material is allowed to settle to its surrounding temperatures, the temperature of the material should be the same as the air surrounding it, allowing thermocouples 1 and 2 to reach the same temperature. Each cycle is given a time between 23 and 28 minutes to let the material settle to its surrounding temperatures. The amount of time seems reasonable considering the thin walls of the jig, but for cycle 1, it seems that the temperatures of thermocouple 1 and 2 are still climbing at the end of its cycle. Having temperatures of 168.3°C and 165.7°C respectively at the first peak, 17:11, and 171°C and 169.2°C respectively, at the end of the cycle (17:37). A rise of 2.7°C and 3.5°C , and a clear sign that thermocouple temperatures were still climbing at the end of cycle 1. For a comparison between the thermocouples and sensor to be valid, one has to be sure that the actual temperature of the material or at least the air surrounding the test surface is at a steady state. Preferably one should do the test over again and let each cycle settle properly.

With that being said, **cycle 2** tells another story. Cycle 2 shows results of an almost steady state oscillation where the temperatures of each device follow each other, with the most significant deviation being 2.4°C between the sensor and the thermocouples over the entire cycle. Through cycle 2, thermocouple 2 and the sensor has zero deviation on three separate occasions, see Section 4.1.1. The temperature of the thermocouples has risen, oscillating between 175.9°C and 180.4°C , as opposed to oscillations between 164.2°C and 171°C in cycle 1. The increase might imply that the surrounding temperatures for the thermocouples have allowed them to settle more. Temperature differences between the first and the third peaks are 0.2°C and 1°C for thermocouples 1 and 2, respectively, confirming a more settled temperature. Sensor temperatures seem to be about the same for cycles 1 and 2. Having oscillations between 174.8°C and 176.6°C in cycle 1, and 175.2°C and 178.6°C for cycle 2. A slight rise in sensor temperature, parallel with the increasing temperatures of the thermocouples. The almost steady state oscillation of cycle 2 indicates that an observation angle of 22.5° on the sensor may be the ideal observation angle for measurements in this setup.

In **cycle 3**, thermocouple temperatures rise, reaching their highest temperature at the first peak of the cycle, with 185.6°C . A significant difference from cycle 2 with a difference of 5.2°C compared to the first peak of cycle 2. However, the first peak in cycle 3 seems to overshoot. Later in cycle 3, thermocouple temperatures settles around 180°C , which is not far from the temperatures of the thermocouples in cycle 2. Cycle 2 were averaging thermocouple temperatures of 178.2°C throughout the cycle. Sensor temperature reads higher values in cycle 3, with oscillations between 176.7°C and 181°C , a lower difference of 1.9°C and a higher difference of 4.4°C compared to cycle 1. However, the highest temperature difference is also influenced by the overshoot of the first peak of cycle 3. Peaks 2 and 3 show more similar values, measuring about 179°C at both peaks. That is about the same temperature as all three peaks in cycle 2. An interesting observation in cycle 3 is the difference between the thermocouples and the sensor after the first peaks drop. At the beginning of peak 2 and throughout of cycle 3, the differences between the thermocouples and sensor stay consistent. With a difference ranging between 1.9°C and 2.5°C considering both

thermocouples.

The same thing occurs in **cycle 4**. Cycle 4 also has an overshoot at its first peak, then have more consistent temperature measurements. This time the differences between the sensor and thermocouples are more significant through peaks 2 and 3. Ranging between 3°C and 4.6°C considering both thermocouples. In addition, cycle 4 measures average temperature by thermocouples 1 and 2 at 182.2°C and 181.5°C , respectively, this is the highest average temperature measured through all of the cycles, see Section B for data. Through the same cycle, the sensor has an average of 177.1°C , lower than both cycle 2 and 3.

Both the greater differences between the thermocouples and the sensor in cycles 3 and 4 and the second lowest average temperature of the sensor in cycle 4 suggests that a lower observation angle than 22.5° gives more inaccurate temperature measurements for the sensor. An observation angle of 22.5° and an emissivity factor of $\epsilon = 0.95$ seems ideal considering cycle 2. Increasing the observation angle beyond 22.5° seems to give inaccurate measurements with a emissivity factor of, $\epsilon = 0.95$.

Otherwise, the differences are not huge between the observation angles. Not considering cycle 1 due to transient oscillations and the overshoots of the first peaks in cycles 3 and 4, the greatest temperature differences between the thermocouples and sensor are 4.6°C at 19:13, for thermocouple 1. Considerations have to be done on the significance of this temperature difference.

There is a possibility that heat reflection from the surroundings affects the readings. At a lower observation angle, the sensor is more exposed to the surroundings as there is an opening right in front of the sensor, see Figure 15. At the other end of this opening is the metal weight used for keeping the jig in place, see Figure 16. It is a chunk of steel that can take a while to heat up. If the heat reflections from the steel chunk are lower than the surrounding temperatures, it decreases the temperature read by the sensor [25]. Further tests have to be done to dispose of this hypothesis.

5.1.2 Melt test

Section 4.1.2 explains the detailed results of the Melt Test. The goal of the test is to find temperatures that show a change in emissivity. Figure 29 displays how the rising temperature from the single burner hot plate affects the melt test specimen (Figure 18a). Figure 29 shows that the sensor is reading temperatures higher than the thermocouples for about 140 seconds, the reason for this can be the thermocouples not having proper contact with the specimen. Figure 31 shows a more prominent mark for where thermocouple 1 was located, leaving a bump after thermocouple 1 has been torn out of the specimen after the test. The mark after thermocouple 2 seems to be the drilled pit sunken due to increasing temperatures. Thermocouple 2 did make contact with the surface but did not need to be torn out of the plastics after the test. Explaining the gentle slope of thermocouple 2 in Figure 29, occurring after 105 seconds into the test. The gentle slope might be that thermocouple 2 loses touch with the surface for a small amount of time before making more contact again after 150 seconds, when it starts to incline at a steady state, almost parallel with thermocouple 1. After 240 seconds, all temperatures seem to converge. Thermocouple 1 displays a temperature of 249.2°C , while thermocouple 2 is reading 222.1°C at the end of the test. Implying that thermocouple 1 has more significant contact with the surface than thermocouple 2. In Figure 30, thermocouple 2 has lost more contact with the surface and measures $50 - 60^{\circ}\text{C}$ lower than thermocouple 1. Together with the evidence from Figure 31 suggests that readings from thermocouple 2 should not be considered in this experiment.

Focusing on thermocouple 1, which has more contact with the surface of the test specimen, considering Figure 31, seems to have more reliable results. Analyzing Figure 30, where the emissivity factor just have been calculated to $\epsilon = 0.856$, thermocouple 1 and sensor readings follow each other at a steady rate. Section 4.1.2 explains where the temperature of thermocouple 1 intersects with the temperature of the sensor. Thermocouple 1 clearly shows higher temperatures in the first 10 seconds. Then the two temperatures intersect several times throughout the test The last intersection occurs at 84 seconds. Readings from thermocouple 1 then start to show lower values than the sensor throughout the rest of the test. Thermocouple 1 reads 1.6°C higher than the sensor at the beginning of the test and 1.9°C lower than the sensor at the end of the test. A difference of 2.5°C . The last intersection at 84 seconds has a temperature of 193.9°C . An interesting observation is the temperature of the intersection between thermocouple 1 and the sensor in Figure 29, being approximately 191°C at 148 seconds. It should be noted that thermocouple 1 does not read the

same temperatures as the sensor up until the point of intersection. However, looking at the slopes of the two temperatures, they follow each other parallel up until 160°C where both temperatures gets a more gentle slope, showing signs of similar behavior in the first 130 seconds. The intersection at 191°C and 193.9°C for emissivity factors, $\epsilon = 0.95$ and $\epsilon = 0.856$, respectively, can mean that a change in emissivity for the material happens around 190°C . The material gets more glossy when it's melted, reflecting more of the heat. The sensor will then read lower values than the actual temperature. An increase in heat reflection would result in lower temperature readings, and this can be the case for thermocouple 1 and the sensor from 148 seconds throughout the test analyzing Figure 29. The crystallization temperature of PA6-CF is 184.6°C while the melting temperature is 218.5°C [28]. Crystallization affects the physical optical property of the material [31], and can alter the rate of radiated thermal energy. How the rate of radiated energy behaves with increasing temperatures has to be researched more. Further research would help map the change of emissivity with increasing temperatures for PA6-CF.

5.1.3 In-process Measurements

Section 4.2.1 explains the results of the In-process measurements. Section 4.2.1 only refers to one of the tests, *v30* out of the 15 tests done, listed in Table 3. Explanation of one In-process measurement is enough to capture the essence of the test method, where the goal is to capture the middle layer temperature. The method introduced in Section 3.5.1 describes how the three middle layers had to be reversed to capture the layer temperature of the previous layer before a new one was printed on top. These three layers are evident in the temperature readings looking at Figure 33 and Figure 34, and these results suggest that the sensor did indeed capture the layer temperature of the previous layer for the three middle layers. The result implies that the sensor aimed correctly at the surface area of the print.

The recorded temperature of the test line, Figure 32, gives a clear indication of proper aiming and the temperature of a freshly laid layer. The test line is printed with the direction of where the sensor is measuring, meaning the sensor is measuring the temperature of the freshly laid test line. The test line tends to be 2-3mm wide (Figure D.1), and as the focal point of the sensor was calculated to be 2.88mm, it can seem that the sensor has been able to capture heat radiation within the width of the test line.

Further, the pattern of Figure 33 tells a story about the different sections of the DogBone (Figure 21). The first 1 minute and 22 seconds show how the temperature increases from the base of the DogBone and further up in the bottom grip of the DogBone, see Section 4.2.1. The increase in temperature is due to heat conservation through the print. The conservation stagnates at 1 minute and 22 seconds, where the temperature readings stay consistent up until 6 minutes and 27 seconds. At this point, the bottom grip of the DogBone has been printed, and the printing of the fillet starts. There are increasing temperatures through the fillet up until approximately 9 minutes. The increase in temperature is due to a reduction in cross-section, allowing for more heat conservation. The heat conservation also stagnates through half of the gauge length of the DogBone, measuring $230 - 235^{\circ}\text{C}$ maximum, up until 12 minutes and 6 seconds. At this time, the three reversed layers get printed, and the temperature drops, resulting in a temperature difference of 15.8°C from the local maximums, considering Figure 34. After the three middle layers are printed, the steady temperature readings of the gauge length continue. The steady readings continue up until 16 minutes and 2 seconds, which steadily decreases due to printing the top fillet, increasing the cross-section, and decreasing heat conservation. A steady maximum temperature is then read at approximately 228°C , between 17 minutes and 22 seconds, to the end of the print at 24 minutes and 16 seconds. This steady temperature measurement is of the top grip of the DogBone, and it reads local maximums over 10°C higher than the bottom grip, suggesting that the heat conservation has increased due printing of a smaller cross-section across the gauge length. The pattern of the DogBone stays consistent through all of the completed tests, see Section B and [30]. Note that 7 out 15 tests failed, likely due to a shortage of glue on the printer bed or bad bed leveling and inconsistent Z-axis offset. The failed tests were considered as the test line, consistent pattern, and the three reversed layers were visible. Analyzing printing of the middle layer by looking at Figure 35, the three distinct parts described in Section 4.2.1 can further be discussed. Analysis during printing with the sensor revealed what causes the three distinct parts of one layer described in Figure 35. Please see Figure A.1 for a video presenting an example of how a reversed layer is

laid. The **first part** is the perimeter being printed, measuring the first line, which is laid with the direction the sensor points, resulting in a high peak of 212.8°C . Note that the peak is not as high as the peak of the test line (Figure 32). The focal point of 2.88mm and is measuring both outside and inside of the perimeter, resulting in lower temperatures than the test line. Next, a slight drop occurs, indicating printing of the perimeter across the thickness of the DogBone. The next drop is measurements while the perimeter is printed towards the temperature sensor. Measuring inside and outside of the cross-section due to the size of the focal point.

The **second part** is the infill deposition, showing consistent readings of approximately 211°C for 1.2 seconds. The temperature decreases as the rectilinear pattern tightens in the cross-section's corners. Measuring more of the edges and outside of the cross-section.

The **third part** shows the redirecting of the extruder. The rectilinear infill pattern ends on the opposite side of the thickness, from where the perimeter starts its line. The hotend needs to travel across the thickness of the cross-section, redirecting the sensor over the newly laid perimeter and infill. The redirecting results in a third peak, with a value of 215.2°C .

Note that the peak in the third part is higher than the peak in the first part, where the sensor measures the temperature of the perimeter as it is printed. Before traveling to starting position of the perimeter, the extruder changes Z-height, allowing the sensor to measure the newly laid infill as it moves across the thickness. Having the focal point over the newly laid layer can be why the third peak is higher than the first.

Using the peak in the second part, where the infill is laid, as a point of layer temperature measurement seems reasonable after many tests and analyses. These points were documented for all printing speeds and compared with specific measurements done on half models of the DogBone, further discussed in Section 5.1.5.

In Section 3.3.1, it was introduced that an observation angle of 31° and a distance between the sensor and object of 13mm gave an FPBL of 11.28mm. The width of the DogBone geometry across the gauge length is 10mm, see Figure 21. The FPBL is longer than the DogBone in the experiments performed and leaves room for errors by having the focal point outside of the desired surface. It is unknown how much the FPBL affects the outcome of the results, and more research is needed to discuss the issue further.

5.1.4 Specific Measurements

Section 4.2.2 explains the results of the Specific Measurements. Figure 36 displays how a typical specific reading looks. All plots of the specific measurements can be found in Section B. The goal of the specific measurements is to assure precise measurements by not having obstacles between the surface measured and not having the hotend present during the measurement. The measurements are intended to confirm In-process Measurements, discussed in Section 5.1.3. Figure 37 shows consistent results, with increasing temperatures for increased printing speeds. There is one printer speed that differs from the other results, $v5$ shows higher temperatures than both $v6$ and $v7$. Several factors have to be considered for the diversion. Especially the chamber temperature tends to overshoot, which can affect the layer temperature. Not monitoring the chamber temperature could have caused the diversion. Nevertheless, other factors like hotend temperature being higher than usual or aiming at a more recent printed area could also be the reason for the diversion. Apart from the diversion with $v5$, the trend is clear.

The method used to obtain the results, introduced in Section 3.5.2, has a travel time before the measurement. The travel time can result in having lower readings of the layer temperature than the In-process Measurements. Calculating travel time can be done by using the last coordinates of the hotend in the G-code and use the coordinates used for the Specific Measurements. Measuring the difference in distance in X and Y-direction and dividing by the travel speed, listed in Table 2, the time of travel is calculated to be 0.1147 seconds. See Section B for calculation. By analyzing the temperature drop of a specific measurement, using $v30$ as an example, there is a temperature drop of 1.3°C between 2 minutes and 32.4 seconds and 2 minutes and 32.6 seconds. 1.3°C drop over 0.2 seconds, see [30] for detailed data. Interpolation can be performed to approximate this value further. However, the drop is not significant but should be considered for more precise analyses.

The aim of Specific temperature measurements of the OneFourth model were to compare with other layer temperature research methods. In Section F, layer temperatures was measured using a Flir One Pro compact thermal camera. The method using the Flir camera entailed opening the chamber and measuring over a OneFourth model of the DogBone, see Section F. In Figure 39 comparisons are made between the method used in this project and the method used with the Flir camera.

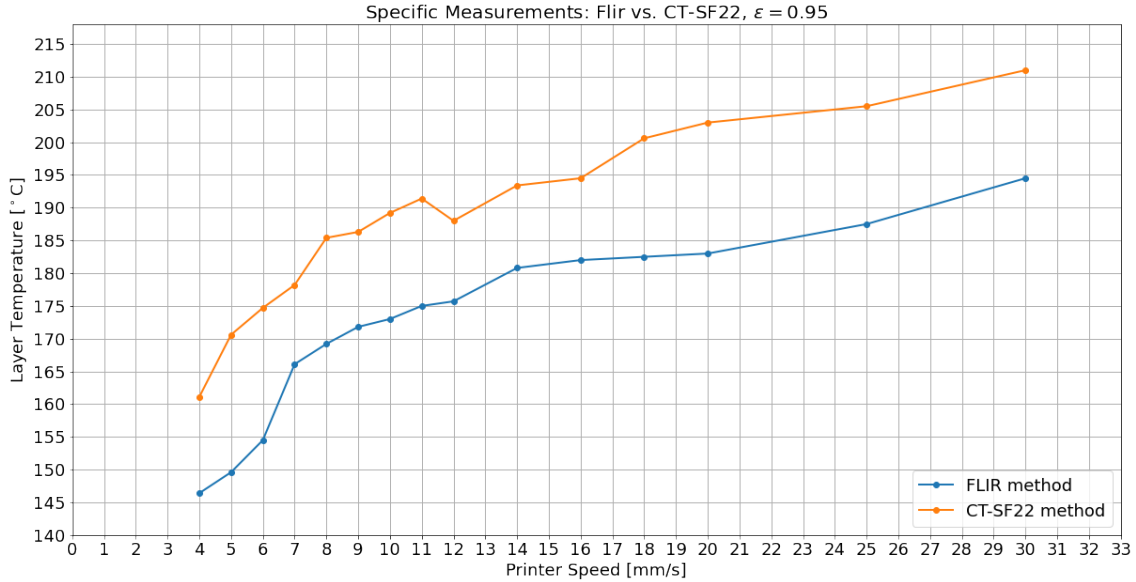


Figure 39: Comparison of two different specific measurement methods. Both methods are performed on a OneFourth model.

Figure 39 shows substantial differences between the two methods. Using the method introduced in this project shows temperature differences of almost 20°C compared to the Flir method, see $v20$ in Figure 39. The comparison shows how the method introduced in Section 3.5.2 may give more accurate measurements than other methods used in the layer temperature research field.

5.1.5 In-Process Versus Specific Measurements

Section 4.2.3 describes the comparison of the Specific Measurements of the Half model versus In-process Measurements. The goal of the comparison is to determine if the In-process Measurements are credible. There are significant differences in the results. While some results overlap well, others deviate considerably. The most significant deviation between specific and in-process measurements was 19.1°C for $v4$, and the lowest deviation was 0.6°C for $v18$. Aiming with the sensor, adjusting the focal point, and assuring the focal point hits the wanted surface are essential for achieving credible results. The results for the In-process measurements were obtained in two rounds, meaning calibrating the sensor two times. One calibration was for printer speeds between 30 and 18mm/s and one for printer speeds of 16 to 4mm/s. The results for the two calibrations are clear in Figure 38. The average deviation for printing speeds between 4 and 16mm/s is 11.6°C , while only 2°C for printing speeds 18 to 30mm/s, see Section B for data. Even though both rounds of testing for In-process measurements used the method introduced in Section 3.5.1, results suggest that the aiming for the two calibrations differed. It indicates the delicacy of the sensor calibration. Proper aiming is essential for accurate measurements, and the deviation between the two calibrations shows inaccurate results.

However, Figure 38 shows similar trends for the two testing methods. The overall result is increasing temperatures for increasing printing speeds, and apart from the deviations mentioned, the in-process Measurement seems to give positive results when compared to the more accurate

Specific Measurements.

It is unclear how much reflected heat from the hotend or how the size of FPBL affects the in-process measurements. Further confirmations of consistency should be done by documenting quantities of data.

5.2 Uncertainties

5.2.1 Emissivity

As discussed in Section 5.1.2, a change in emissivity seems to occur around $190^{\circ}C$ for PA6-CF. How the emissivity changes for PA6-CF with increasing temperatures from this point is uncertain. Obtaining accurate infrared temperature measurements have proven challenging with respect to emissivity [18], and further research is needed.

5.2.2 Geometry

Emissivity is dependent on the geometry of the specimen measured [1]. This thesis did not perform any tests to find if there are differences in emissivity due to changes in geometry. The geometry of the surface area tested in this thesis should be close to flat, and any emissivity differences were not considered.

5.2.3 Angled Measurements

Measurements with an angle cause especially two challenges. Section 4.1.1 and research show that an increase in observation angle causes a decrease in the emissivity factor [24]. An increasing observation angle also increases the FPBL, introduced in Section 3.3.1. An increase in FPBL increases the probability of errors.

5.2.4 Aiming

It cannot be emphasized enough that aiming with the sensor is one of the most critical factors for credible temperature measurements. Results discussed in Section 5.1.3 shows how delicate the aiming is. Ensuring proper aiming with the sensor is essential for achieving credible in-process temperature measurements.

5.2.5 Noise

Figure 33 shows local minimums of approximately $150^{\circ}C$. All In-process Measurements had these results, see Section B. As mentioned in Section 5.1.3, the local minimums likely occur due to the focal point being outside the print surface. These measurements can be considered noise in the readings and should be avoided when obtaining a layer temperature model of components.

5.2.6 Vibrations

The sensor can vibrate as the printing pattern take turns. Max acceleration is set to 900mm/s^2 and travel speed for non-print moves is set to 180mm/s^2 see Table 2. Acceleration, travel speed and printing speed can cause errors in the readings as the sensor setup introduced in Section 3.2 is not tested for vibration errors. However, observations of the temperature sensor in action showed little sign of vibration. To present this, a video is attached to Figure A.2 showing how the sensor operates under a typical in-process measurement.

6 Conclusion

This project aimed to find if a non-contact infrared temperature sensor could monitor and model the layer temperature in-process of FFF. Results in this project show how the CT-SF22 infrared temperature sensor can model layer temperatures through a model down to specific details. The sensor could capture layer patterns so specific that the different parts through a layer were easily identified. However, results between Specific Measurements and In-process Measurements proved to be accurate and inaccurate between two calibrations. The delicacy of aiming with the sensor is vital to comprehend. Even though both calibrations gave positive results in modeling layer temperature and displaying the reversed layers, the differences in deviation became greater for the calibration for printing speeds between 4 and 16mm/s. It is uncertain if this is due to poor aiming, change of emissivity, heat reflection from the hotend, or some other source of error. More experiments should be performed to confirm the results further and better understand the sources of error.

Even so, the results suggest that the sensor captured the designated layer temperature and can model layer temperature through components. With the promising results, further research on strength in components with respect to layer temperature is achievable. Predicting the strength of a component has great potential in FFF, see Section F.

In this project, one sensor was used, setting limitations for which layer temperatures the sensor could capture. Having multiple infrared temperature sensors around the extruder could create full layer temperature models of components in FFF.

7 Future Work

7.1 Accurate Aiming

The sensor setup used in this project worked sufficiently but had several flaws and has room for improvement. Results between calibrations have proven to be inaccurate, as discussed in Section 5.1.3. As it is a **non-contact infrared** temperature sensor, a proper calibration method is needed when trying to read temperatures within sub-millimeter wide lines. The optimal setup can capture layer temperature where a new line of filament will be printed. That means the sensor calibration must be 10mm from the object, so the sensor has a focal point of 0.6mm. The nozzle size is 0.6mm, meaning the sensor can capture the previous line temperature before a new line is extruded on top. The detailed temperature mapping would be immense.

There has to be developed equipment and methods to calibrate the sensor down to a sub-millimeter. It is a need to design and manufacture a calibration setup that fine-tunes the position of the sensor and gives the user the exact location of where the sensor is aiming. A calibration design where the user has complete control over the sensor's focal point.

7.2 Dynamic Emissivity Control

Research on dynamic emissivity in FFF is needed to ensure accurate temperature measurements with infrared temperature sensors. Materials in FFF need to be investigated on how the emissivity changes up to the melting temperature. Large cross-sections will have previous layer temperatures far below melting temperatures. Small cross-sections will have previous layer temperatures closer to melting temperatures. Differences in emissivity depend on the size of the cross-section, the printing distance, and the printing time of *one* layer. A function of emissivity and size of the cross-section has to be developed to achieve accurate measurements. Essentially, creating dynamic emissivity control dependent on the size of the cross-section and printing speed.

7.3 FFF Temperature Modeling

The non-contact infrared temperature sensor results shown in this project are promising. Capturing temperature details in-process of FFF also was validated. The sensor from Micro-Epsilon has excellent accuracy, processing time, weight, and size features. In this project, only one sensor was used, capturing previous layer temperatures in only one extrusion direction. FFF uses all directions within the x and y-plane to deposit material for one layer. Non-contact temperature sensors on each side of the extruder would capture all previous layer temperatures. No matter geometry, infill pattern, or complexity. Eight sensors, four for all straights and four for all diagonals, would be able to model the entire layer temperature with specific details. Combined with the accuracy mentioned in Section 7.1, very detailed temperature models can be achieved.

7.4 Combining G-code and Temperature Modeling

A G-code gives coordinates of how the FFF is executed. The fabrication start at a given time and end at a given time. The same is the for layer temperature modeling. Measurements of the layer temperatures start at one time and ends at another. The start and end times are equal for the two. Combining G-code coordinates with layer temperature measurements would map out exactly where in the model the different layer temperatures are. Knowing the geometry's layer temperatures can predict the strength the component will have at that particular point. Knowing the strength of specific points in AM components will have huge potential.

References

- [1] MICRO-EPSILON, “Operating Instructions thermoMETER CT.” [Online]. Available: <https://www.micro-epsilon.com/download/manuals/man--thermoMETER-CT--en.pdf>
- [2] B. Berman, “3-D printing: The new industrial revolution,” *Business horizons*, vol. 55, no. 2, pp. 155–162, 2012, iSBN: 0007-6813 Publisher: Elsevier.
- [3] I. Gibson, D. Rosen, B. Stucker, and M. Khorasani, “Introduction and Basic Principles,” in *Additive Manufacturing Technologies*, I. Gibson, D. Rosen, B. Stucker, and M. Khorasani, Eds. Cham: Springer International Publishing, 2021, pp. 1–21. [Online]. Available: https://doi.org/10.1007/978-3-030-56127-7_1
- [4] A. Busachi, J. Erkoyuncu, P. Colegrove, F. Martina, C. Watts, and R. Drake, “A review of Additive Manufacturing technology and Cost Estimation techniques for the defence sector,” *CIRP Journal of Manufacturing Science and Technology*, vol. 19, pp. 117–128, 2017, iSBN: 1755-5817 Publisher: Elsevier.
- [5] J. C. Najmon, S. Raeisi, and A. Tovar, “Review of additive manufacturing technologies and applications in the aerospace industry,” *Additive manufacturing for the aerospace industry*, pp. 7–31, 2019, publisher: Elsevier.
- [6] M. Rinaldi, F. Cecchini, L. Pigliaru, T. Ghidini, F. Lumaca, and F. Nanni, “Additive manufacturing of polyether ether ketone (PEEK) for space applications: A nanosat polymeric structure,” *Polymers*, vol. 13, no. 1, p. 11, 2021, publisher: Multidisciplinary Digital Publishing Institute.
- [7] D. E. Cooper, M. Stanford, K. A. Kibble, and G. J. Gibbons, “Additive manufacturing for product improvement at Red Bull Technology,” *Materials & Design*, vol. 41, pp. 226–230, 2012, iSBN: 0261-3069 Publisher: Elsevier.
- [8] I. Gibson, D. Rosen, B. Stucker, and M. Khorasani, “Material Extrusion,” in *Additive Manufacturing Technologies*, I. Gibson, D. Rosen, B. Stucker, and M. Khorasani, Eds. Cham: Springer International Publishing, 2021, pp. 171–201. [Online]. Available: https://doi.org/10.1007/978-3-030-56127-7_6
- [9] F. M. Duarte, J. A. Covas, and C. S. F. da, “Predicting the effect of build orientation and process temperatures on the performance of parts made by fused filament fabrication,” *Rapid Prototyping Journal*, vol. ahead-of-print, no. ahead-of-print, Jan. 2021. [Online]. Available: <https://doi.org/10.1108/RPJ-04-2021-0084>
- [10] H. Li, T. Wang, J. Sun, and Z. Yu, “The effect of process parameters in fused deposition modelling on bonding degree and mechanical properties,” *Rapid Prototyping Journal*, vol. 24, no. 1, pp. 80–92, Jan. 2018, publisher: Emerald Publishing Limited. [Online]. Available: <https://doi.org/10.1108/RPJ-06-2016-0090>
- [11] P. Striemann, D. Hlsbusch, M. Niedermeier, and F. Walther, “Optimization and Quality Evaluation of the Interlayer Bonding Performance of Additively Manufactured Polymer Structures,” *Polymers*, vol. 12, no. 5, p. 1166, May 2020, number: 5 Publisher: Multidisciplinary Digital Publishing Institute. [Online]. Available: <https://www.mdpi.com/2073-4360/12/5/1166>
- [12] A. Das, C. A. Chatham, J. J. Fallon, C. E. Zawaski, E. L. Gilmer, C. B. Williams, and M. J. Bortner, “Current understanding and challenges in high temperature additive manufacturing of engineering thermoplastic polymers,” *Additive Manufacturing*, vol. 34, p. 101218, 2020, iSBN: 2214-8604 Publisher: Elsevier.
- [13] R. Hashemi Sanatgar, C. Campagne, and V. Nierstrasz, “Investigation of the adhesion properties of direct 3D printing of polymers and nanocomposites on textiles: Effect of FDM printing process parameters,” *Applied Surface Science*, vol. 403, pp. 551–563, May 2017. [Online]. Available: <https://www.sciencedirect.com/science/article/pii/S0169433217301137>

- [14] V. E. Kuznetsov, A. N. Solonin, A. Tavitov, O. Urzhumtsev, and A. Vakulik, "Increasing strength of FFF three-dimensional printed parts by influencing on temperature-related parameters of the process," *Rapid Prototyping Journal*, vol. 26, no. 1, pp. 107–121, Jan. 2019, publisher: Emerald Publishing Limited. [Online]. Available: <https://doi.org/10.1108/RPJ-01-2019-0017>
- [15] G. D. Goh, Y. L. Yap, H. K. J. Tan, S. L. Sing, G. L. Goh, and W. Y. Yeong, "ProcessStructureProperties in Polymer Additive Manufacturing via Material Extrusion: A Review," *Critical Reviews in Solid State and Materials Sciences*, vol. 45, no. 2, pp. 113–133, Mar. 2020, publisher: Taylor & Francis eprint: <https://doi.org/10.1080/10408436.2018.1549977>. [Online]. Available: <https://doi.org/10.1080/10408436.2018.1549977>
- [16] V. Kishore, C. Ajinjeru, A. Nycz, B. Post, J. Lindahl, V. Kunc, and C. Duty, "Infrared preheating to improve interlayer strength of big area additive manufacturing (BAAM) components," *Additive Manufacturing*, vol. 14, pp. 7–12, 2017, iISBN: 2214-8604 Publisher: Elsevier.
- [17] J. Butt and R. Bhaskar, "Investigating the effects of annealing on the mechanical properties of FFF-printed thermoplastics," *Journal of Manufacturing and Materials Processing*, vol. 4, no. 2, p. 38, 2020, publisher: Multidisciplinary Digital Publishing Institute.
- [18] E. Ferraris, J. Zhang, and B. Van Hooreweder, "Thermography based in-process monitoring of Fused Filament Fabrication of polymeric parts," *CIRP Annals*, vol. 68, no. 1, pp. 213–216, Jan. 2019. [Online]. Available: <https://www.sciencedirect.com/science/article/pii/S0007850619301556>
- [19] C. Kousiatza, N. Chatzidai, and D. Karalekas, "Temperature Mapping of 3D Printed Polymer Plates: Experimental and Numerical Study," *Sensors*, vol. 17, no. 3, p. 456, Mar. 2017, number: 3 Publisher: Multidisciplinary Digital Publishing Institute. [Online]. Available: <https://www.mdpi.com/1424-8220/17/3/456>
- [20] *Residual Stress, Thermomechanics & Infrared Imaging and Inverse Problems, Volume 6*. [Online]. Available: <https://link.springer.com/book/10.1007/978-3-030-30098-2>
- [21] A. Rogalski and K. Chrzanowski, "Infrared devices and techniques," in *Handbook of Optoelectronics*, 2nd ed., J. P. Dakin and R. G. W. Brown, Eds. Second edition. | Boca Raton : Taylor & Francis, CRC Press, : CRC Press, Oct. 2017, pp. 633–686. [Online]. Available: <https://www.taylorfrancis.com/books/9781482241792/chapters/10.1201/9781315157009-18>
- [22] "Blackbody and other Calibration Sources | Elsevier Enhanced Reader." [Online]. Available: <https://reader.elsevier.com/reader/sd/pii/S1079404209042064?token=7F087AA7E9D6AA8CFCF3715BBEED15C0DE766A27A8FC862D07A36B884B896FC45D1D4F95AF28833E9277&originRegion=eu-west-1&originCreation=20220528163146>
- [23] J. Hartmann, J. Hollandt, B. Khlevnoy, S. Morozova, S. Ogarev, and F. Sakuma, "Chapter 6 Blackbody and other Calibration Sources," in *Radiometric Temperature Measurements: I. Fundamentals*, ser. Experimental Methods in the Physical Sciences, Z. M. Zhang, B. K. Tsai, and G. Machin, Eds. Academic Press, 2009, vol. 42, pp. 241–295, iISSN: 1079-4042. [Online]. Available: <https://www.sciencedirect.com/science/article/pii/S1079404209042064>
- [24] J. A. Sobrino and J. Cuenca, "Angular variation of thermal infrared emissivity for some natural surfaces from experimental measurements," *Applied Optics*, vol. 38, no. 18, pp. 3931–3936, Jun. 1999, publisher: Optica Publishing Group. [Online]. Available: <https://opg.optica.org/ao/abstract.cfm?uri=ao-38-18-3931>
- [25] "How Does Emissivity Affect Thermal Imaging?" [Online]. Available: <https://www.flir.com/discover/professional-tools/how-does-emissivity-affect-thermal-imaging/>
- [26] "Welcome - Klipper documentation." [Online]. Available: <https://www.klipper3d.org/>
- [27] A. Birkelid, S. W. Eikevg, C. W. Elverum, and M. Steinert, "High-performance polymer 3D printing open-source liquid cooled scalable printer design," *HardwareX*, vol. Under Review, Nov. 2021.

-
- [28] Polymide, “PolyMide PA6-CF,” Oct. 2021. [Online]. Available: <http://eu.polymaker.com/product/polymide-pa6-cf/>
- [29] S. W. Eikevg and C. Elverum, “High-performance polymer 3D printing open-source liquid cooled scalable printer design,” vol. 1, Nov. 2021, publisher: Mendeley Data. [Online]. Available: <https://data.mendeley.com/datasets/7sjjmr9bz2/1>
- [30] BenjaminBGAndresen, “Master-Thesis-Appendix,” Jun. 2022, original-date: 2022-06-07T08:56:03Z. [Online]. Available: <https://github.com/BenjaminBGAndresen/Master-Thesis-Appendix>
- [31] C. Yu, Q. Xie, Y. Bao, G. Shan, and P. Pan, “Crystalline and Spherulitic Morphology of Polymers Crystallized in Confined Systems,” *Crystals*, vol. 7, no. 5, p. 147, May 2017, number: 5 Publisher: Multidisciplinary Digital Publishing Institute. [Online]. Available: <https://www.mdpi.com/2073-4352/7/5/147>

Appendix

A Video presentation



Figure A.1: QR-code to video presentation of how a reversed layer is laid.



Figure A.2: QR-code to video presentation of early process of a in-process measurement.

B Data and Calculation

Specific Measurement – Travel Time Calculation

In Figure 1 the last coordinates of the hotend boxed in green. The red box is the coordinates that directs the sensor over the object to be measured.

```
G1 X130.176 Y49.553 E0.06306
G1 X129.247 Y50.482 E0.09910
; INIT stop printing object DogBone_5x10.STL id:0 copy 0
;WIPE_START
G1 F8640;_WIPE
G1 X130.176 Y49.553 E-0.43348
G1 F8640;_WIPE
G1 X130.176 Y48.717 E-0.27585
G1 F8640;_WIPE
G1 X130.169 Y48.723 E-0.00317
;WIPE_END

M760
G1 X149.89 Y48.43 E0
G4 P600000

G1 E-0.03750 F3000
G1 Z33.620000 F10800
```

Figure 1 - Green box: Last coordinates of hotend. Red box: Coordinates to direct the sensor over object.

Travel distance:

Coordinates are given in millimeters. The deviation between the coordinates gives us the travel distance:

Travel distance, x-coordinates: $149.89mm - 129.247mm = 20.643mm$
Travel distance, y-coordinates: $50.482mm - 48.43mm = 2.058mm$

Travel Time:

Travel speed is set for non print moves on the printer, to 180 mm/s.

$$Travel\ time,\ x = \frac{20.643mm}{180mm/s} = 0.1147s$$

$$Travel\ time,\ y = \frac{2.058mm}{180mm/s} = 0.0114s$$

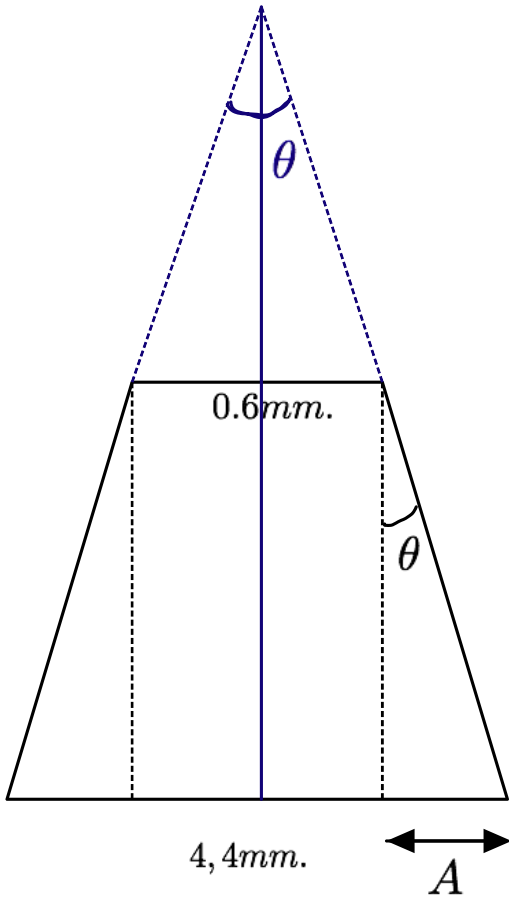
As the stepper motors works simultaneously, it is considered that the time used along the axis with the longest travel distance, is the actual total travel time for both axis. The total travel time is therefore, 0.1147s.

Diagonal aiming: focal point base length - calculation

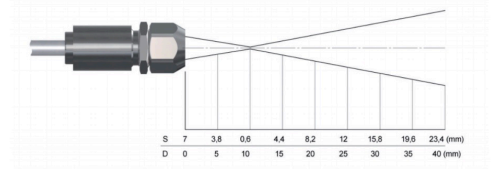
Distance between sensor and object : 13 mm.

Sensor angle: 31 degrees.

Referencing the optical chart, and using the spot sizes between 10 and 15 mm.



CT-SF22 + CF lens
0.6 mm @ 10 mm
0.6 mm @ 8 mm [TM-APLCF-CT]
D:S (far field CF) = 1.5:1



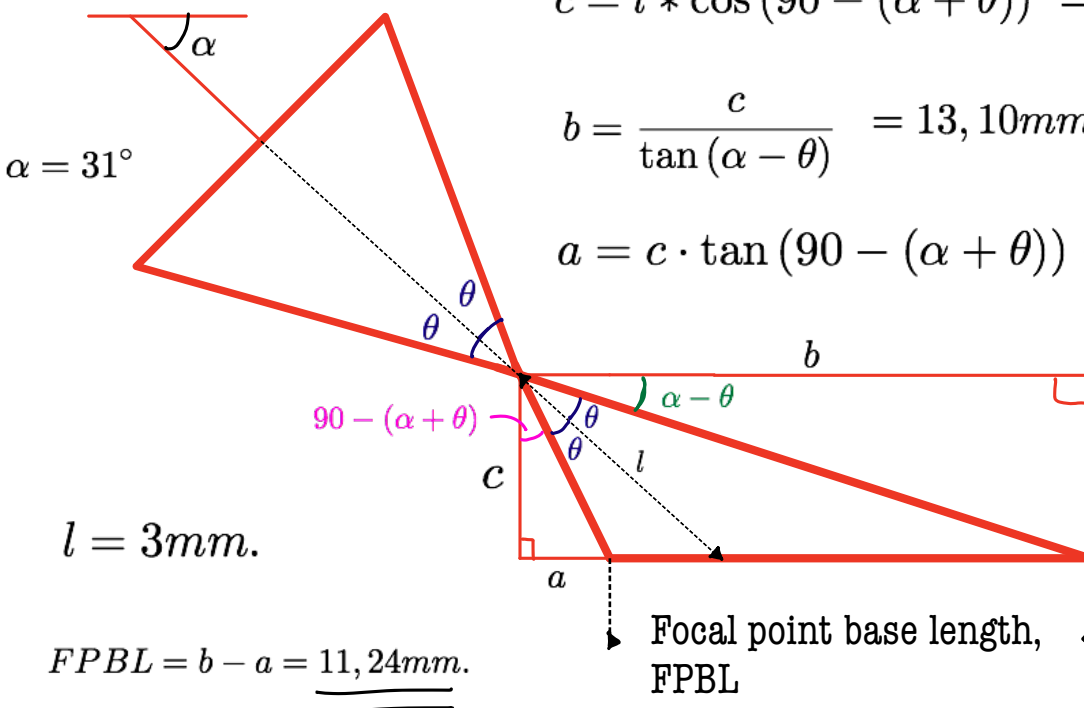
$$A = \frac{4,4 - 0,6}{2} = 1,9mm$$

$$\theta = \tan^{-1} \frac{1,9}{5} = 20,8^\circ$$

$$c = l * \cos(90 - (\alpha + \theta)) = 2,36mm$$

$$b = \frac{c}{\tan(\alpha - \theta)} = 13,10mm$$

$$a = c * \tan(90 - (\alpha + \theta)) = 1,86mm$$



Melt Test Data

Increasing temperature				Decreasing temperature				
Time	Sensor temp	Thermocouple T1	Thermocouple T2	Time	Sensor temp	Thermocouple T1	Thermocouple T2	Deviation: Sensor-T1
0	100	92,2	88,9	0	206	207,6	147,5	-1,6
10	107,1	97,8	95,3	2	205,6	208	146,7	-2,4
20	115,1	104,3	102,8	4	205,4	206,7	146,3	-1,3
30	123,2	112,3	110,3	6	204,8	205,7	145,3	-0,9
40	130,7	119,9	116,8	8	204,5	205,5	144,2	-1
50	137,6	127,5	124,1	10	204,1	205	143,7	-0,9
60	144,4	134,2	129,8	12	203,5	205,3	143,4	-1,8
70	151,5	141,3	137,9	14	203,4	204,5	144,1	-1,1
80	158,5	148,9	143,4	16	204,2	203,9	144,1	0,3
90	162,9	155,4	147,8	18	203,4	203,2	144,6	0,2
100	167,4	161,9	152,8	20	202,8	203,1	144,8	-0,3
110	171,5	166,3	155,2	22	202,8	204,3	144,6	-1,5
120	175,6	170,7	158,1	24	202,1	204	144,2	-1,9
130	179,6	174,5	160,3	26	201,7	203	144	-1,3
140	185,6	184	162,7	28	201,6	202,8	143,9	-1,2
142	187,2	185,7	163,4	30	201	202,3	143,1	-1,3
144	188,2	187,8	164	32	200,6	200,7	142,4	-0,1
146	189,5	190,1	164,6	34	200,2	200	141,9	0,2
148	191,4	191,5	166,5	36	200,2	200,2	141,4	0
150	191,7	192,3	167,5	38	199,8	200	141,2	-0,2
152	193,1	194	169,6	40	199,8	199,8	141,3	0
154	194,1	195,4	172	42	199,6	200,4	141,3	-0,8
156	195,9	197,2	173,5	49	198,7	198	139	0,7
158	197,3	199,4	175,7	50	198,5	198,5	138,7	0
160	198,4	201,8	176,9	52	198,7	198,4	138,5	0,3
162	198,8	203	178,3	54	197,8	197,5	138,9	0,3
164	200	203,8	179,8	56	197,4	196,3	138,6	1,1
166	201	204,8	181,2	58	196,8	196	138	0,8
168	202,4	206,6	183,2	60	196,5	195,7	138,5	0,8
170	203,5	208,4	185	62	196,9	195,6	140,1	1,3
172	204	209,2	187	64	196,7	196,2	141	0,5
174	205,9	211,2	188,4	66	196,5	196,1	140,4	0,4
176	207,4	213,7	189,7	68	195,9	196,2	139,2	-0,3
178	207,9	215,4	191,7	70	195,3	195,1	139,1	0,2
180	210,2	216,1	193,6	72	195,5	193,8	139	1,7
182	210,8	217,2	194,7	74	195,2	193,8	139,2	1,4
184	212,3	219,7	195,7	76	195,1	193,6	138,5	1,5
186	213,2	222	196,9	78	194,9	193,7	138,1	1,2
188	213,6	223,9	199,3	80	194,4	193,4	138,4	1
190	215,5	225,1	202	82	194,1	193,2	138,5	0,9
192	216,6	226	203,3	84	193,9	193,9	138,9	0
194	217,5	227,7	203,8	86	193,6	193,1	138,8	0,5
196	218,1	229,5	204,6	88	193,8	192,5	139,6	1,3
198	219,1	230,9	205,8	90	193,5	191,7	139,8	1,8
200	219,3	231,9	207,7	92	192,9	190,2	139,1	2,7
202	221	233,3	208,7	94	192,9	189,5	139	3,4
204	221,6	234,9	209,6	96	192,7	189,7	138,6	3
206	221,8	235,1	210,8	98	192	189,6	137,4	2,4
208	221,9	235,4	211	100	191,9	189,3	136,7	2,6
210	222,9	235,9	211,2	102	191,6	189,3	136,5	2,3
212	223,2	237	212,4	104	191,2	189,3	135,3	1,9
214	224,2	237,5	213,7	106	191,1	188,8	134,4	2,3
216	224,6	238,3	215,1	108	190,9	188,2	134,2	2,7
218	225,2	239,4	216,1	110	190,4	188,4	134	2
220	225,7	240,6	216,5	112	190,2	187,1	134,1	3,1
222	225,8	241,3	216,4	114	189,8	186,6	133,5	3,2
224	226,4	242,3	216,7	116	189,8	186,5	133	3,3
226	226,7	244	216,8	118	189,4	186,3	132,5	3,1
228	227,6	243,9	216,6	120	188,7	185,9	132,3	2,8
230	228,4	244	217,9	122	188,4	186	132,2	2,4
232	227,9	244,6	219,2	124	188,7	186,8	132,1	1,9
234	228,7	244,3	219,8					
236	229,1	244,2	220,5					
238	228,6	244,1	220,6					
240	229,3	244,2	220,8					
242	230	245,7	222,4					
244	229,9	246,7	222,5					
246	229,8	247,3	222,1					
248	229,7	248,5	222					
250	230,1	247,8	222					
252	229,8	248	221,9					
254	230,1	247,2	222,3					
256	230,3	246,7	222,1					
258	230,2	247,3	221,6					
260	231	247,6	221,5					
262	231,3	248,4	222,6					
264	231,2	249,3	223					
266	231,1	248,7	222,7					
268	231,2	248,9	222,3					
270	230,9	249,2	222,1					

In-process vs. Specific Measurements

Printing Speed	In-process Temperature	Specific Temperature (Half model)	Specific temperature (OneFourth model)	Deviation between In-process and Half	Deviation between In-process and OneFourth	Deviation between Half and OneFourth	Difference between 4 and 30 mm/s, Half	Difference between 4 and 30 mm/s, OneFourth	Difference between 4 and 14, Half model	Difference between 20 and 30, Half model
30	211,1	214,2	211	3,1	0,1	3,2	53,6	49,9	34,4	11,5
25	209,9	207,8	205,5	2,1	4,4	2,3			Average deviation for printing speeds between 4 and 16 mm/s, Half	Average deviation for printing speeds between 18 and 30 mm/s, Half
20	204,9	202,7	203	2,2	1,9	-0,3			11,6	2
18	202,6	202	200,6	0,6	2	1,4				
16	206	197,2	194,5	8,8	11,5	2,7				
14	200,9	195	193,4	5,9	7,5	1,6				
12	202,5	189,3	188	13,2	14,5	1,3				
11	200,3	188,6	191,4	11,7	8,9	-2,8				
10	197,5	185,4	189,2	12,1	8,3	-3,8				
9	195,2	181,9	186,3	13,3	8,9	-4,4				
8	194,8	178,8	185,4	16	9,4	-6,6				
7	188,1	176,7	178,2	11,4	9,9	-1,5				
6	187,7	173,7	174,7	14	13	-1				
5	181,2	179,3	170,6	1,9	10,6	8,7				
4	179,7	160,6	161,1	19,1	18,6	-0,5				

CompactConnect – In-process Measurements

Full diagrams of all In-process Measurements.

Figure 1: v4.

Status: Failed.

Test Line: Visible.

Reversed layer: Visible.

Comment: Most likely reason for failure, bed and z-axis not calibrated properly.

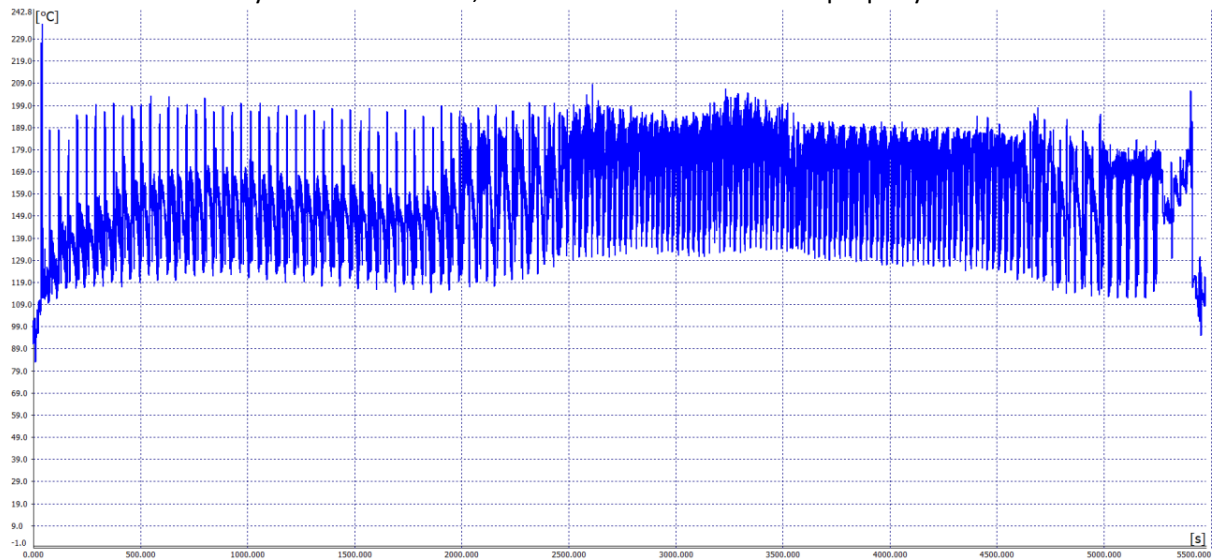


Figure 1 - Printer speed, 4 mm/s.

Figure 2: v5.

Status: Failed.

Test Line: Visible.

Reversed layer: Visible.

Comment: Most likely reason for failure, bed and z-axis not calibrated properly.

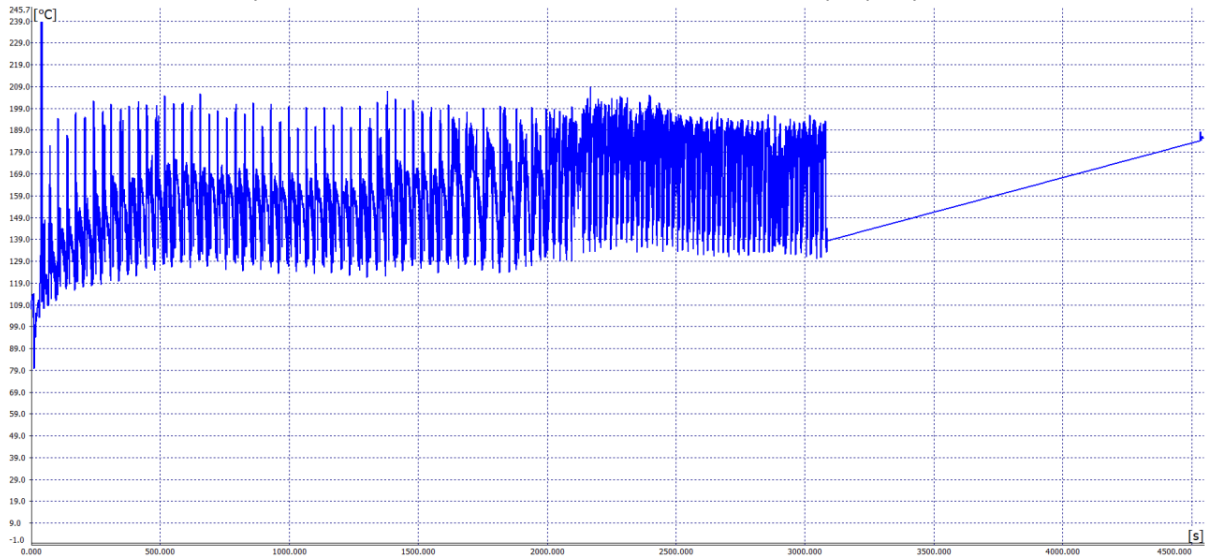


Figure 2 - Printer speed, 5 mm/s.

Figure 3: v6.

Status: Completed.

Test Line: Visible.

Reversed layer: Visible.

Comment:

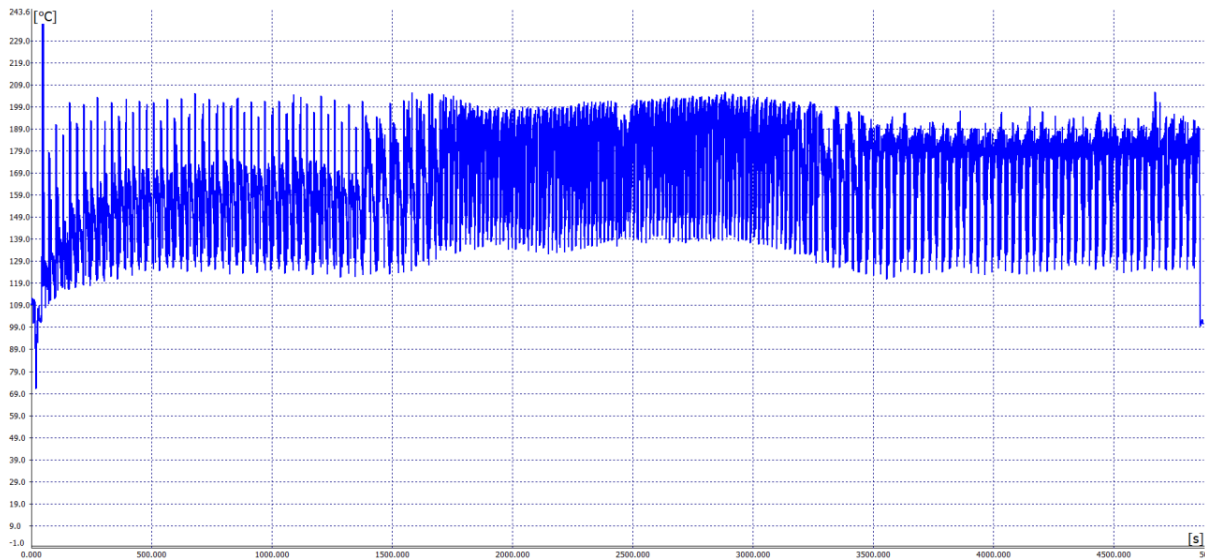


Figure 3 - Printer speed, 6 mm/s.

Figure 4: v7.
Status: Failed.
Test Line: Visible.
Reversed layer: Visible.
Comment: Most likely reason for failure, missing glue on bed.

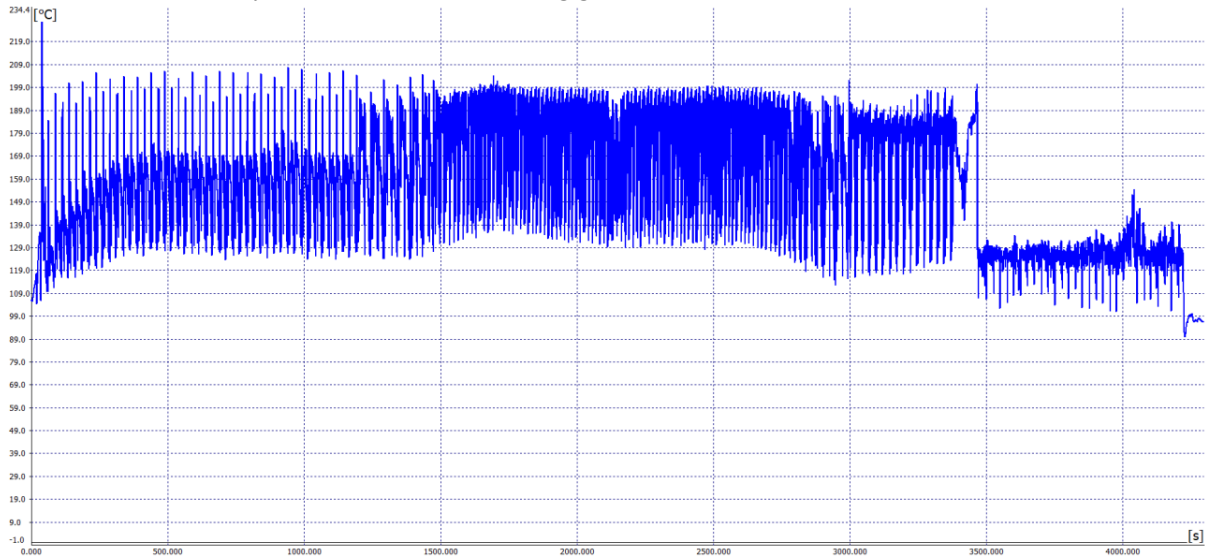


Figure 4 - Printer speed, v7.

Figure 5: v8.
Status: Completed.
Test Line: Visible.
Reversed layer: Visible.
Comment:

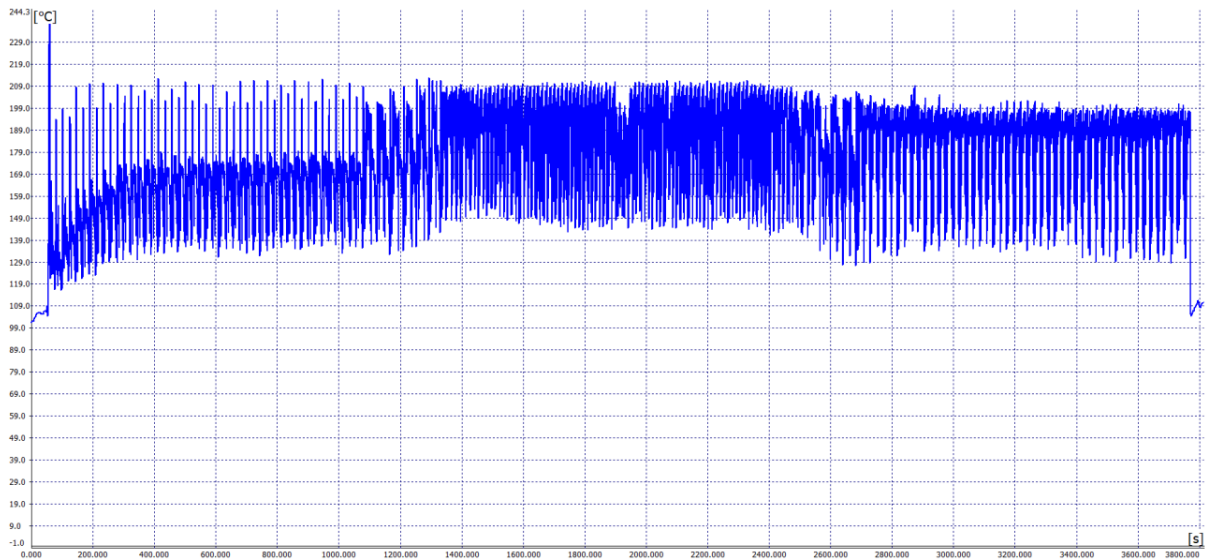


Figure 5 - Printer speed, 8 mm/s.

Figure 6: v9.
Status: Failed.
Test Line: Visible.
Reversed layer: Visible.
Comment: Most likely reason for failure, missing glue on bed.

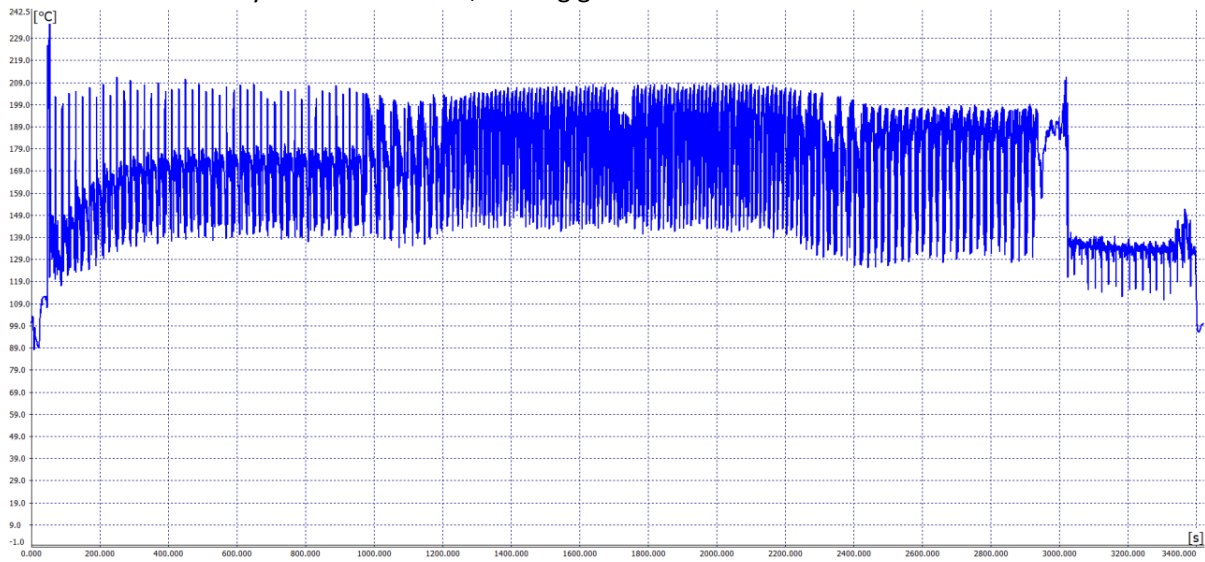


Figure 6 - Printer speed, 9 mm/s.

Figure 7: v10.
Status: Failed.
Test Line: Visible.
Reversed layer: Visible.
Comment: Most likely reason for failure, missing glue on bed.

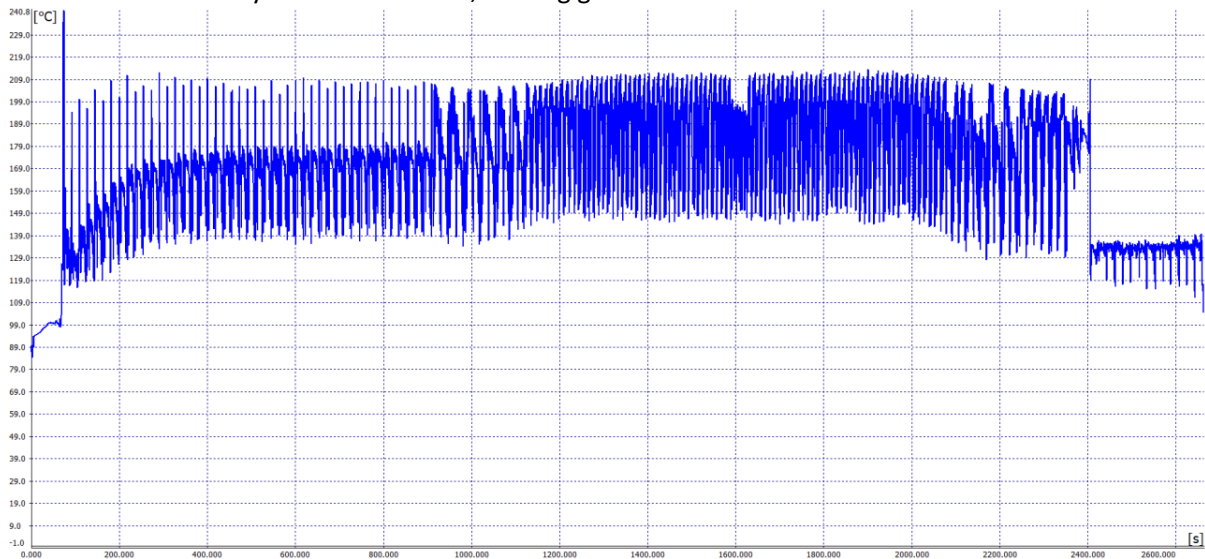


Figure 7 - Printer speed, 10 mm/s.

Figure 8: v11.
Status: Failed.
Test Line: Visible.
Reversed layer: Visible.
Comment: Most likely reason for failure, missing glue on bed.

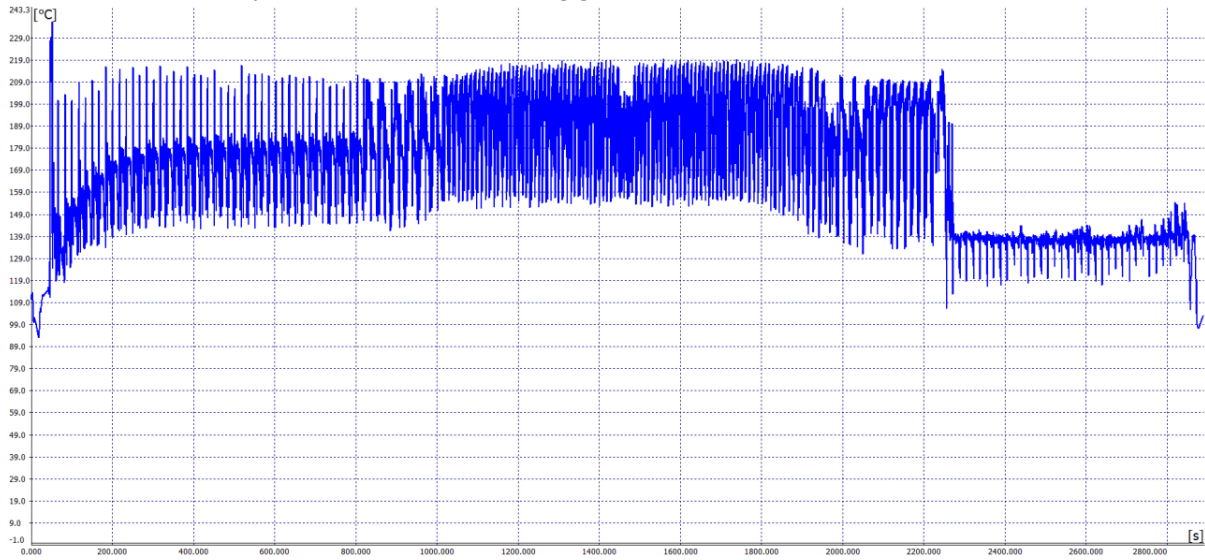


Figure 8 - Printer speed, 11 mm/s.

Figure 9: v12.
Status: Completed.
Test Line: Visible.
Reversed layer: Visible.
Comment: Most likely reason for failure, missing glue on bed.

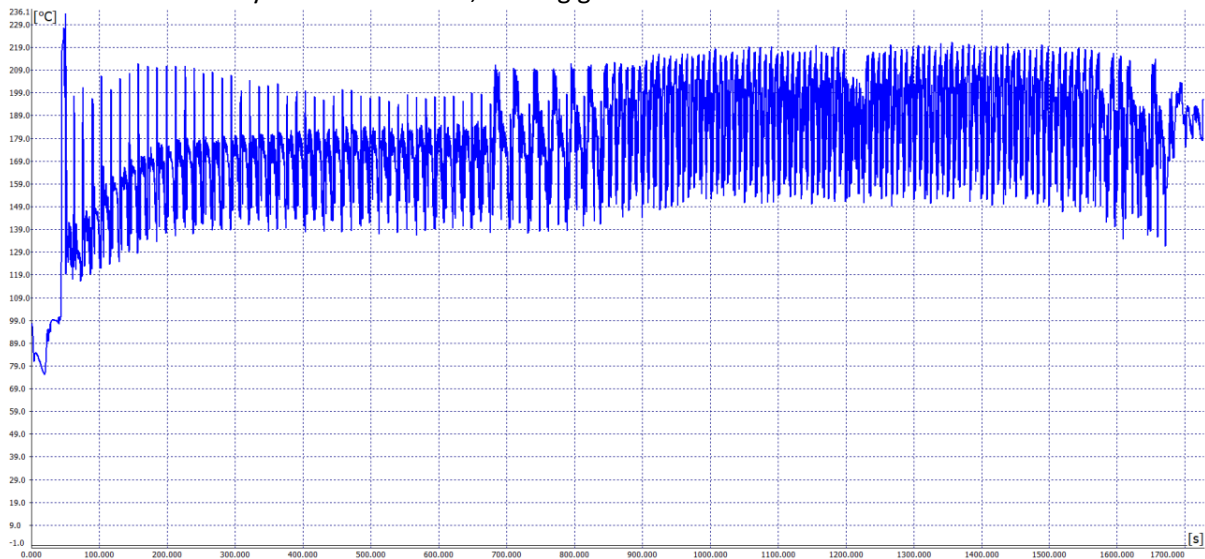


Figure 9 - Printer speed, 12 mm/s.

Figure 10: v14.
Status: Failed.
Test Line: Visible.
Reversed layer: Visible.
Comment: Most likely reason for failure, missing glue on bed.

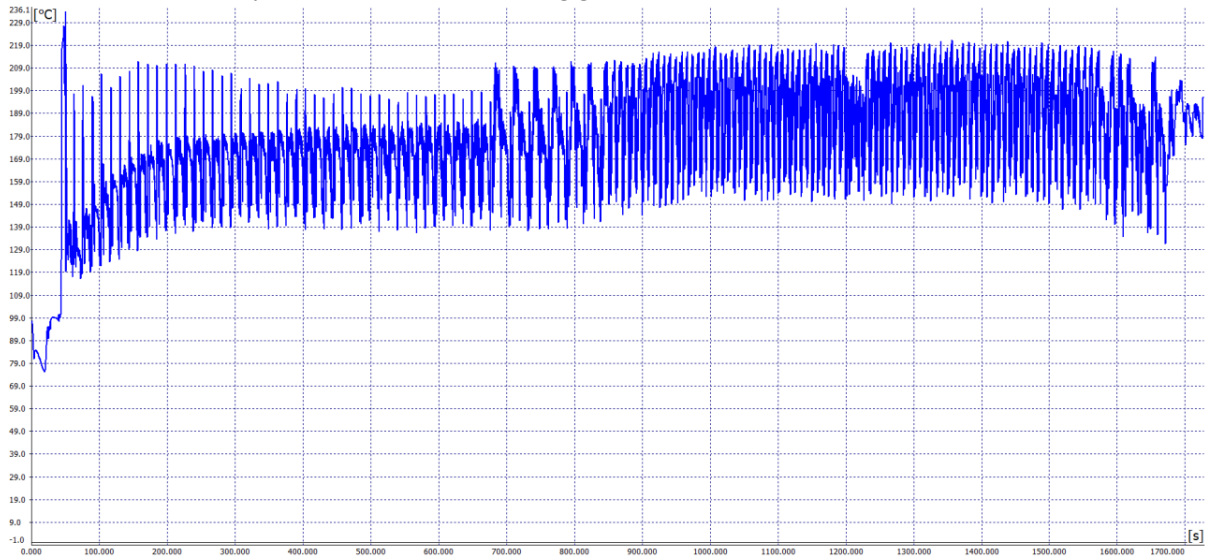


Figure 10 - Printer speed, 14 mm/s.

Figure 11: v16.
Status: Completed.
Test Line: Visible.
Reversed layer: Visible.
Comment:

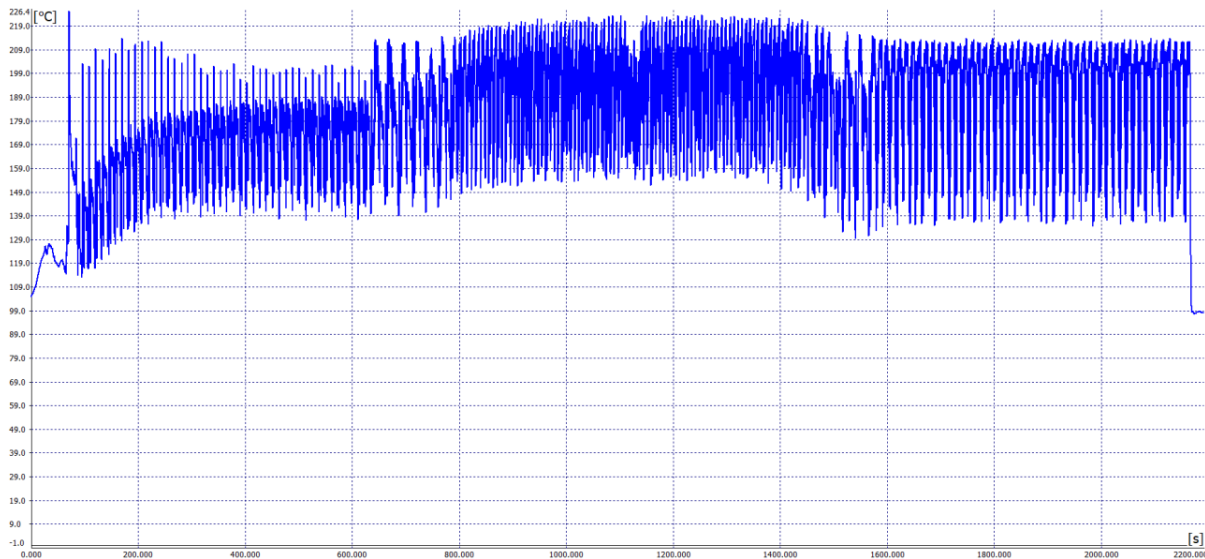


Figure 11 - Printer speed, 16 mm/s.

Figure 12: v18.
Status: Completed.
Test Line: Visible.
Reversed layer: Visible.
Comment:

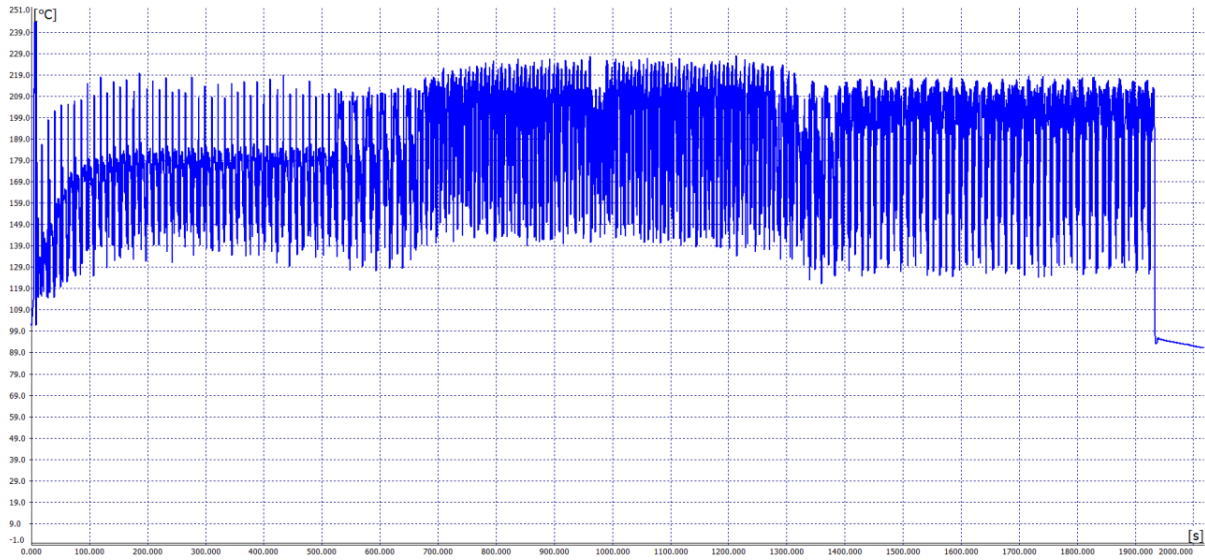


Figure 12 - Printer speed, 18 mm/s.

Figure 13: v20.
Status: Completed.
Test Line: Visible.
Reversed layer: Visible.
Comment:

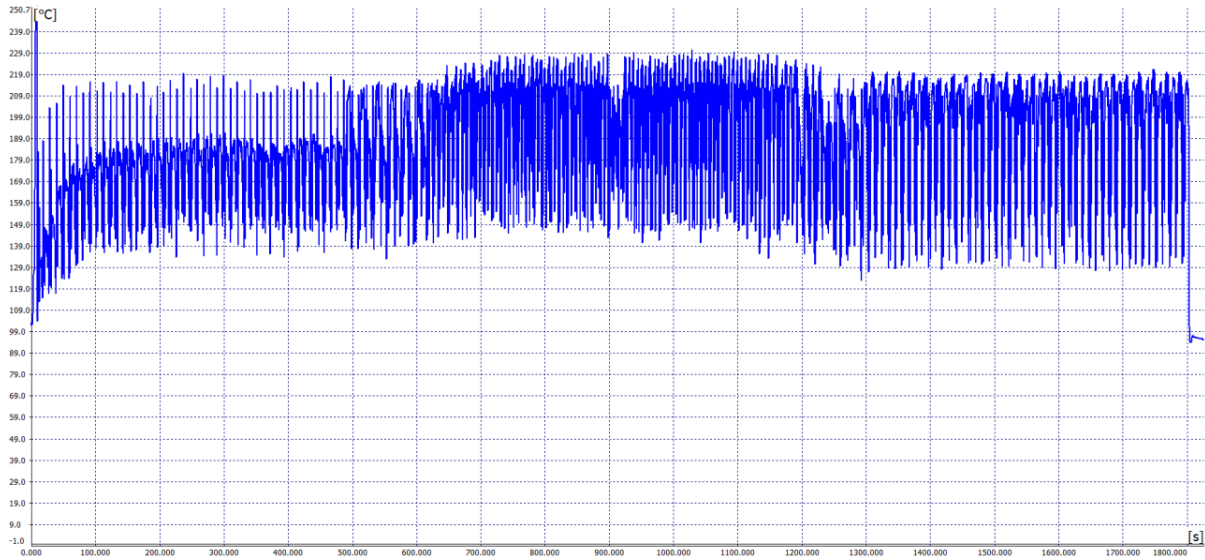


Figure 13 - Printer speed, 20 mm/s.

Figure 14: v25.
Status: Completed.
Test Line: Visible.
Reversed layer: Visible.
Comment:

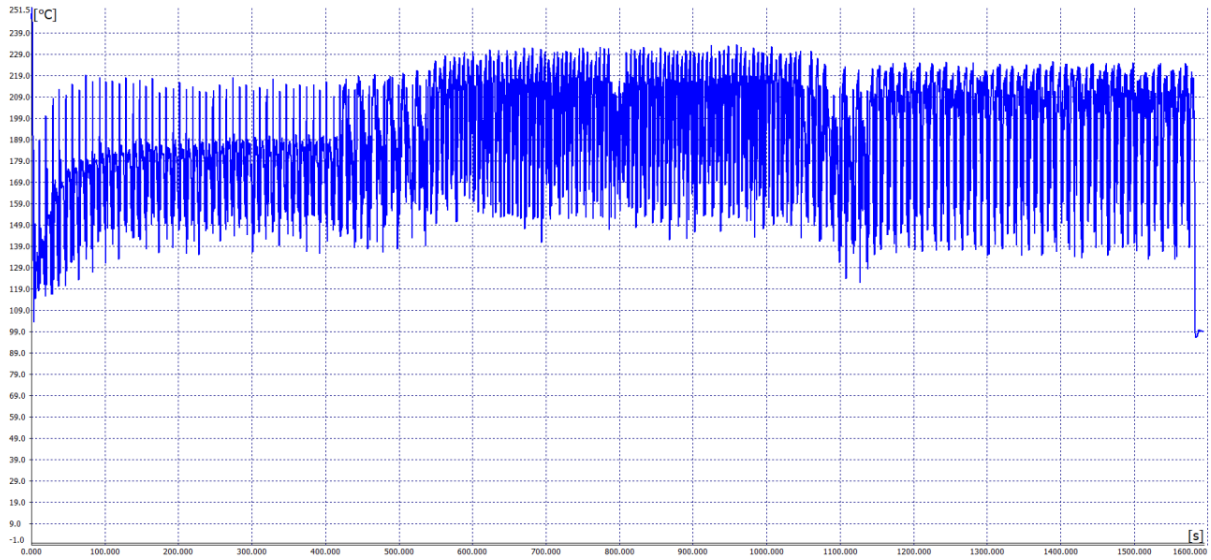


Figure 14 - Printer speed, 25 mm/s.

Figure 15: v30.
Status: Completed.
Test Line: Visible.
Reversed layer: Visible.
Comment:

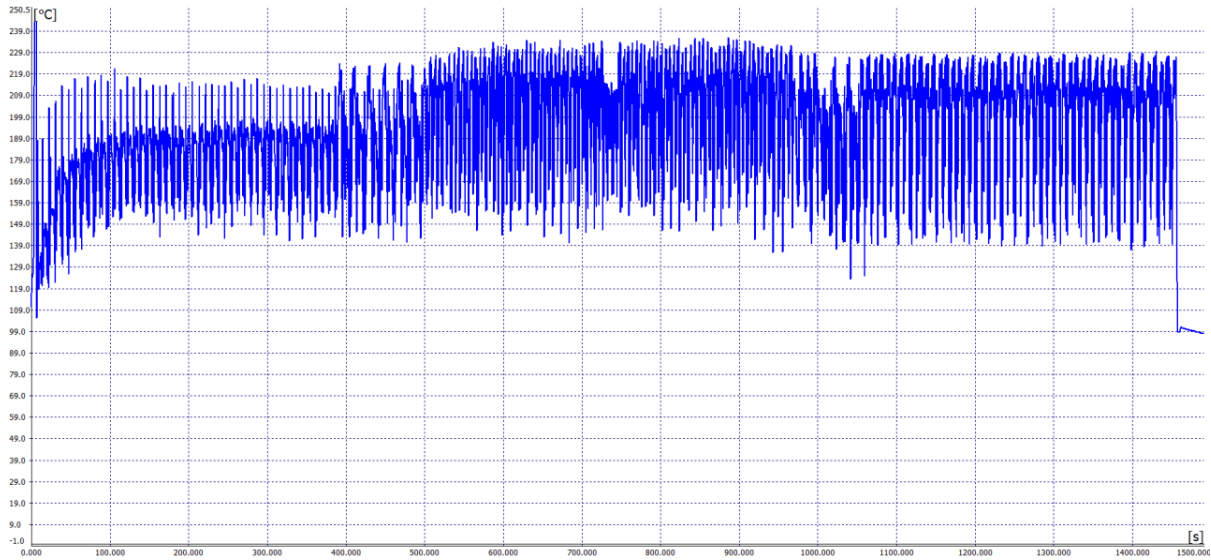


Figure 15 - Printer speed, 30 mm/s.

CompactConnect – Specific Measurements

Full diagrams of specific measurements.

Diagrams of the OneFourth model

Figure 1: v4.
Model: OneFourth.

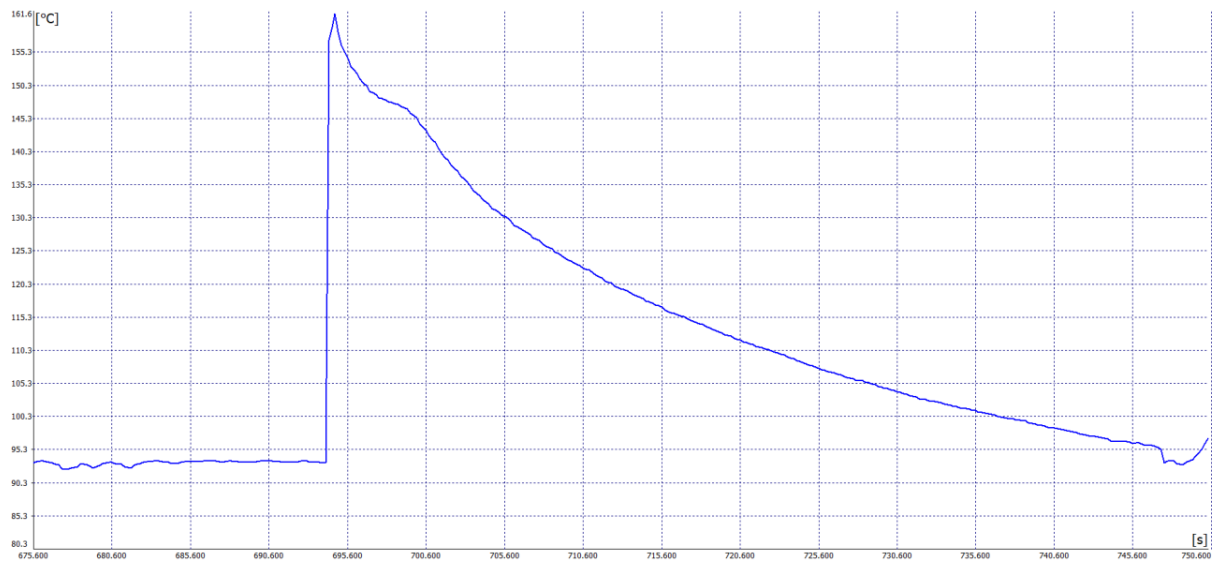


Figure 1 - Specific measurement of v4.

Figure 2: v5.
Model: OneFourth.

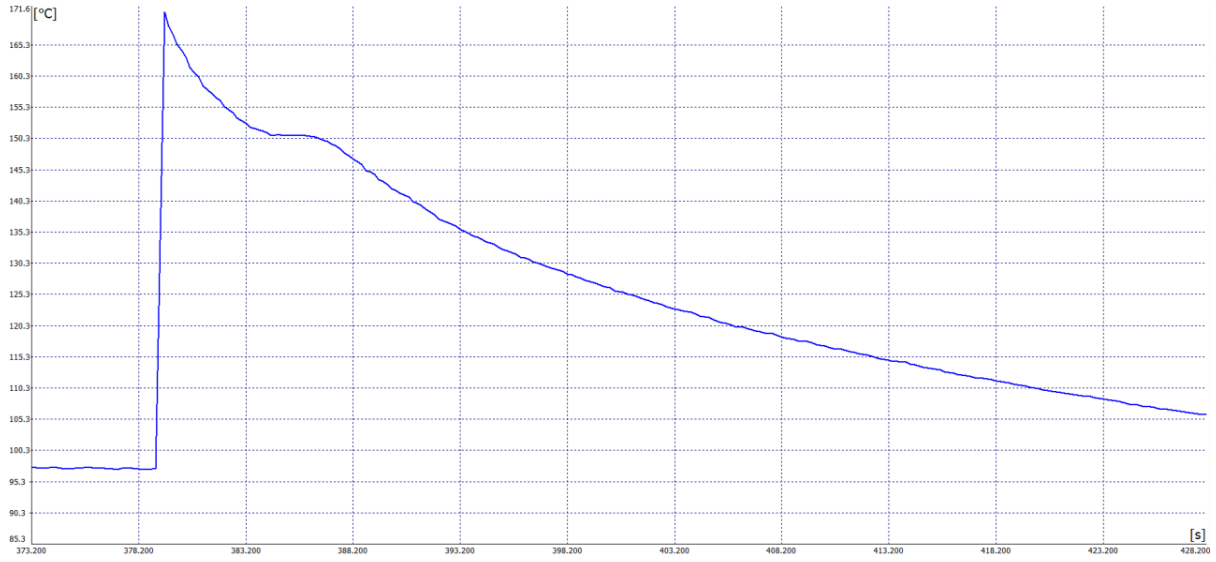


Figure 2 - Specific measurement of v5.

Figure 3: v6.
Model: OneFourth.

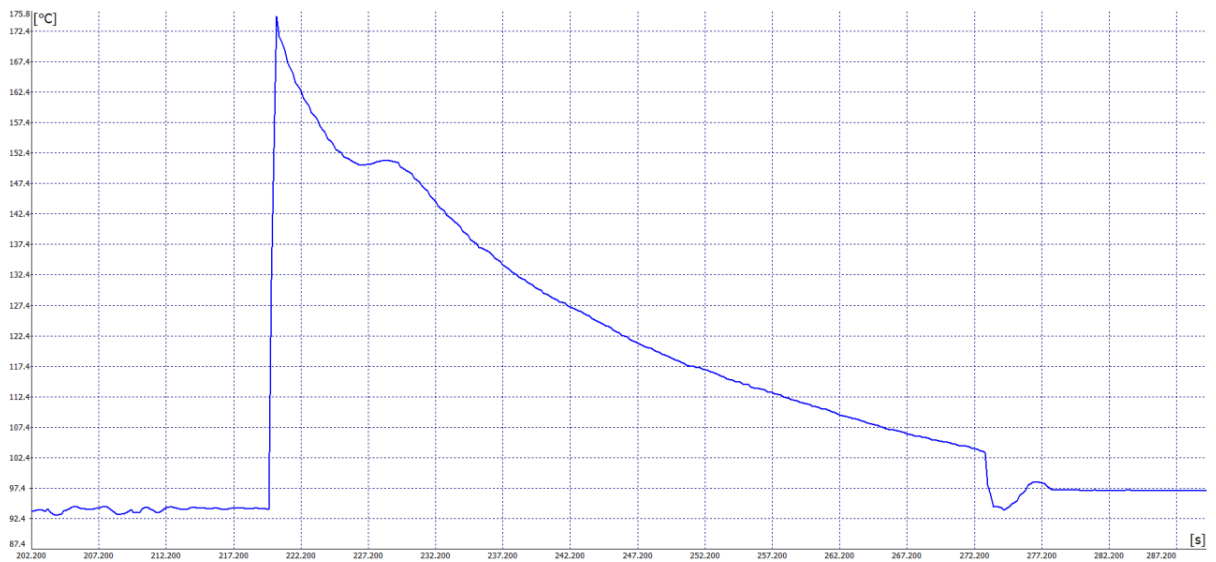


Figure 3 - Specific measurement of v6.

Figure 4: v7.
Model: OneFourth.

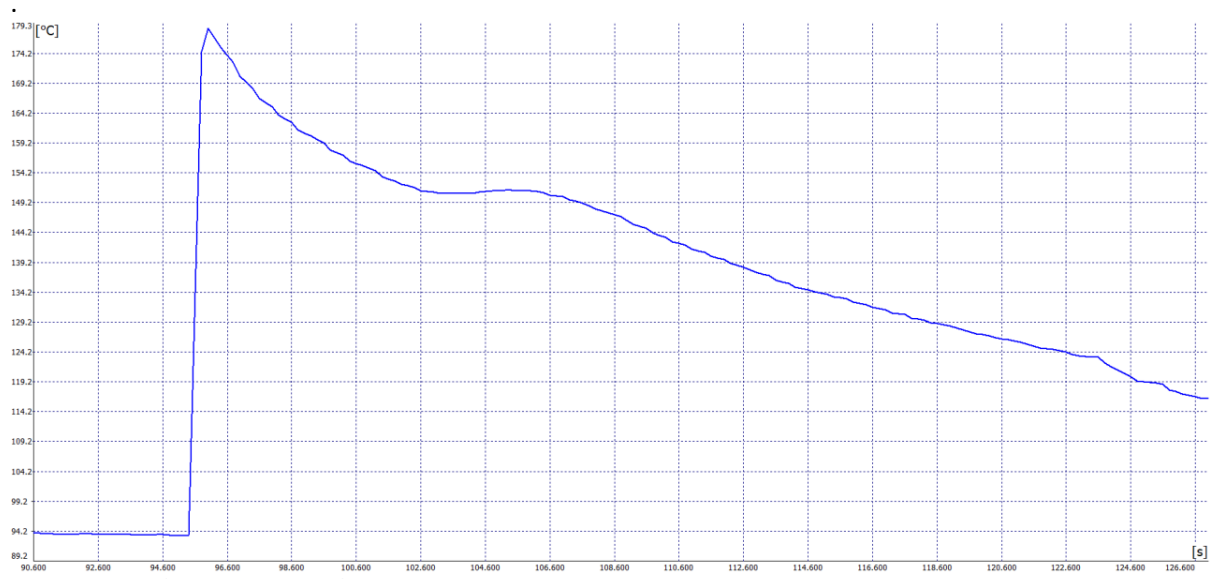


Figure 4 - Specific measurement of v7.

Figure 5: v8.
Model: OneFourth.

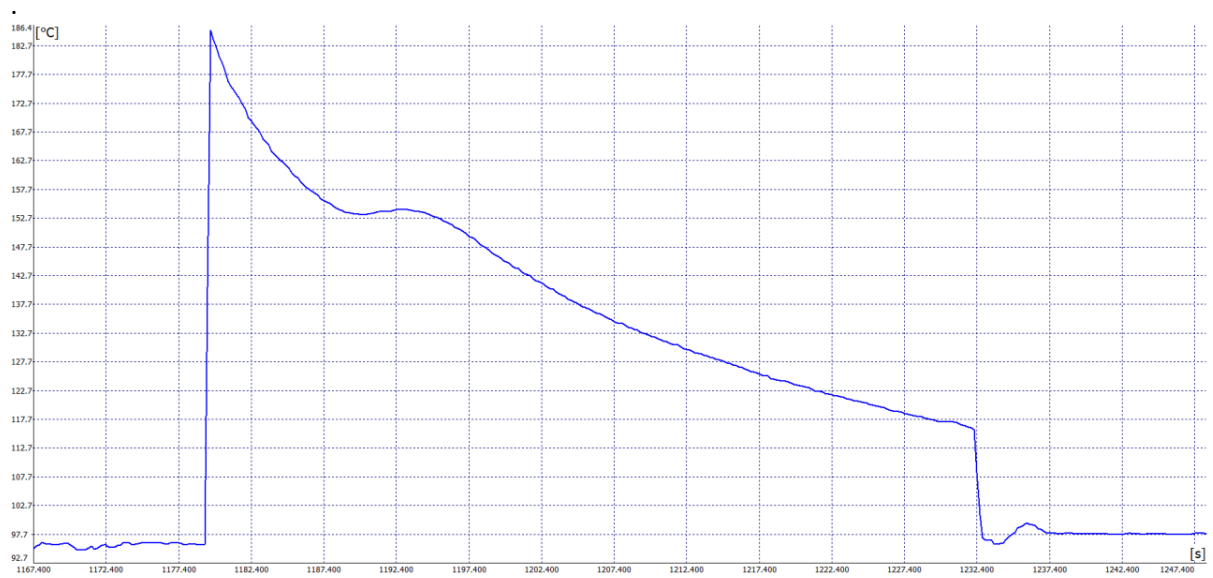


Figure 5 - Specific measurement of v8.

Figure 6: v9.
Model: OneFourth.

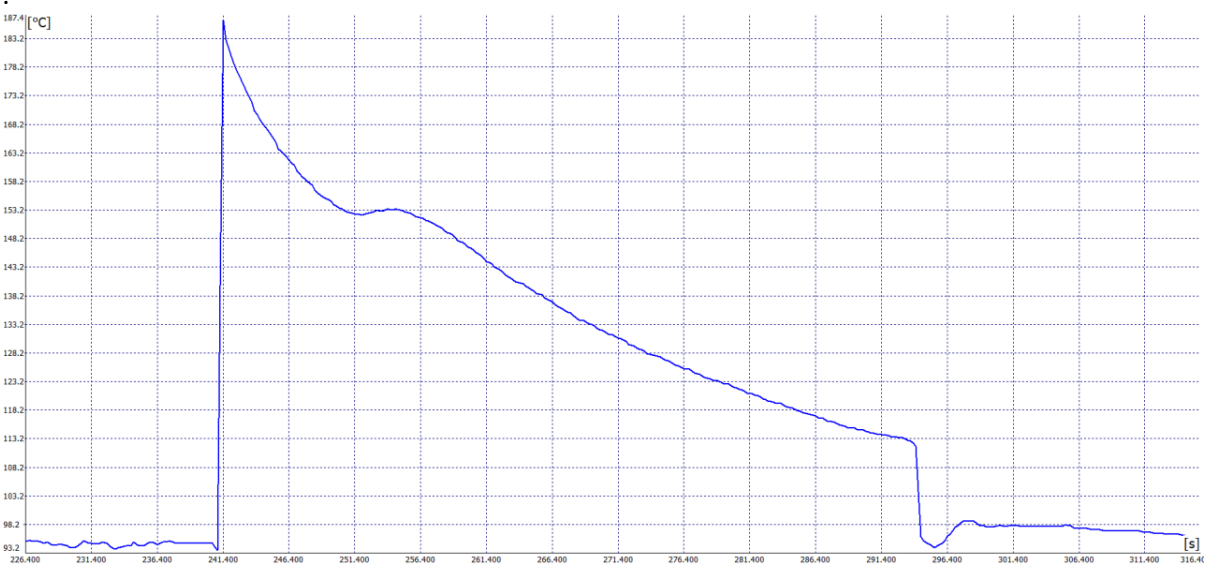


Figure 6 - Specific measurement of v9.

Figure 7: v10.
Model: OneFourth.

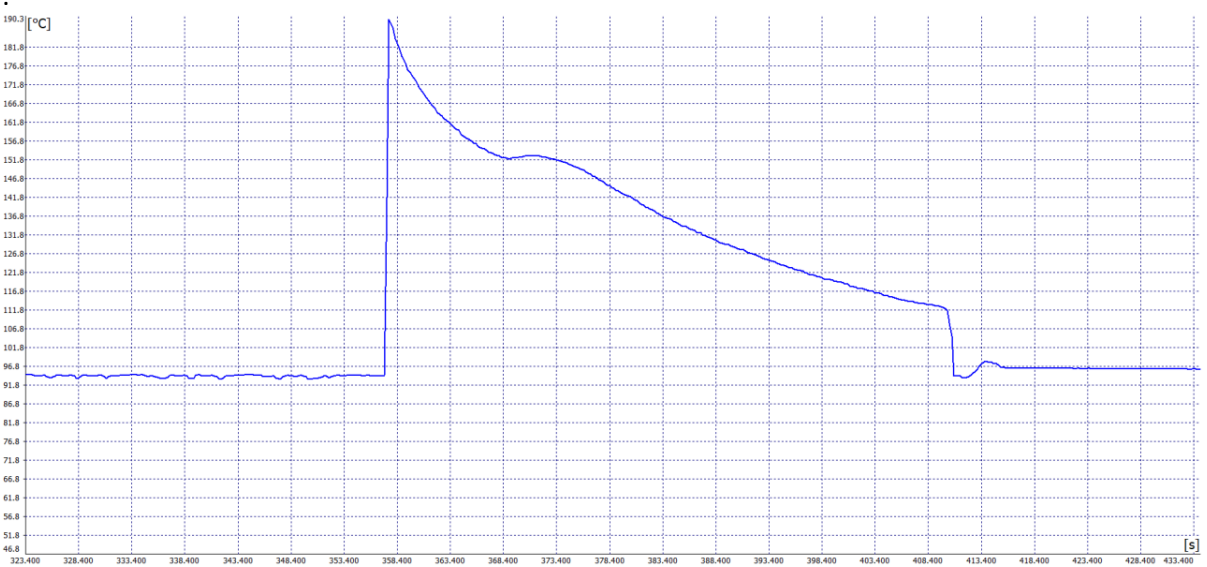


Figure 7 - Specific measurement of v10.

Figure 8: v11.
Model: OneFourth.

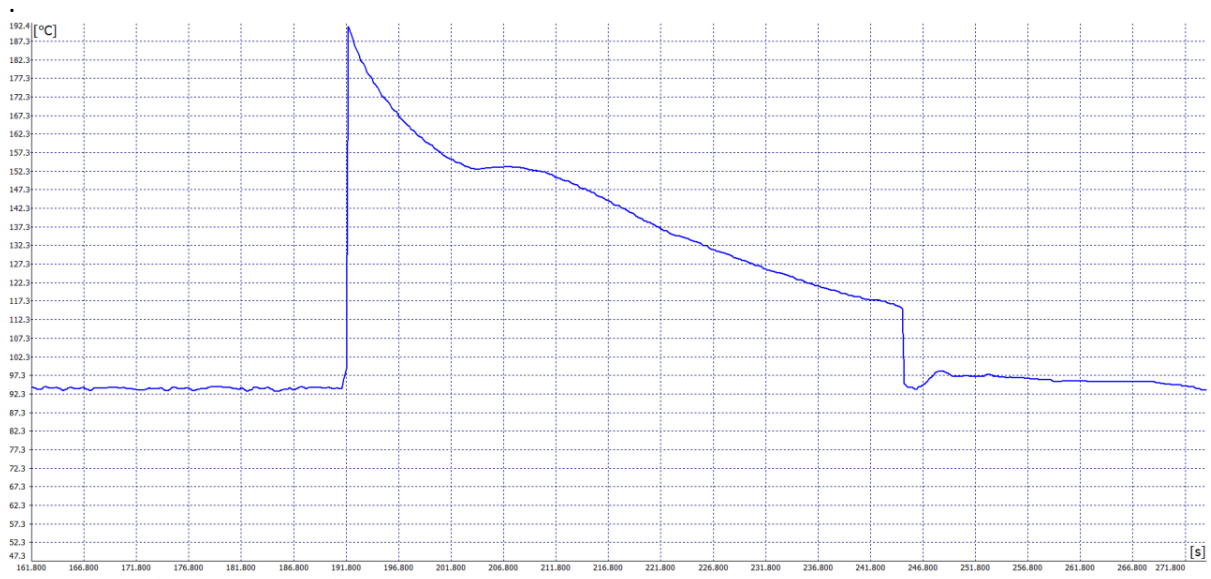


Figure 8 - Specific measurement of v11.

Figure 9: v12.
Model: OneFourth.

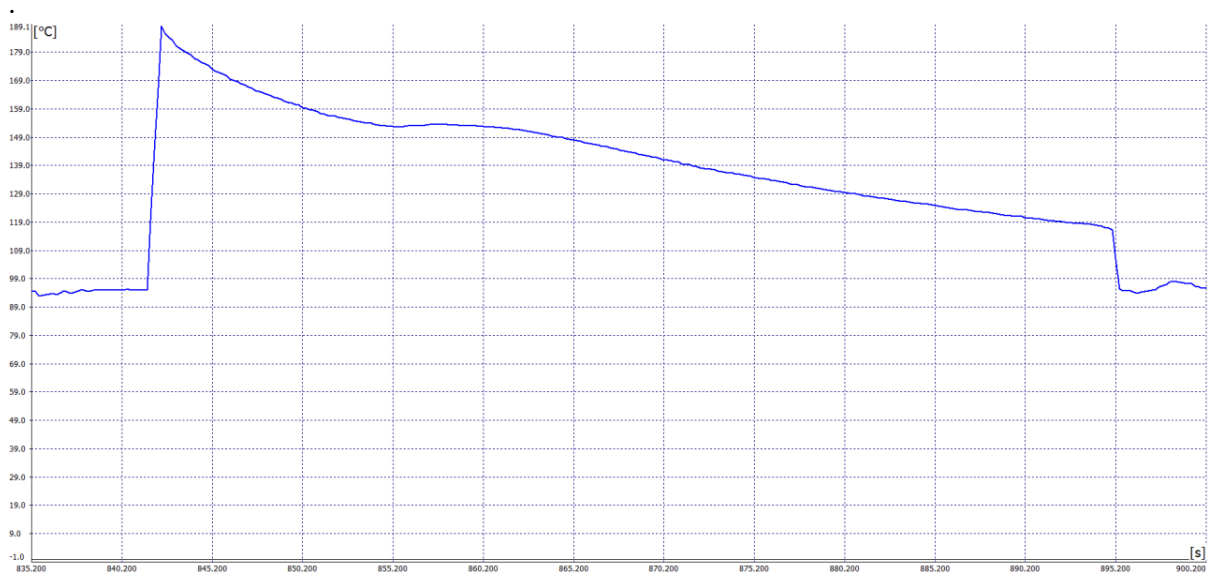


Figure 9 - Specific measurement of v12.

Figure 10: v14.
Model: OneFourth.

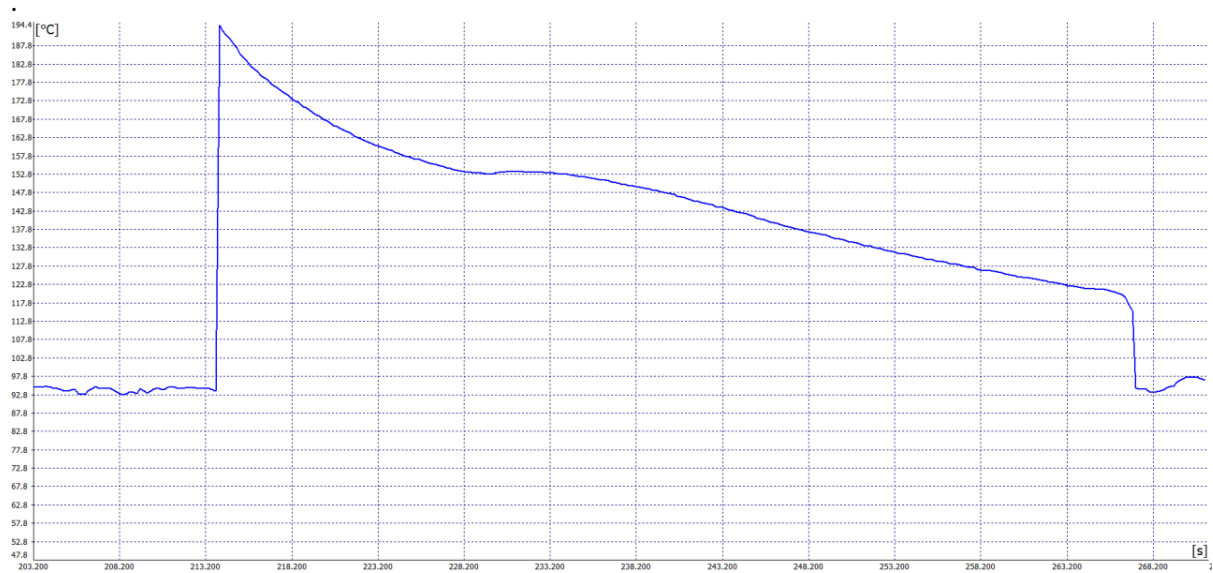


Figure 10 - Specific measurement of v14.

Figure 11: v16.
Model: OneFourth.

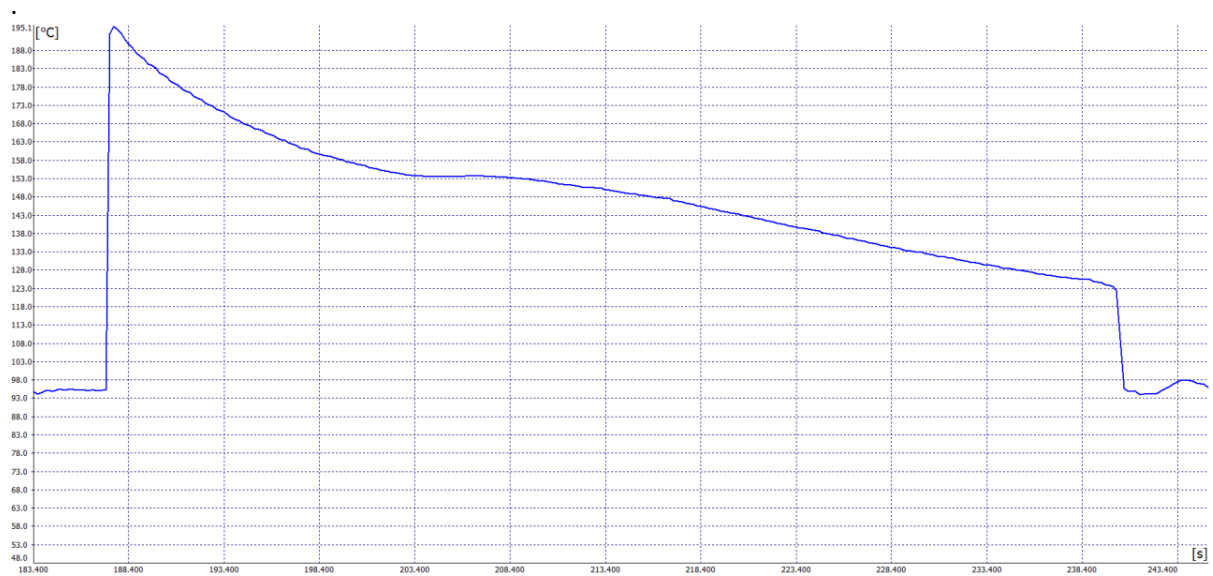


Figure 11 - Specific measurement of v16.

Figure 12: v18.
Model: OneFourth.

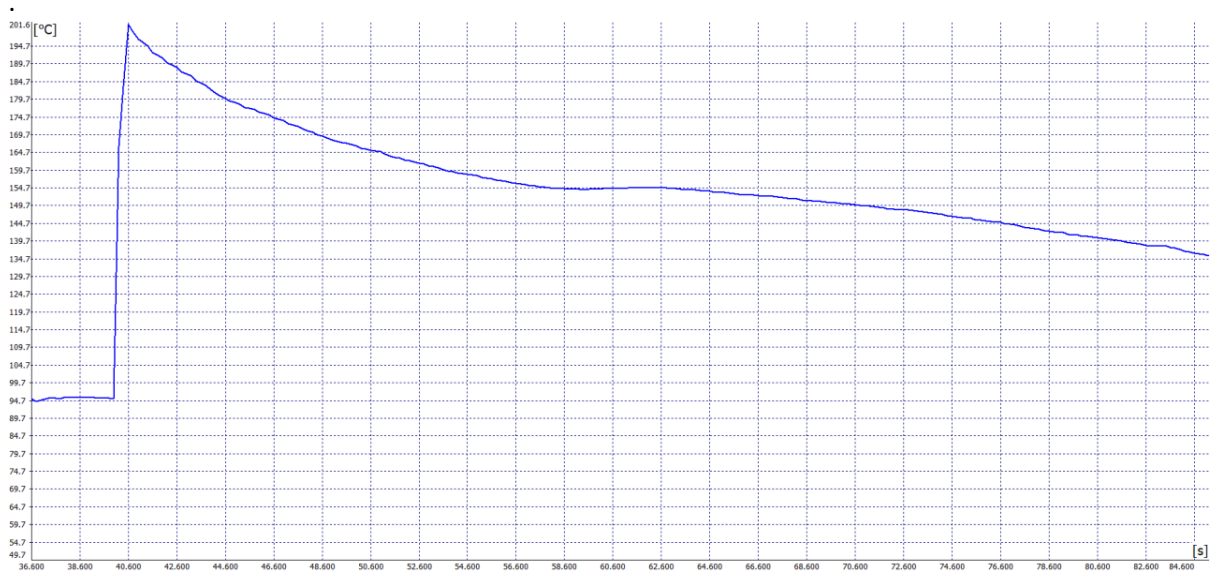


Figure 12 - Specific measurement of v18.

Figure 13: v20.
Model: OneFourth.

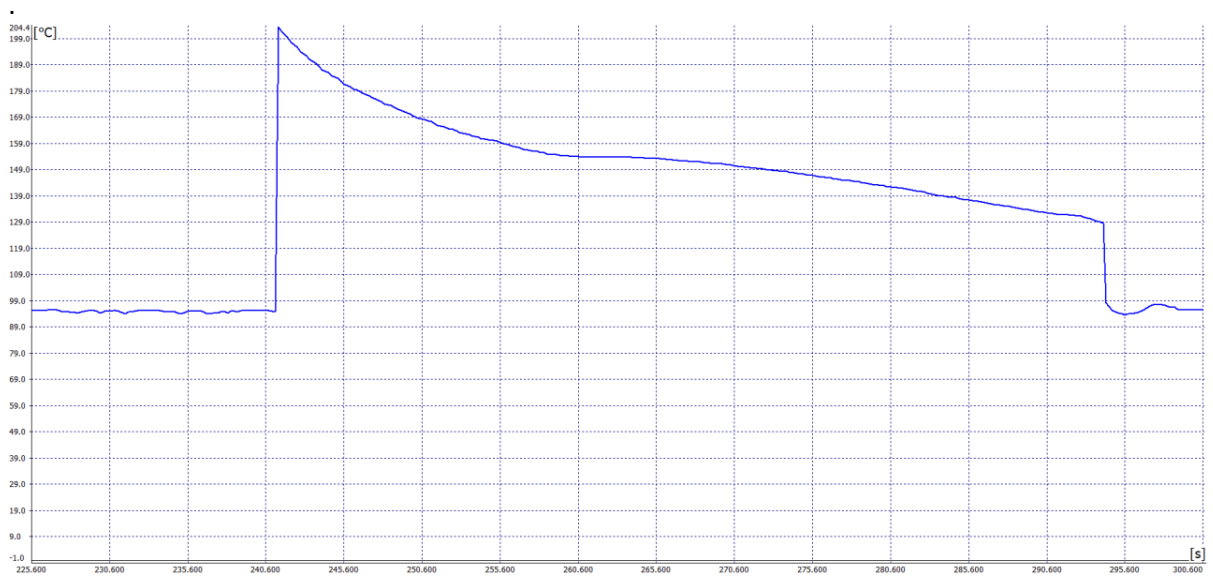


Figure 13 - Specific measurement of v20.

Figure 14: v25.
Model: OneFourth.

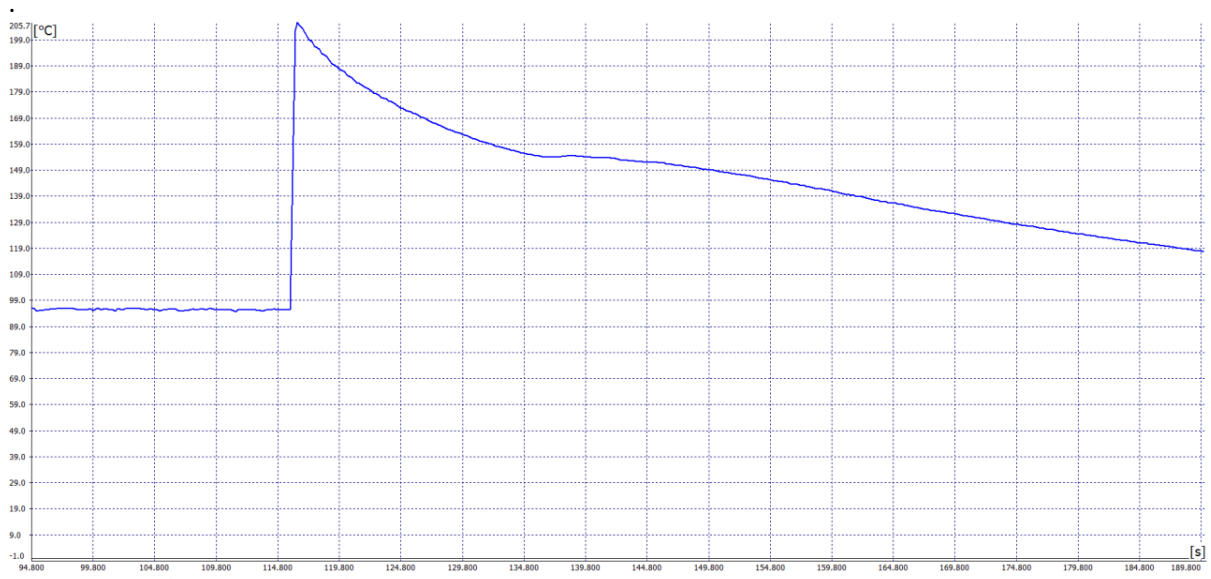


Figure 14 - Specific measurement of v25.

Figure 15: v30.
Model: OneFourth.

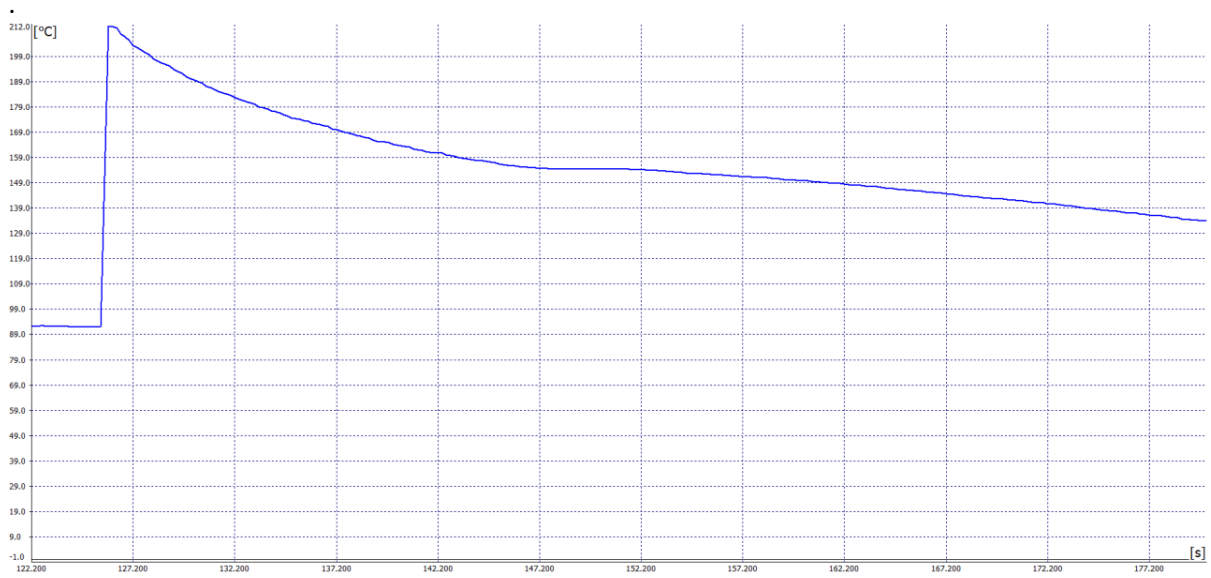


Figure 15 - Specific measurement of v30.

Diagrams of Half model

Figure 16: v4
Model: Half.

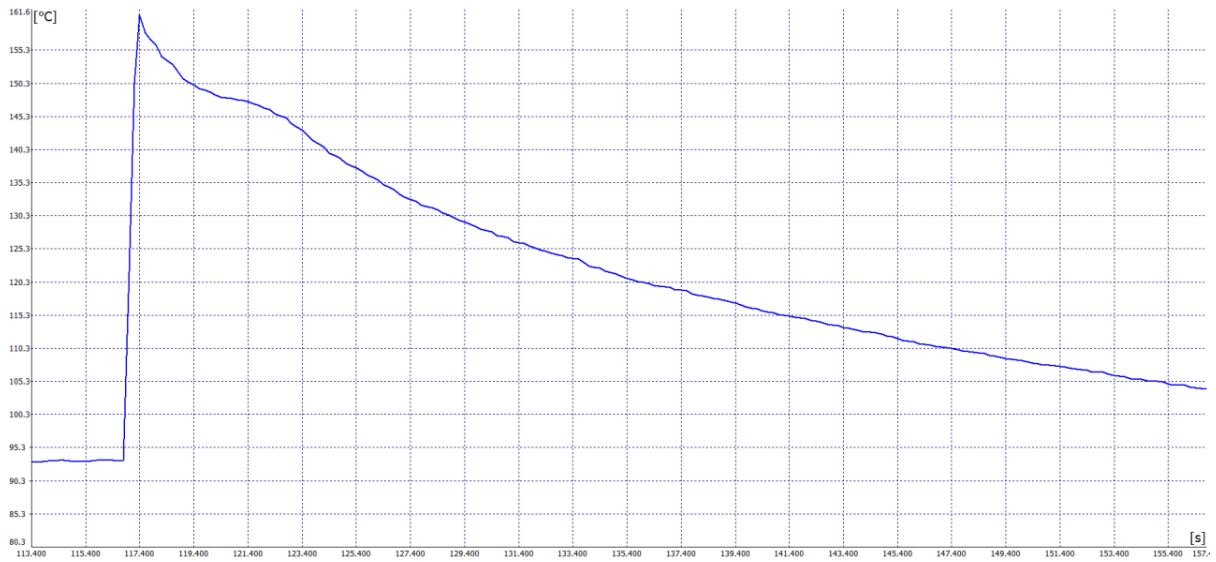


Figure 16 - Specific measurement of v4.

Figure : v5
Model: Half.

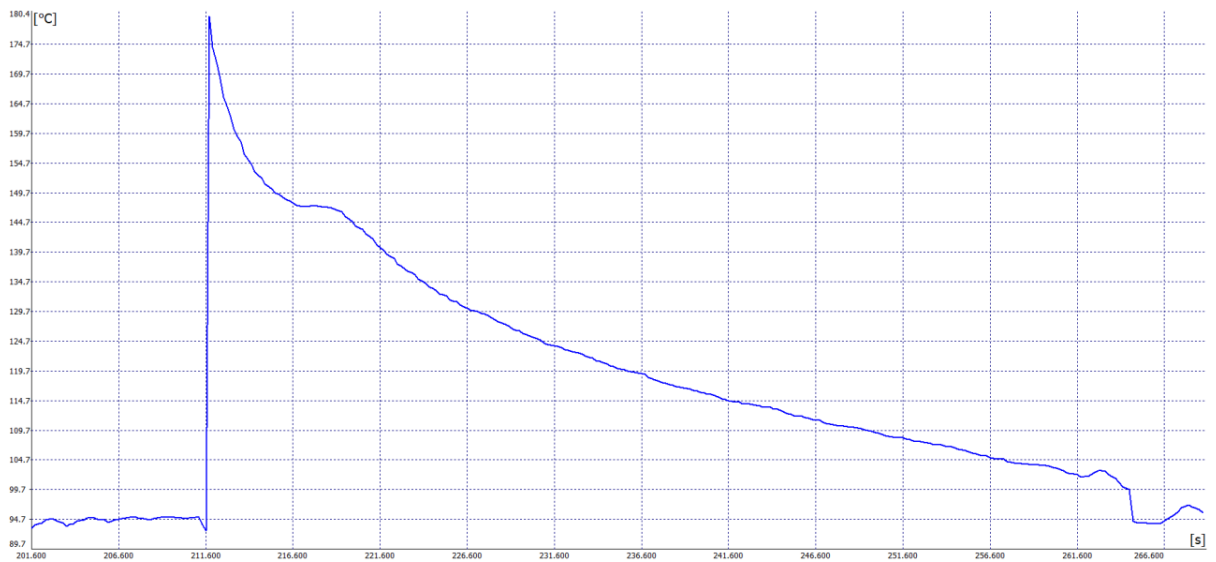


Figure 17 - Specific measurement of v5.

Figure : v6
Model: Half.



Figure 18 - Specific measurement of v6.

Figure : v7
Model: Half.

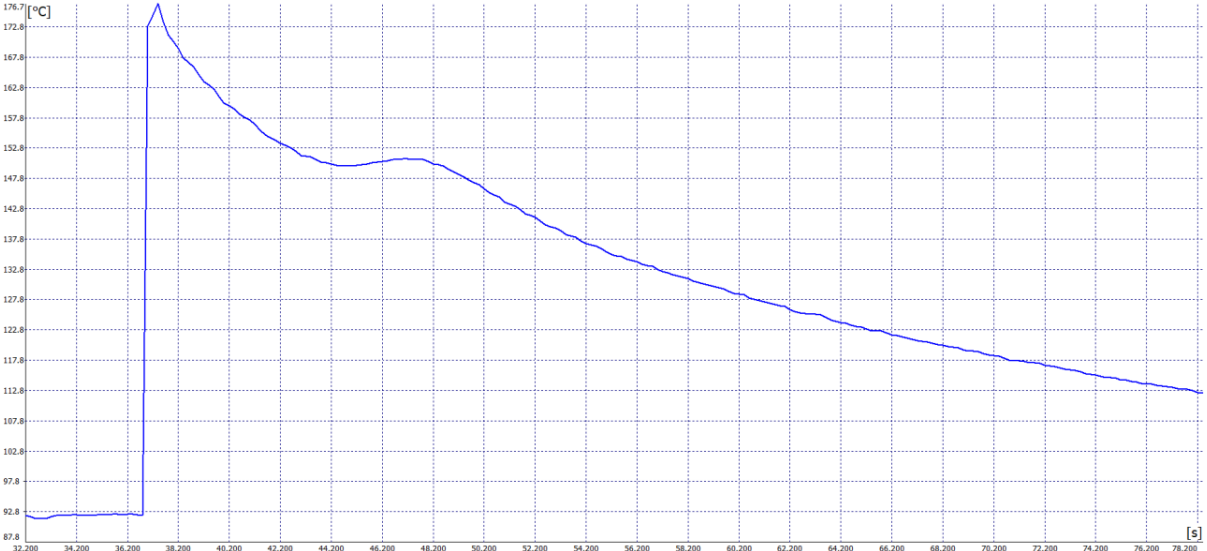


Figure 19 - Specific measurement of v7.

Figure : v8
Model: Half.

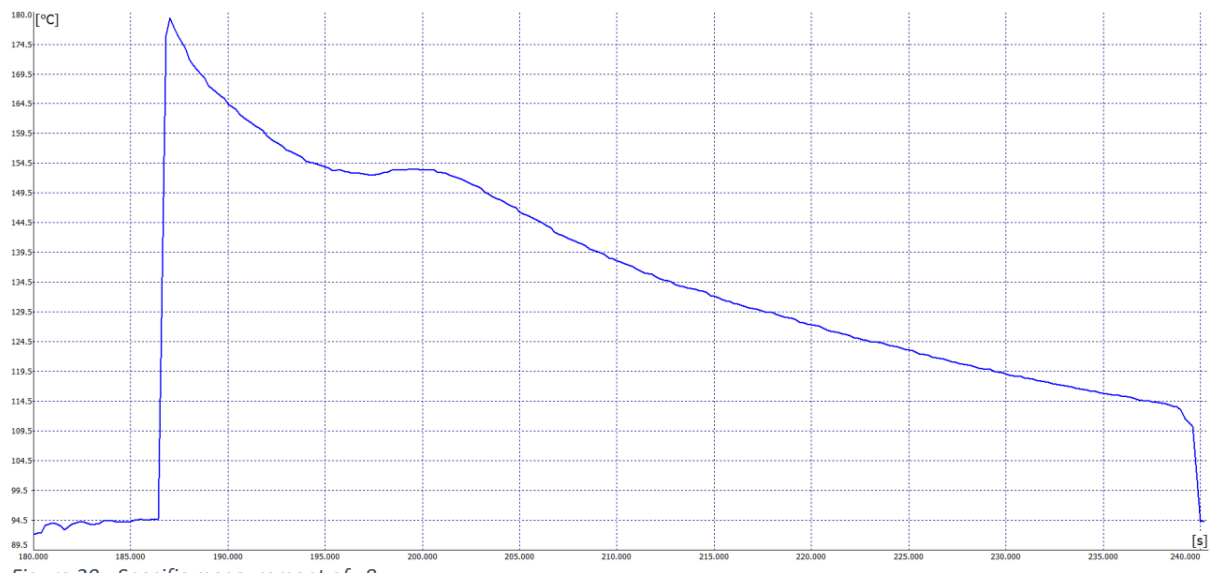


Figure 20 - Specific measurement of v8.

Figure : v9
Model: Half.10

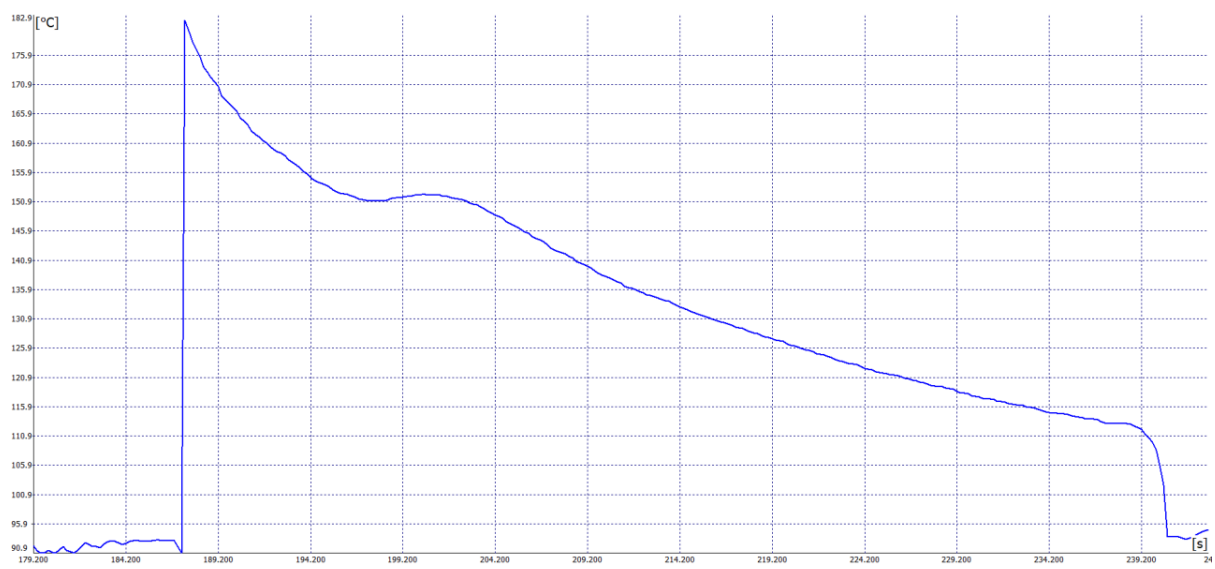


Figure 21 - Specific measurement of v9.

Figure : v10
Model: Half.

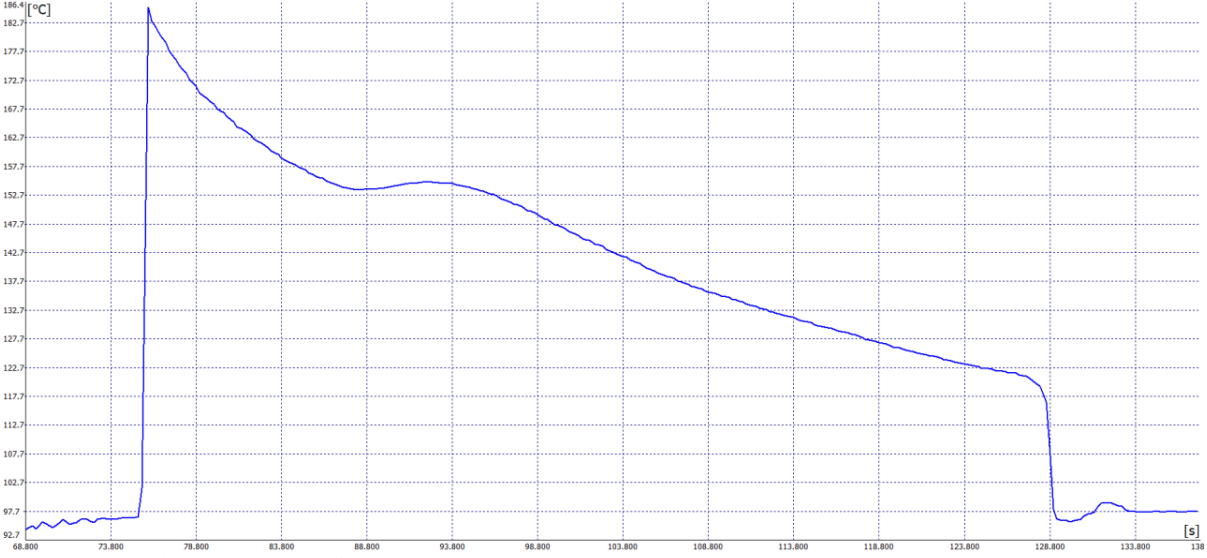


Figure 22 - Specific measurement of v10.

Figure : v11
Model: Half.

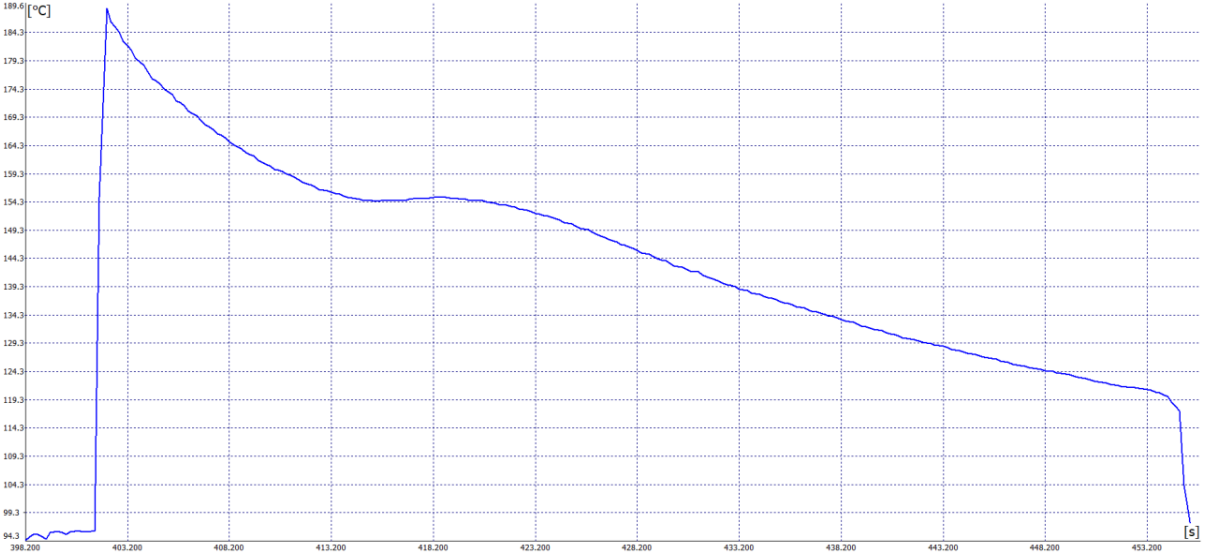


Figure 23 - Specific measurement of v11.

Figure : v12
Model: Half.

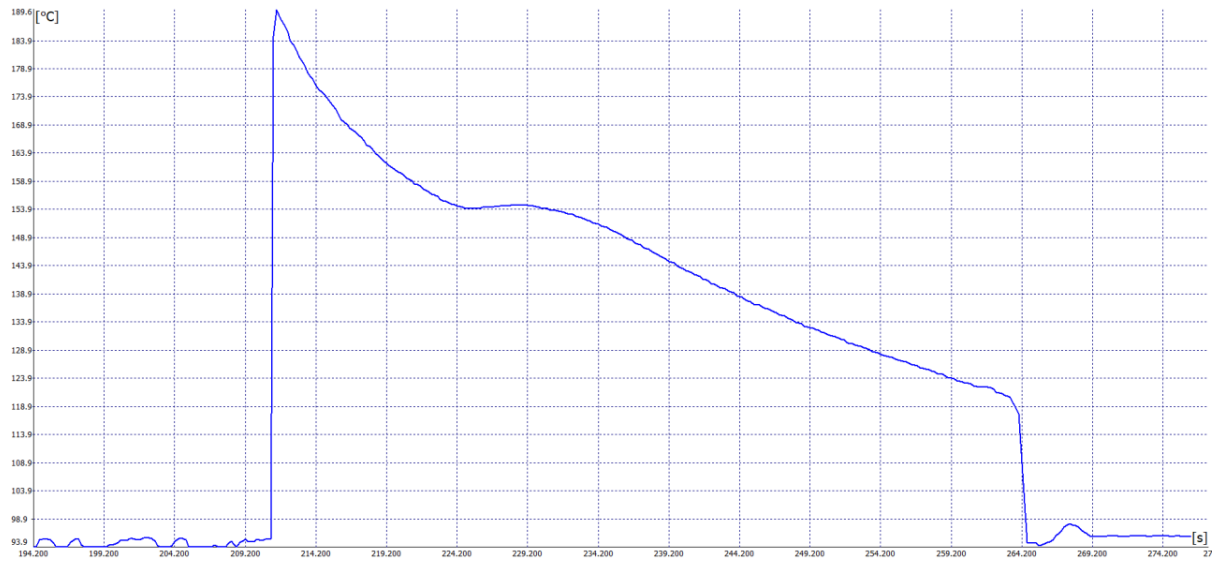


Figure 24 - Specific measurement of v12.

Figure : v14
Model: Half.

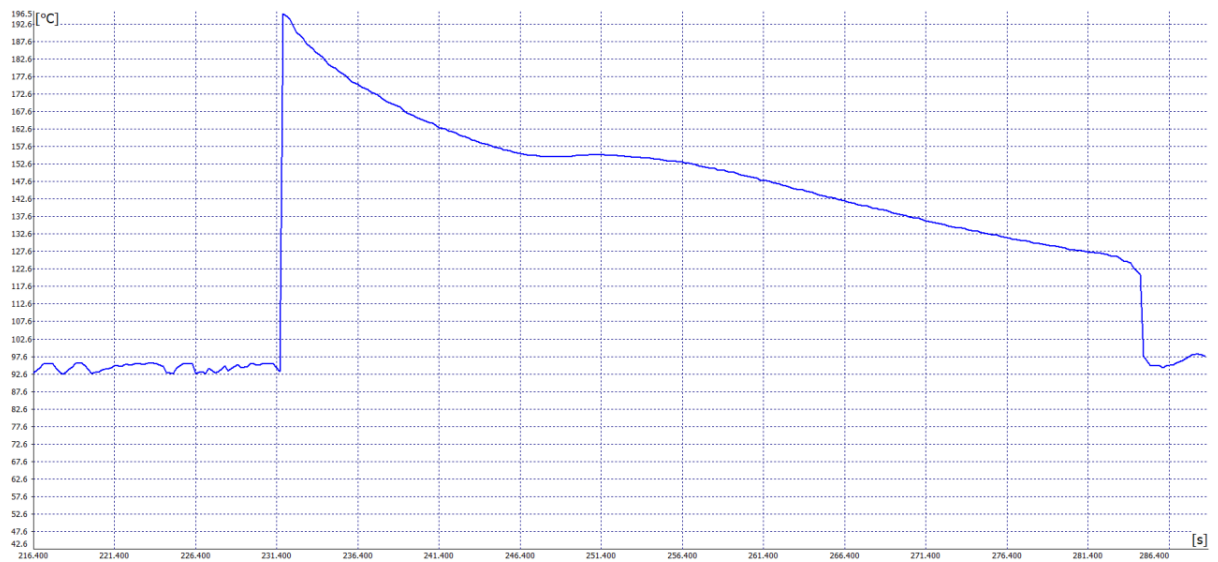


Figure 25 - Specific measurement of v14.

Figure : v16
Model: Half.

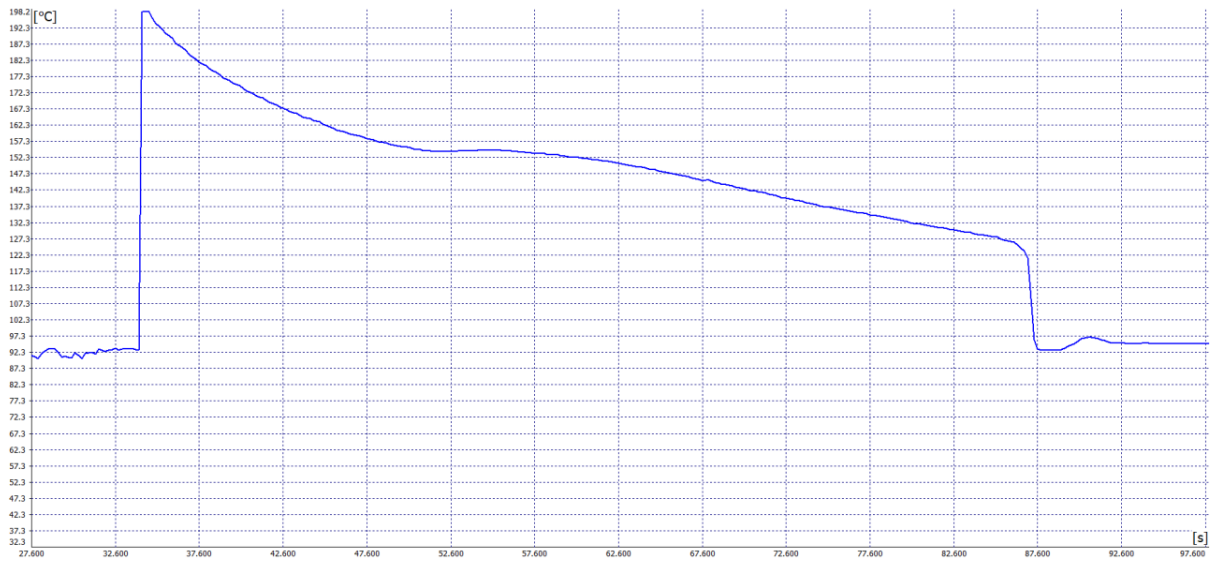


Figure 26 - Specific measurement of v16.

Figure : v18
Model: Half.

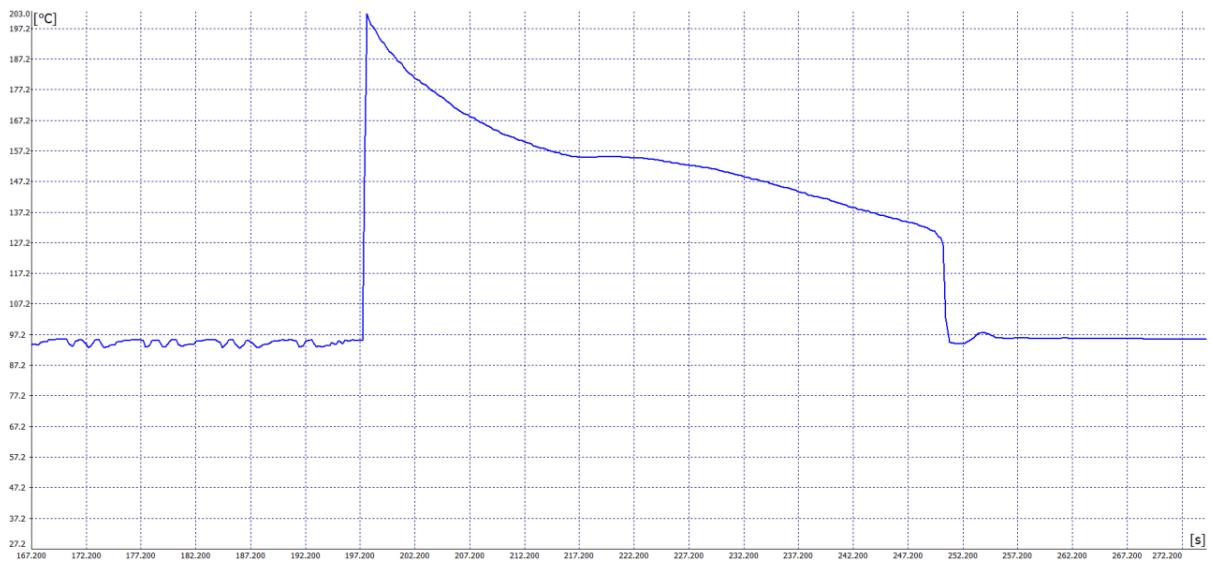


Figure 27 - Specific measurement of v18.

Figure : v20.
Model: Half.

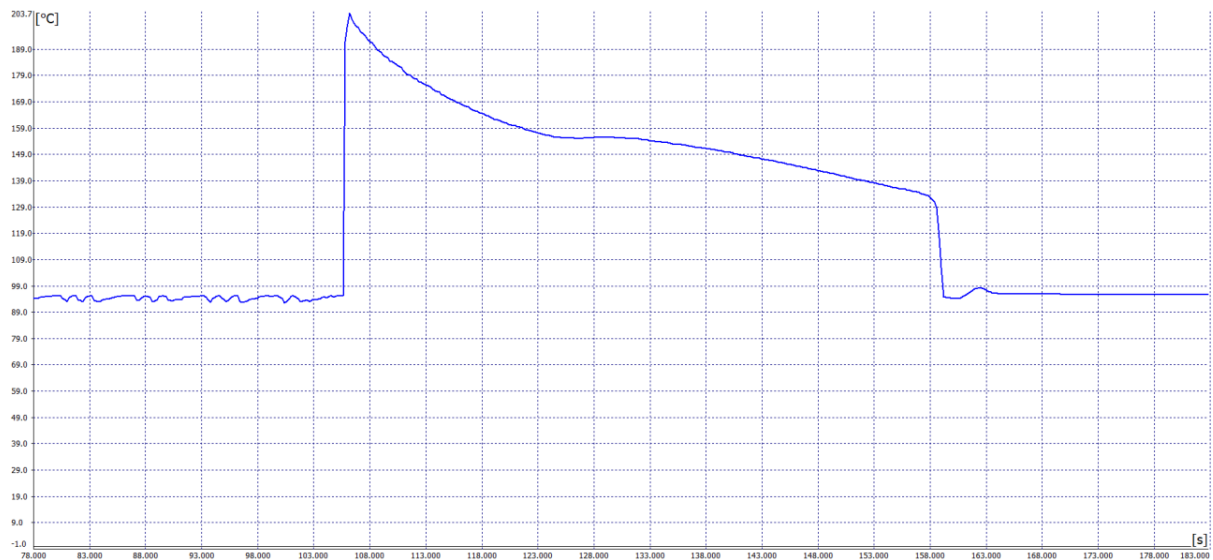


Figure 28 - Specific measurement of v20.

Figure : v25.
Model: Half.

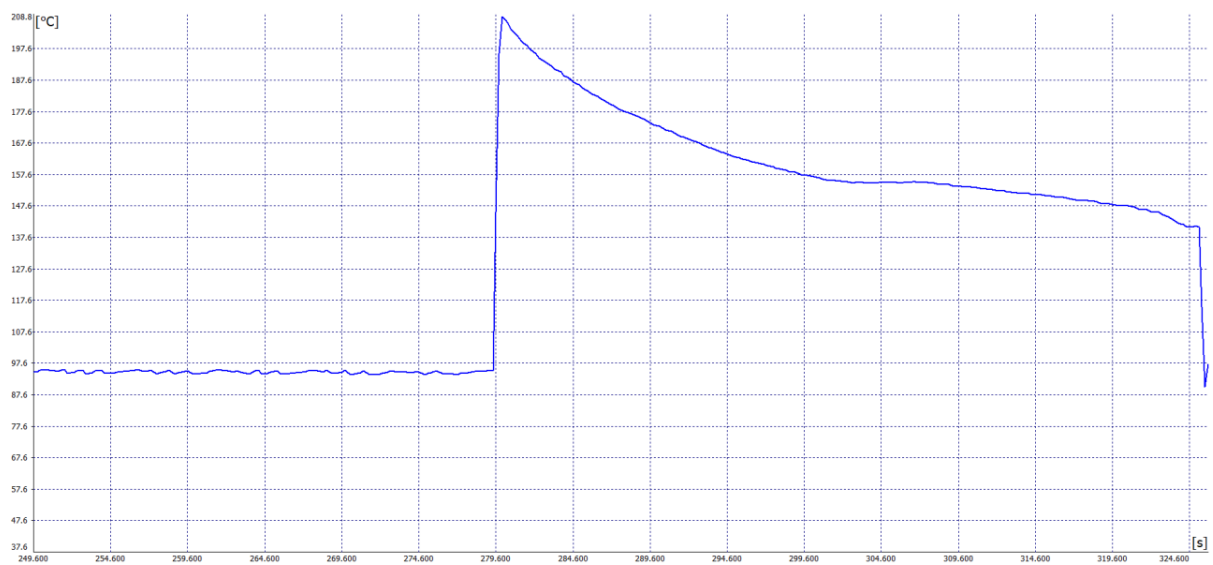


Figure 29 - Specific measurement of v25.

Figure : v30.
Model: Half.

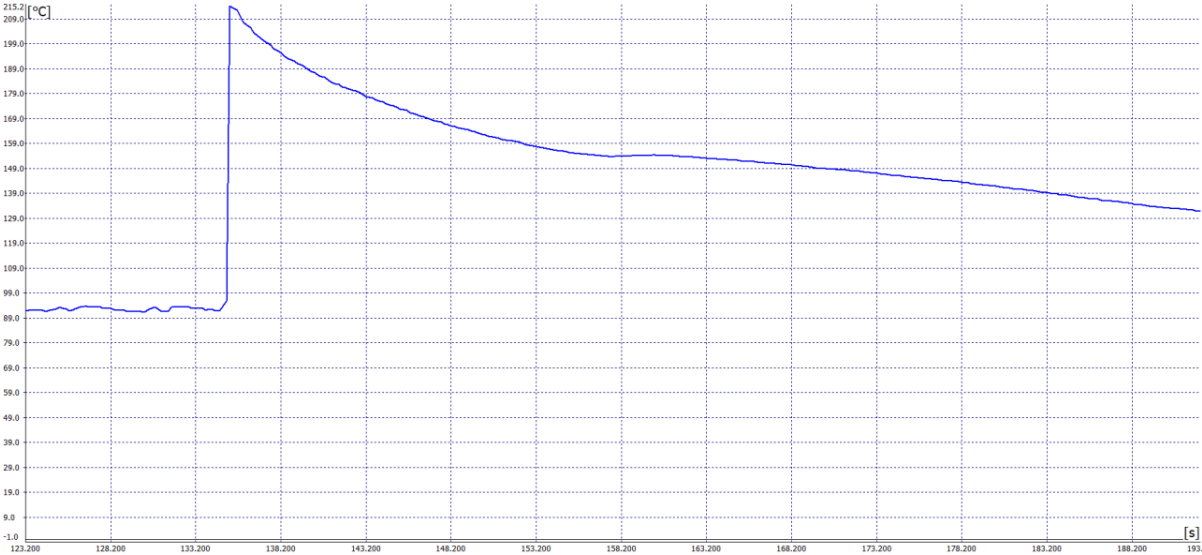
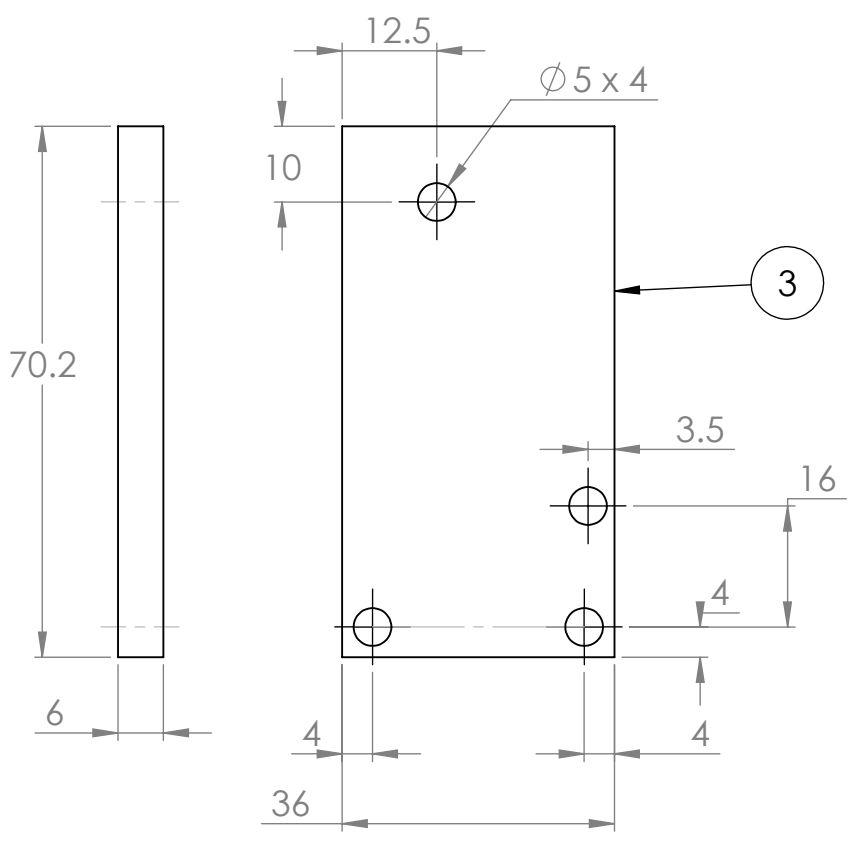
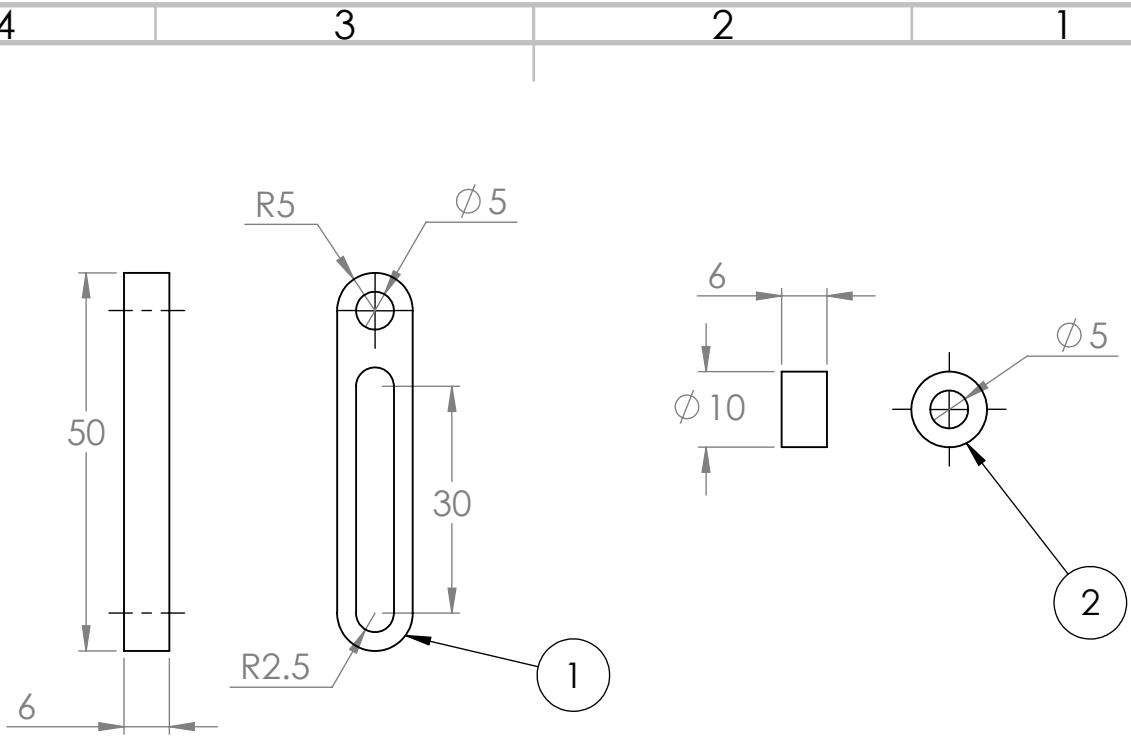


Figure 30 - Specific measurement of v30.

C Mechanical Drawings



UNLESS OTHERWISE SPECIFIED:
DIMENSIONS ARE IN MILLIMETERS

FINISH:

DEBURR AND
BREAK SHARP
EDGES

DO NOT SCALE DRAWING

REVISION

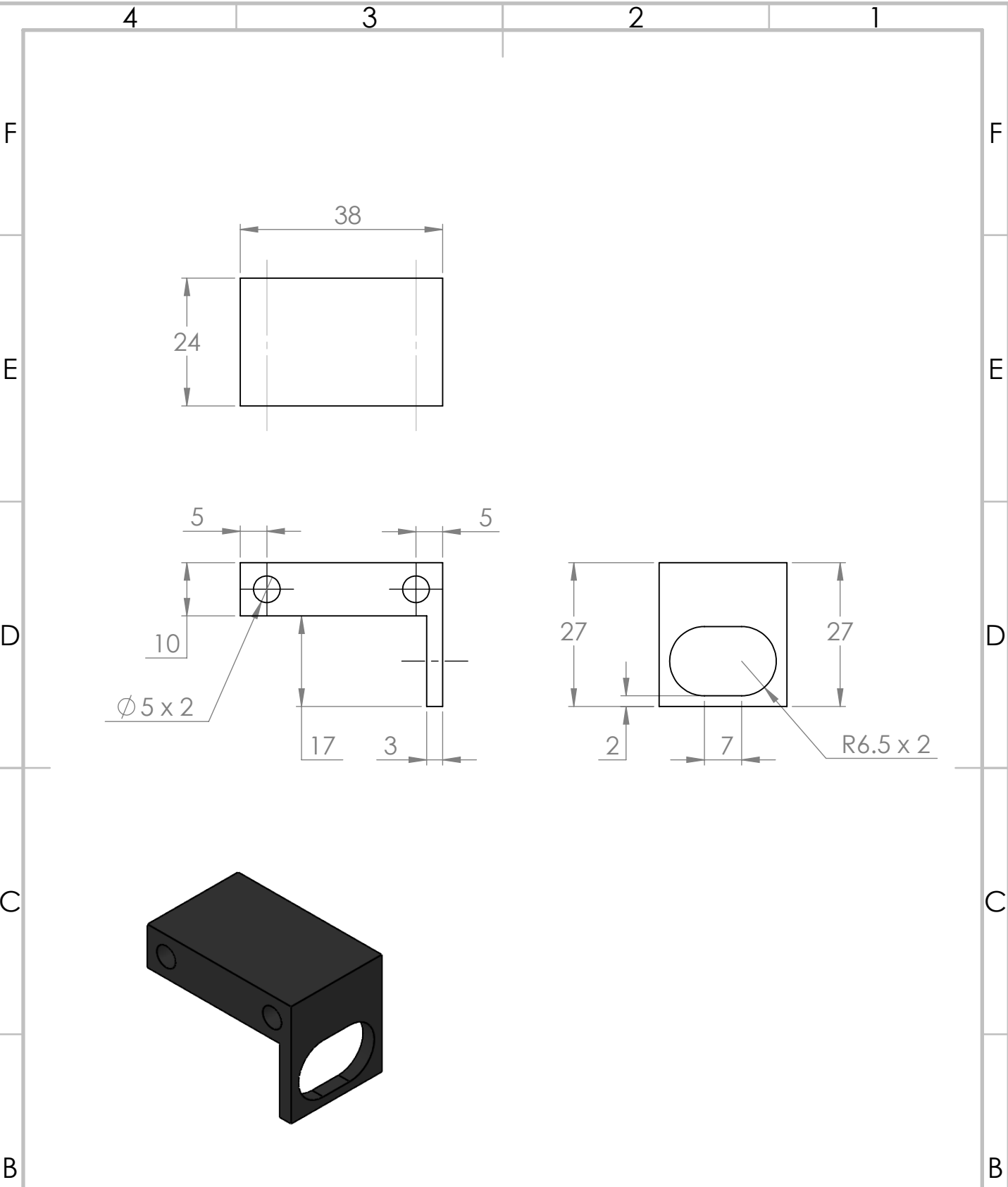
	NAME	SIGNATURE	DATE
DRAWN	Benjamin Andresen		28.05.22
1	Arms		
2	Disc		
3	Base		

TITLE:
Sensor Jig Parts

	MATERIAL:	
	MDF	
	WEIGHT:	

DWG NO.
1

A4
SCALE:1:1
SHEET 1 OF 1



UNLESS OTHERWISE SPECIFIED:
DIMENSIONS ARE IN MILLIMETERS

FINISH:

DEBURR AND
BREAK SHARP
EDGES

DO NOT SCALE DRAWING

REVISION

	NAME	SIGNATURE	DATE
DRAWN	Benjamin Andresen		30.05.22
CHK'D			
APPV'D			
MFG			

TITLE:
Angle-mount

Q.A			

MATERIAL:
PA6-CF

DWG NO.
3

A4

WEIGHT:

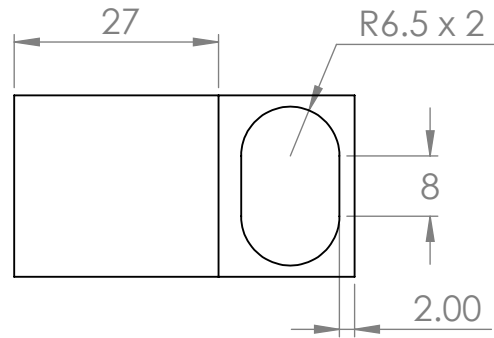
SCALE:1:1

SHEET 1 OF 1

4 3 2 1

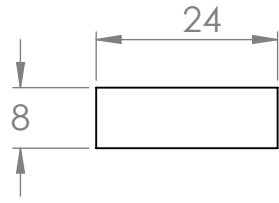
F

F



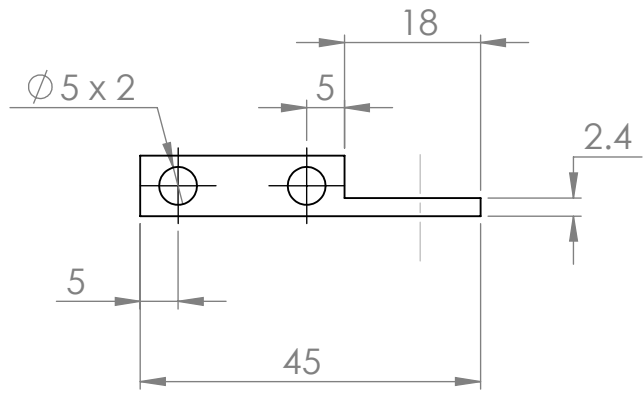
E

E



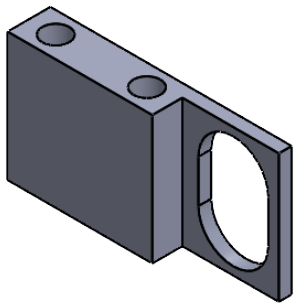
D

D



C

C



B

B

UNLESS OTHERWISE SPECIFIED:
DIMENSIONS ARE IN MILLIMETERS

FINISH:

DEBURR AND
BREAK SHARP
EDGES

DO NOT SCALE DRAWING

REVISION

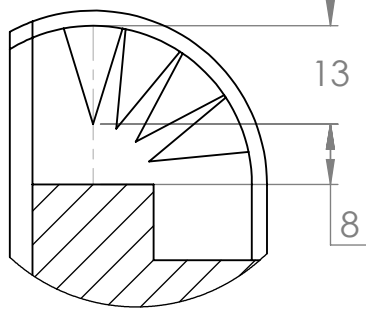
	NAME	SIGNATURE	DATE
DRAWN	Benjamin Andresen		30.05.22
CHK'D			
APPV'D			
MFG			
Q.A			

TITLE:	<h1>Flat-mount</h1>	
DWG NO.	<h1>4</h1>	A4
MATERIAL:	PA6-CF	
WEIGHT:	SCALE:1:1	SHEET 1 OF 1

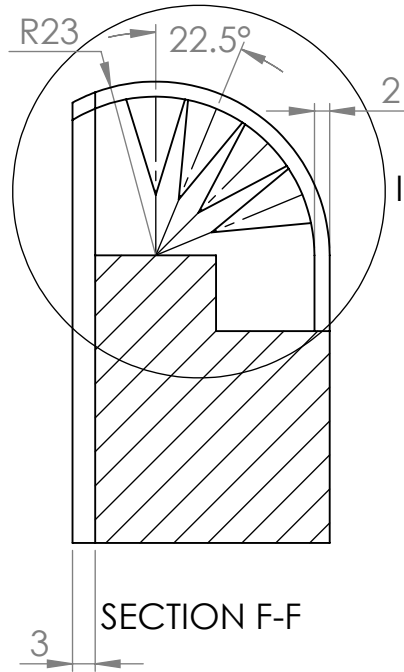
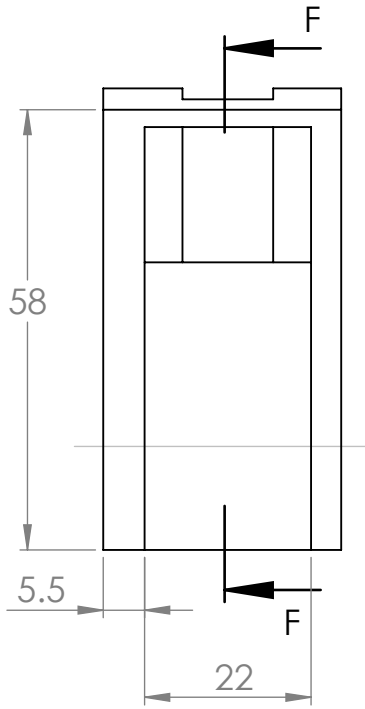
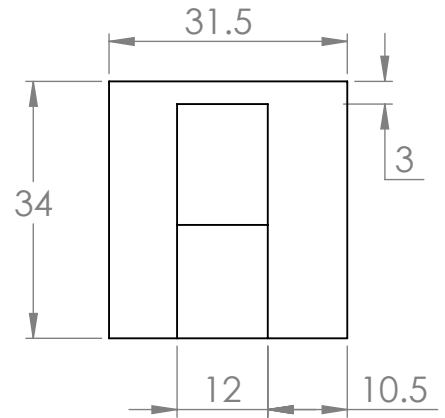
A

A

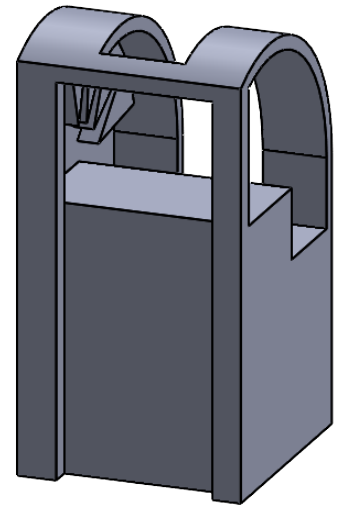
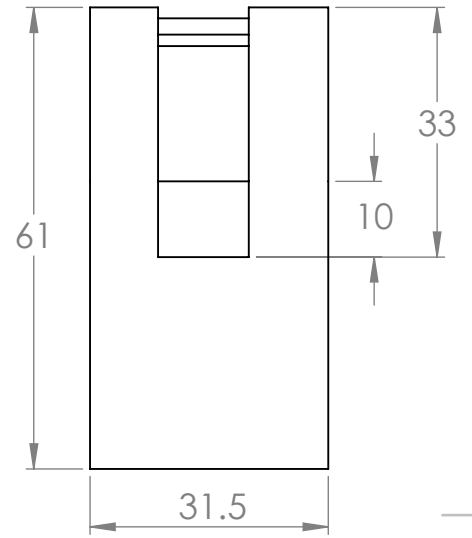
4 3 2 1



DETAIL I



SECTION F-F



UNLESS OTHERWISE SPECIFIED:
DIMENSIONS ARE IN MILLIMETERS

FINISH:

DEBURR AND
BREAK SHARP
EDGES

DO NOT SCALE DRAWING

REVISION

	NAME	SIGNATURE	DATE
DRAWN	Benjamin Andresen		
CHK'D			
APPV'D			
MFG			
Q.A			

TITLE:

Angle Test Jig

MATERIAL:

PA6-CF

DWG NO.

5

A4

WEIGHT:

SCALE:1:1

SHEET 1 OF 1

4 3 2 1

F

F

E

E

D

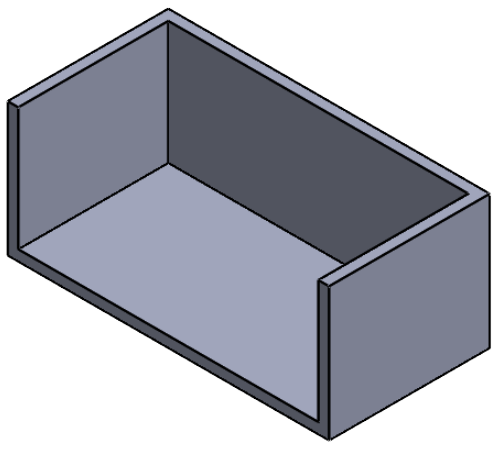
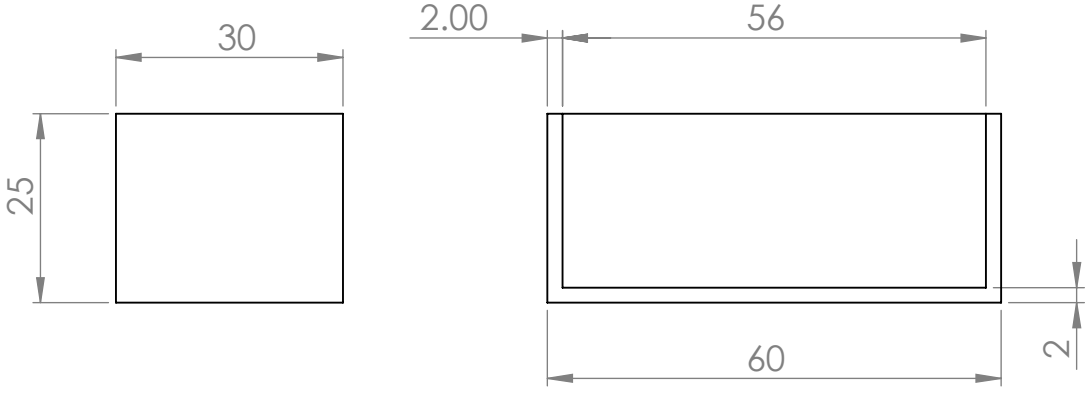
D

C

C

B

B



A

A

UNLESS OTHERWISE SPECIFIED:
DIMENSIONS ARE IN MILLIMETERS
SURFACE FINISH:
TOLERANCES:
LINEAR:
ANGULAR:

FINISH:

DEBURR AND
BREAK SHARP
EDGES

DO NOT SCALE DRAWING

REVISION

	NAME	SIGNATURE	DATE
DRAWN	Benjamin Andresen		
CHK'D			
APPV'D			
MFG			
Q.A			

TITLE:	Melt Test Specimen		
DWG NO.	2	A4	
SCALE:	1:1	SHEET 1 OF 1	

MATERIAL:
PA6-CF

WEIGHT:

4 3 2 1

D Additional Results

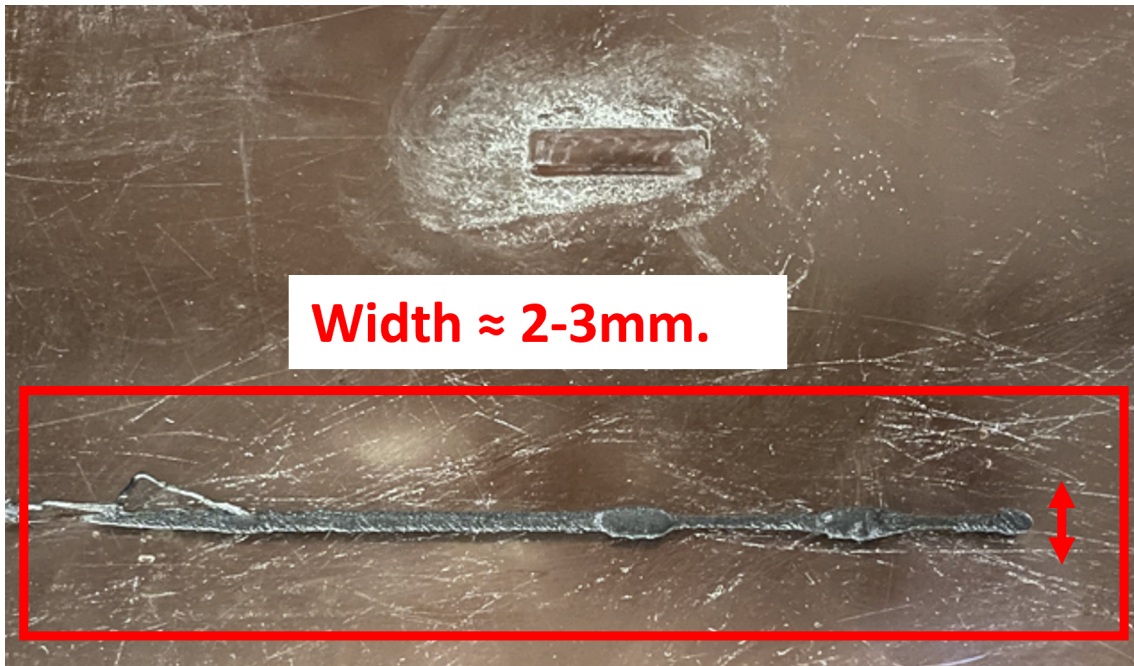


Figure D.1: Test line.



Figure D.2: OneFourth model specimens.



Figure D.3: Half model specimens.



Figure D.4: In-process specimens.

E Python Code

```
#Observation Angle Test  
import pandas as pd  
import matplotlib.pyplot as plt  
import numpy as np
```

```

from numpy import linspace
from numpy import arange

Angle_test_2 = pd.read_csv("C:\\Users\\bbgan\\OneDrive - NTNU\\Desktop\\TROLLlab\\
Master\\Temperatursensorer\\SensorData\\
Test\\Emissitivity_angle_tests\\
Emissitivity_angle_test_2.txt", sep="\\t"
, engine="python", decimal=",")

Angle_test_data=Angle_test_2.to_numpy()

Angle_test_data

Angle_test_time = Angle_test_data[:,0]

Angle_test_ovn = Angle_test_data[:,1]

Angle_test_sensor = Angle_test_data[:,2]

Angle_test_T1 = Angle_test_data[:,3]

Angle_test_T2 = Angle_test_data[:,4]

Angle_test_sensor

Angle_test_sensor
Angle_test_time

fig, ax = plt.subplots(figsize=(20, 10))

y = [170, 170]
x = [-5, 150]

plt.plot(Angle_test_time, Angle_test_sensor, linestyle='-', linewidth=2, color='red
', label = 'CT-SF22')

plt.plot(Angle_test_time, Angle_test_T1, linestyle='-', linewidth=2, color='green',
label = 'Thermocouple 1')
plt.plot(Angle_test_time, Angle_test_T2, linestyle='-', linewidth=2, color='blue',
label = 'Thermocouple 2' )
plt.plot(Angle_test_time, Angle_test_ovn, '--', linewidth=0.5, color='black', label
= 'Oven')
plt.plot(x, y, linestyle='-', linewidth=0.5, color='black')

ax.tick_params(axis='both', which='major', labelsize=18)
ax.tick_params(axis='both', which='minor', labelsize=18)

plt.xticks(arange(150, step=4))
plt.yticks(arange(200, step=10))

ax.set_xlim([0, 140])
ax.set_ylim([25, 190])
ax.set_xlabel('Time', size=18)
ax.set_ylabel('Temperature [ $^{\circ}$ C]', size=18)
plt.xticks(rotation=45)
plt.grid(linestyle='-', linewidth =0.5)

ax.set_title('Angle Test,  $\epsilon=0.95$ ', size=20)
ax.legend(loc='lower right', fontsize = 18)

plt.show()

h70At90 = pd.read_csv("C:\\Users\\bbgan\\OneDrive - NTNU\\Desktop\\TROLLlab\\Master
\\Temperatursensorer\\SensorData\\Test\\
Emissitivity_angle_tests\\2_170C_90.txt",
sep="\\t", engine="python", decimal=",")

H70At90 = h70At90.to_numpy()
H70At90

```

```

h70At67 = pd.read_csv("C:\\Users\\bbgan\\OneDrive - NTNU\\Desktop\\TROLLlab\\Master
                    \\Temperatursensorer\\SensorData\\Test\\
                    Emissitivity_angle_tests\\2_170C_67.5.txt
                    ", sep="\\t", engine="python", decimal=",
                    ")

H70At67 = h70At67.to_numpy()

h70At45 = pd.read_csv("C:\\Users\\bbgan\\OneDrive - NTNU\\Desktop\\TROLLlab\\Master
                    \\Temperatursensorer\\SensorData\\Test\\
                    Emissitivity_angle_tests\\2_170C_45.txt",
                    sep="\\t", engine="python", decimal=",")

H70At45 = h70At45.to_numpy()

h70At22 = pd.read_csv("C:\\Users\\bbgan\\OneDrive - NTNU\\Desktop\\TROLLlab\\Master
                    \\Temperatursensorer\\SensorData\\Test\\
                    Emissitivity_angle_tests\\2_170C_22.5.txt
                    ", sep="\\t", engine="python", decimal=",
                    ")

H70At22 = h70At22.to_numpy()

H70At22

H70At90_time = H70At90[:,0]
H70At90_ovn = H70At90[:,1]
H70At90_sensor = H70At90[:,2]
H70At90_T1 = H70At90[:,3]
H70At90_T2 = H70At90[:,4]
H70At67_time = H70At67[:,0]
H70At67_ovn = H70At67[:,1]
H70At67_sensor = H70At67[:,2]
H70At67_T1 = H70At67[:,3]
H70At67_T2 = H70At67[:,4]
H70At45_time = H70At45[:,0]
H70At45_ovn = H70At45[:,1]
H70At45_sensor = H70At45[:,2]
H70At45_T1 = H70At45[:,3]
H70At45_T2 = H70At45[:,4]
H70At22_time = H70At22[:,0]
H70At22_ovn = H70At22[:,1]
H70At22_sensor = H70At22[:,2]
H70At22_T1 = H70At22[:,3]
H70At22_T2 = H70At22[:,4]

fig, axs = plt.subplots(2, 2, figsize=(20,10))

y = [170, 170]
x = [-5, 150]

##Plotting
#Angle: 90

```

```

axs[0, 0].plot(H70At90_time, H70At90_sensor, linestyle='-', linewidth=2, color='red
              ', label='CT-SF22')
axs[0, 0].plot(H70At90_time, H70At90_T1, linestyle='-', linewidth=2, color='green',
              label='Thermocouple 1')
axs[0, 0].plot(H70At90_time, H70At90_T2, linestyle='-', linewidth=2, color='blue',
              label='Thermocouple 2')
axs[0, 0].plot(H70At90_time, H70At90_ovn, linestyle='--', linewidth=0.5, color='
              black')
axs[0, 0].plot(x, y, linestyle='-', linewidth=0.5, color='black')

axs[0, 0].set_yticks(arange(195, step=5))
axs[0, 0].set_ylim([160, 190])
axs[0, 0].set_ylabel("Temperature [^\circC]", size = 18)
axs[0, 0].set_title('Cycle 1: 0\N{DEGREE SIGN} Reading', size = 20)

#Angle: 45

axs[1, 0].plot(H70At45_time, H70At45_sensor, linestyle='-', linewidth=2, color='red
              ')
axs[1, 0].plot(H70At45_time, H70At45_T1, linestyle='-', linewidth=2, color='green')
axs[1, 0].plot(H70At45_time, H70At45_T2, linestyle='-', linewidth=2, color='blue')
axs[1, 0].plot(H70At45_time, H70At45_ovn, linestyle='--', linewidth=0.5, color='
              black')
axs[1, 0].plot(x, y, linestyle='-', linewidth=0.5, color='black')

axs[1, 0].set_yticks(arange(195, step=5))
axs[1, 0].set_ylim([160, 190])
axs[1, 0].set_xlabel("Time [hh:mm]", size=18)
axs[1, 0].set_ylabel("Temperature [^\circC]", size = 18)
axs[1, 0].set_title('Cycle 3: 45\N{DEGREE SIGN} Reading', size = 20)

#Angle: 67.5

axs[0, 1].plot(H70At67_time, H70At67_sensor, linestyle='-', linewidth=2, color='red
              ')
axs[0, 1].plot(H70At67_time, H70At67_T1, linestyle='-', linewidth=2, color='green')
axs[0, 1].plot(H70At67_time, H70At67_T2, linestyle='-', linewidth=2, color='blue')
axs[0, 1].plot(H70At67_time, H70At67_ovn, linestyle='--', linewidth=0.5, color='
              black')
axs[0, 1].plot(x, y, linestyle='-', linewidth=0.5, color='black')

axs[0, 1].set_yticks(arange(195, step=5))
axs[0, 1].set_ylim([160, 190])
axs[0, 1].set_title('Cycle 2: 22.5\N{DEGREE SIGN} Reading', size = 20)

#Angle:22.5

axs[1, 1].plot(H70At22_time, H70At22_sensor, linestyle='-', linewidth=2, color='red
              ')
axs[1, 1].plot(H70At22_time, H70At22_T1, linestyle='-', linewidth=2, color='green')
axs[1, 1].plot(H70At22_time, H70At22_T2, linestyle='-', linewidth=2, color='blue')
axs[1, 1].plot(H70At22_time, H70At22_ovn, linestyle='--', linewidth=0.5, color='
              black', label='Oven')
axs[1, 1].plot(x, y, linestyle='-', linewidth=0.5, color='black')
axs[1, 1].set_xticks(arange(36, step=2))
axs[1, 1].set_yticks(arange(195, step=5))

axs[1, 1].set_xlabel("Time [hh:mm]", size=18)
axs[1, 1].set_title('Cycle 4: 67.5\N{DEGREE SIGN} Reading', size = 20)

##x-tick range

#Angle: 90
axs[0, 0].set_xlim([0, 22])
axs[0, 0].set_xticks(arange(25, step=2))
#Angle: 45
axs[1, 0].set_xticks(arange(34, step=2))
axs[1, 0].set_xlim([2, 32])
#Angle: 67.5
axs[0, 1].set_xticks(arange(34, step=2))
axs[0, 1].set_xlim([2, 32])

```



```

#Angle: 22.5
axs[1, 1].set_xlim([2, 34])
axs[1, 1].set_ylim([160, 190])

##Grid style

axs[0, 0].grid(linestyle='-', linewidth =0.5) #Setting grids
axs[1, 0].grid(linestyle='-', linewidth =0.5)
axs[0, 1].grid(linestyle='-', linewidth =0.5)
axs[1, 1].grid(linestyle='-', linewidth =0.5)

##Rotation of x-tick

axs[0, 0].tick_params(axis='x', labelrotation=45, size=18)
axs[1, 0].tick_params(axis='x', labelrotation=45)
axs[0, 1].tick_params(axis='x', labelrotation=45)
axs[1, 1].tick_params(axis='x', labelrotation=45)

lines_labels = [axs.get_legend_handles_labels() for axs in fig.axes]
lines, labels = [sum(lol, []) for lol in zip(*lines_labels)]

fig.legend(lines, labels)

plt.rcParams['font.size'] = 18 #Axis fontsize

fig.tight_layout()

plt.show()

```

```

#Melt Test

import pandas as pd
import matplotlib.pyplot as plt
import numpy as np
from numpy import linspace
from numpy import arange

Melt_test_rampup = pd.read_csv("C:\\Users\\bbgan\\OneDrive - NTNU\\Desktop\\
                                TROLLlab\\Master\\Temperatursensorer\\
                                SensorData\\Test\\
                                Melting_test_anti_reflection\\Ramp up
                                trolllab.txt", sep="\t", engine="python"
                                , decimal=",")
Rampup_melt_test=Melt_test_rampup.to_numpy()

Melt_test_rampdown = pd.read_csv("C:\\Users\\bbgan\\OneDrive - NTNU\\Desktop\\
                                TROLLlab\\Master\\Temperatursensorer\\
                                SensorData\\Test\\
                                Melting_test_anti_reflection\\Ramp down
                                trolllab.txt", sep="\t", engine="python"
                                , decimal=",")
Rampdown_melt_test=Melt_test_rampdown.to_numpy()

Melt_komp_rampup = pd.read_csv("C:\\Users\\bbgan\\OneDrive - NTNU\\Desktop\\
                                TROLLlab\\Master\\Temperatursensorer\\
                                SensorData\\Test\\
                                Melting_test_anti_reflection\\Ramp up
                                komposit.txt", sep="\t", engine="python"
                                , decimal=",")
Rampup_komp_test=Melt_komp_rampup.to_numpy()

Rampup_melt_test

Rampup_test_time = Rampup_melt_test[:,0]

Rampup_test_sensor = Rampup_melt_test[:,1]

Rampup_test_T1 = Rampup_melt_test[:,2]

```

```

Rampup_test_T2 = Rampup_melt_test[:,3]

Rampdown_test_time = Rampdown_melt_test[:,0]

Rampdown_test_sensor = Rampdown_melt_test[:,1]

Rampdown_test_T1 = Rampdown_melt_test[:,2]

Rampdown_test_T2 = Rampdown_melt_test[:,3]

Rampup_komp_time = Rampup_komp_test[:,0]

Rampup_komp_sensor = Rampup_komp_test[:,1]

Rampup_komp_T1 = Rampup_komp_test[:,2]

Rampup_komp_T2 = Rampup_komp_test[:,3]

fig, ax = plt.subplots(figsize=(20, 10))

plt.plot(Rampup_test_time, Rampup_test_sensor, linestyle='-', linewidth=2, color='
red', label = 'CT-SF22')
plt.plot(Rampup_test_time, Rampup_test_T1, linestyle='-', linewidth=2, color='green
', label = 'Thermocouple 1')
plt.plot(Rampup_test_time, Rampup_test_T2, linestyle='-', linewidth=2, color='blue'
, label = 'Thermocouple 2' )

ax.tick_params(axis='both', which='major', labelsize=18)
ax.tick_params(axis='both', which='minor', labelsize=18)

plt.xticks(arange(280, step=15))
plt.yticks(arange(270, step=10))

ax.set_xlim([0, 280])
ax.set_ylim([50, 260])
ax.set_xlabel('Time [seconds]',size=18)
ax.set_ylabel('Temperature [ $^{\circ}$ C]',size=18)
plt.xticks(rotation=45)
plt.grid(linestyle='-', linewidth =0.5)
ax.set_title('Sensor Emissivity Factor,  $\epsilon=0.95$ ', size=20)
ax.legend(loc='lower right', fontsize = 18)

plt.show()

fig, ax = plt.subplots(figsize=(20, 10))

plt.plot(Rampdown_test_time, Rampdown_test_sensor, linestyle='-', linewidth=2,
color='red', label = 'CT-SF22')
plt.plot(Rampdown_test_time, Rampdown_test_T1, linestyle='-', linewidth=2, color='
green', label = 'Thermocouple 1')
plt.plot(Rampdown_test_time, Rampdown_test_T2, linestyle='-', linewidth=2, color='
blue', label = 'Thermocouple 2' )

ax.tick_params(axis='both', which='major', labelsize=18)
ax.tick_params(axis='both', which='minor', labelsize=18)

plt.xticks(arange(130, step=15))
plt.yticks(arange(220, step=5))

ax.set_xlim([0, 125])
ax.set_ylim([125, 210])
ax.set_xlabel('Time [seconds]',size=18)
ax.set_ylabel('Temperature [ $^{\circ}$ C]',size=18)
plt.xticks(rotation=45)
plt.grid(linestyle='-', linewidth =0.5)
ax.set_title('Sensor Emissivity Factor,  $\epsilon=0.856$ ', size=20)
ax.legend(loc='lower right', fontsize = 18)

plt.show()

```

```

#In-process measurements

import pandas as pd
import matplotlib.pyplot as plt
import numpy as np
from numpy import arange

HalvProveV30 = pd.read_csv("C:\\Users\\bbgan\\OneDrive - NTNU\\Desktop\\TROLLlab\\
Master\\Temperatursensorer\\SensorData\\
Test\\Anti_hotend_reflection\\
Halvepr ver\\closed_chamber_v30_0.
5_dogBone_Emiss0.95_2.dat", sep="\t",
skiprows=8, encoding = "ISO-8859-1",
engine="python", decimal=",")

ProveV30 = HalvProveV30.to_numpy()

LiveTemp = pd.read_csv("C:\\Users\\bbgan\\OneDrive - NTNU\\Desktop\\TROLLlab\\
Master\\Temperatursensorer\\SensorData\\
Test\\Dog_bones_short_distance\\
CompactConnect\\
DogBone_v30_2ndTest_reversed_infill_middle_layer
.dat", sep="\t", skiprows=8, encoding =
"ISO-8859-1", engine="python", decimal=
",")

TempLive = LiveTemp.to_numpy()

TempLive

FullTime = ProveV30[:,0]

Time = FullTime[650:975]

#for i in range(len(Time)):
#    Time[i] = i + 0.002

FullReading = ProveV30[:,1]
Reading = FullReading[650:975]

FullLiveTime = TempLive[:,0]
FullLiveTemp = TempLive[:,1]

LiveTimes = FullLiveTime[0:7467]
LiveTemps = FullLiveTemp[0:7467]

fig, ax = plt.subplots(figsize=(20, 10))

plt.plot(LiveTimes, LiveTemps, '-', linewidth=2, label = 'CT-SF22 - Live
measurement')

ax.tick_params(axis='both', which='major', labelsize=18)

plt.xticks(arange(7500, step=400))
plt.yticks(arange(245, step=10))
ax.set_xlim([30, 7447])
ax.set_ylim([100, 240])
plt.xticks(rotation=45)

ax.set_xlabel('Time [hhh:mm:ss:ms]', size=18)
ax.set_ylabel('Layer Temperature [°C]', size=18)
plt.grid(linestyle='-', linewidth = 1)
plt.legend(loc=1, prop={'size': 18})
ax.set_title('Full Live Measurement, v30, ε=0.95', size=20)

plt.show()

LiveTimes1 = FullLiveTime[3550:3820]
LiveTemps1 = FullLiveTemp[3550:3820]

```

```

fig, ax = plt.subplots(figsize=(20, 10))

plt.plot(LiveTimes1 ,LiveTemps1, '-', linewidth=2, label = 'CT-SF22 - Live
                measurement')

ax.tick_params(axis='both', which='major', labelsize=18)

plt.xticks(arange(7500, step=20))
plt.yticks(arange(245, step=5))
ax.set_xlim([0, 270])
ax.set_ylim([140, 240])
plt.xticks(rotation=45)

ax.set_xlabel('Time [hhh:mm:ss:ms]',size=18)
ax.set_ylabel('Layer Temperature [^\circC]',size=18)
plt.grid(linestyle='-', linewidth =1)
plt.legend(loc=1, prop={'size':18})
ax.set_title('Section 1 of Live Measurement, v30, $\epsilon=0.95$', size=20)

plt.show()

LiveTimes2 = FullLiveTime[3663:3698]
LiveTemps2 = FullLiveTemp[3663:3698]
fig, ax = plt.subplots(figsize=(20, 10))

plt.plot(LiveTimes2 ,LiveTemps2, '-', linewidth=2, label = 'CT-SF22 - Live
                measurement')

ax.tick_params(axis='both', which='major', labelsize=18)

plt.xticks(arange(7500, step=3))
plt.yticks(arange(245, step=5))
ax.set_xlim([0, 34])
ax.set_ylim([150, 225])
plt.xticks(rotation=45)

ax.set_xlabel('Time [hhh:mm:ss:ms]',size=18)
ax.set_ylabel('Layer Temperature [^\circC]',size=18)
plt.grid(linestyle='-', linewidth =1)
plt.legend(loc=1, prop={'size':18})
ax.set_title('Section 2 of Live Measurement, v30, $\epsilon=0.95$', size=20)

plt.show()

LiveTimes3 = FullLiveTime[0:150]
LiveTemps3 = FullLiveTemp[0:150]

fig, ax = plt.subplots(figsize=(20, 10))

plt.plot(LiveTimes3 ,LiveTemps3, '-', linewidth=2, label = 'CT-SF22 - Live
                measurement')

ax.tick_params(axis='both', which='major', labelsize=18)

plt.xticks(arange(200, step=5))
plt.yticks(arange(270, step=10))
ax.set_xlim([0, 60])
ax.set_ylim([100, 260])
plt.xticks(rotation=45)

ax.set_xlabel('Time [hhh:mm:ss:ms]',size=18)
ax.set_ylabel('Layer Temperature [^\circC]',size=18)
plt.grid(linestyle='-', linewidth =1)

```

```
plt.legend(loc=1, prop={'size':18})
ax.set_title('Test Line of Live Measurement, v30,  $\epsilon=0.95$ ', size=20)

plt.show()
```

```
#Specific measurement

import pandas as pd
import matplotlib.pyplot as plt
import numpy as np
from numpy import arange

HalvProveV30 = pd.read_csv("C:\\Users\\bbgan\\OneDrive - NTNU\\Desktop\\TROLLlab\\
    Master\\Temperatursensorer\\SensorData\\
    Test\\Anti_hotend_reflection\\
    Halvepr ver\\closed_chamber_v30_0.
    5_dogBone_Emiss0.95_2.dat", sep="\\t",
    skiprows=8, encoding = "ISO-8859-1",
    engine="python", decimal=",")

ProveV30 = HalvProveV30.to_numpy()

FullTime = ProveV30[:,0]
FullReading = ProveV30[:,1]

LiveTimes = FullTime[500:1384]
LiveTemps = FullReading[500:1384]

fig, ax = plt.subplots(figsize=(20, 10))

plt.plot(LiveTimes, LiveTemps, '-', linewidth=2, label = 'CT-SF22 - Specific
    Reading')

ax.tick_params(axis='both', which='major', labelsize=18)

plt.xticks(arange(890, step=37))
plt.yticks(arange(245, step=5))
ax.set_xlim([100, 784])
ax.set_ylim([90, 225])
plt.xticks(rotation=45)

ax.set_xlabel('Time [hhh:mm:ss:ms]', size=18)
ax.set_ylabel('Layer Temperature [ $^{\circ}$ C]', size=18)
plt.grid(linestyle='-', linewidth = 1)
plt.legend(loc=1, prop={'size':18})
ax.set_title('Specific Measurement, v30,  $\epsilon=0.95$ ', size=20)

plt.show()
```

```
#Specific layer Temperature vs. Printer Speed

import pandas as pd
import matplotlib.pyplot as plt
import numpy as np
from numpy import arange

dataTemp = pd.read_csv("C:\\Users\\bbgan\\OneDrive - NTNU\\Desktop\\TROLLlab\\
    Prosjektoppgave\\CIRP\\Test Data\\Printer
    Speed vs. Layer Temp.txt", sep="\\t",
    engine="python", decimal=",")

FullTempData=dataTemp.to_numpy()

SensorOneFourth = pd.read_csv("C:\\Users\\bbgan\\OneDrive - NTNU\\Desktop\\TROLLlab
    \\Master\\Temperatursensorer\\SensorData
    \\Test\\Anti_hotend_reflection\\
    Fjerdedelspr ver\\Excel\\
    Printerspeed_vs_layerTemp.txt", sep="\\t",
    engine="python", decimal=",")
```

```

SensorOneFourthData=SensorOneFourth.to_numpy()

SensorHalf = pd.read_csv("C:\\Users\\bbgan\\OneDrive - NTNU\\Desktop\\TROLLlab\\
                        Master\\Temperatursensorer\\SensorData\\
                        Test\\Anti_hotend_reflection\\
                        Halveprøver\\Printerspeed_vs_LayerTemp_0
                        .5.txt", sep="\\t", engine="python",
                        decimal=",")

SensorOneHalf=SensorHalf.to_numpy()

SensorOneHalfdatax = SensorOneHalf[:,0]
SensorOneHalfdatay = SensorOneHalf[:,1]

FullTempDatax = FullTempData[:,0]
FullTempDatay = FullTempData[:,1]

TempDatax = FullTempDatax[0:15]
TempDatay = FullTempDatay[0:15]

SensorOneFourthDatax = SensorOneFourthData[:,0]
SensorOneFourthDatay = SensorOneFourthData[:,1]

TempDatax

fig, ax = plt.subplots(figsize=(20, 10))

plt.plot(SensorOneFourthDatax ,SensorOneFourthDatay, 'o-', linewidth=2, label = 'CT
-SF22 - OneFourth model')
plt.plot(SensorOneHalfdatax ,SensorOneHalfdatay, 'o-', linewidth=2, label = 'CT-
SF22 - Half model')

ax.tick_params(axis='both', which='major', labelsize=18)

plt.xticks(arange(36, step=1))
plt.yticks(arange(222, step=5))
ax.set_xlim([0, 33])
ax.set_ylim([150, 218])

ax.set_xlabel('Printer Speed [mm/s]',size=18)
ax.set_ylabel('Layer Temperature [°C]',size=18)
plt.grid(linestyle='-', linewidth =1)
plt.legend(loc=4, prop={'size':18})
ax.set_title('Specific Measurements,  $\epsilon=0.95$ ', size=20)

plt.show()

fig, ax = plt.subplots(figsize=(20, 10))

plt.plot(TempDatax ,TempDatay, 'o-', linewidth=2, label = 'FLIR method')
plt.plot(SensorOneFourthDatax ,SensorOneFourthDatay, 'o-', linewidth=2, label = 'CT
-SF22 method')
#plt.plot(SensorOneHalfdatax ,SensorOneHalfdatay, 'o-', linewidth=2, label = 'CT-
SF22 method 0,5')

ax.tick_params(axis='both', which='major', labelsize=18)

plt.xticks(arange(36, step=1))
plt.yticks(arange(222, step=5))
ax.set_xlim([0, 33])
ax.set_ylim([140, 218])

ax.set_xlabel('Printer Speed [mm/s]',size=18)
ax.set_ylabel('Layer Temperature [°C]',size=18)
plt.grid(linestyle='-', linewidth =1)
plt.legend(loc=4, prop={'size':18})
ax.set_title('Specific Measurements: Flir vs. CT-SF22,  $\epsilon=0.95$ ', size=20)

```

```
plt.show()
```

```
#In-process measurements vs. specific measurements

import pandas as pd
import matplotlib.pyplot as plt
import numpy as np
from numpy import linspace
from numpy import arange

comparison_measurements = pd.read_csv("C:\\Users\\bbgan\\OneDrive - NTNU\\Desktop\\
TROLLlab\\Master\\Temperatursensorer\\
SensorData\\Test\\
Dog_bones_short_distance\\Live vs.
specific.txt", sep="\t", engine="python"
, decimal=",")

All_measurements=comparison_measurements.to_numpy()

All_measurements

speed = All_measurements[:,0]

live_temp = All_measurements[:,1]

specific_half = All_measurements[:,2]

specific_onefourth = All_measurements[:,3]

fig, ax = plt.subplots(figsize=(20, 10))

plt.plot(speed, live_temp, '-o', linewidth=2, color='red', label = 'CT-SF22 - Live
middle layer temperature - full model')
plt.plot(speed, specific_half, '-o', linewidth=2, color='green', label = 'CT-SF22 -
Specific layer temperature - half model'
)
#plt.plot(speed, specific_onefourth, '-o', linewidth=2, color='blue', label = '
Specific - one fourth model' )

ax.tick_params(axis='both', which='major', labelsize=18)
ax.tick_params(axis='both', which='minor', labelsize=18)

plt.xticks(arange(35, step=1))
plt.yticks(arange(260, step=5))

ax.set_xlim([2, 32])
ax.set_ylim([150, 235])
ax.set_xlabel('Printing speed [mm/s]',size=18)
ax.set_ylabel('Temperature [ $^{\circ}$ C]',size=18)

plt.grid(linestyle='-', linewidth =0.5)
ax.set_title('Specific vs. Live Measurements,  $\epsilon=0.95$ ', size=20)

ax.legend(loc='lower right', fontsize = 18)

plt.show()
```

F Engineering Design and Materials, Specialization Project



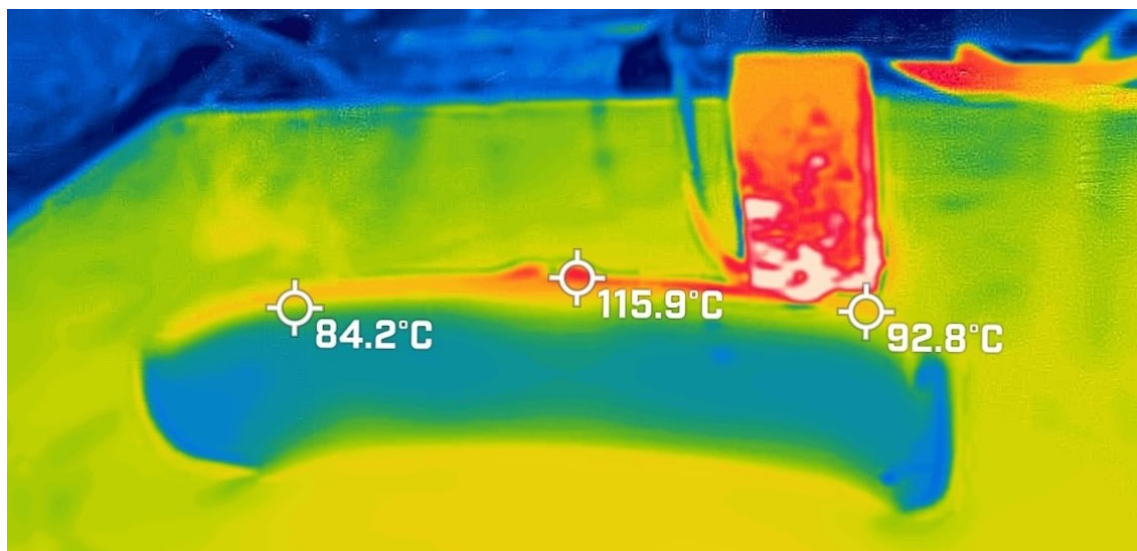
Kunnskap for en bedre verden

DEPARTMENT OF MECHANICAL
AND INDUSTRIAL ENGINEERING

TMM4560

ENGINEERING DESIGN AND MATERIALS,
SPECIALIZATION PROJECT

The effects of layer temperatures in Fused Filament Fabrication and introduction of Thermal Layer Design



Authors:

Benjamin Balder Grønneberg Andresen
Olav Urvold Bjørken

December, 2021

Abstract

Design for Additive Manufacturing is constantly developing and methods to fully utilize material properties while maintaining geometrical tolerances is of high interest. As more engineering grade polymers become available for Fused Filament Fabrication, methods needs to be developed to understand how the materials can be treated and used to manufacture products that utilize the material properties to the fullest.

Through material testing, thermal imaging of layer temperatures and analysis of geometric effects on a component, a relation is presented. The effect of layer temperature on Ultimate Tensile Strength (UTS), surface roughness and geometry is found for PA6-CF. Mapping the behaviour of PA6-CF gives valuable knowledge on knowing which layer temperature will give the higher strength with a satisfying geometry. The thermal distribution changes in layer temperature for a component show that a more massive cross section leads to layer temperatures being more evenly distributed. A simple modification proved to have great effect on controlling layer temperature, with implications of changing the performance.

Based on the results a conference paper is submitted, where we introduce *Thermal Layer Design* as a method to design components for optimal heat distribution of a cross-section. Combining both the material testing and use of Thermal Layer Design has proven to show great potential for implementation in Design for Additive Manufacturing. The project lays a solid foundation for further research in the field of Additive Manufacturing (AM).

Table of Contents

List of Figures	iii
List of Tables	iv
List of Abbreviations	v
1 Introduction	1
1.1 Current Status of AM by FFF	1
1.2 Constrictions and Limits	1
1.3 Project goal	1
2 Preliminary Work	3
2.1 Altering Layer Temperatures	3
2.2 Material Selection	4
2.3 Learning by Burning, then Repairing	4
3 Preparations and Method	5
3.1 Theory and Background	5
3.1.1 Layer Bonding and Testing	5
3.1.2 Thermal Layer Design	5
3.1.3 Materials and Equipment	6
3.2 Specimens	6
3.2.1 Test Specimen Geometry	6
3.2.2 Improving the Quality of Test Specimens	8
3.2.3 Producing Specimens	9
3.3 Gathering Data	10
3.3.1 Measuring Layer Temperature	10
3.3.2 Tensile Testing	10
3.4 Application of Thermal Layer Design on a Component	11
4 Results	13
4.1 Complete results	13
4.1.1 Thermal properties	13
4.1.2 Geometry	14
4.1.3 Ultimate Tensile Strength and machine measured elongation	15
4.1.4 Point of Rupture	16

4.1.5	Thermal Layer Design on Component.	18
4.2	Conference paper	18
4.2.1	Thermal Layer Design in Fused Filament Fabrication	18
5	Discussion	25
5.1	Method and Results	25
5.2	Significance of Findings and Continuation of Work	27
6	Conclusion	28
	References	29
	Appendix	32
A	Calibration, repairing and modification of hardware	32
B	Testing geometries and settings	33
C	Backrest component	34
D	Additional results	35

List of Figures

1	Diagram showing the two main approaches considered to alter layer temperature.	3
2	Iterations on specimen geometry based on ISO527 and ASTM E606/E606M standards with final specimen to the right.	7
3	Dimensions of modified ISO527 specimen.	7
4	Five samples of the same specimen with different printing parameters.	8
5	Comparison of surface quality between two specimen printed at 6 mm/s with different seam placements.	9
6	Mounting of a specimen in the test machine.	11
7	Components and sections printed.	12
8	Printer speed vs. Layer temperature.	13
9	Thermal measurements for layer temperature at four different printing speeds.	14
10	Printer speed vs. Layer temperature.	14
11	Average geometry measurements vs. Layer temperature.	14
12	Average surface roughness vs. Layer temperature.	15
13	Resulting specimens at different printing speeds.	15
14	UTS vs. layer temperature.	16
15	Elongation vs. layer temperature.	16
16	Selection of specimens (from top left): v4_01, v6_01, v8_01, v10_02, v12_01, v16_02, v20_02, v30_01, v50_01.	17

17	Selection of microscopic images of breaking points of specimens (from top left): v4_01, v6_01, v8_01, v10_02, v12_01, v16_02, v20_02, v30_01, v50_01.	17
18	Optimal breaking point, and two questionable breaking points (from left): v5_03, v5_01, v18_03.	18
19	Thermal measurements for layer temperature of the two component cross sections.	18
A.1	First vase mode calibration print.	32
A.2	Modification of mounting for water cooling of hot end.	32
A.3	Second vase mode calibration print.	33
B.1	Failed tensile test prints.	33
B.2	Geometric differences, printer speed 7 mm/s (left) and 25 mm/s (right).	34
C.1	Link to a video of the component failing.	34
D.1	Complete set of measurements from the specimens.	35
D.2	Tensile test data for specimens printed the velocity of 4 mm/s.	35
D.3	Tensile test data for specimens printed the velocity of 8 mm/s.	36
D.4	Slip marks after cancelled tensile test.	36

List of Tables

1	Testing printing settings for specimens 3.1-3.5	8
2	Fixed settings for test specimen production.	9
3	Printing speeds used and designation for specimens	10

Abbreviations

AM Additive Manufacturing.

ASTM American Society for Testing and Materials.

CAD Computer Aided Design.

CF Carbon Fiber.

DfAM Design for Additive Manufacturing.

FFF Fused Filament Fabrication.

ISO International Organization for Standardization.

ME Material Extrusion.

PA6 Polyamide 6.

PEEK Polyether Ether Ketone.

PEI Polyetherimide.

TLD Thermal Layer Design.

UTS Ultimate Tensile Strength.

1 Introduction

1.1 Current Status of AM by FFF

In the field of Additive Manufacturing (AM), there has been a transition from prototyping applications to manufacturing of actual end-use products [1, 2]. AM offers many advantages over conventional manufacturing in terms of possible complexity in the parts, CAD models being directly transferable to the machine via slicing software, and does not require any additional tooling. Where conventional manufacturing needs several machines, tools and operators to shape material into the desired form, AM is generally performed in a single step [2]. The short time from design to finished product makes it highly adaptable and suited for low-volume specialized production. These traits are attractive for specialized markets such as defence, aerospace, competitive sports, automobile and medical [3–6].

The field of Fused Filament Fabrication (FFF) is by far the most widespread in AM, since hardware is accessible both as high end production equipment and as basic machines for consumer use [1, 7]. Most forms of FFF heats up the plastic filament and builds the layers by Material Extrusion (ME) where the molten material is pushed through a round nozzle onto the build plate or previous layers. The size of the nozzle and the height of the path over the foundation below sets a range for possible layer thicknesses as extruded material should be squeezed onto the foundation to properly place it. Deposited material should be semi-melted and to keep ideal shape and size [7]. Molecular diffusion in the material during deposition depends on local temperatures and associated times [8]. For good bonding the residual energy in adjacent regions must be sufficient, or distinct boundaries between new and previously deposited material will occur [7]. Process parameters such as tool path, layer thickness, deposition velocity, infill rate, and environment temperature are factors that affects bonding [9, 10]. Although polymer materials mostly have been used for prototypes, mock-ups and tooling [1], the development of new engineering plastics and fiber reinforced polymers [11] makes it possible to produce load-bearing end-use products with FFF. Combined with possibilities to modify consumer level printers to use these materials [12] research on material properties becomes more available to the community as the entry barriers are lowered.

1.2 Constrictions and Limits

Although AM by FFF offers many advantages over conventional manufacturing, there are still limitations and challenges that must be considered. Whether the technology is utilized as a tool in the design process or to manufacture end-use parts, it is necessary to consider both opportunistic and restrictive Design for Additive Manufacturing (DfAM) aspects [13]. While AM offers possibilities for more complex geometries and fewer steps from design to produced part, there are other considerations. The need for support structure, anisotropic properties in the product and sometimes extensive post processing requires knowledge about materials and limitations of hardware [14]. There is great potential in the field of FFF, but some challenges still remain to fulfill the market potential, as described by Tofail et. Al ” *The challenge remains, however, transfer this ‘making’ into obtaining objects that are functional. A great deal of work is needed in addressing the challenges related to the two key enabling technologies namely ‘materials’ and ‘metrology’ to achieve this functionality in a predictive and reproductive ways.*” [15]. One of the main difficulties hampering the development of end-use production with FFF is the high cost of machines capable of using higher grade polymers and polymer composite materials that are being developed [12]. Currently, there is a lack of research on the thermal effects on high-performance polymers, as most mechanical properties and manufacturing parameters are tested for commodity polymers that are not suitable for load-bearing applications [8, 16–20].

1.3 Project goal

Like stated, the high cost of capable hardware and lack of knowledge on new engineering materials are a limiting factor for the full potential of FFF in AM of structural and load-bearing capacit-

ies. By utilizing a modified commercial printer, our goal is to study the effects of thermal layer temperature on engineering grade filaments. Learning how layer temperatures during printing of components affect the quality and performance of the material used will provide insight into the bonding process. By experimenting with thermal properties and bonding, and establishing a relation between strength and layer temperature, improvements of printing processes and results can be achieved. We will attempt to establish a clear trend between the layer temperature and bonding quality, looking at Ultimate Tensile Strength (UTS), surface roughness and geometrical accuracy. As we are looking for a trend, the focus will be on exploring several combinations of parameters for printing to perform material testing and see if the data can be applied on actual components.

2 Preliminary Work

Preliminary work describes some of the decisions that were made and hardware issues that had to be resolved before the work on printing and material testing could begin. This chapter includes decisions on how work towards controlling layer temperature, choosing a material to work with and repairing the printer used for the project.

2.1 Altering Layer Temperatures

To establish a relation between layer temperature and UTS a structured plan of the process was needed. With a large freedom in terms of parameters, hardware, materials, and settings to decide between, several decisions were made to narrow the options down to a workable solution space. As the focus was set to regulating temperatures during a print, two main approaches were evaluated in terms of available equipment, knowledge on materials, funds, and technical skill set. A decision diagram is shown in Figure 1. On one side modifying hardware allows for installation of more sensors to monitor the temperature and elements to heat the layers, even though it takes more time. There are examples where infrared preheating has been applied on larger printing areas [21]. The advantages of this option were more control over temperature, possibility of live monitoring during printing and more accurate measurements. Increasing the complexity of the system could give additional problems with firmware, mounting and insulation of components. Using the hardware available, and experiment with different slicer settings to change temperatures between layers had the advantage of beginning experimenting straight away. Avoiding spending a lot of time and money on hardware to make physical modifications was considered to be beneficial with the given amount of time for the project and the already high complexity of the printer. Challenges with this option were the lack of knowledge on material properties and uncertainties regarding how extensive alterations of layer temperature it was possible to produce.



Figure 1: Diagram showing the two main approaches considered to alter layer temperature.

Longer projects should include both approaches to increase experience and knowledge. Due to the limited time and already high complexity of the modified printer used in the project, the decision was to modify the settings. By experimenting with print settings and combinations of these, work could begin on studying the effects and changes in layer temperature at an early stage. As there was little knowledge on the effects of printing speed and layer temperature or material properties, this was regarded more of an opportunity to learn and close knowledge gaps on the subject. Exploration on custom G-code tools [22], variations of extruder and chamber temperatures and the implementation of pauses between layers was looked into, but adjustments of printing speed proved to be the fastest and most reliable variable.

2.2 Material Selection

Engineering polymers are becoming more available and there are several alternatives of polymers which can be used in FFF suitable for end-use components. Polymers considered for material testing were PEEK-CF30, Z-PEI 9085, and PolyMide PA6-CF. All of these had material properties suitable for use in the industry. PEEK-CF30 have great material properties in terms of the weight and stiffness ratio, and is frequently used in prototyping and critical areas in the industry such as automotive, aerospace, electronics and drilling industries [23]. Fabrication of PEEK-CF30 requires extreme temperature conditions, with the main challenge being the chamber temperature that is recommended to be between 230°C - 250°C. The modified CR10 printer used in this project has a maximum chamber temperature of 135.6°C and does not meet the recommended settings for PEEK-CF30. While the filament could still be experimented with, it did not suit the goal of the project to a satisfying degree. Z-PEI 9085 has a strength to weight ratio comparable to aluminium 6061, it has great thermal properties and is suitable for industries such as aviation, space, marine, railroad and automotive [24]. Z-PEI 9085 has a tensile strength of 54MPa in the Z-direction. PolyMide PA6-CF delivers engineering properties such as improved stiffness, strength, heat resistant, and warp-free technology due to its carbon fiber reinforcement [25]. It is also a semi-crystalline material, which affects how it is structured for different temperatures and cooling rates [26], therefore the manufacturer recommends annealing of printed parts. PolyMide PA6-CF had a tensile strength of 67.7MPa in the Z-direction and used printer settings suitable for the modified printer. As the printer also uses a hardened steel nozzle, suited for fiber reinforced polymer filaments PA6-CF was chosen as the main material to work with.

2.3 Learning by Burning, then Repairing

As the project is based on an open-source high-performance 3D printer developed by a former master student, challenges with the hardware and software naturally occur. Some initial work with firmware updates, setting up IP-address and network connection as well as maintenance of cooling system had to be done before the printer was ready for use. After some trials with printing of PA6-CF, a vase mode component with one single wall was made (Figure A.1) to see what quality the printer was capable of. Soon after, some major challenges occurred after an unsuccessful calibration of end stops, as the end stop at the Z-axis had loosened which resulted in the nozzle driving into the bed. This broke the heat break and put a stop to printing for a while. During disassembly to replace the heat break, it was discovered that the isolation on both heat sensors and the heating element had degraded and exposed the wires. Spares had to be ordered and lead time on delivery were a few weeks, postponing further experiments with the printer. As parts arrived and were installed, more complications occurred. Regulation of the heating element for the nozzle did not work, nor did the sensors. After troubleshooting, the problem was identified to be a combination of pins dying on the circuit board and a MOSFET failing to regulate the current to the heater. Tightening the Z-axis end stop, changing pins for temperature sensors and replacing the MOSFET made the system work properly again. In addition, a new plate was added to the mounting of the water cooling to the hot end, making sure that the metal spring did not rest on the rollers of the X-axis (Figure A.2). After calibrations a new vase mode component (Figure A.3) was printed and showed improved quality. The malfunctions cost the project four-five weeks of valuable time, but gave a lot of experience on how the system functions.

3 Preparations and Method

This chapter describes the work done to learn about material properties and how they are affected. Iterations and production of test specimens, testing of the material and application of Thermal Layer Design (TLD) on a component is explained.

3.1 Theory and Background

An overview of the central theory and equipment for the methodology used.

3.1.1 Layer Bonding and Testing

A “layer-by-layer” process defines the part’s material properties, determined by the bonds between and within the layers. Interface bonding state, determined by heat transition within the structure, is a determining factor for the mechanical properties. Process parameters such as layer thickness, deposition velocity, infill rate, and environment temperature affect the bonding [9,10]. Adjusting the process parameters changes the mechanical properties of the part manufactured, as the molecular diffusion in the material depends on local temperatures and associated times [8]. Low layer temperatures result in less diffusion, meaning strong bonds between adhesive and adherent do not occur [27]. High temperatures cause the material to flow which may lead to dimensional inaccuracy and loss of strength. Deposition velocity alters the layer temperature by depositing material at a faster pace. The time already deposited material has to cool down before new material is added can cause more or less residual heat energy to activate the surfaces of the adjacent regions, thus molecular diffusion and interlayer tensile strength can be affected by printing speed. Tensile testing of specimens printed in the Z-direction will indicate how well the layers bond. Defining the material properties is needed to determine which layer temperature that gives the highest UTS, see Equation 1.

$$\sigma = \frac{F}{A_{Nominal}} \quad (1)$$

Where σ is the nominal tensile strength based on the peak load, F and the nominal cross-section, A.

3.1.2 Thermal Layer Design

Thermal Layer Design (TLD) is a concept for designing components based on the thermal properties of the material and capabilities of the hardware. This concept emerged during the process of material testing. To produce a component with substantial load-bearing and predictable properties, one must know how the material behaves at different temperatures and design the component so that the material properties are fully utilized. Creating a database for the different materials where expected properties like UTS, strain to failure, stiffness, tolerances, etc. can be estimated based on the layer temperatures would be a powerful tool. By incorporating TLD as a tool of DfAM, where the settings, geometry and tools are all adapted to the material in question, components can be optimized for FFF. The desired functionality and properties in a part could then be designed to reduce anisotropy effects by even heat distribution to give uniform properties in the whole cross section, or to optimize critical areas of the component in terms of strength and allowing non critical areas to have lower quality. The market for such on-demand production has enormous potential, once the ability to produce lightweight, high quality, functional components is possible. Developing and implementing thermal layer design can be a part of the solution for challenges with ‘material’ and ‘metrology’.

3.1.3 Materials and Equipment

An overview of central material information, equipment and software is listed below.

- **Modified Creality CR10** - The printer used to produce material samples and components is a modified Creality CR10 [12] with an upgraded hotend, bed heater, enclosed heating chamber and enclosed filament drying chamber. It uses a hardened steel 0.6mm nozzle [12].
- **Polymaker PA6-CF** - The filament mainly used is Polymaker PA6-CF with a diameter of 1.75mm. The nylon filament contains 20% chopped carbon fibers [25]. The filament reels have been stored at room temperature in closed bags with silica bags for a period of 6 months.
- **SuperSlicer** - The software used to control printer settings and translate models to G-code is SuperSlicer. SuperSlicer is a forked, open access version of PrusaSlicer, allowing more control over settings [28].
- **Meshmixer** - To modify the original model of the component, Meshmixer was used. Meshmixer allows for inflating the model in selected areas, making the process of TLD quick and predictable to implement.
- **Mitutoyo SJ-301** - To measure surface roughness, a Mitutoyo SJ-301 profilometer was used. The profilometer has a total range of 300 μ m and an evaluation length range of 0.3mm - 12.5mm.
- **Spidé HA06** - The annealing of test specimen was done with a Spidé HA06 reflow oven which ensured stable temperatures over a prolonged period.
- **MTS Criterion 5kN** - The machine used for tensile testing was a MTS Criterion Electromechanical Load System, model C42.503 with a load capacity of 5 kN. The load system has an accuracy of $\pm 0.5\%$ and complies with ISO 7500-1 [29].
- **FLIR One Pro** - The thermal imaging and measurements were recorded with a FLIR One Pro compact thermal camera for smart phones. It has a temperature range of -20°C - 400°C, and a normal camera paired with the thermal camera to enhance contrast in the thermal images [30].
- **JupyterLab** - To process and present data, JupyterLab was used. Writing Python code, data was read, organized and used to generate figures.
- **Hirox RH-2000** - To study surface structures of failed specimens, a Hirox RH-2000 3D digital microscope was used. With the capability of layering images to produce a 3D effect, every part of the surface is in focus.

3.2 Specimens

Description of how the tensile test specimens were iterated, modified and produced.

3.2.1 Test Specimen Geometry

There is no standard for tensile testing of specimen produced by FFF, but ISO 527 [31] for injection- or compression-molded polymers is often used. The geometry of the tensile test specimen had to be adapted to allow for more specimens to be produced in the time frame of this project. The main challenge is stability while printing standing specimens, accuracy of the deposition, and the time it takes to produce a given amount of specimens. Two approaches of geometry are tried, basing one on the ISO 527 standard for tensile testing of polymers and the other on the ASTM E606/E606M standard for tension fatigue testing. The cylindrical geometry for fatigue testing is investigated as it could eliminate the problem of square corners becoming rounded due to the

round nozzle. In addition, it could eliminate one variable for the cross section, as only diameter needs to be measured instead of width and thickness.

A plethora of different tensile test specimen geometries are manufactured with an accompanying number of combinations for the printing settings. A representation of the iterations on scaling and modification of geometries is shown in fig Figure 2. Starting with basic specimens for each standard to the left, the down scaled iterations are gradually improved from left to right in the figure. Specimens 1.1-1.3 are too thin for the deposited filament to build upon and instability causes the material to sag out to the sides, resulting in geometrical deficiencies and bulges in the surface of the specimens. The same effects can be observed in specimen 2.1, but specimens 2.2 and 2.3 do not suffer these problems as the larger cross section gives a solid foundation for perimeter and infill. The transition of 2.2 is too steep and this caused a poor surface on the top end. Some additional tests are added in Figure B.1.

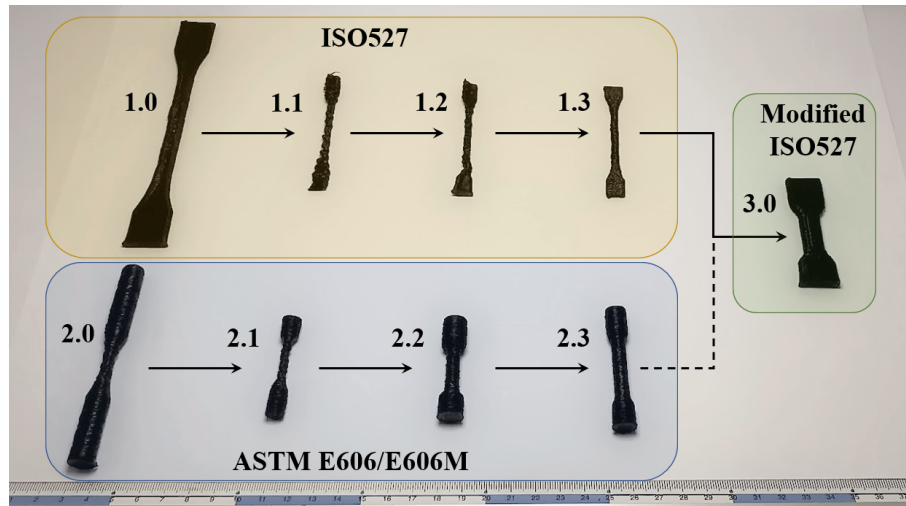


Figure 2: Iterations on specimen geometry based on ISO527 and ASTM E606/E606M standards with final specimen to the right.

Specimen 3.0 is a modified version of ISO 527, and a decision is made that it is favorable to stay close to a tensile testing standard for polymers. By shortening the specimen, production time is reduced by a lot. Increased thickness proves to be more stable during acceleration and deceleration of the bed, reducing defects on the surface. Changing the cross-section also makes the layers larger, giving more room for infill in the specimen. The final dimensions of the test specimen can be seen in Figure 3.

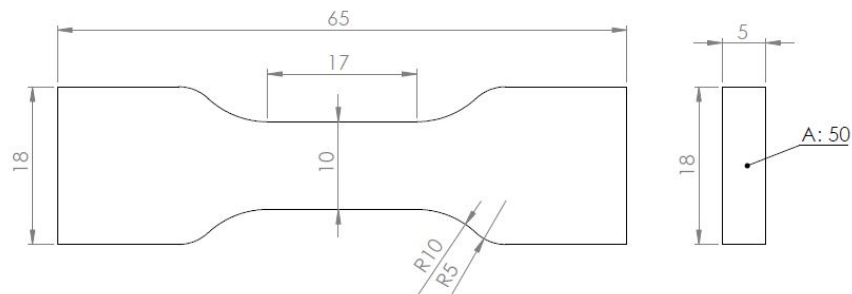


Figure 3: Dimensions of modified ISO527 specimen.

3.2.2 Improving the Quality of Test Specimens

When the geometry for the tensile test specimens is decided, several printing parameters are tested to find a range of qualities as well as the limits. Parameters in the slicer alters the printing approach, changing each parameter changes material properties within a print. Modifying extruder temperature, bed temperature, chamber temperature, and printing speed all regulates layer temperature. Changing all of the parameters simultaneously gives too many parameters to consider or to give a comparable trend. As printer speed is set as the variable to regulate layer temperature, appropriate extruder, chamber, and bed temperatures are needed. Table 1 shows a combination of parameters that are used to produced samples of the test specimen. The results of these samples are presented in Figure 4.

Table 1: Testing printing settings for specimens 3.1-3.5

Specimen	3.1	3.2	3.3	3.4	3.5
Printing speed [mm/s]	2	6	6	35	7
Extruder [°C]	300	290	300	300	300
Bed [°C]	110	110	110	130	110
Chamber [°C]	room temp	80	70	70	70
Perimeter number	1	1	1	1	2
Seam position	aligned	random	aligned	aligned	aligned

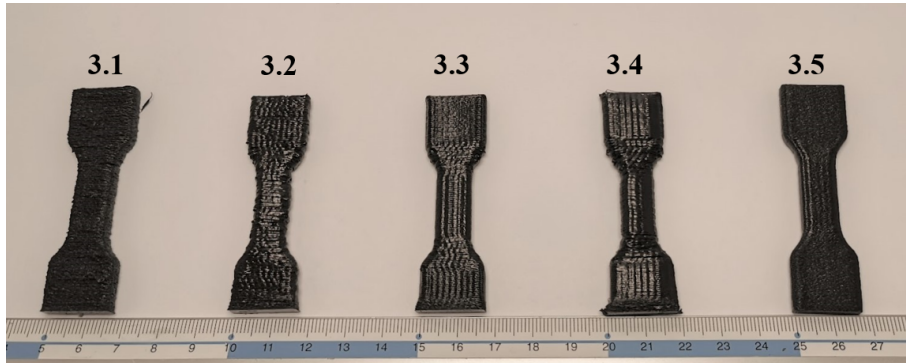
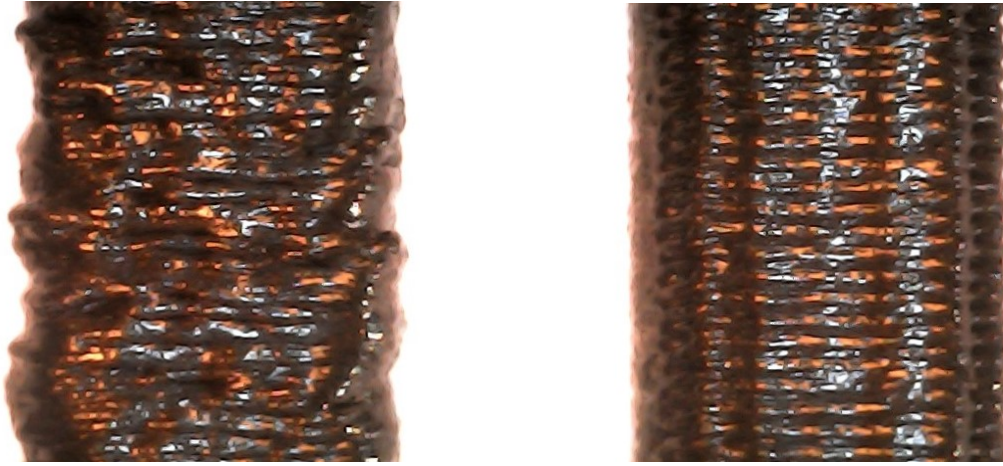


Figure 4: Five samples of the same specimen with different printing parameters.

The surface of specimen 3.1 is porous and coarse, showing close to no signs of melting. Specimen 3.2 has dimples all over the surface caused by the random starting position of each perimeter, it also has several geometrical kinks and an uneven surface, although it showed some melting. In Figure 5 the difference between two specimens with the same settings, except for seam position is shown. Specimen 3.3 has very little geometrical deficiencies and shows an overall melted surface, giving the glossy look as seen in Figure 4. While specimen 3.4 has the most melted surface, showing signs of good bonding, the speed at which it is printed causes more deficiencies to the shape. The overall best geometry and finest surface is that of specimen 3.5 due to the two perimeters giving a more solid outer support. Test prints with printing speeds of 1 mm/s and 2 mm/s at room temperature were developed to find "worst cases", these take a long time produce and shows signs of poor quality. The lower limit is therefore set to 4 mm/s. After several rounds of printing with different combinations of settings, specimen 3.3 is deemed to be adequate for a wide range of printing speeds and its settings is decided to be used for material testing. Although specimen 3.5 has better outside geometry, the double walled perimeter leaves less room for the rectilinear infill which is assumed to be more significant in terms of layer bonding. Specimen 3.5 is also produced at a later stage, after several test specimens are made with the settings from 3.3. A further look at the quality of geometry is added in Section B. The final fixed settings based on specimen 3.3 are given in Table 2.



(a) Surface of a specimen with random seam.

(b) Surface of a specimen with aligned seam.

Figure 5: Comparison of surface quality between two specimen printed at 6 mm/s with different seam placements.

Table 2: Fixed settings for test specimen production.

Setting	Value
Extruder temperature	300°C
Chamber temperature	70°C
Bed temperature	110°C
Perimeters	1
Layer height	0.3mm
Seam position	Aligned
Infill type	Rectilinear
Infill density	100%
Max acceleration X- and Y- direction	900mm/s ²

3.2.3 Producing Specimens

Three specimens are produced for each of the speeds tabulated in Table 3. The specimens are produced together, sequentially completing individual objects before starting on the next one. All three specimens are oriented perpendicular to the X-axis of the printer, with a spacing of 100 mm between them to avoid any collision between the hot end and already completed specimens.

Table 3: Printing speeds used and designation for specimens

Printing speed	Specimen designation
4mm/s	v4_0x
5mm/s	v5_0x
6mm/s	v6_0x
7mm/s	v7_0x
8mm/s	v8_0x
9mm/s	z9_0x
10mm/s	v10_0x
11mm/s	v11_0x
12mm/s	v12_0x
14mm/s	v14_0x
16mm/s	v16_0x
18mm/s	v18_0x
20mm/s	v20_0x
25mm/s	v25_0x
30mm/s	v30_0x
40mm/s	v40_0x
50mm/s	v50_0x

When completed the specimens are removed from the heated chamber and placed in zip lock bags to minimize moisture exposure. After organizing all finished prints, they are measured in length with a caliper. Width and thickness is measured five places along the reduced area using a micrometer and the measurements deviating most from nominal values are documented. After all geometric measurements are made, the specimens are annealed at 100°C for 6 hours following the manufacturer’s recommendations [25]. The specimens are placed on a salt bed in a preheated oven to ensure even heat distribution during annealing. After heat treatment, specimens are placed back into individual zip lock bags.

3.3 Gathering Data

3.3.1 Measuring Layer Temperature

Layer temperature is measured using a FLIR One Pro for each printing speed. Specimens used to measure temperature are cut to be one-quarter of the original dimensions, such that the final layer of the print is within the reduced area of the geometry as well as reducing printing time by removing areas of no interest. The measuring is done by opening one door of the heat chamber of the printer just enough to hold the thermal camera close to the specimen and record the final layers. The recordings start approximately 1-4 minutes before the print is finished, capturing the final layers and retraction of the nozzle before measuring only the surface of the final layer. These recordings are then analyzed frame-by-frame to find the first stable temperature reading for each printing speed.

3.3.2 Tensile Testing

Tensile testing is done according to ISO 527 standards [31]. The machine used to perform the tensile testing is a MTS Criterion Electromechanical Load Systems. Model: C42.503, 5kN. The test speed is set to 2mm/s, with the limit detection load set to 4500N. Testing is performed in batches of 5-20 specimens from 30 minutes to 3 hours after annealing. The specimens are mounted in the grips of the machine like shown in Figure 6. Specimens that fail outside the reduced section are rejected and replaced with new specimens. Raw data from each test is exported with the information of time, crosshead movement and measured load. Tensile strength is calculated with Python, using Jupyter Lab to read and extract data from the raw files. Average UTS for each set

of specimen is then plotted against measured layer temperature. The failure surface is also studied in a Hirox RH-2000 digital microscope for a selection of specimens.

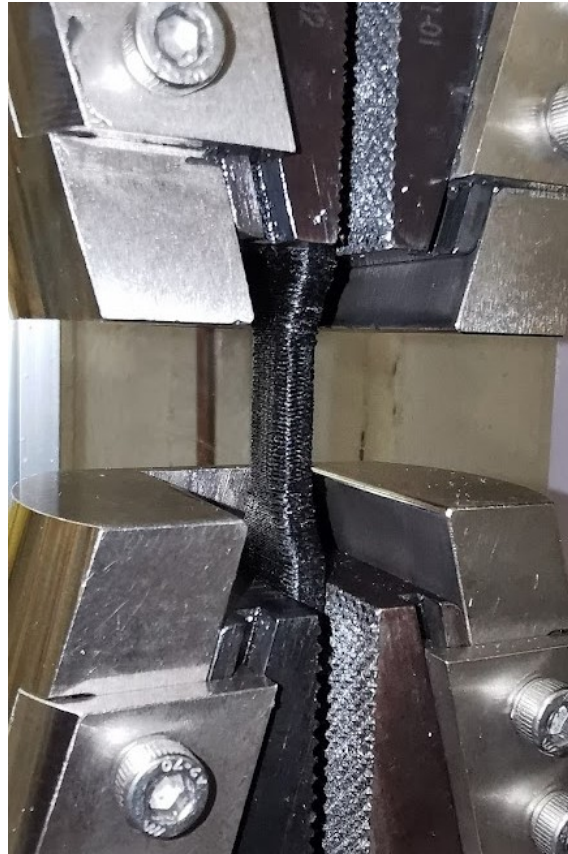
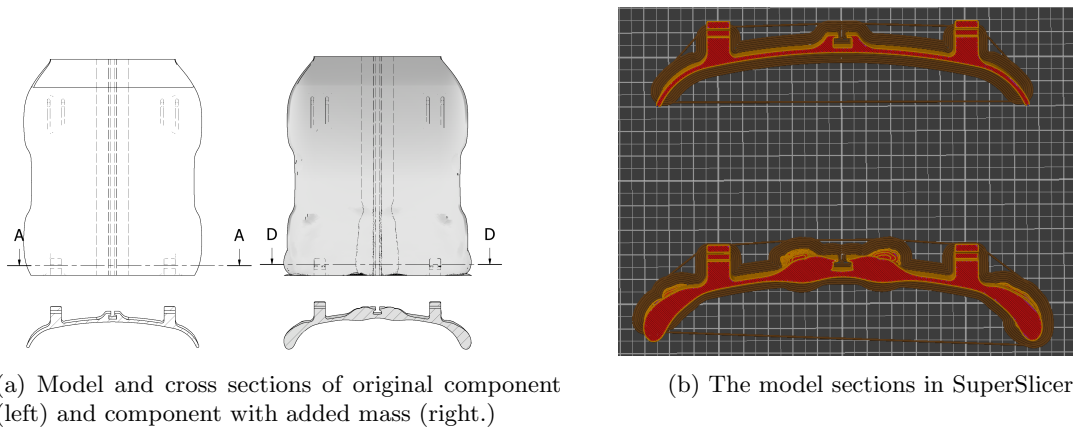


Figure 6: Mounting of a specimen in the test machine.

3.4 Application of Thermal Layer Design on a Component

The component used as a test platform for TLD is a backrest prototype for competitive para-rowing. The component is chosen because it is designed for FFF. A short description of the component and challenges is added in Section C.

To analyze the component design and thermal properties, two models are compared. The original design is left as is, while the TLD component is a modified version of the original design, where mass has been added to key areas. The TLD component is modified in Autodesk MeshMixer, where mass is added to the thin sections in the ends and by the groove chamber in the middle (Figure 7a). The mass is added on the outside, as this side is not constrained in terms of space, unlike the inside which is designed to fit the athlete using the seat rest. Both components are shown in Figure 7a. The models are then reduced to 50% of original size and cut down to the lower 10 mm. The resulting component sections (Figure 7) are then produced with the same fixed settings (Table 2) with a printing speed of 50 mm/s.



(a) Model and cross sections of original component (left) and component with added mass (right.)

(b) The model sections in SuperSlicer.

Figure 7: Components and sections printed.

Bed temperature is reduced to 80°C after the first layer is finished, to give better contrast for the thermal camera. During the last 1-4 minutes of the print, the door of the heated chamber is opened just enough to hold the thermal camera at approximately 10 cm from the specimen to record the temperature of the final layer. The maximum values and dispersion of temperature in the cross section is then evaluated.

4 Results

This chapter presents all of the results from tensile testing, measuring of surface roughness and layer temperature. Most of the data are presented with respect to layer temperature as geometry and material properties differs with a given temperature between deposited layers. Some additional results are added in Section D, where testing outside the standards was done to gain knowledge and experience with PA6-CF.

4.1 Complete results

4.1.1 Thermal properties

The layer temperature measured for each printing speed is plotted in Figure 8. For the range of 146°C to 180.8°C, only minor changes in printing speed are needed to affect the temperature. For 180.8°C and above, much higher printing speeds are needed to increase the temperature. The plot rises in an almost exponential trend.

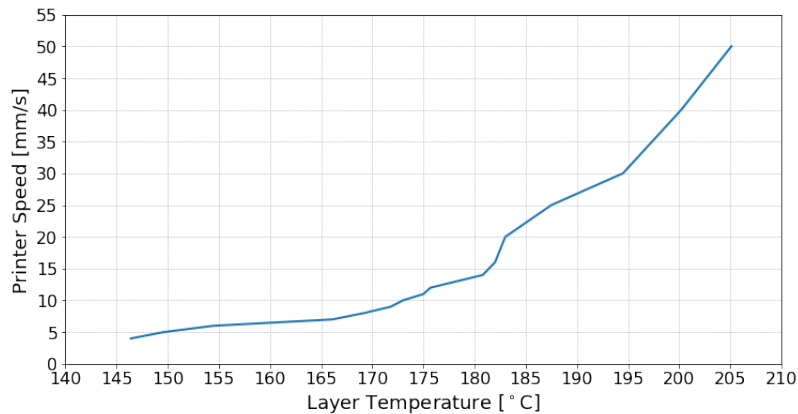


Figure 8: Printer speed vs. Layer temperature.

Figure 9 shows thermal images used to measure layer temperature. The differences between 9a, 9b and 9c are between 20-25°C, while the difference from 9c to 9d is only 12.3°C. The heat dispersion down through the specimen varies for the four specimens. It is possible to see an evolution of the contained heat in the specimen from 9a which has cooled down in the lower part, to 9d which is still warm down to the bottom. The temperatures of the top layer in the three first specimens are also plotted over a period of 90 seconds in Figure 10. Here it is possible to see how the layer temperature decreases over time for the different specimens. Layers with higher initial temperatures cools down at a slower rate than the ones starting at lower temperatures. Note that the graph for v10 is shifted along the Time-axis to start where it intersects with v30. The same is done for v5 to intersect v10 in the starting point.

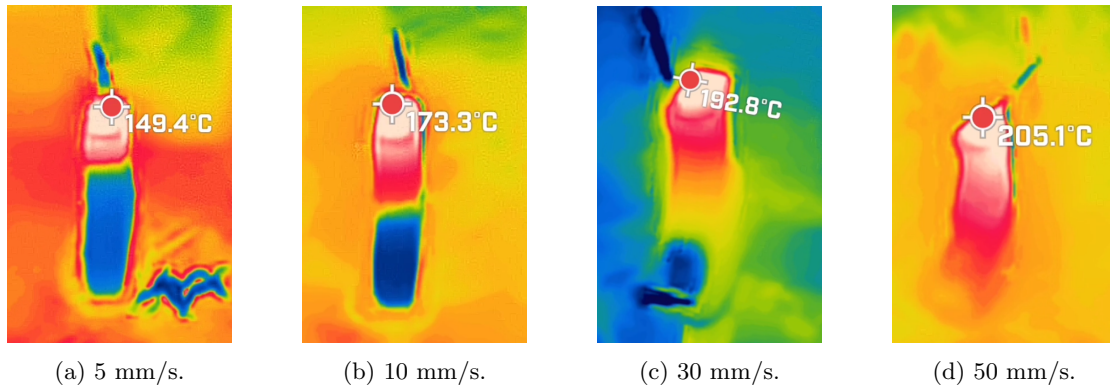


Figure 9: Thermal measurements for layer temperature at four different printing speeds.

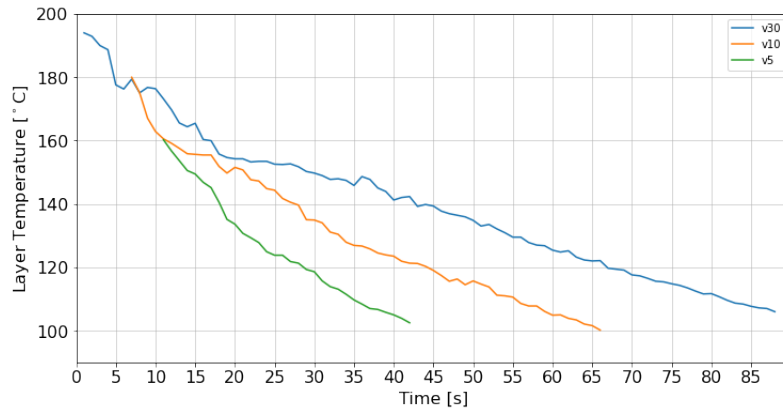


Figure 10: Printer speed vs. Layer temperature.

4.1.2 Geometry

Layer deposition and bonding temperature, in combination with acceleration and deceleration of the bed and nozzle affects the geometry and quality of the printed specimens. Figure 11 shows the average of the measured dimensions on the test specimens and how they change with layer temperature. The length has larger deviations, but does not indicate any clear trend. Meanwhile, as layer temperature increases, the average width decreases at the same time as average thickness increases.

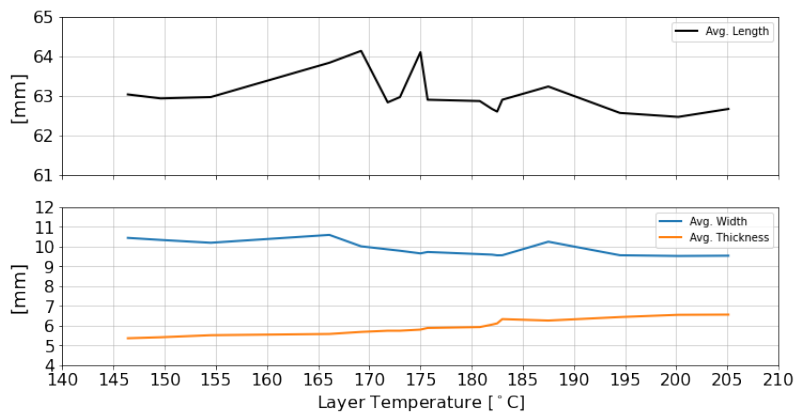


Figure 11: Average geometry measurements vs. Layer temperature.

The surface roughness of specimen printed at speeds from 4 mm/s to 18 mm/s are shown with the relation to layer temperature in Figure 12. The surface roughness is consistent up until the area of 170°C and above, where has higher values.

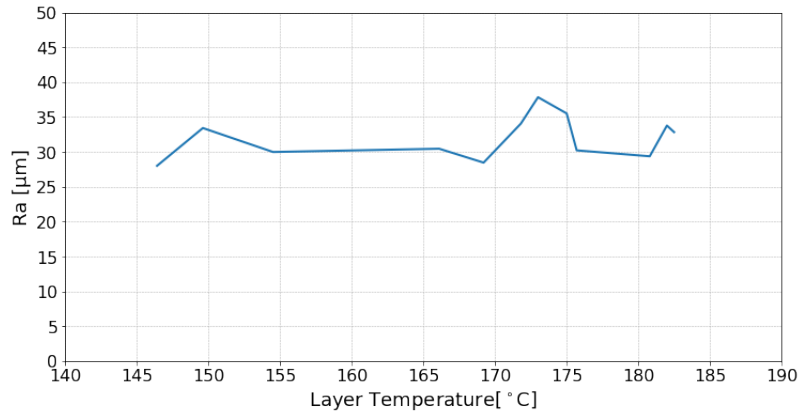


Figure 12: Average surface roughness vs. Layer temperature.

The development of geometry and for six printing speeds is presented in Figure 13. The figure shows increased geometrical problems for increased printing speeds. Specimens from 20 mm/s and above shows deformation in the bottom, where a beard of material is protruding out. The same specimens also show more curvature of the reduced section and additional ghosting.

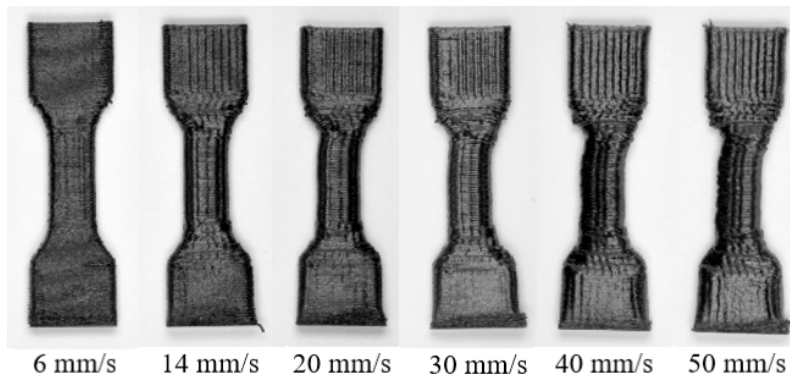


Figure 13: Resulting specimens at different printing speeds.

4.1.3 Ultimate Tensile Strength and machine measured elongation

The average UTS for each set of specimens with standard deviations is plotted in relation to layer temperatures in Figure 14. The UTS increases with the temperature before it peaks at 70-73 MPa with corresponding temperatures of 166-175°C. From this point it rapidly decreases, and it can be noted that the standard deviations are larger above 175°C. The overall trend of the graph shows a gradual increase in UTS leading towards a peak before UTS decreases again.

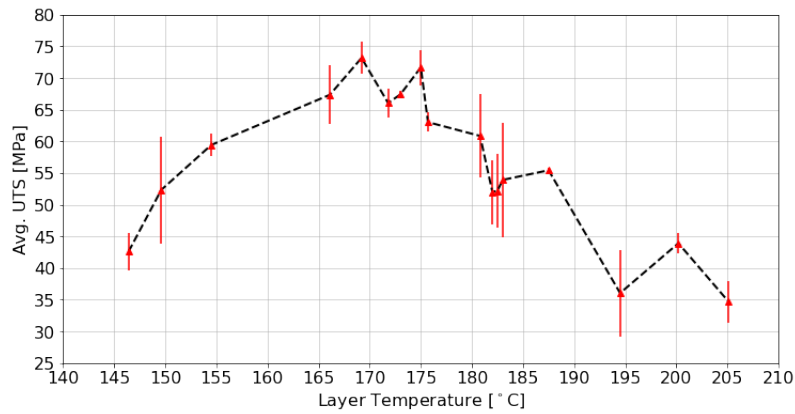


Figure 14: UTS vs. layer temperature.

During tensile testing of the specimens, the machine measures crosshead movement at failure. The average elongation for each set of specimens is plotted against layer temperatures (Figure 15), including standard deviations. Notice the peak between 170°C and 175°C which is much higher than the general trend.

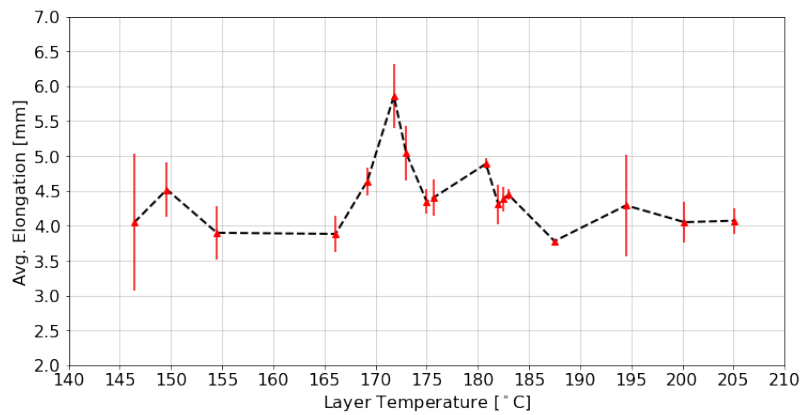


Figure 15: Elongation vs. layer temperature.

4.1.4 Point of Rupture

. Figure 16 displays a selection specimens and their breaking points, corresponding micrographs of the same specimens are displayed in Figure 17. It is evident that all specimens suffered brittle fractures. The micrographs shows a gradual development of the cross section. In some specimens the rectilinear infill is observable, while in others it does not show. Most break surfaces show signs of inter-layer failure. Notice how the specimen v4.01 is close to rectangular and show few noticeable voids, while v8.01 has more noticeable voids due to insufficient infill.



Figure 16: Selection of specimens (from top left): v4_01, v6_01, v8_01, v10_02, v12_01, v16_02, v20_02, v30_01, v50_01.

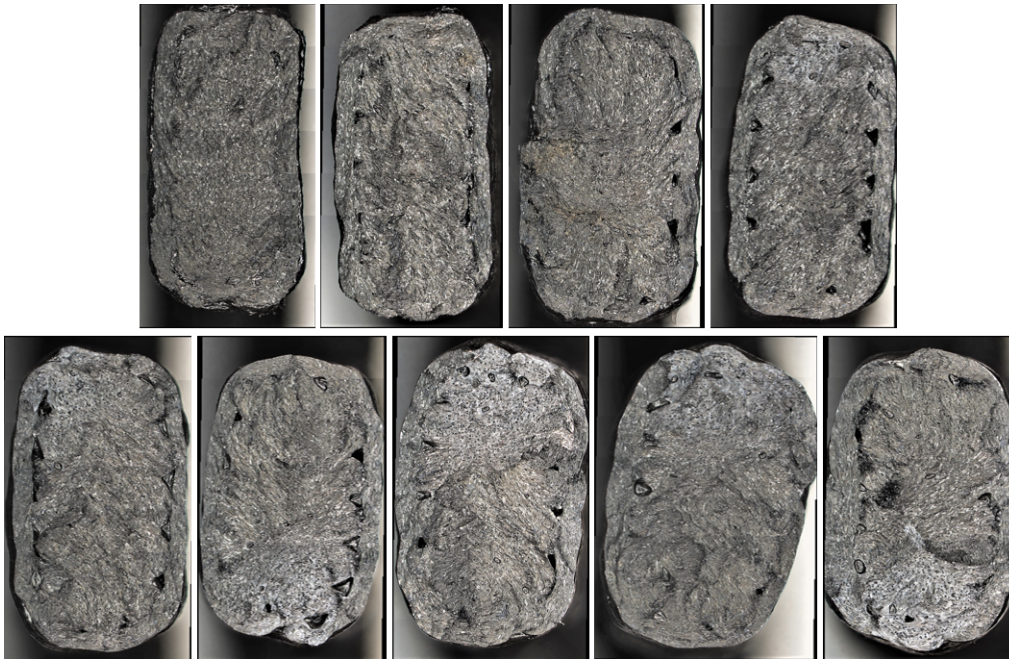


Figure 17: Selection of microscopic images of breaking points of specimens (from top left): v4_01, v6_01, v8_01, v10_02, v12_01, v16_02, v20_02, v30_01, v50_01.

Figure 18 shows three different rupture points. v5_03 broke in the middle of the gauge length. v5_01 broke in the transition and the grip vicinity. Specimen v18_03 broke two places simultaneously, but within the reduced section.

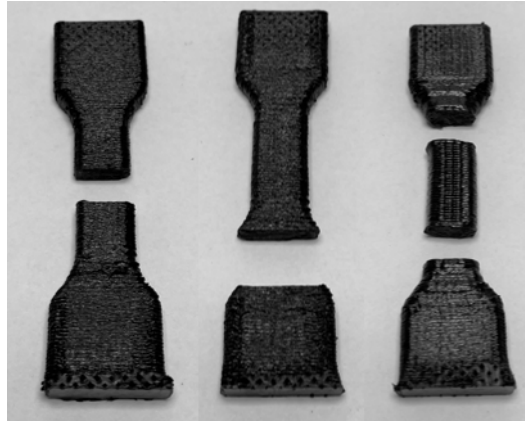


Figure 18: Optimal breaking point, and two questionable breaking points (from left): v5_03, v5_01, v18.03.

4.1.5 Thermal Layer Design on Component.

The printed sections of the original component and TLD component can be seen in Figure 19a, paired with layer temperature distribution in 19b. The latter shows maximum temperature of the original component being 123.9°C , while the maximum temperature for the TLD component is 106.3°C . The lower temperatures at the sides of the original component are colder than the background of the bed at 80°C , while the colour in the thin section of the TLD component is roughly the same as the background colour of the bed.

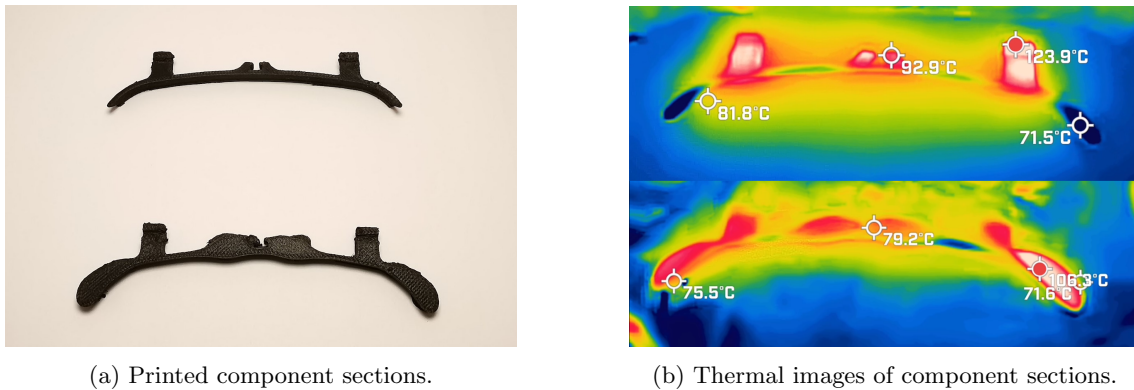


Figure 19: Thermal measurements for layer temperature of the two component cross sections.

4.2 Conference paper

The project work resulted in a conference paper on the relation between strength and layer temperature. We also introduced the term *Thermal Layer Design*, and how the application of TLD affects thermal properties of a component. This paper was submitted on 9th of December 2021 to the 32nd CIRP Design Conference to be held in Paris 2022. The paper was written with guidance and feedback from PhD candidate Sindre Wold Eikevåg, Associate Professor Christer W. Elverum and Professor Martin Steinert.

Note that results for printing speeds of 40 and 50 mm/s, were omitted from the paper. The reason for this was that the results of printing speeds up to 30 mm/s presented the trends sufficiently and further documentation was considered as excess material.

4.2.1 Thermal Layer Design in Fused Filament Fabrication

32nd CIRP Design Conference

Thermal Layer Design in Fused Filament Fabrication

Olav U. Bjørken^a, Benjamin Andresen^a, Sindre W. Eikevåg^{ab}, Martin Steinert^a,
Christer W. Elverum^{a*}

^aDepartment of Mechanical and Industrial Engineering, Norwegian University of Science and Technology, 7491 Trondheim, Norway

^bDepartment of Civil and Environmental Engineering, Center for Sports Facilities and Technology, Norwegian University of Science and Technology, 7491 Trondheim, Norway

* Corresponding author. Tel.: +4799382272. E-mail address: Sindre.w.eikevag@ntnu.no

Abstract

Design for additive manufacturing (DfAM) is limited by material properties and effects of production parameters. As more engineering grade polymers become available for Fused Filament Fabrication (FFF), the design and process must be adapted to fully utilize these materials. Effects of layer temperature on strength, surface roughness, and dimensional accuracy of PA6-CF were found by material testing and the concept of Thermal Layer Design (TLD) was demonstrated on a component. TLD proved to have a major effect on layer temperature and heat distribution. Implementing TLD in DfAM is a big leap for designing high-performance polymer components.

© 2022 The Authors. Published by ELSEVIER B.V.

This is an open access article under the CC BY-NC-ND license (<https://creativecommons.org/licenses/by-nc-nd/4.0>)

Peer-review under responsibility of the scientific committee of the 32nd CIRP Design Conference

Keywords: High-performance polymers; Fused filament fabrication, Additive manufacturing, Design for additive manufacturing

1. Introduction

Fused filament fabrication (FFF) is one of the most popular additive manufacturing (AM) processes where material is extruded to build 3D models layer by layer from digital information [1]. AM omits many of the constraints associated with conventional manufacturing processes, yet most AM technologies have several limitations such as anisotropic material properties and the need for supports and post-processing [2]. Whether the technology is utilized as a tool in the design process or to manufacture end-use parts, it is necessary to consider both opportunistic and restrictive Design for Additive Manufacturing (DfAM) aspects [2]. One of the considerations regarding FFF is that the “layer-by-layer” process defines the part’s material properties, determined by the bonds between and within the layers. Interface bonding state, determined by heat transition within the structure, is detrimental to the mechanical properties.

Process parameters such as layer thickness, deposition velocity, infill rate, and environment temperature affect the bonding [3], [4]. Thus, adjusting these parameters changes the mechanical properties of the part manufactured. Molecular diffusion in the material during deposition depends on local temperatures and associated times [5]. Altering deposition velocity alters the layer temperature, thus the molecular diffusion and interlayer tensile strength. For polylactide (PLA), it has been shown that the deposition of a new layer increases the temperature of the preceding layer above the glass transition temperature [6].

Low layer temperatures result in less diffusion, meaning strong bonds between adhesive and adherent do not occur [7]. Too high temperatures cause the material to flow which may lead to dimensional inaccuracy and loss of strength. For low-cost commodity materials such as PLA, maintaining a layer temperature within the lower and upper bound is generally not a challenge. However, for high-performance polymers this may be an issue. As more high-performance polymers and

polymer composites become available as filaments [8], the design of AM components must be adapted to utilize the properties of these materials. Currently, there is a lack of research on high-performance polymers as most mechanical properties and manufacturing parameters are tested for commodity polymers that are not suitable for load-bearing applications [9]–[11].

This study explores how the temperature between the layers in the weak direction affects properties such as ultimate tensile strength (UTS), surface roughness, and geometrical tolerances using an engineering grade, high-strength carbon fiber reinforced polymer composite. Through tensile testing and measuring layer temperature in different designs, differences in material properties through a component can be assumed. To complement existing DfAM guidelines, we introduce the concept of Thermal Layer Design (TLD) and demonstrate the impact geometrical changes have on the layer temperature of a component.

As more hardware to deposit high-performance polymers become available, open-source machines such as the one used in this study [12], as well as commercial alternatives TLD will become more relevant for high-end polymer components.

2. Method

Layer deposition temperature is a crucial factor in the layer adhesion quality of FFF components and affects properties such as UTS, surface roughness, and dimensional tolerances. This effect was investigated by 1) Material testing: tensile test specimens were produced and tested to gather data on material properties and measure their corresponding layer temperatures 2) TLD applied on a component: layer temperature within a designed part was measured to estimate the strength based on the material testing. The component was then modified by adding mass in thin sections before the layer temperature was measured and compared to the original component.

2.1. Material testing

The procedure for manufacturing and testing material specimens is given in Fig. 1. Specimens were printed in the Z-direction to investigate the influence of layer deposition temperature on material properties, using three samples for each printing speed. The printer used to print test specimens is a modified Creality CR-10 [12].

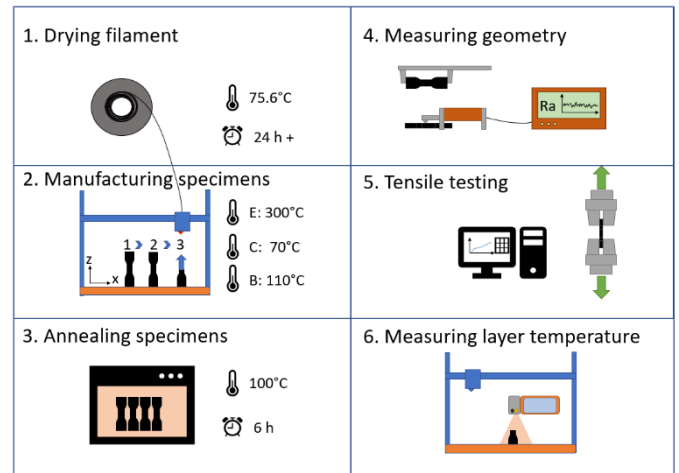


Fig. 1. Procedure for production of tensile test specimens.

The filament used was Polymaker Polymide PA6-CF of diameter 1.75 mm. The filament contains 20 wt% chopped carbon fibers [13]. Before use, the filament had been stored at room temperature for six months in vacuum bags filled with silica. Prior to manufacturing the specimens, the filament was dried at 75.6°C for 24 hours and kept at this temperature continuously during printing. The specimen geometry is based on ISO 527 and was adapted to reduce printing time due to the large number of samples needed. The thickness was increased and the width was slightly reduced, as thinner geometries tend to overflow and create variable geometries. The cross-section of the reduced section is 50 mm². Fig. 2 shows the nominal dimensions.

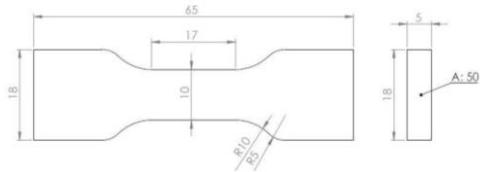


Fig. 2. Nominal dimensions of tensile test specimen.

Superslicer, a forked open-source version of Prusa Slic3r, was used to modify the settings for the printing process [14]. The specimens were printed with several fixed parameters, using the printing speed to manipulate layer temperatures. The essential parameters are listed in Table 1.

Table 1. Settings in Superslicer for production of tensile testing specimens.

Fixed parameters	Value
Extruder temperature	300°C
Bed temperature	110°C
Chamber temperature	70°C
Infill pattern	Rectilinear
Infill density	100%
Max allowed acceleration	900mm/s
Printing speed	(4, 5, 6, 7, 8, 9, 10, 11, 12, 14, 16, 18, 20, 25, 30)mm/s

The specimens were printed sequentially, completing individual objects before starting the next one. Placing the samples with the width side perpendicular to the x-axis on the bed allowed for higher print speeds with fewer geometrical defects. The specimens were removed from the heated chamber and placed in zip lock bags to minimize moisture exposure. After organizing all finished prints, the specimens were measured in length, width, and thickness using calipers and micrometers. Measurements were taken several places on the specimen, and the most significant deviation was documented. As the geometrical details of the specimens change with the printing speeds, the average centerline roughness, Ra, was measured using a Mitutoyo SJ-301 surface roughness profilometer. After all geometric measurements were made, the specimens were annealed at 100°C for 6 hours following the manufacturer’s recommendations [15]. The specimens were placed on a salt bed in a preheated oven to ensure even heat distribution during annealing. After heat treatment, specimens were placed back into individual zip lock bags. Tensile testing was performed 30 minutes to 3 hours after annealing, as the specimens were annealed in batches. Tests were performed using MTS Criterion Electromechanical Load Systems. Model: C42.503, 5kN. The loading system has a speed accuracy of ±0.5% and complies with ISO 7500-1 [16]. Tensile test speed was set to 2mm/min as recommended for the ISO 527 [17]. The raw data was collected and plotted using Jupyter Lab and Python. Measuring layer temperature was done using a segment of the specimen. The layer temperature was gathered halfway through printing a specimen with a FLIR One Pro thermal camera [18]. As the nozzle moves away from the specimen, the camera measures the first seconds of stable layer temperature before it cools down (Fig. 1). A selection of three thermal recordings at printing speeds 5, 10, and 30 mm/s were used to plot layer temperature over 90 seconds.

2.2. Application of thermal layer design on a component

The component is a prototype backrest for rowing, designed to be produced by AM. The original design, and the TLD with added mass is presented with cross sections in Fig. 3.

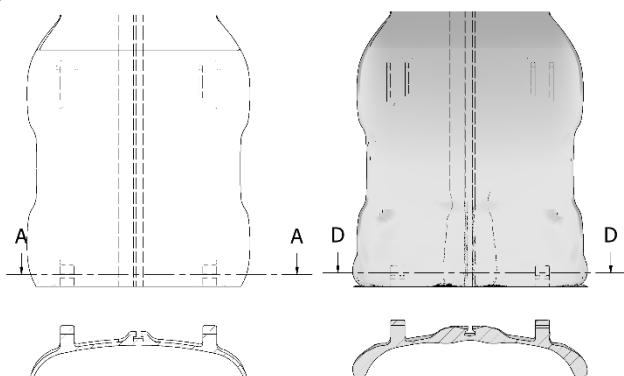


Fig. 3. Original model of component (left) and TLD model with added mass (right) with respective cross sections.

The TLD model of the backrest was redesigned in Autodesk Meshmixer, where mass was added to the free ends and on the chamber of the groove in the middle. Cutouts were printed with the same filament and settings (Table 1) but with a printing speed of 50 mm/s. After the first layer, the bed temperature was reduced from 110°C to 80°C to give the camera a better thermal contrast. Cross-section layer temperature was recorded with the thermal camera during the final layer. The thermal recordings were then compared between the two designs of the backrest. Material data from the test specimens may then be used to estimate the mechanical properties of the component.

3. Results

3.1. Material data

Fig. 4 shows how layer temperature changes with the print speed.

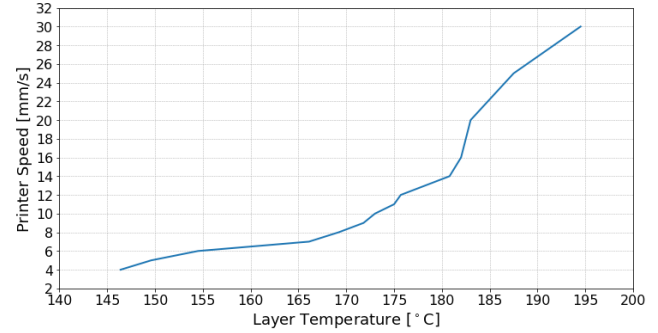


Fig. 4. Recorded layer temperature in relation to the set printing speed.

Fig. 5 shows the average ultimate tensile strength of test specimens versus the layer temperature. The UTS initially increases with the layer temperature from 145°C until it peaks in the range 166°C - 175°C. The red lines indicate the standard deviation for each specimen. Note that the deviation is more extensive for 180°C and higher temperatures.

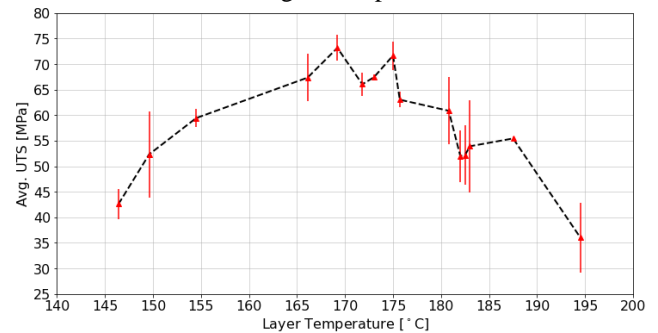


Fig. 5. Ultimate tensile strength versus layer temperature in specimens with standard deviation.

Average surface roughness for the specimens is plotted against temperature (Fig. 6). The plot only goes up to 182.5°C, as geometrical defects for higher temperatures were out of range for the measuring equipment. Note that the roughness ranges between 30-35 µm up to 170°C, before it

increases to 40 μm at 173°C. The increase in surface roughness correlates with the peak in UTS in Fig. 5. It then decreases gradually for higher temperatures until the surface is no longer measurable.

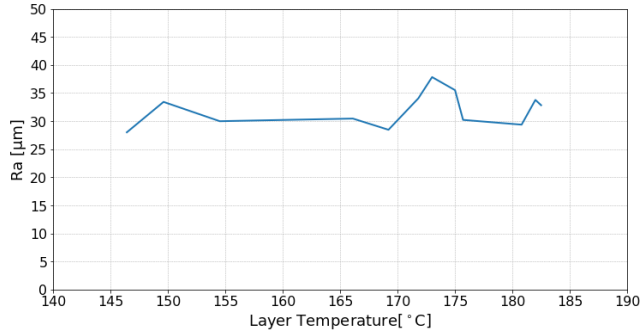


Fig. 6. Average surface roughness in relation to layer temperatures.

Fig. 7 displays how the geometrical dimensions differ with layer temperature. While there is a steady decrease in width for rising layer temperatures, the thickness steadily increases at a similar rate.

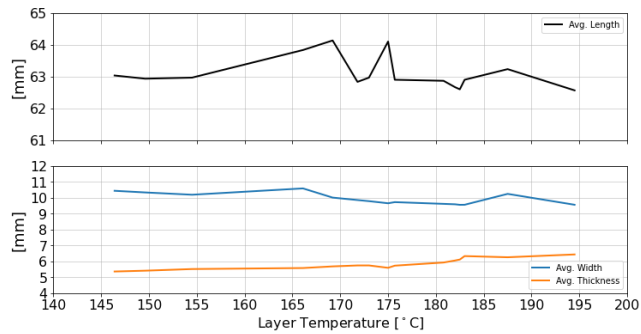


Fig. 7. Average geometrical measurements of test specimens.

Thermal images for three different temperatures (Fig. 8) show that layer temperature as well as heat retention increases with increasing printing speed.

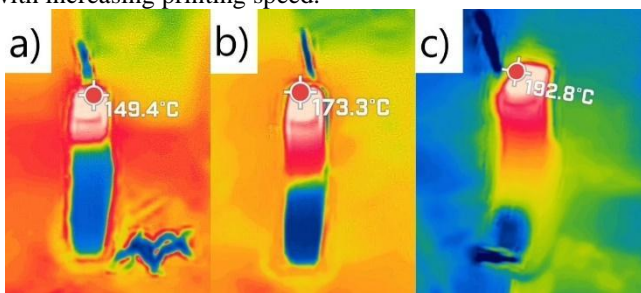


Fig. 8. Thermal images of layer temperature for specimens printed at speeds of a) 5 mm/s, b) 10 mm/s, and c) 30 mm/s.

Fig. 9 shows heat loss over time for the specimens. Samples with higher initial temperature cool down at a slower rate than samples with a lower initial temperature. The time-axis in the figure is offset to show decline in temperature from the first equivalent temperature in the closest graph.

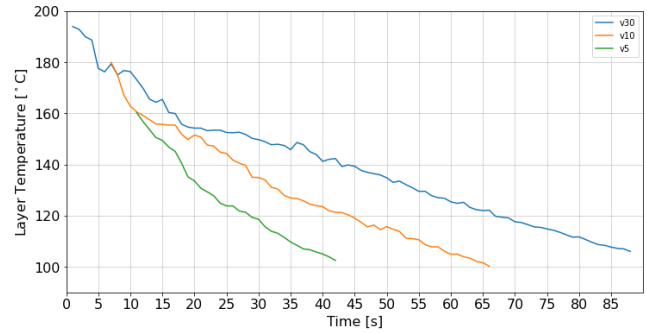


Fig. 9. Thermal decline over time in the layer temperature for three specimens.

3.2. Component results

Thermal distribution of the cross sections of the two designs is shown in Fig. 10. This figure shows that the thin-walled sections of the original component cool down rapidly before a new layer is started, while the larger areas of the component with added mass keep a more evenly distributed temperature.

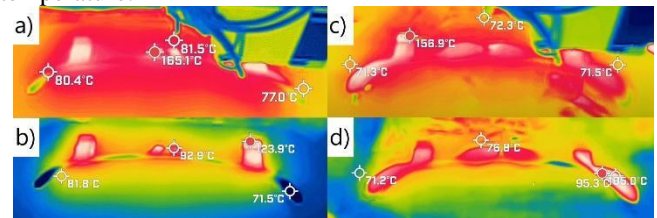


Fig. 10. Thermal distribution mid-printing and as the layer is completed, a) and b) for the original component, c) and d) for the component with added mass, respectively.

4. Discussion

4.1. Method and results

The main variable investigated in this study was layer temperature, controlled by adjusting the printing speed. Here it is important to point out that the print speed and the resulting layer temperature are not transferable to other geometries and were only used to obtain the specimen test data. For the component a print speed of 50 mm/s was used, which is within the recommended range provided by the material manufacturer. Due to acceleration and deceleration, the actual speed will deviate from the set speed.

Using TLD, the mass of the component was increased in areas with the lowest layer temperature. As seen in Fig. 9, the effect of having increased thermal mass.

The layer temperature was measured using a thermal camera where the temperature reading was found in the first frames of stable temperature reading. This manual reading may vary with the person using the camera. Another source of uncertainty is the emissivity of the deposited material changing with temperature. A study of Acrylonitrile Butadiene Styrene (ABS) found that this effect led to a misread of 36 °C at a 240 °C readout temperature [19].

However, because the increase in layer temperature is caused by increase in speed, the trend should be intact.

Fig. 5 shows that peak UTS is reached in the layer temperature range of 167-175°C. This range also resulted in the smallest deviation between specimens. The UTS results are reaching the higher end of the reported 67.7 ± 4.7 MPa by the manufacturer [15], despite being in the same range as the largest average surface roughness in Fig. 6. The UTS in this study is based on the nominal cross-section, and there may be some difference between nominal and true stress. According to Fig. 7, however, the average width decreases, and the average thickness increases with the increasing layer temperature and the same amount of filament was being extruded, which supports the use of nominal dimensions. Specimens of the lower range temperatures have a reduction in cohesion as well as imperfections and voids, making it difficult to predict the behavior during tensile testing. Specimens in the highest temperature range began to melt and overflow. Especially the transition of the specimens had uneven geometry, which may be further affected by the higher printing speeds. Higher speeds mean that the filament gets extruded on a hot layer, while both the nozzle and bed accelerate and decelerate rapidly during the infill for such a small area of the specimen and leads to melting and inaccuracy of the deposited material on the surface of the previous layer. Melted, uneven geometry causes specimens of higher temperatures to have more deviations during testing, as they are more prone to cracks initializing in the uneven surface.

Using three specimens for each layer temperature shows the progression displayed in Fig. 5, but more samples would clarify the trend and deviations. Specimens printed in various locations on the printer bed could influence the quality of the print as the bed has irregularities. The bed mesh had to be calibrated two times in the time it took to produce all samples used in this study. Samples had different prerequisites before printing, making minor differences in printing quality between samples. Using sequential production of three samples at a time means that the first samples stayed in the heated chamber temperature of 70°C for a longer period than the last samples of the same print. As PA6 is a semi-crystalline thermoplastic, this might have had an effect on the crystallization of the specimens. However, annealing all specimens at 100°C for 6 hours is thought to have a greater effect.

Several specimens failed in the transition, caused by the geometry of the tensile tests. The ISO 527 standard requires injection- or compression-molding, which is far from optimal for FFF, and other methods such as tabs should be considered. Several samples were discarded due to unsatisfying failures in the transition region before failing in another location, meaning that the transition region did withstand loads greater than expected. However, these failures were not used in the data set for this study but replaced by new samples. The layer temperature varied with printing speed and gave differences in heat distribution. Comparing the slower printed specimen in Fig. 8 a), b), and c), the speed causes a different depth of

heat. While the specimen at 5mm/s only has a shallow hot area below the top layer, the specimen at 30mm/s contains heat almost down through the specimen. The printing speed affects the heat dispersion through the entire sample as it also reduces time per layer. This can also be observed in Fig. 10, as the added mass increases the heat retention and causes a more even heat distribution through the cross-section, but the additional time it takes to produce the larger area allows the layer to cool down more.

4.2. Application and significance of findings

Using TLD on the component to improve thermal properties in each layer resulted in better heat distribution. However, peak temperatures were lower due to longer printing time for the larger layer, providing more even properties through the cross-section of the TLD component compared to the original design, as seen in Fig. 10. As the thin-walled sections are well below the low-end temperatures of Fig. 5, they would not contribute to the component strength in a way one would expect from an engineering material like PA6-CF. The initial thin-walled design allows the layers to cool down to the extent that the mechanical advantages of PA6-CF over commodity materials are lost. Even though these simple geometry changes did not result in an optimal layer temperature, it clearly shows the effect on layer temperature distribution.

With the increasing availability of both machines and AM-tailored engineering polymers, customized or low-volume production with FFF becomes a reality. However, the design of components must take into account aspects that are not normally considered when using commodity polymers, such as layer temperature. By implementing TLD into the DfAM process, even properties can be achieved throughout the entire component or critical areas can be strengthened while allowing for faster prints in non-critical sections.

5. Conclusion

Based on the findings from material testing, it is evident that the layer temperature of PA6-CF plays a key role in the quality of the bonding during FFF. It affects properties such as UTS, surface roughness, and geometrical tolerances. The results showed how the optimal layer temperature range of 166-175°C, gives the highest UTS while having minor geometrical deviations. Thermal imaging analysis gives insight into the development of layer temperature and how it decreases over time, as well as how temperature is distributed through multiple layers of the specimens during manufacturing.

The component data reveals how extensive the reduction of the expected material properties is. The thin-walled sections cool down far below the optimal temperature range before a new layer is applied. By applying TLD on components, thermal properties of the layers are significantly improved. The layer temperatures in the TLD component are more

evenly distributed, which leads to more uniform properties throughout the whole cross-section.

With the implementation of TLD significant improvements can be made in DfAM applied on engineering polymers and polymer composites. To realize the market potential for specialized AM components manufactured with FFF, more knowledge and research into TLD for engineering polymers is needed. This will make it possible to tailor component design to achieve the best possible material properties and produce predictable, high-quality components. These are crucial steps if FFF of engineering polymers and polymer composites are to be used for end-use parts.

References

- [1] S. Saleh Alghamdi, S. John, N. Roy Choudhury, and N. K. Dutta, "Additive Manufacturing of Polymer Materials: Progress, Promise and Challenges," *Polymers*, vol. 13, no. 5, Art. no. 5, Jan. 2021, doi: 10.3390/polym13050753.
- [2] I. Gibson, D. Rosen, B. Stucker, and M. Khorasani, "Design for additive manufacturing," in *Additive manufacturing technologies*, Springer, 2021, pp. 555–607.
- [3] H. Li, T. Wang, J. Sun, and Z. Yu, "The effect of process parameters in fused deposition modelling on bonding degree and mechanical properties," *Rapid Prototyping Journal*, vol. 24, no. 1, pp. 80–92, Jan. 2018, doi: 10.1108/RPJ-06-2016-0090.
- [4] P. Striemann, D. Hülsbusch, M. Niedermeier, and F. Walther, "Optimization and Quality Evaluation of the Interlayer Bonding Performance of Additively Manufactured Polymer Structures," *Polymers*, vol. 12, no. 5, Art. no. 5, May 2020, doi: 10.3390/polym12051166.
- [5] F. M. Duarte, J. A. Covas, and C. S. F. da, "Predicting the effect of build orientation and process temperatures on the performance of parts made by fused filament fabrication," *Rapid Prototyping Journal*, vol. ahead-of-print, no. ahead-of-print, Jan. 2021, doi: 10.1108/RPJ-04-2021-0084.
- [6] P. Wolszczak, K. Lygas, M. Paszko, and R. A. Wach, "Heat distribution in material during fused deposition modelling," *Rapid Prototyping Journal*, vol. 24, no. 3, pp. 615–622, Jan. 2018, doi: 10.1108/RPJ-04-2017-0062.
- [7] R. H. Sanatgar, C. Campagne, and V. Nierstrasz, "Investigation of the adhesion properties of direct 3D printing of polymers and nanocomposites on textiles: Effect of FDM printing process parameters," *Applied Surface Science*, vol. 403, pp. 551–563, 2017.
- [8] A. Das *et al.*, "Current understanding and challenges in high temperature additive manufacturing of engineering thermoplastic polymers," *Additive Manufacturing*, vol. 34, p. 101218, Aug. 2020, doi: 10.1016/j.addma.2020.101218.
- [9] R. Hashemi Sanatgar, C. Campagne, and V. Nierstrasz, "Investigation of the adhesion properties of direct 3D printing of polymers and nanocomposites on textiles: Effect of FDM printing process parameters," *Applied Surface Science*, vol. 403, pp. 551–563, May 2017, doi: 10.1016/j.apsusc.2017.01.112.
- [10] V. E. Kuznetsov, A. N. Solonin, A. Tavitov, O. Urzhumtsev, and A. Vakulik, "Increasing strength of FFF three-dimensional printed parts by influencing on temperature-related parameters of the process," *Rapid Prototyping Journal*, vol. 26, no. 1, pp. 107–121, Jan. 2019, doi: 10.1108/RPJ-01-2019-0017.
- [11] G. D. Goh, Y. L. Yap, H. K. J. Tan, S. L. Sing, G. L. Goh, and W. Y. Yeong, "Process–Structure–Properties in Polymer Additive Manufacturing via Material Extrusion: A Review," *Critical Reviews in Solid State and Materials Sciences*, vol. 45, no. 2, pp. 113–133, Mar. 2020, doi: 10.1080/10408436.2018.1549977.
- [12] A. Birkelid, S. W. Eikevåg, C. W. Elverum, and M. Steinert, "High-performance polymer 3D printing – open-source liquid cooled scalable printer design," *HardwareX*, vol. Under Review, Nov. 2021.
- [13] "PolyMide_PA6-CF_PIS_EN_V1.2.pdf." Accessed: Nov. 25, 2021. [Online]. Available: https://polymaker.com/Downloads/PIS/PolyMide_PA6-CF_PIS_EN_V1.2.pdf
- [14] S. W. Eikevåg, C. W. Elverum, A. Birkelid, and M. Steinert, "High-performance polymer 3D printing – open-source liquid cooled scalable printer design," *Mendeley*, no. V2, Nov. 2021, doi: 10.17632/7sjjmr9bz2.1.
- [15] "Polymaker - PolyMide_PA6_CF_TDS_V5.pdf."
- [16] E. ISO, "7500-1. CEN EN ISO 7500-1 Metallic materials-Verification of static uniaxial testing machines-Part 1: Tension/compression testing machines-Verification and calibration of the force-measuring system. sl: European Committee for Standardization, August de 2004," *Document Information*.
- [17] H. Fahrenholz, "The 2012 version of ISO 527 Plastics: Determination of tensile properties," p. 27, 2012.
- [18] "FLIR ONE PRO, Android USB-C," Nov. 23, 2021. <https://support.flir.com/DsDownload/Assets/435-0007-03-en-US.html> (accessed Nov. 23, 2021).
- [19] K. Pooladvand, A. D. Salerni, and C. Furlong, "In-situ thermal monitoring of printed components during rapid prototyping by fused deposition modeling," in *Residual Stress, Thermomechanics & Infrared Imaging and Inverse Problems, Volume 6*, Springer, 2020, pp. 131–140.

5 Discussion

5.1 Method and Results

When the approach to alter and study the effects of modifying settings on thermal properties of the layers was chosen, this was largely based on the available time frame of the project and hardware that was accessible at the time. The method of altering layer temperatures with printing speed set some constraints on how much control over the temperature in the layers it was possible to achieve. Since the goal of the project was to find the relation between layer temperature and material properties, full control over exact temperature was not a priority. Documenting the temperature for different speeds was part of the discovery process. Modification of settings being the constraint of control was also part of the inspiration for TLD. Looking at Figure 8, printing speed grows exponentially with layer temperature and there seems to be a limit where layer temperature converges towards extruder temperature. The constraints of printing speed led to a discussion on how to alter the component to better fit the obtainable settings.

Iterations for the specimen geometry and quality resulted in specimens that were deemed to be sufficient. As mentioned in Section 3.2.1, the ISO 527 standard is not suited for printing standing specimens, as the layer-by-layer breakdown of the CAD-model struggles to compensate for the 0.3 mm thickness of the layers. In addition, the instabilities caused by the inertia of accelerating and decelerating the bed are amplified with thin, standing specimens. In several test specimens this caused a crooked shape to become apparent at 20 mm/s and above (Figure 13). The uneven geometry of specimens at higher printer speeds also leaves the question of how much of the reduced performance is due to layer temperature and how much is caused by the worsened geometry. While all specimens above 20 mm/s had geometrical deformities and could be disregarded, they were included to the study to study if higher layer temperatures would affect the strength even if the geometry was poor. However, due to the large deformations and small increase in layer temperature, specimens above 30 mm/s were omitted from the paper, as they did not add any further value to the results. Figure 12 displays the progress of surface roughness with increasing layer temperature. The final temperature, approximately 182°C corresponds to a printer speed of 18 mm/s. A higher printing speed of 18 mm/s caused a surface roughness out of bounds for the measurement tool, indicating geometries are getting too rough. Some specimens also showed deformations at the bottom where some material was protruding out from the bottom of the specimen that stood on the bed, and can be observed in specimens with printing speeds of 20 mm/s and higher (Figure 13). The deformations of the bottom might cause shortening of the specimen. Shorter prints cause problems for the layer bonding higher up in the print, as the nozzle rises by the set layer thickness for each layer. If the specimen is shortened by deformations at the bottom, the material in the upper parts is deposited at a higher elevation over the previous layer than intended and causes worse bonding with more voids and less accuracy. Another development with speed and temperature is the change in width and thickness (Figure 11). Looking at the cross-sections in Figure 17 it is clear that the geometry starts to deviate quite fast from the original dimension as printer speed and layer temperature increases. v4_01 and the following velocities up to v12_01 have more consistent cross-sections, but as layer temperature increases (v16_02 and up), the cross-sections become more rounded and inconsistent. The production and treatment of specimens was a time-consuming process. Having only three specimens in each set for sprinting speed was sufficient to provide the data needed to study performance over a wide range of layer temperatures. However, more specimens for each set would produce more data on standard deviation to clarify the trend better. There were also some inconsistencies as the bed of the printer had to be calibrated and meshed two times in the period where specimens were produced. Additionally, the first specimens printed in the sets of three would stay in the chamber temperature of 70°C for more time than the last one, which might affect the structure slightly as PA6-CF is a semi-crystalline material. The annealing of all specimens at 100°C for 6 hours is thought to even out these changes somewhat.

Tensile testing is one of several relevant test methods to determine material properties. Due to anisotropy and weaker bonds in the Z-direction of components produced by FFF being a constraining factor, testing of tensile performance was considered as a good method to discover the quality of layer bonding. Tensile testing specimens with lower quality geometry led to complications with the breaking points of the specimens. Specimens with more uneven geometry often broke near lumps

where stress concentrations tend to build up, usually in the transition of the specimen, leading to questions regarding the quality of the prints and results. Specimens breaking outside of the gauge length were eliminated, specimens considered to have break point within the gauge length were included in the data set. All specimens in Figure 16 are considered to be within the gauge length and are therefore included in the data set. Figure 18 displays a good breaking point (specimen v5_03), but specimen v5_01 broke in the grip area and the test data for this one was discarded. The breaking points are totally different for two specimens built with the same printing speed, proving experiments with the material is difficult to predict. Similar tests like v5_01 were disregarded and replaced by new ones, which gave similar breaking points to those in Figure 16. Voids caused by insufficient infill are weak points within the part [32] and it is important to notice which layer temperatures leaves larger voids and which one doesn't, see Figure 17. Voids are not visible in v4_01, but appears more and more from v6_01 up to v20_02, then it seems to fade away again. Even though no voids is visible in v4_01 it has a nominal UTS of 44.6 MPa, compared to v8_01 which has a UTS of 76.0 MPa (Section D), and clearly has voids. This indicates that the quality of bonding is far more important than the amount of infill. The optimal combination would of course to have no voids in the specimen with best bonding. There is much room for improvements in the printing process, and creating infill that eliminates voids should improve strength considerably.

The elongation data in Figure 15 is based on crosshead measurements from the test machine, which have some sources of error. Specimens with printing speed of 9 mm/s slipped during testing (Figure D.4) and was therefore mounted grip-paper to prevent slipping. The slipping led to artificial measurements of elongation, causing the highest peak in Figure 15. Adjusting the tightening of the grips helped reduce slip without the use of grip-paper, but still some indications of slipping could be observed on some of the specimens and needed to be done over. Elongation data was considered to be flawed and of poor quality, and is therefore only considered an indication of the development, and not as actual material data. For this reason, strain was not calculated, as it would be based on averages of very approximate values on both elongation and original length of the specimens. This is also why strain data was not included in the paper, and why Young's modulus was not studied. Figure 15 does show somewhat longer elongation for temperatures with higher UTS (Figure 14), even when disregarding the artificially high peak. In later testing these factors must be prioritized to gather more detailed data of materials experimented with.

The measuring of layer temperatures was performed with a compact thermal camera for use with smartphones. As the temperatures were read off of a video from the first few frames after the nozzle moved away from the surface of the print, there are several uncertainties in addition to the $\pm 3^\circ\text{C}$ accuracy of the camera itself. Layer temperatures at the surface of prints quickly dropped after the nozzle moved away, and video recordings were manually studied frame by frame to find measured layer temperatures. This introduces variations in temperature readings in each recording. Another factor is the change in emissivity of the material as temperature rises. One study found that this effect lead to a misread of 36°C when readout temperature was 240°C for Acrylonitrile Butadiene Styrene (ABS) [33]. While temperature readings might be somewhat inaccurate, the trend in material properties for changes in layer temperatures is still reliable.

With the differences between temperatures in the specimens (Figure 9) and the component sections (Figure 19), it became apparent that the combination of geometry and settings proved to be more significant than first expected. While the cross-section of the component was expected to need a higher printing speed to achieve temperatures close to those of the specimens, the limitations of how high printing speed can be used was a demonstration of the limited control by modifying printing speed. This sparked the idea that settings alone will not be enough to optimize layer temperatures in printing of components. Components should be designed with thermal layer properties in mind, ensuring the layers are built such that optimum temperature is reached. TLD is based on design of components and appropriate settings which makes applicable for a wider range of printers, without making hardware modifications. By purely looking at the layer temperature, it might seem that hardware able provide exact layer temperature makes the idea of TLD irrelevant. However, since the main goal of TLD is to find the right combination of material-, printer- and printing- properties, there will always be ways to optimize the design of a component based on thermal properties. TLD is not only adjustments of settings, but a way of thinking for designing AM components for FFF.

Application of TLD on a component, proved to have a noticeable effect on the layer temperatures.

The effects of added mass and change in cross-section clearly had an effect on the heat distribution and overall layer temperature (Figure 19b). The heat became more evenly distributed, although the highest temperature was lower at 106.3°C. Adding mass showed to have great effect, as the peak temperature in the original component was 123.9°C for the thicker section. The lower temperatures are not measured accurately due to limitations of the thermal camera, but it is clear that they are below the temperature of the bed at 80°C in the original model. Even the TLD model shows low temperatures in the thin cross-sections that were left unchanged. Note however, that none of the temperatures in the component reaches the temperatures measured in the material tests, and it is not possible to assume the properties throughout the part. Judging by the graph in Figure 14 it can be expected that the bonding in the components are far below the optimum UTS of the material. Although there are improvements within the TLD component, these simple changes are not enough to utilize the engineering polymer, essentially wasting valuable mechanical properties. The results showcase how printing speeds to alter layer temperature is not a scalable factor, but depends on several factors and thus supports the claim that TLD is powerful tool to ensure optimal quality in FFF.

The main results presented in Section 4.2 are the relations between layer temperature and UTS (Figure 14) as well as the thermal effects of adding mass to a component (Figure 19). Figure 14 shows the relation between layer temperatures and strength, indicating that there is an optimal temperature range for layers to bond. Peak values are reaching the higher end of the reported 67.7 ± 4.7 MPa by the manufacturer [25]. Overall, it must be noted that the UTS is calculated based on a nominal cross-section, and the actual values will differ. The reduction of strength at low and high temperatures shows the trend that was expected. An interesting observation is that the temperature range with the highest UTS, 166°C–175°C, is also the same range with the lowest standard deviation (Figure 14) and highest surface roughness values (Figure 12). The elongation (Figure 15) is generally somewhat longer in this range, even when disregarding the values caused by slipping. Specimens of the respective printing speeds also indicated inter-layer failures, meaning the brittle fracture occurred across layers. Inter-layer failures indicate that the bonding between layers is quite good and that the crack must develop through weak spots in several layers, not only the interface between two layers. These effects show how the strength is improved for the optimal layer temperature through better bonding between layers.

5.2 Significance of Findings and Continuation of Work

TLD is highly relevant for DfAM in the current development of FFF of engineering grade polymers and polymer composites. The work presented in Section 4.2.1 is submitted to the CIRP Design Conference to show the relations between layer temperatures and UTS, geometrical tolerances and surface roughness, in addition to the effects of design on the layer cross-section. These findings are a step toward solving some of the main challenges with ‘material’ and ‘metrology’ in AM [15], by developing better production methods and design principles for advanced FFF materials. As there is limited research on effects, the goal of publishing this paper is to encourage further research and highlight the possibilities and need for optimization of layer temperature to produce reliable, high-quality components. Specialized sectors like defense and aerospace, sporting equipment, automobile, and other areas where the ability to produce advanced components on-site is of great value. While the results in this project are dependent on the material used, the methodology and study of thermal effects on the material is highly relevant. The work and results presented in this project scratches the surface of a complex and growing field in AM. As new polymer materials are developed and filaments with various fiber reinforcements and printers become more advanced and available, there are many unknowns regarding structure and material properties. The testing of settings and TLD was only performed with one material, additional filaments need to be explored and experimented with similarly. Finding the properties of more materials will be important to gain the knowledge needed to choose the right material and production method for end applications. Furthermore, the quality of the specimens used for material testing are not optimal, and there is much room for improvement of design, production and testing of the material. Testing the performance of actual components with several variations and iterations on design and print settings is needed to better understand the actual performance of printed parts.

6 Conclusion

The goal of the project was to study thermal effects in the interlayer bonding with different layer temperatures to look for the effect on material performance. The work has resulted in a relation between strength and layer temperatures in FFF of PA6-CF. The methodology used gives results that are consistent and can be implemented into further development of optimal strength within 3D printed structures. The results show that the optimal layer temperatures for PA6-CF in the range of 166-175°C, gives the highest UTS, despite causing minor geometrical deviations in surface roughness and cross section. Thermal imaging analysis provides insight into the development of layer temperature with different settings, and how the temperature decreases over time in the test specimens. It also shows how temperature is distributed down through multiple layers of the specimens during manufacturing. Using material testing to determine strength while documenting corresponding layer temperature creates data that can be used to predict strength through printed parts, by monitoring layer temperature during printing. However, the effects on component properties was limited to the thermal distribution in this project. Mechanical properties in the component based on thermal measurements is not defined as of yet, but should be continued in later work. Furthermore, by learning more about 'material' and 'metrology', Thermal Layer Design can be used as a tool to optimize the design of a component based on layer temperatures. TLD has proven to be a useful tool to ensure even layer temperatures, adding value to the toolbox of DfAM. Component data reveals how extensive the reduction of bonding temperatures is for a design based solely on looks and fit, without taking material properties into account. By applying TLD on components, thermal properties of the layers are significantly improved. Publishing an article on the subject is a step in the right direction to push for more research in the community and for further development of predictable strength through 3D printed components. Additional work should be done on live measuring of layer temperature combined with TLD to find methods that can be implemented for production of high quality 3D printed structures. TLD does set some restrictions on the design, however, it can be developed into a highly efficient tool if the design can be adjusted to fit materials used. Furthermore, results of the relation between strength and layer temperature can be used in later work with PA6-CF. There is still much room for improvement on settings and hardware. Upgrading the hardware with live layer temperature measurements while adjusting the layer temperature would lead to the optimal solution for achieving concise layer temperature, regardless of cross-section. There must be done research on more engineering plastics to widen knowledge and applications for FFF.

Ultimately the goal of finding relations between layer temperatures and material properties was achieved and was applied in a conference paper submission. The application and comparison of material test data on a component was unfortunately not completed, and may be continued in future work.

References

- [1] B. Berman, “3-D printing: The new industrial revolution,” *Business horizons*, vol. 55, no. 2, pp. 155–162, 2012, iISBN: 0007-6813 Publisher: Elsevier.
- [2] I. Gibson, D. Rosen, B. Stucker, and M. Khorasani, “Introduction and Basic Principles,” in *Additive Manufacturing Technologies*, I. Gibson, D. Rosen, B. Stucker, and M. Khorasani, Eds. Cham: Springer International Publishing, 2021, pp. 1–21. [Online]. Available: https://doi.org/10.1007/978-3-030-56127-7_1
- [3] A. Busachi, J. Erkoyuncu, P. Colegrove, F. Martina, C. Watts, and R. Drake, “A review of Additive Manufacturing technology and Cost Estimation techniques for the defence sector,” *CIRP Journal of Manufacturing Science and Technology*, vol. 19, pp. 117–128, 2017, iISBN: 1755-5817 Publisher: Elsevier.
- [4] J. C. Najmon, S. Raeisi, and A. Tovar, “Review of additive manufacturing technologies and applications in the aerospace industry,” *Additive manufacturing for the aerospace industry*, pp. 7–31, 2019, publisher: Elsevier.
- [5] M. Rinaldi, F. Cecchini, L. Pigliaru, T. Ghidini, F. Lumaca, and F. Nanni, “Additive manufacturing of polyether ether ketone (PEEK) for space applications: A nanosat polymeric structure,” *Polymers*, vol. 13, no. 1, p. 11, 2021, publisher: Multidisciplinary Digital Publishing Institute.
- [6] D. E. Cooper, M. Stanford, K. A. Kibble, and G. J. Gibbons, “Additive manufacturing for product improvement at Red Bull Technology,” *Materials & Design*, vol. 41, pp. 226–230, 2012, iISBN: 0261-3069 Publisher: Elsevier.
- [7] I. Gibson, D. Rosen, B. Stucker, and M. Khorasani, “Material Extrusion,” in *Additive Manufacturing Technologies*, I. Gibson, D. Rosen, B. Stucker, and M. Khorasani, Eds. Cham: Springer International Publishing, 2021, pp. 171–201. [Online]. Available: https://doi.org/10.1007/978-3-030-56127-7_6
- [8] F. M. Duarte, J. A. Covas, and C. S. F. da, “Predicting the effect of build orientation and process temperatures on the performance of parts made by fused filament fabrication,” *Rapid Prototyping Journal*, vol. ahead-of-print, no. ahead-of-print, Jan. 2021. [Online]. Available: <https://doi.org/10.1108/RPJ-04-2021-0084>
- [9] H. Li, T. Wang, J. Sun, and Z. Yu, “The effect of process parameters in fused deposition modelling on bonding degree and mechanical properties,” *Rapid Prototyping Journal*, vol. 24, no. 1, pp. 80–92, Jan. 2018, publisher: Emerald Publishing Limited. [Online]. Available: <https://doi.org/10.1108/RPJ-06-2016-0090>
- [10] P. Striemann, D. Hülsbusch, M. Niedermeier, and F. Walther, “Optimization and Quality Evaluation of the Interlayer Bonding Performance of Additively Manufactured Polymer Structures,” *Polymers*, vol. 12, no. 5, p. 1166, May 2020, number: 5 Publisher: Multidisciplinary Digital Publishing Institute. [Online]. Available: <https://www.mdpi.com/2073-4360/12/5/1166>
- [11] A. Das, C. A. Chatham, J. J. Fallon, C. E. Zawaski, E. L. Gilmer, C. B. Williams, and M. J. Bortner, “Current understanding and challenges in high temperature additive manufacturing of engineering thermoplastic polymers,” *Additive Manufacturing*, vol. 34, p. 101218, 2020, iISBN: 2214-8604 Publisher: Elsevier.
- [12] A. Birkelid, S. W. Eikevåg, C. W. Elverum, and M. Steinert, “High-performance polymer 3D printing – open-source liquid cooled scalable printer design,” *HardwareX*, vol. Under Review, Nov. 2021.
- [13] M. K. Thompson, G. Moroni, T. Vaneker, G. Fadel, R. I. Campbell, I. Gibson, A. Bernard, J. Schulz, P. Graf, and B. Ahuja, “Design for Additive Manufacturing: Trends, opportunities, considerations, and constraints,” *CIRP annals*, vol. 65, no. 2, pp. 737–760, 2016, iISBN: 0007-8506 Publisher: Elsevier.

- [14] I. Gibson, D. Rosen, B. Stucker, and M. Khorasani, “Design for Additive Manufacturing,” in *Additive Manufacturing Technologies*, I. Gibson, D. Rosen, B. Stucker, and M. Khorasani, Eds. Cham: Springer International Publishing, 2021, pp. 555–607. [Online]. Available: https://doi.org/10.1007/978-3-030-56127-7_19
- [15] S. A. Tofail, E. P. Koumoulos, A. Bandyopadhyay, S. Bose, L. O’Donoghue, and C. Charitidis, “Additive manufacturing: scientific and technological challenges, market uptake and opportunities,” *Materials today*, vol. 21, no. 1, pp. 22–37, 2018, iSBN: 1369-7021 Publisher: Elsevier.
- [16] R. Hashemi Sanatgar, C. Campagne, and V. Nierstrasz, “Investigation of the adhesion properties of direct 3D printing of polymers and nanocomposites on textiles: Effect of FDM printing process parameters,” *Applied Surface Science*, vol. 403, pp. 551–563, May 2017. [Online]. Available: <https://www.sciencedirect.com/science/article/pii/S0169433217301137>
- [17] V. E. Kuznetsov, A. N. Solonin, A. Tavitov, O. Urzhumtsev, and A. Vakulik, “Increasing strength of FFF three-dimensional printed parts by influencing on temperature-related parameters of the process,” *Rapid Prototyping Journal*, vol. 26, no. 1, pp. 107–121, Jan. 2019, publisher: Emerald Publishing Limited. [Online]. Available: <https://doi.org/10.1108/RPJ-01-2019-0017>
- [18] G. D. Goh, Y. L. Yap, H. K. J. Tan, S. L. Sing, G. L. Goh, and W. Y. Yeong, “Process–Structure–Properties in Polymer Additive Manufacturing via Material Extrusion: A Review,” *Critical Reviews in Solid State and Materials Sciences*, vol. 45, no. 2, pp. 113–133, Mar. 2020, publisher: Taylor & Francis eprint: <https://doi.org/10.1080/10408436.2018.1549977>. [Online]. Available: <https://doi.org/10.1080/10408436.2018.1549977>
- [19] V. Kishore, C. Ajinjeru, A. Nycz, B. Post, J. Lindahl, V. Kunc, and C. Duty, “Infrared preheating to improve interlayer strength of big area additive manufacturing (BAAM) components,” *Additive Manufacturing*, vol. 14, pp. 7–12, 2017, iSBN: 2214-8604 Publisher: Elsevier.
- [20] J. Butt and R. Bhaskar, “Investigating the effects of annealing on the mechanical properties of FFF-printed thermoplastics,” *Journal of Manufacturing and Materials Processing*, vol. 4, no. 2, p. 38, 2020, publisher: Multidisciplinary Digital Publishing Institute.
- [21] V. Kishore, C. Ajinjeru, A. Nycz, B. Post, J. Lindahl, V. Kunc, and C. Duty, “Infrared preheating to improve interlayer strength of big area additive manufacturing (BAAM) components,” *Additive Manufacturing*, vol. 14, pp. 7–12, Mar. 2017. [Online]. Available: <https://www.sciencedirect.com/science/article/pii/S221486041630330X>
- [22] A. Gleadall, “FullControl GCode Designer: open-source software for unconstrained design in additive manufacturing,” *Additive Manufacturing*, vol. 46, p. 102109, 2021, iSBN: 2214-8604 Publisher: Elsevier.
- [23] Tecafil, “TECAFIL PEEK VX CF30 black 1,75 mm - 500g,,” Dec. 2021. [Online]. Available: <https://filaments.ensingerplastics.com/products/carbon-fiber-peek-filament-tecafil-peek-vx-cf30-black-1-75-mm-500g>
- [24] Zortrax, “Z-PEI 9085 Aerospace-Grade Flame-Retardant Filament,,” Dec. 2021. [Online]. Available: <https://zortrax.com/filaments/z-pei-9085/>
- [25] Polymide, “PolyMide™ PA6-CF,,” Oct. 2021. [Online]. Available: <http://eu.polymaker.com/product/polymide-pa6-cf/>
- [26] J. Liang, Y. Xu, Z. Wei, P. Song, G. Chen, and W. Zhang, “Mechanical properties, crystallization and melting behaviors of carbon fiber-reinforced PA6 composites,” *Journal of Thermal Analysis and Calorimetry*, vol. 115, no. 1, pp. 209–218, 2014, iSBN: 1588-2926 Publisher: Springer.
- [27] R. H. Sanatgar, C. Campagne, and V. Nierstrasz, “Investigation of the adhesion properties of direct 3D printing of polymers and nanocomposites on textiles: Effect of FDM printing process parameters,” *Applied Surface Science*, vol. 403, pp. 551–563, 2017, iSBN: 0169-4332 Publisher: Elsevier.

-
- [28] S. W. Eikevåg and C. Elverum, “High-performance polymer 3D printing – open-source liquid cooled scalable printer design,” vol. 1, Nov. 2021, publisher: Mendeley Data. [Online]. Available: <https://data.mendeley.com/datasets/7sjjmr9bz2/1>
- [29] MTS, “MTS,” Dec. 2021. [Online]. Available: <https://www.mts.com/en/products/materials/static-materials-test-systems/criterion-electromechanical>
- [30] FLIR, “FLIR ONE PRO, Android USB-C,” Dec. 2021. [Online]. Available: <https://support.flir.com/DsDownload/Assets/435-0007-03-en-US.html>
- [31] H. Fahrenholz, “The 2012 version of ISO 527 Plastics: Determination of tensile properties,” p. 27, 2012.
- [32] M. Fernandez-vicente, W. Calle, S. Ferrándiz, and A. Conejero, “Effect of Infill Parameters on Tensile Mechanical Behavior in Desktop 3D Printing,” *3D Printing and Additive Manufacturing*, vol. 3, pp. 183–192, Sep. 2016.
- [33] K. Pooladvand, A. D. Salerni, and C. Furlong, “In-situ thermal monitoring of printed components during rapid prototyping by fused deposition modeling,” in *Residual Stress, Thermo-mechanics & Infrared Imaging and Inverse Problems, Volume 6*. Springer, 2020, pp. 131–140.

Appendix

A Calibration, repairing and modification of hardware



Figure A.1: First vase mode calibration print.

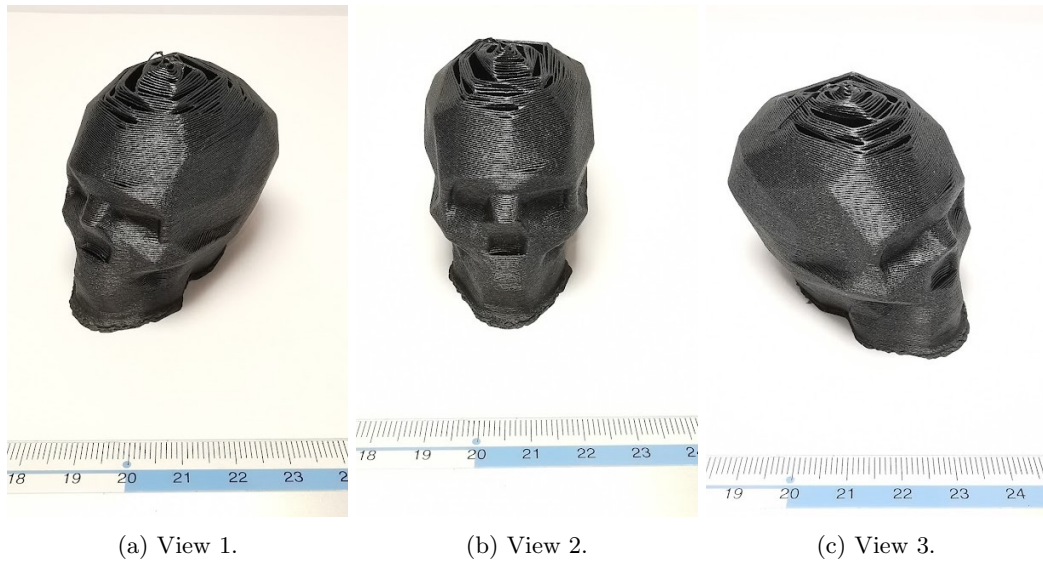


(a) Steel spring resting on the roller, causing friction.



(b) Aluminium plate mounted to keep the steel spring away from the rollers.

Figure A.2: Modification of mounting for water cooling of hot end.



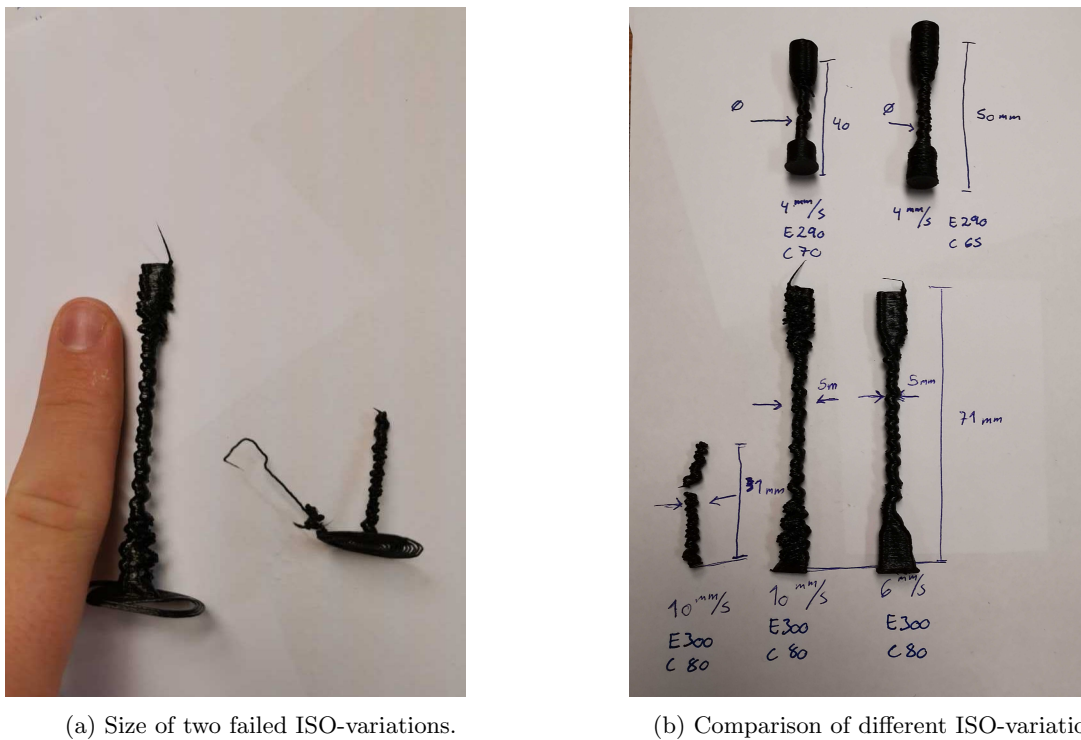
(a) View 1.

(b) View 2.

(c) View 3.

Figure A.3: Second vase mode calibration print.

B Testing geometries and settings



(a) Size of two failed ISO-variations.

(b) Comparison of different ISO-variations.

Figure B.1: Failed tensile test prints.

Figure B.2 Shows a micrography of two specimens. Several pictures are stitched together to show the geometric quality. Left: specimen printed with a printer speed of 7 mm/s and two perimeters. Right: specimen printed with a printer speed of 25 mm/s and one perimeter. The specimen to the left has a smoother surface and better shape than the specimen to the right, which shows geometric kinks, especially in the transition.



Figure B.2: Geometric differences, printer speed 7 mm/s (left) and 25 mm/s (right).

C Backrest component

The component was designed for prototyping and produced in PLA. It introduced some interesting failures during testing, which can be seen by scanning the code in Figure C.1. When mounted on a test rig and mounted with a strap on the backrest to hold the person using the rig, the prototypes made with this design tended to break horizontally in plane with the layers. The main problems were deformations during testing that introduced bending moments in the component. Small cracks initializing in the thin sides of the backrest grew into larger cracks during cyclic loading. Cracks also initiated in the grooved area in the middle of the backrest, resulting in the failure of the backrest after a short period of only 5-10 cycles.

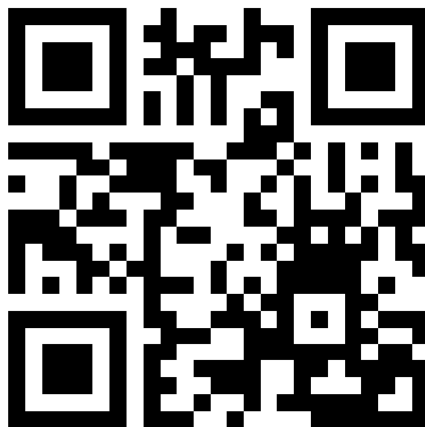


Figure C.1: Link to a video of the component failing.

D Additional results

Specimen	Length Actual (mm)	Length Deviation (mm)	Width Actual (mm)	Width Deviation (mm)	Thickness Actual (mm)	Thickness Deviation (mm)	Ra (mikro_m)
v50_01	62.6	2.4	9.46	0.54	6.63	1.63	Non Measurable
v50_02	62.8	2.2	9.66	0.34	6.59	1.59	Non Measurable
v50_03	62.6	2.4	9.46	0.54	6.44	1.44	Non Measurable
v50_04	0	65	10	10	5	5	Non Measurable
v40_01	62.5	2.5	9.51	0.49	6.56	1.56	Non Measurable
v40_02	62.2	2.8	9.49	0.51	6.52	1.52	Non Measurable
v40_03	62.7	2.3	9.54	0.46	6.55	1.55	Non Measurable
v30_01	62.7	2.3	9.49	0.51	6.49	1.49	Non Measurable
v30_02	62.1	2.9	9.65	0.35	6.4	1.4	Non Measurable
v30_03	62.9	2.1	9.51	0.49	6.4	1.4	Non Measurable
v25_01	63.2	1.8	10.18	0.18	6.83	1.83	Non Measurable
v25_02	63.2	1.8	10.24	0.24	6.19	1.19	Non Measurable
v25_03	63.3	1.7	10.28	0.28	5.74	0.74	Non Measurable
v20_01	62.6	2.4	9.59	0.41	6.65	1.65	Non Measurable
v20_02	63.2	1.8	9.55	0.45	6.19	1.19	Non Measurable
v20_03	62.9	2.1	9.51	0.49	6.14	1.14	Non Measurable
v18_01	62.2	2.8	9.49	0.51	6.18	1.18	28.95
v18_02	62.6	2.4	9.61	0.39	6.06	1.06	38.92
v18_03	63	2	9.54	0.46	6.09	1.09	30.64
v16_01	62.2	2.8	9.53	0.47	6.05	1.05	28.97
v16_02	62.8	2.2	9.58	0.42	6.11	1.11	32.91
v16_03	63	2	9.63	0.37	5.99	0.99	39.46
v14_01	63.3	1.7	9.6	0.4	5.88	0.88	34.3
v14_02	62.9	2.1	9.61	0.39	5.92	0.92	30.81
v14_03	62.4	2.6	9.61	0.39	5.97	0.97	23.01
v12_01	62.8	2.2	9.74	0.26	5.89	0.89	27.35
v12_02	63	2	9.69	0.31	5.87	0.87	33.09
v12_03	62.5	2.5	10.25	0.25	5.42	0.42	Non Measurable
v11_01	64.1	0.9	10.14	0.14	5.42	0.42	42.24
v11_02	63.2	1.8	10.35	0.35	5.76	0.76	41.46
v11_02	64.1	0.9	9.41	0.59	5.98	0.98	38.42
v11_03	64.1	0.9	9.38	0.62	5.99	0.99	25.9
v10_01	62.6	2.4	9.71	0.29	5.76	0.76	32.06
v10_02	63.3	1.7	9.95	0.05	5.71	0.71	42.39
v10_03	63	2	9.67	0.33	5.75	0.75	39.09
v9_01	62.5	2.5	9.56	0.44	5.7	0.7	28.51
v9_02	63.1	1.9	10.19	0.19	5.79	0.79	40.86
v9_03	62.9	2.1	9.79	0.21	5.73	0.73	32.8
v8_01	63.5	1.5	10.05	0.05	6.27	1.27	48.77
v8_02	63.2	1.8	9.89	0.11	5.14	0.14	33.74
v8_03	62.7	2.3	9.94	0.06	5.63	0.63	30.12
v8_01	64.1	0.9	10.45	0.45	5.77	0.77	29.6
v8_02	64.2	0.8	9.77	0.23	5.78	0.78	27.4
v8_03	64.1	0.9	9.78	0.22	5.82	0.82	28.39
v7_01	63.4	1.6	10.63	0.63	5.63	0.63	30.54
v7_02	64.1	0.9	10.83	0.83	5.6	0.6	32.4
v7_03	64	1	10.27	0.27	5.5	0.5	28.43
v6_01	62.5	2.5	10.41	0.41	5.46	0.46	30.36
v6_02	63	2	10.03	0.03	5.56	0.56	27.54
v6_03	63.4	1.6	10.1	0.1	5.52	0.52	32.06
v5_01	63.5	1.5	10.45	0.45	5.41	0.41	37.82
v5_02	62.3	2.7	10.29	0.29	5.37	0.37	25.53
v5_03	63	2	10.23	0.23	5.45	0.45	36.93
v4_01	63.4	1.6	10.47	0.47	5.34	0.34	33.34
v4_02	63.1	1.9	10.36	0.36	5.39	0.39	27.07
v4_03	62.6	2.4	10.45	0.45	5.35	0.35	23.61

Figure D.1: Complete set of measurements from the specimens.

Tensile test data from the MTS Criterion machine.

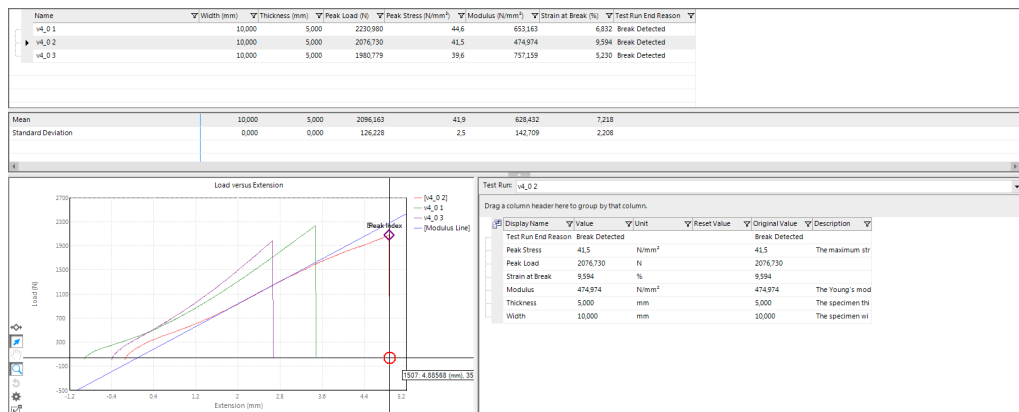


Figure D.2: Tensile test data for specimens printed the velocity of 4 mm/s.

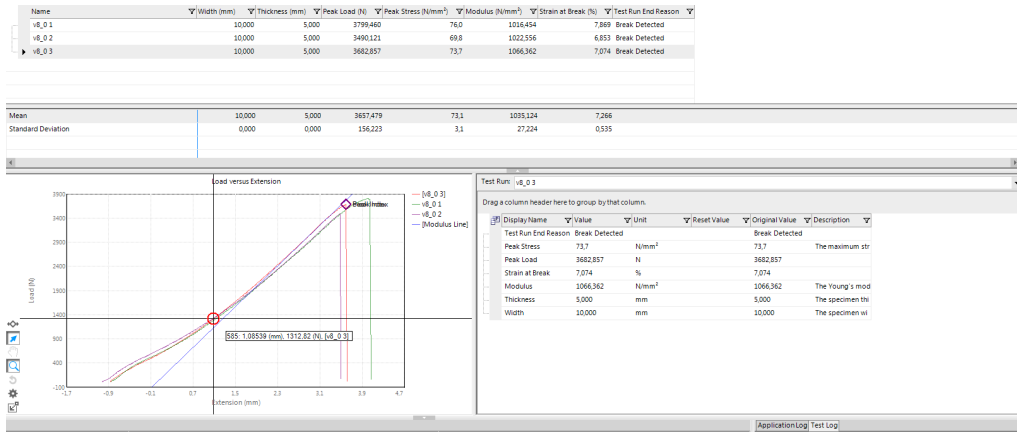


Figure D.3: Tensile test data for specimens printed the velocity of 8 mm/s.



Figure D.4: Slip marks after cancelled tensile test.

